PARTICLE TRANSPORT, INTERACTION AND AGGLOMERATION FOR NUCLEAR REACTOR AND NUCLEAR WASTE FLOW APPLICATIONS

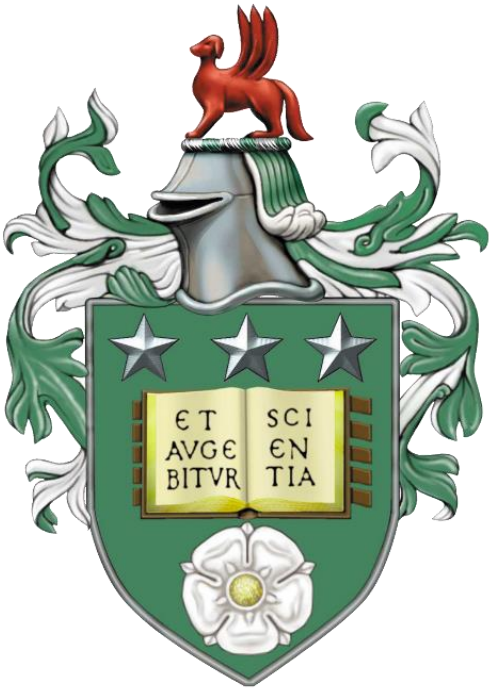

Lee Francis Mortimer

The University of Leeds

School of Chemical and Process Engineering

Submitted in accordance with the requirements for the degree of

Doctor of Philosophy

March 2019

DECLARATION

The candidate confirms that the work submitted is his own, except where work which has formed part of jointly authored publications has been included. The contribution of the candidate and the other authors to this work has been explicitly indicated below. The candidate confirms that appropriate credit has been given within the thesis where reference has been made to the work of others.

Results chapter 1:

Conference proceedings - PARTICLES 2017 - Particle concentration and Stokes number effects in multi-phase turbulent channel flows - L. F. Mortimer, M. Fairweather, D. O. Njobuenwu

Results chapter 2:

Conference proceedings - ETMM11 - Effect of four-way coupling on the turbulence field in multi-phase channel flows - L. F. Mortimer, M. Fairweather, D. O. Njobuenwu

Conference proceedings - THMT18 - Near-wall interparticle collision dynamics in multi-phase turbulent channel flows - L. F. Mortimer, M. Fairweather, D. O. Njobuenwu

Results chapter 3:

Conference proceedings - ETMM12 - Dynamics of fully resolved binary particle interactions in isotropic turbulence - L. F. Mortimer, M. Fairweather, D. O. Njobuenwu

For all jointly authored publications, other authors contributed to biweekly supervisory meetings, sharing ideas and offering guidance, as well as proof reading the papers. The simulation and analysis work, as well as writing of the papers, is attributed to myself.

ACKNOWLEDGEMENTS

Here, I would like to take the opportunity to offer my deepest thanks to all those who have supported me throughout this PhD.

First of all, my sincere gratitude is offered to my supervisor, Professor Mike Fairweather, for providing the knowledge, encouragement and patience to see my project through to the end. His endless advice, motivation and guidance is greatly appreciated. I'd also like to thank Dr. Derrick Njobuenwu for offering his expertise and support when I first joined the school.

I am grateful to all the members of the nuclear research group for sharing their ideas and advice whenever I hit dead ends, and to the students and research fellows in office 2.22 who were a pleasure to work with.

I'd like to thank the organisers of the Next Generation Nuclear CDT for the valuable opportunities I was offered outside of the University. I am also grateful to members of my cohort, including Dan, Alex and Kevin, for all the Manchester meetups and conflabs.

I must extend my gratitude to my family who have all supported me throughout my PhD. My thanks go to my mother, Debbie and my father, Nigel; to my late stepfather, Tim and to my brothers, Warren and Cody. Thanks also go out to my good friends Mike, Sarah and Ollie.

Finally to my better half, Marie, to who I am utterly grateful. I am confident that none of this could have happened without her endless emotional support.

ABSTRACT

The work presented explores the dynamics of multiphase turbulent flows, with particular emphasis on micro-scale particle-fluid and particle-particle interactions and their effects such as turbulence modulation, and particle collisions and agglomeration. A range of simulation techniques are used to elucidate the dynamics that underpin the fine-scale motions of varying particle-fluid density ratio flows, with particle behaviours ranging from tracer-like to inertial, momentum-driven.

To study the bulk behaviour of high-concentration dispersions, a single-phase turbulent channel flow at a shear Reynolds number of 180 is obtained and investigated using a spectral element-based direct numerical simulation (DNS) code. To model large quantities of dispersed solids, a Lagrangian particle tracker (LPT) is developed, with both simulation tools validated against recent DNS-based results, with strong agreement shown. The LPT is used primarily to study bulk flow mechanisms such as dispersion, interaction and agglomeration for both tracer-like and inertial particles. Phenomenon not explained in the literature is elucidated using a range of analytical techniques. In particular, the existence of near-wall increased particle streamwise velocity fluctuations is explained through the generation of understanding on particle migration mechanisms using turbulence classification techniques. Two-way coupling and particle-particle collisions are explored which relate the dynamics of the particulate phase to the turbulent structures experienced within the channel flow.

Finally, an immersed boundary method is implemented to perform fully-resolved binary particle collision simulations in different scales of turbulence. Inter-surfacial forces such as van der Waals attraction and electric double layer repulsion are explicitly calculated to study interaction and agglomeration events on the particle scale. Results indicate that particles are more likely to aggregate and remain bound in regions of low turbulence, provided they collide. Investigations are also performed surrounding the variation of chemical and mechanical properties, with the coefficient of restitution exhibiting the greatest effect on the resulting dynamics.

CONTENTS

LIST OF TABLES

LIST OF FIGURES

NOMENCLATURE

Roman letters:

A	Linear forcing function coefficient
$\boldsymbol{A}$	Orientation matrix
C_D, C_L	Drag and lift coefficient
$\boldsymbol{D}$	Fluid velocity deviatoric tensor
d_P	Particle diameter
d_P^*	Particle diameter in bulk units
$E(\kappa)$	Energy of eddy with wavenumber κ
E_i	Number of SEM elements in direction i
$\boldsymbol{F}$	General force vector
Fr	Froude number
$\boldsymbol{f}_{LF}$	Linear forcing function
$\boldsymbol{f}_{2W}^{*i}$	PSIC momentum coupling force
f_D	Drag force empirical correlation function
f_L	Shear lift force empirical correlation function
$\boldsymbol{g}$	Acceleration due to gravity vector
H	Hamaker constant
H_{kl}	Intersurfacial distance between particle *k* and *l*
H^*	Hamaker constant in bulk units
I_{sphere}	Spherical moment of inertia
k	Turbulence kinetic energy
k_B	Boltzmann's constant
L	General characteristic length scale
l	Eddy length scale
M_{VM}	Virtual or added mass term
m_P	Particle mass
N_f	Total number of faces in IBM mesh
N_P	Total number of particles
p	Pressure
$\boldsymbol{Q}$	Quaternion vector

Q	Q-criterion
q_i	Quaternion component
R	Third invariant of velocity gradient tensor
Re	General Reynolds number
Re_η	Reynolds number based on Kolmogorov scale
Re_λ	Reynolds number based on Taylor microscale
Re_τ	Reynolds number based on shear flow scale
Re_B	Reynolds number based on bulk flow scale
Re_C	Reynolds number based on the centreline velocity
Re_P	Particle Reynolds number
Re_P	Reynolds number of local shear flow
St_B	Particle Stokes number based on bulk flow scales
St_K	Particle Stokes number based on the Kolmogorov scale
St_τ, St^+	Particle Stokes number based on shear flow scales
$\boldsymbol{T}$	Viscous torque vector
T_F	Fluid temperature
t	Time
t_{col}	Collision overlap time
t^*	Time in bulk units
t^+	Time in shear units
U	General characteristic velocity scale
$\boldsymbol{u}_{F,P}$	Local instantaneous fluid/particle velocity vector
$\boldsymbol{u}^*_{F,P}$	Local instantaneous fluid/particle velocity vector in bulk units
$\boldsymbol{u}^+_{F,P}$	Local instantaneous fluid/particle velocity vector in shear units
$\overline{\boldsymbol{u}}_{F,P}$	Time-averaged local fluid/particle velocity vector
$\boldsymbol{u}'_{F,P}$	Local instantaneous fluid/particle velocity fluctuation vector
$\boldsymbol{u}^*_S$	Particle-fluid slip velocity in bulk units
$u_{F,P}$	Streamwise (x) instantaneous fluid/particle velocity component
u'_{rms}	Root mean square fluid velocity fluctuation

u_η	Kolmogorov velocity scale
V_F	Fluid volume
V_P	Particle volume
$v_{F,P}$	Wall-normal (y) instantaneous fluid/particle velocity component
$w_{F,P}$	Spanwise (z) instantaneous fluid/particle velocity component
$\boldsymbol{x}$	General position vector
$\boldsymbol{x}^*$	General position vector in bulk units
$\boldsymbol{x}^+$	General position vector in shear units

Greek letters:

β	Ratio between shear flow and particle Reynolds numbers
δ	Channel half-height
δ_0	Minimum contact distance for VDV attraction
ϵ	Energy dissipation rate
Θ	Reduced surface potential
θ	General angle
η	Kolmogorov length scale
ϕ_P	Particulate phase volume fraction
κ	Eddy wavenumber
κ	Inverse Debye length
λ	Taylor microscale
μ_F	Fluid dynamic viscosity
ν_F	Fluid kinematic viscosity
ρ_F, ρ_P	Fluid and particle phase density
ρ_P^*	Particle-fluid density ratio
$\boldsymbol{\tau}^*$	Newtonian deviatoric stress tensor in bulk units
τ_F	Fluid time scale
τ_P	Particle relaxation time scale
τ_η	Kolmogorov time scale
τ_P^+	Particle relaxation time scale in shear units

τ_P^*	Particle relaxation time scale in bulk units
$\boldsymbol{\omega}_F^*$	Fluid vorticity in bulk units
$\boldsymbol{\omega}$	Particle angular velocity vector
ω_i	Particle angular velocity component

LIST OF ABBREVIATIONS AND ACRONYMS

Acronyms:

AGR	Advanced gas-cooled reactor
CFD	Computational fluid dynamics
CRUD	Chalk River / corrosion related unidentified deposit
DNS	Direct numerical simulation
EDL	Electric double layer
FGMSP	First generation Magnox storage pond
HPIV	Holographic particle image velocimetry
HWA	Hot-wire anemometry
IBM	Immersed boundary method
LDA	Laser doppler anemometry
LDV	Laser doppler velocimetry
LES	Large eddy simulation
LPT	Lagrangian particle tracking / tracker
PDA	Phase-Doppler anemometry
PFSP	Pile fuel storage pond
PIV	Particle image velocimetry
PSIC	Particle-source-in-cell
PWR	Pressurised water reactor
NS	Navier-Stokes
RANS	Reynolds-averaged Navier-Stokes
SEM	Spectral element method
SGS	Sub-grid scale
VDV	van der Waals

1 INTRODUCTION

1.1 Background

The transportation of particles in fluid flows through varying geometries stands as an interest which is of great importance and significance in many industrial sectors and to numerous environmental issues. Aerosol dispersion (Inthavong et al., 2006), chemical and mineral processing (Guha et al., 2007), lung airway biology (Walters and Luke, 2010), tidal currents (Wang et al., 2010) and liquid-fueled combustion (Gosman and loannides, 1983) are but a few of the fields where a detailed understanding of the flow mechanisms and properties are pertinent to the industries' overall quality and efficiency. To obtain such insight, accurate prediction of particle-system and particle-particle interaction dynamics such as dispersion, deposition, interparticle collisions and agglomeration is imperative. With advances in the understanding of these mechanisms, properties such as flow, deposition and aggregation rates can be optimised and existing equipment and processes can be improved in their efficiency and effectiveness. Furthermore, future proposals can be designed to perform more efficiently, reducing costs and improving safety.

Typically, transportive flows are wall-bounded and fall into one of three geometric categories: pipe, duct or channel, with the term ‘duct’ encompassing any polygon-prism. Despite pipe flows occurring most commonly in industry, particle dynamics are more suitably studied in a channel flow wherein the geometry is Cartesian and mean flow properties show sole dependence on their proximity from the wall. This work considers dilute and dense particle dispersions in wall-bounded flows of relevance in nuclear reactor and nuclear waste processing applications.

1.2 Overview of UK nuclear industry

The UK began its journey into nuclear technologies in 1956 with the opening of Calder Hall. The design consisted of four 60 MWe reactors capable of generating electricity for the national grid, the first of its kind to do so. Up until 1964, the primary purpose assigned to the reactors was to produce weapons-grade plutonium, suitable for use in the manufacture of atomic bombs. As the industry matured, and with the construction of new plants, focus shifted to primarily energy generation. Nuclear power currently provides around 21% of the UKs total electricity supply, with 15 reactors operational at present. These consist of 14 advanced gas-cooled reactors (AGR) and a single pressurised water reactor (PWR). Alongside infrastructure for energy generation, Britain also houses the reprocessing and spent fuel storage facility, Sellafield.

As with all widely used energy generation methods, nuclear power offers a range of benefits. Unlike gas and coal plants, nuclear power stations emit approximately zero greenhouse gases such as CO_2 and methane . Their generation is not weather or time-of-day dependent like wind and solar farms. The energy-density of fissile material is extremely high when compared to fossil fuels, therefore there is practically no risk of losing supply, ensuring continuous energy production. A lot of the perceived negatives stem from the fact that the industry generates radioactive waste, with around 27 tonnes of unprocessed spent fuel per 1000MWe plant produced annually (World Nuclear Association, 2018). With a developing nuclear infrastructure, the UK has the framework to provide a stable, reliable and safe means of generating energy. This said, public opinion on nuclear power has had a very long and contentious history. Despite providing a significant portion of the UK's energy, there are safety issues concerning plant operation, waste generation, reprocessing and ethical disposal. These factors must be addressed in detail and with great care in order to improve the public's perception of the industry, which is currently considered by a significant demographic to be a controversial means of power generation. In a 2017 UK survey, 38% of participants supported the use of nuclear energy (BEIS, 2017), an improvement over the past few years, with the Fukushima nuclear accident in Japan inspiring major concerns in 2011. A NEA report 'Five Years after the Fukushima Daiichi Accident – Nuclear Safety Improvements and Lessons Learnt' (NEA, 2016) emphasizes the necessity for safety enhancements as a result of external hazard reassessments.

Alongside improvements to safety, new techniques must be developed to deal with legacy waste generated over the last 50 years. In early 2015, the National Audit Office estimated the clean-up cost at Sellafield Ltd. to be greater than £53 billion (NAO, 2015), contributing to around three quarters of the total UK nuclear clean-up cost (around £70 billion). A primary concern for both the public and those in charge of the clean-up operations is the treatment of the nuclear waste currently residing on the site. The legacy waste is at present stored in ponds and silos awaiting a suitable decommissioning plan wherein the waste will be processed and sent for final disposal in a geological disposal facility.

The first generation Magnox storage pond (FGMSP), which began as a temporary storage solution in the 1950s, is a 6m depth pond designed to hold spent fuel from the original Magnox plants (NDA, 2017). It now contains a highly radioactive sludge (a liquid carrier fluid with solid suspensions such as corroded fuel cladding, other miscellaneous waste and algae). A solution will involve transporting the radioactive sludge away from the FGMSP, whilst preserving the water, which currently acts as a radioactive shield. In recent years, work has begun to remove the sludge, with around 10% of the original volume having now been retrieved, with a current expected completion date of around 2033. A secondary storage facility is the pile fuel storage pond (PFSP) which is a pond designed to hold spent fuel from the original UK nuclear weapons programme. Current work on the removal of radioactive sludge from the PFSP has begun, with material being pumped into a treatment plant close-by. In the near future, other storage facilities such as the pile fuel cladding silo and the Magnox swarf storage silo have been prioritised for clean-up.

In order to improve the rate of processing and removal, new techniques and understanding must be developed surrounding the mobilisation and transportation of these wall-bounded two-phase systems. Firstly, both of the above solutions require knowledge of the material and chemical properties/composition of the sludge, and certain acceptance criteria must be met before a solution can be developed based on the temperature, pressure, flow rate, particle size/shape, concentration and volume of sludge batches (WMSYM, 2016). Once this information is obtained, in order to design (or improve upon a current design) a pump and slurry (waste sludge mixed with water) system, the dynamics of both phases need to be well understood in order to foresee potential issues and maximise efficiency. For instance, a common occurrence with high concentration wall-bounded liquid-solid flow

systems is blockages due to local concentration increases, and so being able to predict and adapt to situations such as these would be invaluable. These can arise due to various dynamic processes: deposition of solids on the outer pipe walls; agglomeration of particles (which depends on the chemical properties of the flow); and particle settling leading to the formation of beds. All of these mechanisms show a strong dependence on the bulk flow properties.

Moving away from waste-processing, similar two-phase systems can be found in reactor operation. The coolant circuit in many nuclear reactors are prone to acquiring particulate phases due to the buildup of CRUD (Chalk River unidentified deposit or corrosion related unidentified deposit) which is a form of ejected material caused by spallation or erosion. These aggregates have been known to deposit on the fuel rods, which can subsequently lead to a variety of issues directly effecting the fuel's performance. For instance, one effect is CRUD-induced localized corrosion, in which poor heat-transfer properties promote local corrosion (Short et al., 2013). Other effects include increased fuel rod radioactivity due to neutron activation in the corrosion products, and CRUD-induced power shift due to boron neutron absorbers (Secker et al., 2004).

1.3 Industrial relevance

Outside of those covered in the nuclear industry, wall-bounded turbulent flows are commonplace throughout many other industrial and natural environments. The transportation of multiphase liquids and gases is a vital process in most industries, whether that be on a small laboratory scale or a large plant/geographical scale. Most plants designed for chemicals, pharmaceuticals or food use pipelines for local transportation (typically a few metres in length). At the other end of the scale, the world’s longest slurry flow is the Black Mesa pipeline from Arizona to Nevada, United States, engineered to transport coal. In general, these transportation systems are fully enclosed and consist of a square or circular cross-section pipe.

As flow-rates increase, instabilities caused by excess kinetic energy and viscosity damping effects in the fluid often lead to the generation of vortices and consequently, turbulence. Above this point it becomes increasingly difficult to predict the motion and behaviour of both the fluid and the dispersed solid phase. In fact, chaotic behaviour within the system means that we are unable to obtain the statistics of the flow theoretically. The

existence of solutions to the Navier-Stokes (NS) equations, used to mathematically describe the motion of viscous fluids, remain presently one of the biggest unsolved physics problems (Claymath, 2018). Hence, without a suitable theoretical solution, one must either (i) simplify the problem by making assumptions surrounding the properties or resolution of interest of the system, or (ii) obtain a computational solution. The latter solution spans a broad field entitled computational fluid dynamics (CFD). Generally, should industry need to model an unladen flow for a certain purpose, the Reynolds-averaged Navier-Stokes (RANS) method of simulation is adopted which resolves solely the mean flow quantities, with the effects of any turbulent fluctuations approximated through modelling. In order to obtain a more accurate representation of the system, we must employ more rigorous simulation techniques.

1.4 Simulation background

With the acceleration of modern computing performance and increasing processing power, CFD has greatly improved its capabilities over the last few decades. A large amount of work into simulation methods of turbulent fluid flow under a range of different geometries has been undertaken during this time. This has generated great interest both in academic and industrial environments. Over the years, three distinct simulation methods capable of modelling turbulence in fluid flows have been developed. Each of these possesses different strengths and weaknesses based on the required computational resources and solution accuracy.

The RANS method decomposes the flow variables into both their time-averaged value and their temporal fluctuations. The NS equations are then solved, obtaining only the averaged flow variables which is a much less computationally intensive process than solving the Navier-Stokes equations directly. However, due to the nature of the averaging method, a lot of information and precision is lost about the turbulent length-scale behaviour of the fluid. This method is employed frequently in industrial investigations due to its swift computational return times.

Large eddy simulation (LES) uses a low-pass filter to remove the smallest turbulence scales from the NS solution. By concentrating only on the large scales, we reduce the computational cost whilst preserving the most important flow details. Similar to RANS, an altered filtered version of the NS equations is solved. To compensate for not explicitly

resolving the small scales, a turbulence model is used to approximate the filtered out effects on the sub-grid scale (SGS). This involves making use of the information we have available about the smallest length scales. Although we do not obtain as precise a solution as if we were to solve the NS equations directly, the LES method still provides us with more accurate flow information than the RANS method and is a good compromise, computationally.

Direct numerical simulation (DNS) solves the NS equations at all relevant turbulence length and time scales. This involves calculation on a mesh which has a maximum nodal spacing which is less than the Kolmogorov length scale, η (the length scale associated with the smallest eddies in the flow). Due to this, the amount of grid points needed for a given domain in order to resolve these scales is very high. Hence, the amount of computations needed per timestep is also very large; the number of floating point operations needed to fully simulate the flow is proportional to Re^3. Here, Re is a dimensionless quantity which is the Reynolds number of the fluid. It is calculated for a given system as the ratio of inertial to viscous forces acting on fluid elements and can be used also as a measure of turbulence level. Therefore, although it is capable of generating precise solutions, DNS is only suitable for specific flows with low Reynolds number and is generally impractical in most engineering scenarios, where time and resource efficiency is valued more so than precision. Despite this, for situations where the interest is in the physical behaviour of the system and obtaining information used to elucidate the flow dynamics, DNS is a very strong option.

In industry, multiscale modelling is a very important tool used to fully understand all features of a system at various different length and time scales. It is often that the study of very fundamental-level physical processes has consequences and knowledge which, when fed back into the bigger picture, can provide a much more insightful overview of the system as a whole. Multiphase transport processes operate on three levels:

- Bulk / macroscopic flow level, which pertains to the macroscopic quantities of the flow such as flow-rate, Reynolds number, bulk flow velocity, dispersed phase concentration, typical aggregate morphology and degree of deposition.

- Turbulence / microscopic level, which refers to the motion of individual fluid elements as well as groups of particles within those elements. Quantities

associated with this level include local particle/fluid velocities, fluid temperatures and pressures, particle densities.

- Particle level, the scale at which individual particles interact with each other. Typical quantities include interparticle distance, van der Waals and electric double layer surface-surface potentials.

Each of these must be understood and modelled suitably to obtain a complete and accurate representation of a particle-laden flow transport process. For existing RANS codes to be improved and adapted to accurately predict multi-phase flows, understanding must be generated surrounding the complexities of the more fundamental processes.

Simulations can also be used to provide information where experiments are difficult to perform, which is particularly an issue in the nuclear industry. Not only are waste slurries very difficult to observe and quantify in terms of their flow characteristics, but we are limited to the study of very specific setups. This removes the ability to determine the effect of modifying flow and material parameters. Simulation allows for us to be very specific and precise about system conditions. This means more efficient use of time and resources, and a greater focus on elucidating the dynamics. In summary, results from high accuracy simulations can be used to reinforce experimental work, predict failures with current designs and provide insight into optimising future systems by determination of operating parameters for best performance, cost-effectiveness and safety.

1.5 Project overview and objectives

As covered in the previous section, fundamental computational and mathematical models provide the basis for accurate modelling of particle and fluid transport processes which are prevalent in industry, nuclear or otherwise. For the work presented in this thesis, we are interested in determining and understanding the behaviour of wall-bounded particulate flows containing both a fluid and particulate phase, similar to those which might exist in the nuclear industry. Exploration into these dynamics should be carried out at various scales, with an emphasis on the more fundamental processes that are likely to impact the bulk motion of the flow.

More specifically, this research aims to provide insight into the dynamics of aggregation-based processes such as CRUD formation by improving our understanding of dispersion,

agglomeration and particle-particle interaction effects both in nuclear waste flows and reactor circuits. This is to be carried out through performance and analysis of fine-tuned multiple simulations, which aim to elucidate the dynamics which underpin the above mechanisms of interest. Furthermore, we aim to employ high fidelity simulation methods, such as DNS, to provide an increased level of accuracy. This will involve designing, implementing and validating new techniques and models, and make use of in-house high performance processing capabilities. The results and knowledge generated from these simulations will be highly valuable in an industrial setting.

Since the research presented in this thesis relies greatly on understanding the physics at micro-particulate scales, we have chosen to pursue utilising a readily available DNS solver. For this project the computer code Nek5000 has been chosen for its good parallel processing scaling and high accuracy capabilities. The single phase simulations will be carried out on a Kolmogorov-scale resolving mesh and performed at a shear Reynolds number of 180. This is due to extensive previous investigations having been carried out at the Reynolds number, and therefore the results can be suitably validated against alternative solution. For modelling particles, a Lagrangian particle tracker (LPT) will be developed, capable of accurately simulating a multi-phase fluid flow.

As detailed above, flows in industry may consist of relatively viscous carrier liquids such as water, and could contain high volume fractions of dispersed media. In these regimes, standard particle simulation techniques need extending in order to account for more complex mechanisms which are likely to have an impact on the flow dynamics. This research aims to investigate the impact which the inclusion of two-way coupling (particle-fluid interaction) and four-way coupling (particle-particle collisions) have on the turbulence field. This will be achieved in stages, but each stage should be capable of producing its own results and physical understandings.

Finally, the LPT approach is highly effective in studying large ensembles of particles, where mean quantities can be studied to understand macroscopic behaviour. However, to fully determine the dynamics of small-scale motion and interaction (which are fundamental to and underpin the large scales), the flow field surrounding the particle must be fully resolved. To study binary particle interactions and agglomerations, an immersed boundary method (IBM) solver is to be developed and implemented.

Below is a list of project objectives:

- Obtain a statistically settled single-phase flow field for a turbulent channel flow at shear Reynolds number $Re_\tau = 180$ using the DNS CFD code, Nek5000. This will be compared with previous DNS and experimental results for validation purposes. A grid-scale sensitivity test close to the Kolmogorov scale will also be carried out.

- Develop a one-way coupled LPT which runs concurrently with Nek5000, advecting the particles using information from the instantaneous flow field. All relevant forces for the range of length and time scales of interest should be implemented. Validation should be performed using previous one-way coupled simulations.

- Conduct one-way coupled multi-phase turbulent channel flow studies using the LPT, paying close attention to the effect of particle phase parameters (size, density) on the resulting trajectories and bulk motion. Analysis should aim to elucidate the mechanisms by which particles are transported throughout regions of the flow, which in turn should provide insight into the potential for dispersion, deposition and resuspension.

- Extend the LPT by implementing two-way coupling and particle-particle collision mechanisms using suitable collision detection algorithms to ensure runtimes remain reasonable.

- Obtain results from one-way, two-way and four-way coupled particulate flows in a low density ratio medium such as water, and a high density ratio medium such as air. The effect of density ratio and concentration on the resulting turbulence statistics for each degree of coupling should be explored in detail. Particle collision statistics should be gathered for each region of the channel to be used in later work.

- Extend the LPT by implementing a deterministic particle-particle agglomeration model, capable of carrying out particle aggregation based on energy-balance considerations.

- Perform simulations of multi-phase channel flows with all coupling mechanisms and agglomeration. Analysis should focus on collision and aggregation rates. The effect of this mechanism on the turbulence field should also be examined and assessed.

- Implement the IBM within Nek5000, wherein particles are modelled as individual meshes within the fluid domain. Pressure, viscous, electric double layer and van der Waals forces should be used to obtain particle motion.

- Generate periodic boxes of isotropically forced turbulence based on typical turbulence levels present in regions of the $Re_\tau = 180$ channel flow. These should be validated against previous DNS results.

- Use the IBM to perform binary particle collisions based on typical interactions as observed in channel flows. Analysis should focus on the effect of turbulence, material properties and chemical properties on the resulting interaction dynamics.

1.6 Thesis organisation

The content within the remaining chapters of this thesis is as follows. Chapter 2 forms a review of relevant literature. We begin by exploring previously performed experimental work to obtain an overview of the types of phenomenon observed in wall-bounded multiphase flows. Previous work using computational modelling and simulation to predict particle-laden flows will also be covered in detail. Chapter 3 will cover the methodology associated with DNS, LPT and IBM methods. Chapter 4 presents the single-phase channel at a shear Reynolds number of 180, along with a validation of the continuous phase solver. Analyses of one-way coupled particle-fluid simulations are also present to introduce and explore some of the dynamic processes observed in these systems. Chapter 5 will introduce the concept of two- and four-way coupling along with particle-particle agglomeration. The focus of this section is to evaluate the effect of particle concentration on particle-turbulence interaction. The remaining results section, Chapter 6, involves using the immersed boundary method to simulate binary particle interactions in varying levels of turbulence. Here we aim explore the conditions under which particle agglomerations take place. Finally, the thesis will be summarised in Chapter 7, where conclusions will be drawn based upon the knowledge obtained throughout the project. Ideas for extending the work presented here will also be discussed.

2 LITERATURE REVIEW

2.1 Introduction

In this review, the relevant terms and concepts which are to be considered and discussed within the literature shall first be introduced. Then, the previous studies based on experimental and computational work on predicting single-phase wall-bounded turbulent flows shall be evaluated. In doing so, an understanding surrounding the flow features a secondary dispersed phase is likely to experience and interact with will be considered. Next, a review of multi-phase flow theory, experiments and simulation work will be carried out. Finally, the review will focus on particle-fluid coupling regimes, interaction and agglomeration LPT and IBM methods, with emphasis on the recently performed simulation techniques that this thesis aims to build upon.

2.2 Turbulence

Due to the nature of the work presented in this thesis, this review will begin with an introduction to the relevant parameters used to describe and quantify turbulent fluid flows.

2.2.1 Reynolds number

In general, any flow can be categorized as either laminar, transitional or turbulent. In a laminar flow, an injected drop of dye (sometimes referred to as a fluid tracer) will follow the streamlines of the fluid precisely. Early researchers, such as Leonardo da Vinci, studied velocity streamlines in various fluid systems. It was noticed that as certain properties of the flow were changed, instabilities in the laminar motion of the flow grew until eddies or vortices were formed. This is commonly referred to as the ‘onset of turbulence’. In contrast with laminar flows, an injected tracer dye would interact with this new flow regime in a chaotic manner, meaning trajectories are unpredictable. Later researchers would attempt to quantify this phenomenon through study of the flow parameters which lead to turbulence, which generated the notion of Reynolds number (Stokes, 1851; Reynolds, 1895). To determine this property, one must assess the ratio

between the inertial forces to the viscous (or friction) forces. For a given system with a characteristic velocity scale U, length scale L and fluid kinematic viscosity ν_F, the Reynolds number is given by:

$$Re = \frac{UL}{\nu_F}. \tag{1}$$

2.2.2 Reynolds' decomposition and turbulence kinetic energy

A turbulent flow field $\boldsymbol{u}_F(\boldsymbol{x}, t)$ can be split up into a mean and time dependent component as follows:

$$\boldsymbol{u}_F(\boldsymbol{x}, t) = \bar{\boldsymbol{u}}_F(\boldsymbol{x}) + \boldsymbol{u}'_F(\boldsymbol{x}, t), \tag{2}$$

where $\boldsymbol{u}_F(\boldsymbol{x}, t)$ is the local instantaneous fluid velocity vector at position $\boldsymbol{x}$ and time t, $\bar{\boldsymbol{u}}_F(\boldsymbol{x})$ is the mean fluid velocity at $\boldsymbol{x}$ and $\boldsymbol{u}'_F(\boldsymbol{x}, t)$ is the instantaneous velocity fluctuation due to turbulence. The overbar refers to a time-averaged quantity, with sample time much greater than the time scales associated with the turbulence. This is Reynolds decomposition and it allows us to obtain a measure of the turbulence through the follow quantities. The root mean square fluid velocity fluctuation (or turbulence intensity when non-dimensionalised against the bulk flow velocity) is defined as:

$$u'_{rms}(\boldsymbol{x}) = \sqrt{\overline{\boldsymbol{u}'_F(\boldsymbol{x}, t)^2}}. \tag{3}$$

This quantity is used throughout the literature as a primary indicator of the level of turbulence in a particular region of a flow. Finally, the fluctuations can be related to the turbulence kinetic energy, k, by:

$$k = \frac{1}{2}\langle \boldsymbol{u}'_F \cdot \boldsymbol{u}'_F \rangle = \frac{1}{2}(\overline{u'^2_F} + \overline{v'^2_F} + \overline{w'^2_F}). \tag{4}$$

2.2.3 Kolmogorov's theory of energy cascade

Turbulent flows were also observed to contain eddies with varying sizes, with larger eddies actually governing the motion of smaller ones (Richardson, 1922). Work investigating this led on to another important concept in turbulence, which is Kolmogorov's theory, which describes the manner in which energy is transferred between vortices and across the length scales (Pope, 2001). Kolmogorov explored the notion of energy dissipation in turbulence. Larger eddies possess instabilities and break up into smaller eddies, transferring their energy to their children. This continues until the Reynolds number associated with the eddy motion is small enough such that viscous forces dissipate the energy into local heat. The energy dissipation rate is represented by ϵ. Kolmogorov (1941) argues that at small scales, direction bias is lost and the turbulence is isotropic such that $\overline{u_F'^2} = \overline{v_F'^2} = \overline{w_F'^2}$. This implies that at small length and time scales, the statistics of the fluid motion are geometry independent. These scales are the Kolmogorov scales and are as follows:

$$\eta = \left(\frac{\nu_F^3}{\epsilon}\right)^{\frac{1}{4}}, \tag{5}$$

$$\tau_\eta = \left(\frac{\nu_F}{\epsilon}\right)^{\frac{1}{2}}. \tag{6}$$

Here, η is the Kolmogorov length scale and τ_η is the Kolmogorov time scale. Note that the relation $Re_\eta = \eta u_\eta / \nu_F = 1$ holds, where Re_η is the Reynolds number based on the Kolmogorov scale and $u_\eta = (\epsilon \nu_F)^{1/4}$ is the Kolmogorov velocity scale.

2.2.4 Taylor microscale

An intermediate length scale is the Taylor microscale, which falls within the inertial subrange, larger than the dissipative Kolmogorov-scale eddies but smaller than the integral length scale where most of the energy-containing eddies reside. For isotropic turbulence, the Taylor microscale is as follows:

$$\lambda = \left(\frac{10\nu_F k}{\epsilon}\right)^{\frac{1}{2}}. \tag{7}$$

From this we can define a Reynolds number based on the Taylor microscale as:

$$Re_\lambda = \frac{u'_F \lambda}{\nu_F}. \tag{8}$$

2.2.5 Energy spectra

In turbulence theory, it is often of interest how the energy is distributed between different eddy sizes. This distribution is referred to as an energy spectrum, which is a mapping between an eddy wavenumber κ and the energy associated with that eddy size, $E(\kappa)$. The wavenumber κ is given by $\kappa = 2\pi/l$ where l is the eddy length scale. A generalised illustration of a typical energy spectrum for a given turbulent system is presented below in Figure 2.1.

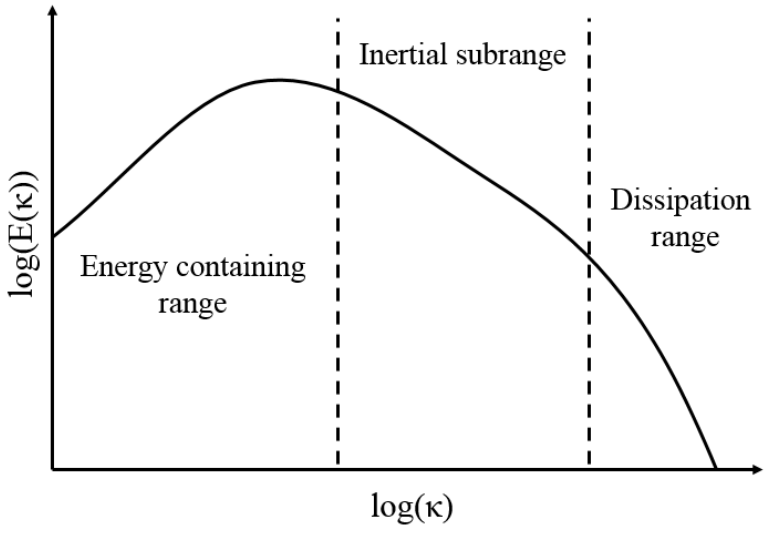

Figure 2.1: Typical energy spectrum for turbulent system. $E(\kappa)$ is the energy contained within an eddy of wavenumber κ.

Expanding on early work performed by other authors (Pao, 1965; Lin, 1972; Hill, 1978), which offered good agreement for different regions of the spectrum, Driscoll et al. (1983) developed a simple empirical model capable of producing the full isotropic turbulence energy spectrum $E(\kappa)$ as a function of the Taylor microscale Reynolds number, Re_λ.

2.3 Single-phase turbulent fluid flows

There exists a wide range of studies concerning analysis of solely turbulent fluid flow through wall-bounded geometries, with pipes and ducts forming the majority of experimental rigs used in such studies. In this section, the most common experimental techniques shall first be introduced. Next, the extent to which these systems have been experimented within shall be reviewed, with an aim to highlight some of the important methods and flow-features. Throughout, a need for simulation in cases where experiment is unable to provide the depth necessary to fully understand the dynamics shall be identified.

2.3.1 Experimental techniques

Hot-wire anemometry (HWA) was one of the earliest flow measurement techniques developed, with original designs dating back to around 1910. The tool became commercially available during the 1950s. The method relies on heat transfer between a 'hot-wire' and the fluid to determine mean and fluctuating velocities along with temperature. The device consists of two probes and a connecting tungsten, platinum or platinum-iridium wire, through which an electrical current is passed. This causes the wire to heat up, but when the wire is immersed within a flow field, the local fluid velocity causes some of the heat to be removed. The relation between the transfer of energy to the flow (by means of a temperature sensor) can be used to determine the local velocity, with reasonable accuracy (Perry, 1982). Despite this, the method is sensitive to a number of system parameters such as ambient temperature fluctuations and wall proximity (Comte-Bellot, 1976). Errors can propagate from various sources such as calibration measurements, operating at high frequencies, low spatial flow resolution and flow disturbance along with other approximations. Typical measurement errors on various flow rms quantities such as Nusselt number, Reynolds number, Mach number and Flow angle range between 2% to 5%.

Developed in the 1960s to increase the accuracy of low velocity measurements (Yeh and Cummins, 1964), laser Doppler anemometry (LDA) or laser Doppler velocimetry (LDV) exploits Doppler shifting properties of the interaction between light and a moving surface. Reflected light is detected in a photomultiplier tube which converts photon energy into an amplified electric current. Using information about the incident and scattered photon frequencies, along with detector orientation, a calculation can be made concerning the speed of the surface. This provides a means to measure the velocity of reflective neutrally buoyant particles dispersed within a flow. This method is nonintrusive and has been developed (Durst et al., 1976) and used widely over the last few decades. Since calibration is unnecessary, typical errors associated with measurements of mean and rms velocities are below 1%.

Particle image velocimetry (PIV) relies on taking two exposures of a flow containing dispersed tracer particles. Using digital image processing techniques, the particle displacements are calculated between both frames in order to determine an instantaneous velocity field in two dimensions. Due to its accuracy relying on camera quality and algorithm performance, PIV is perhaps the most widely used fluid imaging technique today. Like LDA, it is nonintrusive and with current data processing capabilities, a large amount of information can be obtained in a short amount of time. PIV also show high degrees of accuracy when compared to theoretical predictions. Errors propagate from two main sources, which are mean bias errors and random errors. The former arise due to insufficient resolution in the camera which means the particle centroid is computed incorrectly. The latter is due to imperfections in the particle shapes and other electronic noise. Particle locations in each timestep are measured to within around 10% of their diameter typically, however this is highly sensitive to pixel resolution. More information can be found in the following review (Grant, 1997).

Expanding on techniques used in PIV, holographic particle image velocimetry (HPIV) allows for instantaneous measurement of all three components of the velocity vectors throughout a flow field. Experimental apparatus for this method is more sophisticated than standard PIV, and more processing is needed to reconstruct the particle position data after recording the scattered light on a holographic plate. The errors associated with PIV are also abundant in HPIV, along with further holographic reconstruction errors associated with optical alignment. A review paper by Hinsch (2002) provides more information on HPIV.

2.3.2 Experimental studies

In general, channel flow investigations are difficult to setup and perform experimentally due to their periodic nature. It is problematic to obtain an experimental flow setup which mimics the mean flow symmetry inherent in a channel flow, which is by definition infinite in the streamwise and spanwise directions. The concept of a channel is usually used as a theoretical notion to consider near-wall statistics rather than replicate real systems.

The closest experimental analogue to a channel geometry is a duct, in which the flow is fully enclosed by four perpendicular walls. With early studies of the flow statistics and turbulent structures present in these types of geometries, carried out in the 1920s by Nikuradse (1926) and Prandtl (1927), it was noticed that the mean streamwise velocity contours would tend to curve outwards towards the corners of the duct. Prandtl claimed that this was due to secondary turbulent motions whereby the fluid would possess different flow characteristics in the corners.

In 1962, Hoagland (1962) investigated this type of phenomenon in more detail, setting up duct rigs of three different aspect ratios (1:1, 2:1 and 3:1). The author employed the HWA technique to obtain more accurate and quantitative information about the secondary flows in rectangular duct flow. It was observed that the secondary flows showed similar behaviour and magnitude in all three aspect ratios, and that they had a major effect on the primary flow distribution. The results obtained in this experiment were subject to uncertainty based on the way turbulence intensities cause inaccuracies in hot wire measurements. Furthermore, other quantities relating to turbulence such as the Reynolds stress components were not measured.

Brundrett and Baines (1964) attempted to examine some of these statistical quantities in 1964. By positioning the HWA probes in various orientations across a duct flow apparatus, the authors were able to take readings of the velocity vector on three axes, providing ample information to determine the flow field statistics both in magnitude and direction. This information was also used to calculate the Reynolds stress tensor (an instantaneous array of measurements based on velocity derivatives in all directions). Moreover, the authors analysed the flow field and determined that the vorticity production is directly related to the proximity to the wall. It was also shown that the Reynolds number of the flow has little effect on the secondary flow patterns, however, as it increases, the secondary currents move closer to the wall boundaries.

This phenomenon was further investigated by Gessner and Jones (1965) using the same experimental technique. They considered the secondary flow velocities under different Reynolds numbers and determined that after being non-dimensionalized by either the bulk or centreline mean velocity, the secondary flow velocities would tend to decrease as the Reynolds number increased. It was also concluded that in the regions close to the duct corners where the secondary flow velocities are greatest the greatest vectors of wall-shear stress skewness were observed.

Other investigations were carried out by Launder and Ying (1972) who considered the effects of using a duct with roughened boundaries. Their work showed that the modification of rough walls had no effect on the secondary flow velocities, once they had been normalized as previously.

Melling and Whitelaw (1976) used LDA to analyse turbulent flows in 1976, exploiting the fact that this technique is a non-intrusive method of extracting information about the flow velocities. Using this method they were able to obtain more accurate measurements of the secondary velocities as well as the mean velocities and most of the Reynolds stresses. Their results compared well with some of the mathematical models present in previous literature.

Kreplin and Eckelmann (1979) performed experimental work in an oil channel, examining the fluctuating velocities and shear stresses very close to the wall of turbulent flows. They noted that in previous experimental investigations, there existed much greater scatter in these particular statistical quantities. The work described was carried out using HWA and hot film techniques, using sensor probes to analyse the turbulent micro-structures in the flow. This method is more suited for low Reynolds numbers in which the turbulent structures in the viscous sublayer can be resolved to a high resolution. It was observed that coherent turbulence structures were orientated in the streamwise direction and were subject to rotation whilst maintaining their form.

The LDA method was used widely in the following years and a review of experiments which were carried out was written by Demuren and Rodi (1984). In this review the works of Po (1975), Lund (1977) and Gessner et al. (1979) were compared and analysed with good qualitative agreement being observed. However, the author notes that the mathematical stress model used by Launder and Ying (1972) predicted discrepancies

when compared to the experimental data. The authors discuss adaptations to this model in order to improve accuracy. This review also covers experiments carried out in ducts of non-square geometries such as rectangles (Gessner and Jones, 1965; Tracy, 1963) and triangles (Aly et al., 1978).

The HPIV technique was applied by Zhang et al. (1997) to obtain information about a low Reynolds number turbulent flow field inside a square duct. Their results were in very good agreement with previous experimental studies and simulation predictions. As an attempt to improve turbulence modelling for LES techniques, SGS models were compared against data collected from PIV methods, but at the time there existed no three dimensional distributions at high Reynolds number. In 1999, Tao et al. (1999) carried out HPIV measurements at a bulk flow Reynolds number of 120,000 in order to assess the quality of recent eddy viscosity models and a critical analysis of the strengths and weaknesses that they currently possessed.

More recently, further experiments using micro-pillar wall-shear stress sensors have been performed by Große and Schröder (2008) in order to measure the dynamic wall shear stresses in more detail by employing an extendable micro-pillar on the inner wall boundaries. This technique works by recording the deflection of the tip, from which one can derive a value for the wall shear stress. The experimental results show good agreement with both previous experimental techniques and DNS results from the literature.

Despite losing some of the interesting emergent phenomena associated with ducts (such as the secondary flows) when switching from a square to a circular cross section geometry, there also exists a lot of interest surrounding turbulent pipe flows due to both its prevalence in industry and inherent geometric symmetries. These two factors make the study of these types of flows relevant, interesting and informative, and so there currently exists many experimental investigations examining flows of this kind.

In 1954, Laufer (1954) made use of HWA to collect mean and statistical quantities describing a fully developed turbulent pipe flow. The author observed that turbulence energy rates (associated with dissipation, production and diffusion) were highest within the viscous sublayer. Further work to analyse the boundary layer experimentally was carried out by Bradshaw (1967) during which the author demonstrated evidence which

backs up the theory earlier suggested by Townsend (1961) which relates to sectioning the boundary layer into an active part and an inactive part. Bradshaw made measurements of the frequency spectra within the boundary layer, identifying these two sections.

Similar investigations were carried out by Patel and Head (1968), in which they observed a divergence from the predicted inner-law mean velocity distributions when high pressure gradients are present within the boundary layer. They also observed the tendency for these conditions to cause the boundary layer to laminarize. The authors used their results to create a set of criteria concerning the mean shear-stress gradients located in the wall region, above which the layer is likely to transition to a laminar state.

Building on the work carried out by Laufer (1954) concerning turbulent energy diffusion rates, Lawn (1971) performed further measurements of this quantity as well as the spectral distributions of the stress components. In this work, the author highlights inconsistencies with Laufer's results regarding dissipation due to his assumption of isotropy when calculating the quantity using fewer measurements.

Bremhorst and Walker (1973) presented measurements surrounding the spectral components of turbulence momentum transfer, highlighting two processes close to the wall in which this type of behaviour is likely to occur. These processes are related to the wavenumbers in the turbulence energy spectrum and the author shows an inverse relation between the frequency magnitude and the net momentum transfer.

Wallace (1985) provided a discussion surrounding the existence of ‘hairpin vortices’. These are defined by Moin and Kim (1985) as “an agglomeration of vortex lines in a compact region (with higher vorticity than the neighbouring points) that has a hairpin or horseshoe shape”. Their work was based upon experimental evidence and theory presented in the literature (Willmarth and Tu, 1967; Willmarth, 1975) of coherent turbulence structures within the boundary layer. They theorised that these hairpin-esque structures dominate the boundary layer and are created through the bending and deformation of vortex ‘tubes’ orientated downstream.

Willmarth and Lu (1972) performed HWA measurements of the near-wall flow field in a turbulent boundary layer, focusing on the product uv and the correlation between streamwise velocity fluctuations and streamwise vorticity. The greatest correlation was found to be through lines inclined at 10° to the wall surface at a fixed velocity point.

Further experiments to further probe the nature of near-wall turbulence structures were performed by Kovasznay et al. (1970) and Blackwelder and Haritonidis (1983), both of which showed a streamwise tilt of downstream velocity correlation contours. Similar observations were made by Brown and Thomas (1977), with an inclination angle this time found to be 18° throughout the boundary layer. Throughout all these studies, due to the nature of the experimental measurement techniques, the hairpin vortices could not be concluded as observed. To perceive such, all three components of vorticity in a local region of the turbulence field need to be resolved, which was beyond experimental capabilities during this period.

Moving away from studies aimed at elucidating dynamics within the boundary layer, Sabot and Comte-Bellot (1976) carried out work in 1976 concerning themselves with the presence of turbulent structures within the core of a turbulent pipe flow. In this work, the authors measured the cross-sectional shear stress fluctuations and discussed the existence both spatial and temporal processes which can occur in this region, comparing with the processes which occur closer to the wall.

Westerweel et al. (1996) used a digital version of the previously mentioned PIV technique to measure flow velocities within a turbulent pipe at a bulk Reynolds number of 5300. The author's results were used to determine the accuracy of the new method when compared to other well established techniques such as standard PIV and LDA. When analyzed, digital PIV provided accuracy on the same level as standard PIV. However, the interrogation time required is much lower for the digital method and so this technique is shown to be less time-consuming, making it more efficient.

An investigation into the effect of Reynolds number on mean flow statistics was carried out by Den Toonder and Nieuwstadt (1997) using LDV. Their results were shown to match previous studies for the lowest Reynolds number experiment and throughout, the turbulence statistics were observed to be Reynolds number dependent. In particular, the authors note that one of these dependencies lies with the constants associated with the law of the wall (as theorized by Von Kármán (1931) to predict the mean streamwise velocity in the eponymously named 'logarithmic layer').

This scaling was further investigated by Zagarola and Smits (1998) who considered a much larger range of bulk Reynolds numbers from 31,000 to 35,000,000. Their results

were used to extend the current theory regarding scaling, and regions were identified in which different contributing factors apply. The resultant expressions provided good agreement between the velocity profiles associated with differing Reynolds numbers across the range, however there was some discussion surrounding the error in certain measurements due to the nature of the pressure tapping. To probe the pressure within the flow, the tap consists of a hole through (and perpendicular to) the wall. This can directly skew the streamlines of the flow past the gap and so the recorded pressure will be different to the actual value.

Work was performed on calculating the above correction factor by McKeon and Smits (2002). Here, the authors propose that the correction term also scales with Reynolds number which had not been taken into consideration in previous studies. Mckeon et al. (2004) went on to repeat the work of Zagarola and Smits (1998) with their new information surrounding the errors in mind. The measurements were made this time using a smaller probe, reducing the overall error. They report differences in both the region limits and log-layer constants, ascertaining that their findings for the constants were within a 95% confidence level.

2.3.3 Turbulent flow simulations

Attempts to study turbulent flows in detail using computational modelling began around the late 1960s, with increases in computation performance leading to reasonable simulation timeframes. An LES was carried out at high Reynolds number in 1970 by Deardorff (1970). In this work, the author proposes a model made up of 6720 grid points based upon a three dimensional channel. The SGS Reynolds stresses were estimated using eddy coefficients as proposed in the study concerning LES methods by Smagorinsky (1963). The authors made observations about general flow patterns, comparing to existing experimental data obtained by Laufer (1951), however, the agreement was poor. The author addressed this and stated that the main error contributions stemmed from the choice of the SGS Reynolds stresses and boundary-condition assumptions, the latter of which could be improved with more computing power.

Moin and Kim (1985) performed an LES to further investigate the nature of ‘hairpin vortices’ present in the boundary layer of turbulent flows. They analyzed the vorticity field throughout and, using their definition as stated earlier, provided evidence for vortical structures orientated 45° to the channel wall. The authors also observed horseshoe shapes

formed from instantaneous plots of vorticity lines. The authors later extended the analysis of their work to more closely examine turbulence producing events, based on the near-wall bursting process. It is here that the authors introduced the notion of sweep (inverted horseshoe) and ejection (upright horseshoe) vortex motions. The authors also concluded that since these structures are solely a result of vortex stretching, that they are present in all turbulent shear flows, irrespective of the wall-condition. These structures were also identified far away from the boundary.

Kim et al. (1987) performed a DNS of a turbulent channel flow at a bulk Reynolds number of 3300. In order to obtain their solutions, the authors use a spectral method numerical scheme whereby the solutions to the differential equations (Navier-Stokes and continuity) were expanded on either a Fourier series or Chevychev polynomial basis. The results of the simulations were compared with experimental data. Despite generally fair agreement, there were some discrepancies in the wall region. It is suggested that this was due to the wall-shear velocity measurement in the experiment. Moreover, very good agreement was obtained upon renormalizing the profiles with the value observed during the experiment. The authors also propose that the discrepancy may be due to the aspect ratio of the experimental set-up not resembling a true two dimensional flow, hence the simulated results would differ slightly.

A DNS of a curved turbulent channel flow at low Reynolds number was later carried out by Moser and Moin (1987) and published during the same year. Their work was directed towards investigating the degree of streamline curvature associated with the concave and convex channel boundaries. In previous experimental work into this type of geometry, authors such as Wilcken (1967) and Wattendorf (1935) observed behaviour concerning the change in mean flow quantities as a result of curving the channel, suggesting further investigation into the mechanics behind this phenomenon. In the work of Moser and Moin, the authors assess the extent to which the centrifugal force influences the flow statistics and they show that this is a contributing factor to the skew in flow profiles.

Madabhushi and Vanka (1991) carried out an LES (using the Smagorinsky SGS model) at a bulk Reynolds number of 5810. The authors observed the expected secondary velocities and provided accounts for all turbulence quantities and statistics. This was shortly after followed up by Kajishima and Miyake (1992) who considered two different

bulk Reynolds numbers, 6200 and 67,400, the latter being comparable to (and offering strong agreement with) existing experimental data.

Gavrilakis (1992) performed a DNS of turbulent duct flow obtaining detailed information about the mean flow variables and turbulence statistics. Although descriptive, the author did not build upon the explanations provided by Kajishima and Miyake (1992). Other authors such as Su and Friedrich (1994) obtained similar results using LES, noting that the secondary flows tend to form very slowly and that a fairly high resolution is required in order to capture them. They also plotted streaklines for the flow, providing a clear visualisation of the secondary flows.

Eggels et al. (1993) carried out another DNS at low Reynolds number, and in this study the authors chose to adopt a cylindrical geometry matching that of a pipe. This time, the authors made use of the finite volume technique in order to solve the NS equations. Comparing to experimental pipe flow data generated from LDA and PIV techniques, their results were in good agreement. In contrast with the discrepancies highlighted in the DNS work carried out by Kim et al. (1987), it was suggested that the general increase in accuracy may have been due to adoption of the finite volume method.

Eggels et al. (1994) continued their work the following year when they published a paper comparing their cylindrical geometry-based DNS results with those of Kim et al. (1987). By simulating the axisymmetric pipe flow at a Reynolds number equal to that of the plane channel setup, the authors were able to study the differences in the mean velocity distributions. In contrast with the logarithmic velocity profiles seen in the plane channel flow, the pipe flow results (validated by experiment) suggested an increase in the mean velocity close to the wall. The change in the behaviour between flows in different geometries underlines the importance of their effect on the system, particularly if the results are going to be applied to situations which are sensitive to accuracy. On the other hand, when considering velocity fluctuations, the authors noted that the change to pipe geometry did not appear to have as much of an effect.

Work associated with the application of LES techniques to cylindrical geometries is relatively sparse. An investigation, carried out by Rudman and Blackburn (1999), analyses an LES of turbulent pipe flow at a shear (or friction) Reynolds number of 1920. Despite the inherent axisymmetric layout, the authors choose to base their geometry on a

Cartesian co-ordinate system. Their results were in good agreement with experimental data, verifying that LES is capable of modelling flows in less simple geometries. However, the SGS method implemented in this work involved knowledge about the shear stress on the boundaries which is unnecessary in other models. In this case, the authors chose to model the near-wall SGS stresses using van Driest damping in a form suggested by Piomelli et al. (1988) which allows the turbulent mixing length to decay as the wall is approached to compensate for the fine mesh spacing close to the boundary.

Work on straight wall-bounded turbulent flows was continued by Kim et al. (1987) in 1999 when they performed a DNS at two higher shear Reynolds numbers ($Re_\tau \approx 395$ and $Re_\tau \approx 590$) in order to determine the effects of a flow with stronger turbulence levels. The authors also generated results at $Re_\tau = 180$, comparing these to their original channel flow DNS findings. This work assessed the magnitude of low-Reynolds number effects and indicated that at $Re_\tau \approx 590$, most of these are reduced. For instance, the ratio of production to dissipation of the turbulence kinetic energy tends to reach a limit over the log-region range where it is approximately one. This was reflected in the results, suggesting that, for this particular property of a turbulent flow, the Reynolds number was high enough to ignore low-Reynolds number effects.

A report was published by Schmidt et al. (2001) which compares results from a DNS with LES, this time looking at both Cartesian and cylindrical geometries. Once again implementing the spectral element method, the simulations produced flow statistics which were in very good agreement with experimental data. This work not only stressed the accuracy of both DNS and LES methods in terms of reflecting real flow situations, but it also implies that in some cases, LES is sufficiently capable of reaching a similar level of accuracy as DNS provides, in terms of mean flow statistics at least.

Wu and Moin (2008) used DNS to explore turbulent pipe flow at a bulk Reynolds number of 44,000, this time using a second order finite difference method of integration. Good agreement was shown when predictions were compared with experimental data and the boundary region statistics were investigated and compared with a run carried out at $Re_B = 5300$. The authors provide visualizations of the flow hinting at large-scale axial structures of comparable azimuthal size for both Reynolds numbers, which were confirmed when two point correlations were calculated.

More recently, Boersma (2011) carried out a DNS covering bulk Reynolds numbers up to 61,000 using a highly accurate numerical model. The author compares results with previous DNS runs as well as experimental data for which excellent agreement is obtained. An interesting finding is the presence of a non-vanishing auto correlation function in the streamwise direction which suggests long axial structures at high Reynolds numbers, which is in agreement with the findings of Wu and Moin (2008).

Four DNS simulations at $Re_\tau = 180, 360, 550$ and 1000 were performed by El Khoury et al. (2013) using the spectral element-based solver, Nek5000 (Fischer et al., 2008). The authors compare to previous DNS results both in pipes and other geometries and it is observed that pressure is the main quantity that differs between systems. Conversely, turbulence kinetic energy profiles were indistinguishable in the near-wall region. Finally, the authors indicate Reynolds number dependencies for many statistical quantities.

More recently, Vreman and Kuerten (2014) compared DNS databases of different simulation methods and regimes to determine the reproducibility of certain flow statistics, all at $Re_\tau = 180$. For all the simulations compared, maximum deviations were determined to be less than 0.2% for the mean velocity, and less than 1% for the root-mean-square (rms) velocities and pressure fluctuations. These properties underline the accuracy and reproducibility associated with DNS, and further confirm the hypothesis that a turbulent wall-bounded flow has only one unique statistically stationary state. Furthermore, the authors analysed the dissipation spectra and confirmed that mesh spacings need to be fine enough to resolve the smallest scales and eddies associated with energy dissipation.

2.4 Particle-laden turbulent flows

The remainder of this literature review shall consider the theory, techniques and previous work associated with performing experiments on and simulating a particle-laden turbulent fluid flow.

2.4.1 Flow regimes and solid-phase parameters

Based solely on the bulk parameters (volume fraction, density, particle size) of a monodispersed flow, it is possible to classify the flow regime that is likely to be observed. The volume fraction is defined as:

$$\phi_P = N_P V_P / V_F, \tag{9}$$

where N_P is the number of particles dispersed within the flow geometry, V_P is the volume of each particle and V_F is the volume of the flow geometry (including the space occupied by the particles). This, along with particle Stokes number based on the Kolmogorov time scale, St_K, can be used to predict a particle-laden flow regime, as suggested originally by Elghobashi (Elghobashi, 1994; Elghobashi, 1991), and later updated and improved (Elghobashi, 2007). The most up-to-date version aligned with present knowledge of the classification diagram is presented in Figure 2.2.

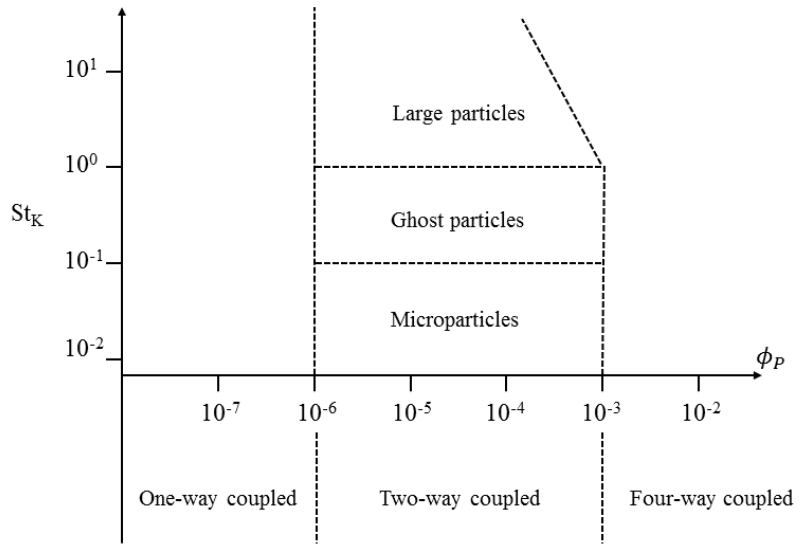

Figure 2.2: Regime classification for isotropic particle-laden turbulence.

For $\phi_P \leq 10^{-6}$ the flow is considered 'one-way coupled' which means that particles have negligible effect on the fluid and, in particular, the turbulence field. Therefore under this regime, the dynamics are solely based on particles being influenced by the fluid velocity field, and the momentum transfer back from the particles to the fluid is very small.

For $10^{-6} < \phi_P \leq 10^{-3}$ the flow is considered 'two-way coupled' in that the momentum transfer between the solid phase and the fluid phase is significant enough to affect the turbulence field. This is a region of interest where the Stokes number parameter (related to the size and/or density of the particle) becomes a factor which influences the overall

effect of particles on the turbulence. For larger particles ($St_K > 10$), vortex shedding occurs which enhances the turbulence kinetic energy production. For smaller particles, a secondary classification is suggested.

Particles with very low Stokes numbers are referred to as 'microparticles' and behave as flow tracers, but at high volume fractions these particles increase the rate of energy dissipation and reduce the decay rate of turbulence kinetic energy.

For 'large' particles in the regime where $1 > St_K \geq 10$, the particles have a much greater response time than the Kolmogorov time scale, and find it difficult to follow the fluid streamlines, often crossing through fluid trajectories. When encountering vortices, it often occurs that these particles are ejected. The effect on the resulting turbulence field is that the turbulence kinetic energy (TKE) and its dissipation rate will be reduced.

For the regime in which $0.1 > St_K \geq 1$, particles are referred to as 'ghost particles' in that the effects of both microparticles (increased TKE) and large particles (reduced TKE) are cancelled out and hence have little effect on the resulting turbulence field. At the upper limit, particles with $St_K \approx 1$ are labelled 'critical particles' since they tend to show enhanced rates of preferential accumulation when compared to other particle sizes. This effect shall be discussed in more detail in the following subsection.

Finally, for $\phi_P > 10^{-3}$, flows are described as 'four-way coupled' in that particle-particle collisions occur frequently enough within the flow that both the particle and fluid behaviour is modified. It is important to note that for greater Stokes numbers, this mechanism becomes important sooner as volume fraction is increased.

2.4.2 Turbophoresis and preferential concentration

Of great importance in particle-laden flows is the phenomenon of turbophoresis which describes the turbulence-induced drift of inertial particles towards a wall. With increased momentum, the trajectories of such particles decouple from local vortex motion (Fessler et al., 1994) and accumulate in certain regions leading to preferential concentration. The extent to which this mechanism occurs in wall-bounded flows has been shown by Crowe et al. (1985) to be governed by the particle viscous Stokes number St^+, which is the ratio of the particulate phase relaxation time to the viscous flow time scale.

For very low Stokes numbers ($St^+ \ll 1$), particles behave as tracers and follow the fluid streamlines. This type of system exhibits a homogenous concentration profile, and mean particle motion statistics match those of the fluid.

Conversely, for very large Stokes numbers, the particle response time is much greater than that of the associated fluid time scale, so particles decouple from the turbulent fluctuations. These heavy particles migrate towards the near-wall region and exhibit behaviour different to that in the bulk flow. For example, studies in channels (Li et al., 2001; Zhao et al., 2015; Rouson and Eaton, 2001) predict increased particle turbulence intensities close to the wall for high Stokes numbers.

Likewise, certain mid-range Stokes number particles in this region are subject to local segregation and accumulation in low-speed streaks (Picciotto et al., 2005; Dritselis and Vlachos, 2008; Marchioli and Soldati, 2002; Lee and Lee, 2015). Studies also indicate that particle positions in the viscous sublayer and the buffer region correlate with the local flow topology for low Stokes numbers (Soldati and Marchioli, 2009). More recent work (Sardina et al., 2012; Sardina et al., 2014) has demonstrated a strong link between the two mechanisms of wall accumulation and local particle clustering intensity.

2.4.3 Experimental studies

Experimental work concerning particle-laden flows in simple geometries is relatively sparse, when compared to those performed via simulation. This is due to the inherent difficulties in using techniques such as PIV and HPIV to separate the fluid phase (containing tracer particles) from the particulate phase. In many cases, the focus of experiments performed was on the deposition properties. Below is a review of attempts to perform such studies.

Perhaps the earliest experimental study considering two-phase turbulent flows is that of Friedlander and Johnstone (1957) who measured concentrations of depositing particles on the inner surface of glass and brass tubes in 1957. Despite the lack of accurate measurement technology at that time, they managed to observe some of the key mechanisms present in such flows. For instance, they concluded that the rate of deposition showed dependence on both the particle-to-wall transfer rate as well as the re-entrainment rate. They also observed that larger particles were more easily resuspended than smaller ones. Finally, they offered discussion surrounding the ways particles start to behave

unlike the fluid as the wall is approached, in that eddies carry particles towards the boundary.

Matsumoto and Saito (1970), studied the suspension behaviour of densely dispersed polystyrene, copper and glass beads in a $6m$ horizontal duct flow by analysing photographs of the moving particles, illuminated by a slit of stroboscopic light. The experiments showed that the particles were rotating with very high angular velocities, which would consequently increase the lift force, providing a mechanism for the observed increased suspension.

Later, Liu et al. (1974) performed experiments to analyse aerosol deposition in vertical pipe flows at bulk Reynolds numbers $Re_B = 10{,}000$ and $Re_B = 50{,}000$. They related deposition velocity to particle relaxation time, τ_P^+. For instance, they concluded that at small τ_P^+, deposition velocity increased with particle diameter, whereas beyond $\tau_P^+ = 30$, deposition velocity scaled only with τ_P^+. A review of similar experiments was presented in McCoy and Hanratty (1977), who compared deposition data from sources such as Farmer (1969), Forney and Spielman (1974), Ilori (1971) and Sehmel (1980). They concluded that aside from Farmer (1969), the range of droplet sizes studied in previous experiments were much smaller than those of interest in two-phase pipe flows. It was observed by Farmer (1969) that deposition rate showed a dependence on particle diameter, but further studies and drop-size measurement techniques were required to obtain more reliable understanding.

Burmester de Bessa Ribas et al. (1980) studied the motion of glass beads in a rectangular duct turbulent gas flow with emphasis on the effect of mass loading on turbulence properties. Bulk observations such as particle concentration and velocity were analysed and the effect of two-way coupling on the turbulence field was discussed.

Lee and Durst (1982) performed an LDV study considering the dispersion and deposition of glass particles in air through a vertical pipe motivated by the discrepancies that were present at the time between measured and theoretically predicted rates of deposition. Their results demonstrated peculiar particle behaviours and it was noticed that the velocity profiles seemed to fit in better with what would be expected for a laminar shear flow. The work was accompanied by a theoretical analysis which suggested that particles

may become unresponsive to the turbulent flow fluctuations after a certain cut off frequency.

In the same year, Tsuji and Morikawa (1982) performed LDV measurements of a two-phase turbulent pipe flow with inner diameter $30mm$. Separation between the two particle species (plastic observed and ammonium chloride tracer) was achieved by setting threshold values for measured components of the photomultiplier signal. The asymmetry of the mean velocity profile of both the fluid and particle phases was more enhanced with increasing mass-loading and decreasing flow rate. Furthermore, particle size was observed to have varying effects on the turbulence in that the larger particles enhanced it while the smaller particles attenuated it. The authors repeated the study (Tsuji et al., 1984), this time in a vertical pipe arrangement. This time, for smaller particles the mean fluid velocity profile was flattened and larger particles enhanced the turbulence. A remarkable observation was that for medium-sized particles, both turbulence enhancement and attenuation were observed simultaneously in different regions of the pipe flow.

Fessler et al. (1994) investigated particle concentrations using digital analysis of photographs of illuminated flows. The particulate phase consisted of spherical glass and copper beads which were injected into a channel flow with half-height $20mm$. The authors compared the dispersive properties of different relaxation times (or Stokes numbers) and observed clustering and deviation from random distribution when the relaxation time was on the order of the Kolmogorov scale associated with the flow. It was also observed that the larger, denser particles would have the effect of attenuating the local turbulent fluctuations.

Turbulent gas flows containing solid particles were also considered by Longmire et al. (2001). In their work, the investigated channel rig consisted of a constant cross section of 153 mm by 14.7 mm. The flow was maintained using a centrifugal blower and regular meshing to control the mean velocity. Their work presents a method of determining the planar particle and fluid fields simultaneously using PIV techniques and was applied at a bulk Reynolds number of 9000 to obtain statistics. These were to be used by following simulations for validation purposes.

Kussin and Sommerfeld (2002) used a technique called phase-Doppler anemometry (PDA) to distinguish simultaneously between air and spherical glass particle velocities in a horizontal channel flow. The emphasis was on the effect of wall roughness, and so multiple wall plates were used to study the effect of this property on particle concentration, mean velocity and fluctuating velocities. They concluded that by using rough walls, the mean particle streamwise velocity is hindered, but fluctuations are enhanced due to random wall collisions. The authors also observed the two-way coupling effect, in that wall-roughness increased turbulence dissipation, and so the extent of turbulence modulation was analysed for different particle sizes and mass loadings. During the same year, Laín et al. (2002) also performed a PDA experiment to study a similar channel flow, this time to provide validation data for a four-way coupled RANS-based LPT. Results from the simulation were found to be in good agreement with those obtained from the experiment.

The following year, Caraman et al. (2003) performed a similar study using the same technique to study particle-particle collisions, this time in a horizontal pipe. They concluded that interparticle collisions have little effect on the longitudinal velocity fluctuations, but strongly affect the radial fluctuations. The authors also determined that near-wall collisions have a large effect on the kinetic-energy balance within the pipe. This work was extended by Borée and Caraman (2005), where the authors this time considered a bidispersed two-phase pipe flow. An important conclusion was that even at increased mass loadings, the time between collisions is still larger than the particle's aerodynamic time constant, and so collisions have little effect on the particle's fluctuating motion. This means that transport effects based on the particle's fluctuating kinetic stresses are still dominant, despite the increased volume fraction and collision rate.

Sippola and Nazaroff (2004) studied particle deposition in steel and insulated ducts of hydraulic diameter $15.2cm$. It was observed for the steel duct that deposition rates were greatest on the floor and ceiling, whereas for insulated ducts the rate was similar for all four wall boundaries. For both systems, mean deposition velocity increased for larger particles and greater flow velocity.

Li et al. (2012) performed a two-phase PIV experiment focusing on turbulence modification in the boundary layer of a horizontal channel flow at $Re_\tau = 430$. The particulate phase consisted of $60\ \mu m$ polythene beads and three volume fractions were

studied. It was observed that the mean and rms fluid properties were modified, and in particular the peak of the streamwise velocity fluctuations was increased, with the maximum turbulence intensity moving closer to the wall boundary. Other phenomena such as increased wall roughness due to particle sedimentation were discussed and the effect on turbulence structures was also accounted for. Interestingly, the coherent turbulent structures close to the wall were observed to have been reduced in size with the addition of particles, which was accounted for by crossing-trajectory effects as a result of particle resuspension near the wall. The following year, Li et al. (2013) performed a study on particle deposition on the inner wall of a 180° bend. The experimental side of the project used LDV to observe deposition patterns for various different parameters including bend material, curvature ratio, particle concentration and inlet velocity. It was observed that the general deposition pattern was similar in all variations of the parameters mentioned, but changing particle concentration had the greatest effect on steady deposition time. The authors concluded that larger particles and greater inlet velocity conditions would lead to reduced deposition rates.

The following subsections aim to introduce the various regimes under which wall bounded particle-laden turbulent flows can be simulated, based on a previously obtained turbulent Eulerian flow field.

2.4.4 Particulate-phase simulation techniques

Building upon the success and applicability of both DNS and LES methods applied to various geometries to obtain accurate turbulent flow fields, simulation work began to transition towards the inclusion of micron-scale particles which are dispersed within the fluid. Particle-laden turbulent flows reflect commonly occurring processes in nature and industry more realistically and have been shown to both be governed by and even, in certain cases, modify the dynamics of the flow. Therefore, to create a more accurate representation of the system in question, it is important to include the effects of any particle phases present.

A review paper by Elghobashi (1994) describes some of the earlier challenges encountered when considering the inclusion of a secondary dispersed particle phase in turbulent flows. One of the more important problems faced is that there is a computational limit of the resolution of the flow around the particles. For instance, particles with diameters much lower than the smallest length scale are difficult to simulate due to the

lack of knowledge surrounding the flow and its influence on the dynamics of the particle. On the other hand, particles larger than the smallest length scale may be subject to large velocity gradients across its diameter and so more rigorous force calculations must be carried out, with the particle no-longer being able to be treated as spherical. The review also describes the current mathematical models used to track the particles and their behaviour within the fluid.

The first model described in the review paper is a 'two-fluid approach' wherein the particulate phase is assumed to behave as a continuum and is governed by equations akin to those of the carrier fluid. However, each set of equations is modified with a coupling force term, used to describe the interaction between the two phases. The increase in the number of equations along with the complexity of the interaction terms makes this method very computationally intensive to carry out and so the equations are generally averaged (in a similar fashion to the RANS method discussed earlier). This approach has more widely been referred to as an Eulerian particle tracking method due to its global description of the particles as opposed to modelling individual particles and their location, velocity and properties.

One way in which the particle phase can be modelled is via Lagrangian particle tracking (LPT), which is a point-particle approach where each solid element is represented by a computational sphere (or ellipsoid). Here, for a solid sphere to be considered as point-like, the particle diameter must be smaller than the Kolmogorov scale of the surrounding flow. The LPT method simulates particle motion by solving the Maxey-Riley (Maxey and Riley, 1983) equation (or a variant) for each particle in the system alongside the continuous phase solver. Terms calculated in this force-balance equation usually include buoyancy / gravity, drag, lift, pressure-gradient, added-mass and the Basset history force (though the latter is often ignored due to its high computational cost and negligible effect on the resulting particle trajectories). This equation and its derivation is covered in more detail within the methodology section of this thesis.

LPT methods are further subcategorised by their coupling with the surrounding flow field. As covered earlier, if the volume fraction of the particulate phase is low enough, then there is no influence of the particles on the fluid, and particle trajectories are solely functions of the instantaneous fluid velocity field at each timestep. This is referred to as one-way coupling. At higher volume fractions, particles begin to influence the Eulerian

phase (two-way coupling) and eventually interact with other particles (four-way coupling).

Finally, an additional level of detail is offered with particle-resolved methods, under which the flow around the particle boundary itself is resolved. This entails more intensive computational requirements, in that the fluid mesh needs to have grid-spacings more dense than is necessary to solely resolve the Kolmogorov length scale, particularly for complex particle shapes. It is often under these circumstances that the particle boundary will not coincide with the continuous phase mesh. One solution to this is to approximate the no-slip boundary condition on the surface of the particle via, for example, an immersed boundary method, which recouples the particle dynamics and motion to that of the fluid.

The extent to which each of these particulate phase modelling regimes have been studied and applied in the literature shall be covered in the following subsections.

2.4.5 One-way coupled LPT simulations

An initial attempt to perform LPT in turbulence began with Riley and Patterson Jr (1974). From a previously obtained decaying homogeneous, isotropic box of turbulence, the authors injected 432 particles. Here they chose to consider only the effect of drag forces when calculating the resulting trajectories. The focus of the analysis was on determining autocorrelations between particle and fluid velocity, and it was established that the particle velocity correlation increased with particle Stokes number. Discussions were made into how future work could be improved, with increasing the number of grid points from $(32)^3$ to $(64)^3$ being predicted as having the greatest impact on accuracy. However, due to the underdeveloped technology at that time, this would have entailed its own issues surrounding handling of large amounts of data.

Yeung and Pope (1989) considered varying interpolation techniques which are used to predict the velocity (or its derivatives) of the fluid at the centre of the particle when calculating various terms in the force balance equation. They concluded that at least third order accurate interpolation methods are necessary, but improving the nodal density of the fluid phase solution grid also has a strong effect on accuracy. A similar study was performed the same year by Balachandar and Maxey (1989).

Turbulent channel flows were also studied by McLaughlin (1989) during the same year, who performed a particle-laden simulation at $Re_B = 2000$. The fluid phase in the vertical channel was obtained via a pseudospectral method and the emphasis of the study was on particle-wall deposition. It was observed that particles were accumulating in the viscous sublayer, and that those that deposit on the wall possessed wall-normal velocities similar to the wall-normal intensities of the bulk region. Another interesting observation was that the lift force was seen to have significant effect on the particle trajectories in the viscous sublayer, but little effect elsewhere.

Li and Ahmadi (1992) considered the dispersion and deposition of micro- and nano-scale injected spherical particulate phases at a point source using a mean velocity field coupled with instantaneously generated turbulence fluctuations. Each particle's equation of motion took into account lift, drag and Brownian motion contributions, but the authors chose to neglect virtual mass and pressure gradient forces due to their magnitude in relation to the Stokes drag force. The authors made a variety of conclusions from their results, notably that deposition rates increase with particle size and that Brownian motion is a significant contributing factor when considering the dispersion of nano-scale particles.

Li et al. (1994) used simulated mean flow fields with turbulent fluctuations as previously described to consider flows through an obstructed duct to investigate the flow and deposition around an object causing an obstruction (in this case taken to be a cuboidal block). Their results showed a significant increase in deposition rate which was reduced if the obstruction was streamlined, and they confirmed that the most significant factor for particle dispersion was due to the turbulence.

Later, Wang and Squires (1996b) carried out an LES of turbulent channel flow with a dispersed particulate phase at two shear Reynolds numbers, 180 and 644. The authors used the LES flow to calculate the forces on the particles at each time step, taking into account drag and gravitational forces. Results are compared with DNS and experimental studies and their findings for the dispersed phase show better agreement at lower Reynolds number. The authors also offer visualizations, exploring the preferential concentrations and obtaining distributions similar to that of DNS. Wang and Squires (1996a) followed up this work with a similar investigation into vertical pipe flow, with a focus on deposition. Results indicated that the deposition rates for particles with identical

non-dimensionalised relaxation times, but in flows of differing Reynolds numbers, were unchanged.

The first numerical simulations in pipe-like geometries were carried out by Uijttewaal and Oliemans (1996). Their work consisted of three simulations, one DNS for a lower Reynolds number and two LES for higher Reynolds numbers, all of which were combined with an LPT to model the particulate phase. The authors considered particle dispersion, deposition and concentration distributions and demonstrated that deposition was governed by the near-wall flow characteristics for small particles and by the turbulent dispersion for larger particles. It was also indicated that over time, a segregation of particles towards the wall becomes apparent.

Rouson and Eaton (2001) also considered preferential concentration, this time predicting the carrier phase using DNS, and modelling particles in a flow at a shear Reynolds number of 180. The authors present concentration histograms and examine further the level of order present in the particle distributions. It is indicated that at areas of low instantaneous fluid velocity magnitude, where particles have previously been observed to preferentially concentrate, the particles' velocities are suppressed.

Portela et al. (2002) further examined the wall region with respect to particle behaviour in order to obtain a better understanding of the deposition process in pipes. The authors carried out a DNS, modelling the particles as points using the LPT method. In their work they demonstrated the difference between elastic and absorbing walls and showed that local-equilibrium models for the turbophoretic effect are capable of simulating the process well except for very close to the wall.

The deposition process was later revisited by Marchioli et al. (2003), who performed a one way coupled LPT using DNS of a turbulent pipe flow. For this investigation, the authors also considered resuspension. The flow was such that the streamwise velocity was directed vertically upwards and so gravitational effects were also considered. The Reynolds number associated with the continuous phase was 337 and drag, lift and gravitational forces for the particulate trajectories were considered. The authors demonstrated a migration of particles towards the boundary layer and showed that the particle fluxes were directly related to the instantaneous realizations of Reynolds stresses.

Winkler et al. (2004) used LES for the carrier phase to investigate particle-laden vertical duct flow at a shear Reynolds number of 360. Using volume-fraction ratio arguments, the authors neglected to include particle-particle interactions as well as assuming that the particles would have no influence on the continuous phase. When considering the motion of the particles, the authors included the force contributions from lift, drag and gravity. Results included probability distribution functions relating to the particles preferred concentrations, and a trend between particle locations and regions of low vorticity was identified. This work was followed up by the same authors (Winkler et al., 2006) which focused on wall deposition. Their results suggested that higher Stokes numbers would increase the average non-streamwise velocities (the two wall normal components) and a general increase in deposition was found when compared with a pipe flow under the same Stokes and Reynolds number conditions.

The first DNS of particle-laden square duct flow was carried out by Sharma and Phares (2006) at a shear Reynolds number of 300 in the same year. The authors chose to include only the effect of drag when calculating the forces on the particles in order to fully resolve the effect that the secondary flow velocities have on the particle distributions. In particular, the authors noted that tracer particles and those with low inertia would mix laterally due to the presence of these flows, whereas heavier particles would be more likely to mix in the streamwise direction. The authors also provided visualizations of the particle distributions obtained in flows such as these.

A paper of particular value in this field which fully reflects the scope of many investigations is that by Marchioli et al. (2008) who compared the results of different computational codes, designed to simulate the dispersion of particles in wall-bounded turbulent channel flows. The codes tested were all primarily DNS-based and used Lagrangian particle tracking techniques to generate their results. The equation of motion for the particles only considered drag forces, arguing that the other forces considered in Elghobashi (1994) are magnitudinally irrelevant for density ratios greater than unity. The analysis indicated good agreement between all of the codes tested and the authors were able to generate a database of particle-laden turbulent flow statistics. In particular, attention was paid to the response of these statistics to different Stokes numbers. It was observed that for higher Stokes, the turbulent fluctuations in the span and wall-normal directions were dampened.

Picano et al. (2009) also simulated a turbulent pipe flow at $Re_B = 3000$. The focus of this study was on turbophoresis, the process where particles migrate towards and accumulate at the wall. To study this in more detail, particles were injected near the centre-line and the level of migration processes such as spreading and segregation was quantified by studying a Shannon-like entropy function. An interesting observation was that accumulations of particles are dragged towards the wall by short, rare turbulence events, whereas motion away from the wall is more frequent but smoother.

Dispersion in a turbulent duct flow was further investigated by Fairweather and Yao (2009) at a bulk Reynolds number of 250,000 which considered a wide range of particle sizes from 5 μm to 1 mm. The authors used LES to model the continuous phase and considered the forces of Stokes drag, gravity and buoyancy when calculating the motion of the particulate phase. By considering gravitational effects, the authors were able to show this force competes with the secondary flows to dominate the dispersion of the particulate phase. It is demonstrated, however, that for less inertial particles, the secondary flows are the main contributing dispersion factor. The authors also observe, as in previous literature, the tendency for particles to migrate to low streamwise velocity regions. Despite this, it was also noticed that deposition tended to occur more in the corner regions.

More recently, Yao and Fairweather (2010) studied particle resuspension (or the migration of particles from the duct wall to the bulk flow) under approximately the same simulation conditions as in Fairweather and Yao (2009). This time, the particles had diameters ranging from 5 μm to 500 μm and drag, lift, buoyancy and gravitational forces were taken into account. The authors showed that the secondary flows present in duct geometries are a contributing factor in the resuspension process and they demonstrate the importance of the various forces in different orientations.

Njobuenwu and Fairweather (2015a) used LPT to study single disc, sphere and needle shaped particles in an LES simulation of a turbulent channel flow at $Re_\tau = 300$. Euler parameters (or quaternions) were used to track orientation as in previous work, and torque was split up into three components: torque due to the centre of mass being offset from the centre of fluid pressure (incident on the particle); resistive torque due to the fluid possessing unequal angular momentum to the rotating particle; and finally a crossterm component based on fluid rotation due to perpendicular axes was included in the angular

equation of motion. Releasing the particles in different regions of the flow, statistics surrounding the temporal translational and orientational behaviour were provided over time and a range of motional modes was identified.

2.4.6 Two-way coupled LPT simulations

For increased volume fractions, the method in which particle-laden flows are simulated needs to be amended to account for the momentum feedback from the particles to the fluid. This entails various complexities which must be addressed in order to obtain an accurate representation of this process.

Firstly, the particle force-balance equation terms all require knowledge of the undisturbed fluid velocity at the particle centre point, which is not an issue for one-way coupled flows. However, with particle-fluid coupling, there are inherent modifications to the fluid velocity. A resolution to this issue was posed by Boivin et al. (2000) who argued that if the particle diameter is smaller than the grid spacing, then the disturbed and undisturbed velocities will be sufficiently similar. For point-particle DNS techniques, we already ensure that the particle diameter is less than the Kolmogorov scale, which is on the order of the minimum grid spacing. Therefore, this issue is usually resolved.

Secondly, particle forces exerted on the fluid are represented by a Dirac delta function, in that they apply a localised force onto the surrounding fluid. In practice, the total force from all particles in an Eulerian cell is attributed to the momentum feedback term when solving for that cell's updated velocity. This is referred to as a particle-source-in-cell (PSIC) method.

Pan and Banerjee (1996) performed a two-way coupled particle-laden turbulent channel flow simulation at around $\phi_P = 4 \times 10^{-4}$. To achieve coupling, the velocity disturbance was derived and calculated each timestep, with the assumption of a locally Stokesian flow. Preferential accumulation of particles in low-speed streaks was observed and small particles were found to suppress turbulence, while large particles enhanced it, a result observed experimentally.

Years later, Zhao et al. (2010) simulated a two-way coupled turbulent channel flow at $Re_\tau = 180$ with a focus on how the particulate phase affected the turbulence field. It was observed that the addition of particles had the surprising effect of increasing the bulk flow

rate, whilst also increasing the size of the coherent turbulent structures in the wall region of the flow. Again, streamwise turbulence enhancement was detected, whereas the spanwise and wall-normal components of the velocity fluctuations were attenuated.

Motivated by experimental work carried out by Kiger and Pan (2002) which suggested that inertial particles are capable of modifying the turbulent properties of the carrier phase, Zamansky et al. (2011) further examined flows at high Stokes and Reynolds numbers. The authors were successfully able to observe the predicted effects which include particle segregation and clustering using a DNS and an LPT. They also compared their DNS results with an extended LES which was capable of taking the subgrid acceleration contribution into account. This showed better accuracy than the standard LES when compared to the DNS results.

An investigation into the effect of Stokes number at constant mass fraction was performed by Lee and Lee (2015), who revisited the two-way coupled turbulent channel flow at $Re_\tau = 180$. They observed that lower Stokes number particles increased the rms velocity fluctuations while large Stokes numbers decreased them. An analysis of the near-wall turbulent events (sweeps and ejections) helped to explain this phenomenon.

2.4.7 Four-way coupled LPT simulations

At volume fractions, $\phi_\mathrm{P} > 1 \times 10^{-3}$, particle collisions occur frequently enough that they modify both the fluid and particle dynamics, as compared to a one-way or two-way coupled system. This added complexity is usually dealt with either deterministically, wherein all (or most of) the particle collisions are identified and simulated, or stochastically, where collision probabilities are used to determine whether a particle undergoes a collision (and what with) during any given timestep.

Furthermore, the way in which the post-collision dynamics are handled usually falls into one of two methods. The hard-sphere method does not allow two particles to overlap, and uses conservation of momentum and energy arguments to determine the resulting velocities of both particles. The soft-sphere method relies on the mechanical properties of the colliders to generate a repulsive contact spring force, which scales with overlap distance.

Li et al. (2001) considered inter-particle collisions (or four-way coupling) in their investigation into the behaviour of densely dispersed particle laden gases. The flow consisted of a vertical channel at $Re_B = 7000$. It was observed that at low mass loadings, the particles increase the overall mean velocity profile and hence the flow rate. The turbulence statistics were also modified such that the streamwise velocity fluctuations peak was skewed toward the centreline and the transverse fluctuations were dampened.

Vreman et al. (2009) considered the effect of four-way coupling in their LES of a vertical turbulent multi-phase channel flow. This time, the volume fraction was on the order of $\phi_P \sim 10^{-2}$ and so the effect of the dispersed phase on the fluid statistics was very strong. The simulation predicted a greatly flattened mean velocity profile along with a thinner boundary layer. Furthermore, the turbulence statistics were enhanced in the streamwise direction and dampened in the transverse directions as observed (albeit on a much smaller scale) by Li et al. (2001). They concluded that the inclusion of four-way coupling is vital for accurate simulations of particulate phases with volume fractions around 1%.

Breuer et al. (2012) performed a four-way coupled LES of a turbulent channel flow at $Re_B = 11{,}900$. In their paper, they describe an efficient deterministic search algorithm for particle-particle collisions, which reduces the computational cost from the order $O(N_P^2)$ to $O(N_P)$. Their results are shown to be in good agreement with experimental work.

A comprehensive framework for the prediction of flows containing non-spherical particles was provided by van Wachem et al. (2015) who used the model along with a DNS-LES fluid simulation to study their reaction to the flow, together with four-way coupled responses to the dispersed phase. To model the non-spherical particles, quaternions were used to track orientation. The authors state that the choice to transition from three to four degrees of freedom is worth the extra computation in the long run, as it avoids numerical issues during integration such as singularities. The results of their simulations concluded that there is a preferential orientation of the particles in order to maximise the drag force, which involves the semi-major axis aligning perpendicular to the flow. Other statistics such as velocity and turbulence intensity profiles were also provided.

Zhao et al. (2015) performed similar calculations, however their focus was on the coupling with the carrier phase and the effects of Stokes number and particle shape. Simulating at $Re_\tau = 150$, their results indicated that the turbulence is attenuated by the non-spherical particles, such that there is a reduction in intensities in the near wall region. During the same year, Vreman (2015) simulated a four-way coupled vertical channel flow at $Re_\tau = 642$, with a focus on the effect of wall roughness. It was observed that the rough walls increased the degree of turbulence attenuation. Discussion was also offered surrounding the attenuation being linked to the non-uniform region of the mean particle force profiles.

Kuerten and Vreman (2015) also studied collision dynamics in a turbulent channel flow at $Re_\tau = 150$. Collision frequency distributions were presented, and linked to the particle concentration profile, with an indication that turbophoresis drives increased particle-particle collisions in the near-wall region. Furthermore, the authors studied the effect of particle clustering in low-speed streaks on collision density.

Further post-collision mechanisms such as agglomeration have been sparsely implemented. Techniques to model inter-particle forces can be separated into attractive and repulsive potentials. An attempt to obtain a potential encompassing van der Waals attraction and electric double-layer Coulombic repulsion was made by DLVO-theory (Derjaguin and Landau, 1941; Verwey and Overbeek, 1955). A further proposition by Schenkel and Kitchener (1960) considers the retardation of the electromagnetic waves wave velocity at small separations, removing the assumption that the particles are aware of each other instantly.

Breuer and Almohammed (2015) performed a four-way coupled LES in a turbulent channel flow, with a van der Waals model to predict particle agglomeration. Their work simplified the post-collision dynamics by assuming the new particle cluster is spherical, with various models being tested for the properties of the new aggregate. The analysis focused on collision and agglomeration event frequency throughout the wall-normal channel direction.

Njobuenwu and Fairweather (2015b) implemented a deterministic algorithm for the prediction agglomeration events in an LES of a turbulent channel flow. Their model includes the effects of van der Waals interaction, inelastic particle-particle collisions and

an energy momentum balance. Their results demonstrate the agglomeration model and they observe an increase in aggregation with decreasing particle and fluid inertia and normal restitution coefficient.

2.4.8 Interface tracking

At an increased level of detail, the flow around the actual boundary of the particle can be resolved, with trajectories being calculated due to the fluid hydrodynamic forces being calculated on each face of the particle mesh. This methodology offers a large increase in accuracy, and allows for certain flows to be predicted at a very fundamental level, allowing for verification of force coefficient correlations and validation of low particle number flows. This is very computationally expensive regime to simulate within, and with present resources we are limited to simulating few particles in simple flow geometries.

In 2003, Bagchi and Balachandar (2003) performed a DNS of a single spherical particle in an isotropic turbulence field to verify drag and lift coefficients. Here, the particle was stationary and the fluid was resolved on the boundary of the particle. They used various particle sizes down to 1.5 times the Kolmogorov scale, and determined that standard drag correlations are fairly accurate when calculating the drag force on spherical particles. They did note, however, that this accuracy diminishes slightly with increasing particle size. They also observed that the inclusion of added mass and history forces offered no improvements to the predictions for larger particles.

A similar method was applied by Vreman (2016), who used DNS to study homogeneous isotropic turbulence at $Re_\lambda = 32$ in the vicinity of 64 fixed spherical particles with diameters twice the Kolmogorov scale. The author observed turbulence attenuation, but commented that it was less than expected. It is likely that due to the particles being fixed, the loss of information surrounding inertial effects and turbulence interaction may cause this underprediction.

Uhlmann (2005) implemented an immersed boundary method to study various situations involving suspended rigid particles, wherein the Eulerian grid was fixed. His method used direct forcing to predict the fluid-solid interaction, and particle motion was smooth. Their results were tested against a Taylor-Green flow and high accuracy was demonstrated.

Mark and van Wachem (2008) detailed and demonstrated a second-order accurate immersed boundary method to simulate flow around suspended bodies. They compared two different forcing methods, with a mirroring (or ghost-cell) method leading to a good validation of simulations of the flow around a sphere at various particle Reynolds numbers.

Picano et al. (2015) used DNS coupled with the immersed boundary method to study 10,000 neutrally buoyant spheres in a turbulent channel flow. They observed that the mean flow statistics were altered by the presence of particles, depending on their volume fraction. It was also observed that the velocity fluctuations were increased at their highest volume fraction.

2.4.9 Particulate-phase fundamental studies

This final subsection aims to draw attention to and discuss some of the more fundamental studies concerning the dynamics of particles subject to turbulence. A review by Balachandar and Eaton (2010) discusses the complexities associated with both experimental and computational techniques for predicting such flows, with a focus on preferential concentration, interphase coupling and turbulence modulation.

Contrary to tradition particle dispersion theories, particles in turbulence have a tendency to form dense clusters, which is discussed extensively in a paper by Eaton and Fessler (1994). Their work discusses the important role of particle relaxation time or Stokes number in determining the extent of preferential concentration. They also identify the mechanisms by which particles are subject to this phenomenon by linking the motion to the local turbulence structures. It is suggested that particles centrifuge away from vortex cores and congregate in convergence zones.

A study performed by Maxey (1987) determined the effect of particle-fluid density ratio on the motion of spherical particles within a flow field. Their results indicated that the particle inertia plays a key role in the resulting particle trajectories. This work was expanded upon by (Squires and Eaton, 1991) who studied inertial particles and their motion in homogeneous isotropic turbulence. They discovered that the peak level of local concentration occurred at a Stokes number of 0.15 based on the relevant box integral scales.

A lot of work has been carried out to determine the validity of the point-particle approximation, particularly in the case for two-way coupled flows, where the information surrounding the undisturbed local flow field is often unavailable. The simulation of particles larger than the Kolmogorov length scale has been considered by Bagchi and Balachandar (2003) who used DNS to study the effect of turbulence under freestream conditions on the various drag and lift force components for spherical particles. It was observed that for increasing particle size, the accuracy of the drag prediction using standard correlations decreases. Various other works which are covered in Balachandar and Eaton (2010) determine that for small particles, no special treatment is required, and the standard semi empirical force-balance equation is sufficient to accurately predict trajectories. A final caveat to this is discussed in Balachandar (2009) which requires that, due to the effects of self-induced vortex shedding, the particle Reynolds number must be sufficiently low, which is usually the case for the flows of interest.

Finally, for more information surrounding the experimental and computational prediction and understanding of multiphase flows, the reader is referred to the textbooks of Crowe et al. (1998) and Crowe (2005).

2.5 Conclusions of the Literature Review

In this chapter, the key pieces of literature relevant to studying single and multi-phase flows in various geometries have been summarised and detailed. Upon doing so, it becomes apparent that there is an abundance of work carried out over the last few decades surrounding both experiment and simulation of particle-laden turbulent flows.

From an analysis of the direction of experimental work, it seems that there is great interest in the behaviour of turbulent flow structures, and the interaction between those and solid particles. However, in order to resolve these, highly resolved simultaneous three dimensional velocity fields must be captured. This is a very difficult process to achieve in a real system, but is very feasible with a highly-resolved DNS.

Present simulation work is mainly focused on systems with high density ratio flows such as those in air, whereas multi-phase simulations carried out at low density ratios are sparse. This gap in the literature is capable of being filled by carrying out a piece of work directed towards accurately simulating turbulent channel flows in a viscous media such as water containing a particulate phase. Furthermore, to consider accurate representations

of dense flows, it is evident from previous literature that two- and four-way coupling must be considered. Previous work on agglomeration techniques employing potential barriers as detailed by DLVO theory is also sparse, hence this is to be considered when determining post-collision events.

A strong understanding concerning the dispersive behaviour of particulate phases present in horizontally directed turbulent channel flows at low density ratios would not only benefit and build upon the current literature but it is also capable of generating new avenues for analysis and discussion; a comparison with simulation under the inclusion of other physical processes such as agglomeration, deposition and resuspension for instance.

Finally, in the past decade new potential (in terms of methods and computational power) for highly accurate simulations has become possible, with front-tracking methods forming the majority of fundamental particle-level multiphase flow research. Combining the recent interest in particle agglomeration events with these new techniques would allow detailed elucidation of particle-particle collision and aggregation processes, at a level of detail surpassing that of a standard LPT simulation.

In the present work, therefore, studies will be made of multi-phase turbulent flows using high-accuracy simulation techniques, with an emphasis on elucidating the dynamics surrounding how particles interact with both the turbulence itself and other particles in the presence of turbulence.

3 METHODOLOGY

3.1 Introduction

Within this chapter the relevant theory and numerical methods used within this project to accurately simulate particle-laden turbulent flows shall be presented in detail. First, the spectral element-based fluid phase DNS solver, Nek5000, shall be introduced. To simulate the particulate phase both an LPT and IBM are developed to run alongside the DNS solver and so these shall also be explored.

3.2 Fluid-phase modelling

3.2.1 Navier-Stokes equations

Modelling the temporal evolution of the fluid phase is based upon solutions to the fundamental equations which arise due to enforcing conservation of mass, momentum and energy across a small three-dimensional fluid element. For all simulations performed for the work presented in this thesis, we assume that the fluid is incompressible and Newtonian. With these conservation laws and assumptions in place, the resulting equations are the Navier-Stokes (NS) equations. These are fundamental to the field of fluid dynamics, and are listed below:

Mass: $$\boldsymbol{\nabla} \cdot \boldsymbol{u}_F^* = 0, \tag{10}$$

Momentum: $$\frac{\partial \boldsymbol{u}_F^*}{\partial t^*} + \boldsymbol{u}_F^* \cdot \boldsymbol{\nabla} \boldsymbol{u}_F^* = -\boldsymbol{\nabla} p^* + \frac{1}{Re_B} \boldsymbol{\nabla} \cdot \boldsymbol{\tau}^* + \boldsymbol{f}_{PG}^* + \boldsymbol{f}_{2W}^{*i}. \tag{11}$$

Here, $\boldsymbol{u}_F^*(\boldsymbol{x}^*, t^*)$ is the non-dimensionalized (using the bulk velocity, U_B) fluid velocity vector at position vector $\boldsymbol{x}^* = \boldsymbol{x}/\delta$, t^* is the non-dimensionalized time ($t^* = tU_B/\delta$), δ is the channel half-height, p^* is the non-dimensionalized pressure ($p^* = p/\rho_F U_B^2$), ρ_F is the continuous phase density, Re_B is the bulk Reynolds number of the flow ($Re_B =$

$U_B\delta/\nu_F$), ν_F is the kinematic viscosity of the fluid phase, and $\boldsymbol{\tau}^*$ is the non-dimensionalized deviatoric stress tensor for a Newtonian fluid. This is given by:

$$\boldsymbol{\tau}^* = \boldsymbol{\nabla u}_F^* + \boldsymbol{\nabla u}_F^{*T}. \tag{12}$$

The final two terms in the momentum equation are additional fluid forces. $\boldsymbol{f}_{PG}^*$ represents a constant pressure gradient forcing term used to obtain a steady flow, and $\boldsymbol{f}_{2W}^{*i}$ is an arbitrary cell-dependent forcing term which accounts for the two-way momentum exchange between particles in that cell and the surrounding fluid. This term is zero for single-phase investigations. For two-way coupled simulations, this term will be defined and explored further in the LPT section. These equations, along with the appropriate boundary conditions, formulate a fluid dynamics system, and the bulk of the single-phase study revolves around solving such problems.

3.2.2 Direct numerical simulation

As the focus of the work is on fundamental dynamics and small-scale particle interactions in turbulence, it is important that all relevant spatial and temporal scales are resolved when obtaining a mathematical description of the fluid phase. This means that the Kolmogorov scale, η, up to the integral length scale, L, must be resolved on the computational solution mesh. By ensuring this condition is met upon the solution grid, and by utilising a time stepping procedure which resolves the smallest time scales associated with the turbulent eddies, a direct numerical simulation is being performed. This creates a high-fidelity solution for the fluid velocity and pressure fields and all elements and structures associated with the turbulence should be captured.

3.2.3 Nek5000 solution algorithm

Due to its efficient parallelisation capabilities and extensive testing and validation history, the numerical code Nek5000 is used extensively throughout this project in order to obtain a high-resolution representation of the carrier phase through DNS. Nek5000 is based around the spectral element method (SEM) as described in (Patera, 1984), which is a combination of finite element and high-order accuracy spectral methods.

The SEM is a high-order weighted residual technique which is implemented by splitting the domain into multiple hexahedral subdomains or elements which form the full system. This provides enhanced flexibility in the case of complex geometries. The solution is then represented as N^{th} order tensor-product polynomials within each of these elements. For all simulations performed within this project we choose polynomial $N = 7$, which corresponds to 8^3 gridpoints per element.

Within the SEM, the Navier-Stokes equations undergo a weak formulation transformation, which entails multiplying them by test functions before integrating over each element in the domain. Spatial discretisation is obtained via use of the Galerkin approximation. Solution bases for velocity and pressure are N^{th} and $(N\text{-}2)^{th}$ order Lagrangian polynomial interpolants, respectively, following (Maday and Patera, 1989). The calculations within each of these elements are capable of being performed in parallel, allowing for good time efficiency when carrying out the necessary computations.

Time-stepping is treated semi-implicitly. The non-viscous terms use a third order extrapolation scheme and the viscous terms use implicit third order backward differentiation. Upon solving the equations at each time-step, a velocity and pressure field is obtained across a Cartesian coordinate system, as specified by the user.

3.2.4 Channel flow computational domain

Throughout the first two results chapters of this study, the system geometry consists of a rectangular channel. The streamwise direction runs between $x^* = -7$ to $x^* = 7$ in non-dimensional half-height units and is periodic. The wall-normal direction runs between $y^* = -1$ to $y^* = 1$ and no-slip and impermeability conditions are enforced at either end. Finally, the spanwise direction runs between $z^* = -3$ to $z^* = 3$ and is also periodic. This is illustrated in Figure 3.1. The mesh generated to represent this geometry consists of $27 \times 18 \times 23$ 7^{th} order elements (i.e. 3.9M nodes). The elements are scaled such that those closest to the wall are distributed more densely. This is important since the near-wall regions (viscous sublayer and buffer layer) contain most of the smallest turbulence scales, which must be resolved completely to take into account their effects on the dispersed phase. The element distribution is illustrated in Figure 3.2.

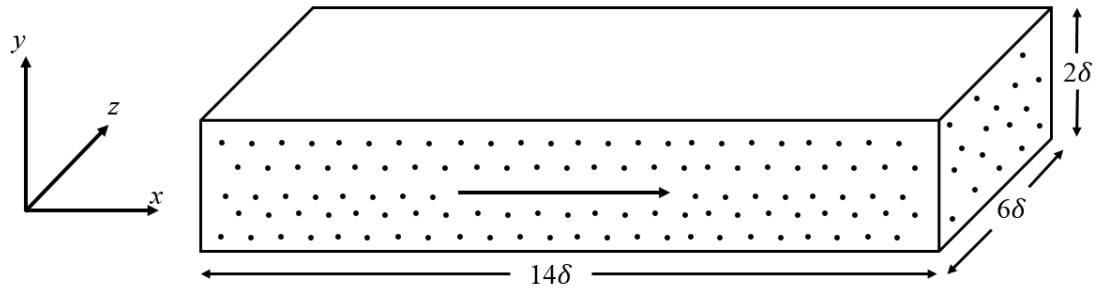

Figure 3.1: Schematic of multi-phase turbulent channel flow computational domain.

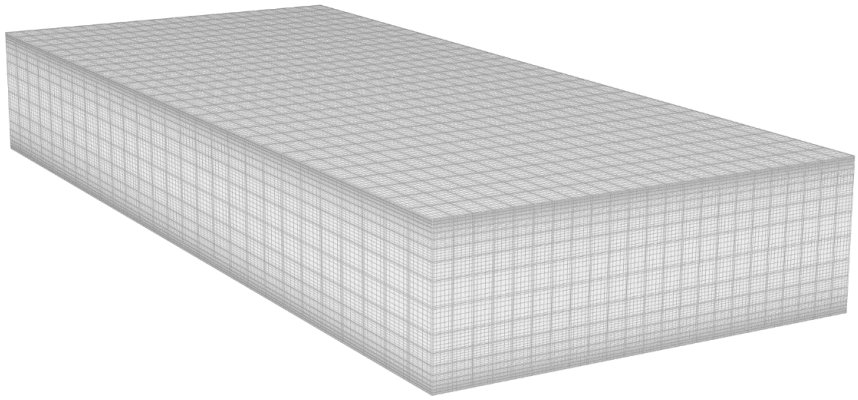

Figure 3.2: Computational mesh demonstrating element spacings and increased near-wall nodal density.

3.2.5 Channel flow forcing and turbulence onset

The channel flow is driven and maintained by a constant pressure gradient in the streamwise (x^*) direction. Using non-dimensional parameters, its magnitude is:

$$\frac{\partial p^*}{\partial x^*} = \left(\frac{Re_\tau}{Re_B}\right)^2 \tag{13}$$

where $Re_\tau = u_\tau \delta / \nu_F$ is the shear Reynolds number, which uses the shear velocity, $u_\tau = \sqrt{\tau_W / \rho_F}$, where τ_W is the mean wall shear stress. For the first two results chapters, the continuous phase parameters used for the analysis and validation grids are presented in Table 1

Table 1: Parameters for DNS of turbulent channel flow. $L_{x,y,z}$ represents the Cartesian lengths of the domain, $E_{x,y,z}$ are the number of elements in each direction.

$\boldsymbol{Re_\tau}$	$\boldsymbol{Re_B}$	$\boldsymbol{L_x \times L_y \times L_z}$	$\boldsymbol{E_x \times E_y \times E_z}$
150 (LPT Validation)	2100	$14\delta \times 2\delta \times 6\delta$	$27 \times 18 \times 23$
180 (Analysis)	2800	$14\delta \times 2\delta \times 6\delta$	$27 \times 18 \times 23$

3.2.6 Periodic box computational domain

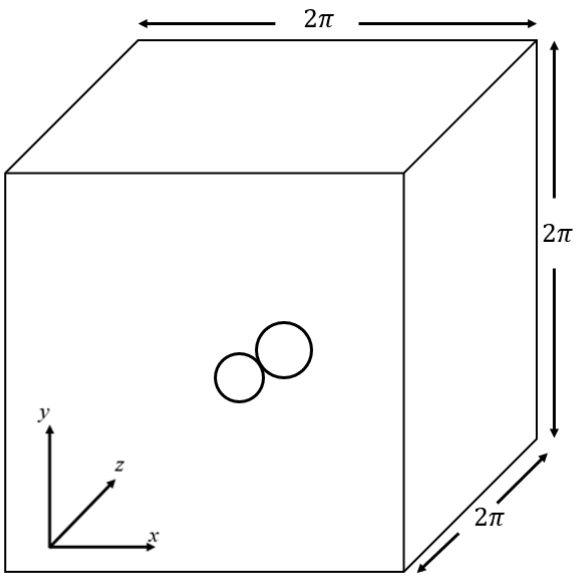

Figure 3.3: Schematic of isotropic periodic box of turbulence.

The computational mesh consists of a box with length 2π in each direction, discretized into 48 × 48 × 48 equally distributed cubic spectral elements of order $N = 7$. Periodic boundary conditions are enforced at $\pm\pi$ in each direction. This is illustrated in Figure 3.3.

3.2.7 Periodic box linear forcing method and turbulence onset

The linear forcing method (Rosales and Meneveau, 2005; Lundgren, 2003) is used to drive the system to isotropic homogenous turbulence at four different Reynolds numbers (based on the Taylor microscale, λ). These are $Re_\lambda = 29$, 51, 120 and 197, where $Re_\lambda = \langle u_{rms}{}' \rangle \lambda / \nu_F$. Here, $\langle u_{rms}{}' \rangle$ is the averaged root mean square velocity fluctuation and ν_F is the kinematic viscosity of the fluid. In a turbulent channel flow, these Reynolds numbers are typical of the bulk flow, log-law, buffer layer and viscous sublayer regions, respectively.

The linear force per unit mass term is given by $\boldsymbol{f}_{LF} = A\boldsymbol{u}_F$, where A is a specified parameter relating to an eddy turnover time scale. Tuning of this parameter allows one to obtain a desired turbulence level. The fluid-phase parameters are presented in Table 2

Table 2: DNS parameters for periodic cubes of linearly forced isotropic turbulence.

$\boldsymbol{Re_\lambda}$	**29**	**51**	**120**	**197**
N_E	48^3	48^3	48^3	48^3
A	0.0667	0.2	1.0	0.1667
ρ_F	1	1	1	1
ν_F	4.491×10^{-3}	4.491×10^{-3}	1.272×10^{-2}	3.256×10^{-4}

3.3 Lagrangian particle tracking

3.3.1 Introduction

To model transport of the dispersed phase, a Lagrangian particle tracker (LPT) has been developed which interfaces concurrently with Nek5000. By tracking individual particles through the flow, we obtain a representation of the system which is close to reality and allows for flexibility in the way we analyse particle and fluid behaviour. The LPT solves the non-dimensional equations of motion for each particle at timesteps equal to that of the single-phase solver. The full Newtonian equation, its origin and its derivation are presented below.

For this work, we have chosen to consider contributions from drag, lift, virtual mass and pressure gradient forces. The Basset history force is ignored due to its high compute time

and the negligible impact it has been found in to have in previous studies (Fairweather and Hurn, 2008). The fourth order Runge-Kutta scheme is applied for accurate integration of the differential equations in order to obtain each particle's position and velocity at every timestep. This is considered in more detail below.

3.3.2 Particle equation of motion

The choice of the particle equation of motion used is a decision which should be made based upon both the properties of the particles (size, shape, density, etc.) and the environment which they are subjected to (turbulence, boundaries, etc.). There has been a great amount of work performed in recent decades surrounding the form of the particle equation of motion. In our work, we choose to use a modified version of the Maxey and Riley equation (Maxey and Riley, 1983). The equations of motion for a spherical particle are presented in Eqns. (14) and (15):

$$\frac{\partial \boldsymbol{x}_P^*}{\partial t^*} = \boldsymbol{u}_P^*, \tag{14}$$

$$\frac{\partial \boldsymbol{u}_P^*}{\partial t^*} = \frac{1}{M_{VM}}\left[\underbrace{\frac{3C_D|\boldsymbol{u}_S^*|}{4d_p^*\rho_P^*}\boldsymbol{u}_S^*}_{Drag} + \underbrace{\frac{3}{4}\frac{C_L}{\rho_P^*}(\boldsymbol{u}_S^* \times \boldsymbol{\omega}_F^*)}_{Lift} + \underbrace{\frac{1}{2\rho_P^*}\frac{D'\boldsymbol{u}_F^*}{Dt^*}}_{Virtual\ Mass} + \underbrace{\frac{1}{\rho_P^*}\frac{D\boldsymbol{u}_F^*}{Dt^*}}_{Pressure\ Gradient}\right]. \tag{15}$$

A detailed derivation and explanation for each contribution to these equations is found below.

3.3.3 Non-dimensional parameters

Since the NS equations in Nek5000 are presented and solved non-dimensionally, it is natural to cast the particle equations of motion in the same form. In order to obtain a set of non-dimensional equations to be integrated by the LPT, we must first define some parameters. The non-dimensional quantities (using bulk properties of the flow) for an arbitrary length (x), velocity (u), density (ρ) and time (t) are given as follows:

$$x^* = \frac{x}{\delta}, \tag{16}$$

$$u^* = \frac{u}{U_B}, \tag{17}$$

$$\rho^* = \frac{\rho_P}{\rho_F}, \tag{18}$$

$$t^* = \frac{tU_B}{\delta}. \tag{19}$$

We may also define a particle Stokes number which is the ratio of the fluid and particle characteristic time-scales. The fluid time scale associated with bulk motion is:

$$\tau_{F,B} = \frac{\delta}{U_B}. \tag{20}$$

The time scale associated with the particulate phase is known as the particle relaxation time. This is a characteristic particle parameter which is based upon the time scale within which the particle adjusts to the flow based upon a newly entered local velocity field. This property is based upon both the particle density and diameter, with relaxation time increasing more rapidly with the latter. It is given by:

$$\tau_P = \frac{\rho_P d_P^2}{18\,\mu_F\, f_D}, \tag{21}$$

where $f_D$is a non-dimensional Stokes' drag function defined in the following subsection. Hence the particle Stokes number based on the bulk velocity scale is given by:

$$St_B = \frac{\tau_P}{\tau_{F,B}} = \tau_P^* = \frac{d_P^{2^*} \rho_P^* Re_B}{18 f_D} \tag{22}$$

We may also use the shear velocity scale to define the particle Stokes number. The time scale associated with the shear at the solid boundary is:

$$\tau_{F,\tau} = \frac{\nu_F}{u_\tau^2}, \tag{23}$$

and hence the associated particle Stokes number is:

$$St_\tau = \frac{\tau_P}{\tau_{F,\tau}} = \tau_P^+ = \frac{d_P^{2^*} \rho_P^* Re_\tau^2}{18 f_D}. \tag{24}$$

We can then obtain an expression relating the particle's two Stokes numbers based on different fluid time scales:

$$\frac{St_\tau}{St_B} = \frac{Re_\tau^2}{Re_B}, \tag{25}$$

which allows one to switch between the two Stokes numbers using only fluid-phase system properties. An interesting observation is that this ratio is precisely the induced pressure gradient.

3.3.4 Stokes drag force

Generally, the most dominant force in a fluid-particle system with micron-scale particles is due to frictional drag. The force on the curved surface of spherical particle subject to fluid impact (in dimensional form) is given by the following expression:

$$\boldsymbol{F}_D = \frac{3\rho_F m_P C_D(\boldsymbol{u}_F - \boldsymbol{u}_P)|\boldsymbol{u}_F - \boldsymbol{u}_P|}{4\rho_P d_P} \tag{26}$$

where ρ_P is the density of the particle phase, m_P is the mass of the particle, d_P is the diameter of the particle, C_D is the drag coefficient, $\boldsymbol{u}_F$ is the instantaneous fluid velocity at the position of the particle and $\boldsymbol{u}_P$ is the particle instantaneous velocity. The drag coefficient, C_D, is a function of the particle's Reynolds number, Re_P where:

$$Re_P = \frac{\rho_F d_P|\boldsymbol{u}_F - \boldsymbol{u}_P|}{\mu_F}. \tag{27}$$

We can make a useful substitution by defining the slip velocity, $\boldsymbol{u}_S$, which is the instantaneous velocity of the fluid in the particle's reference frame. Hence:

$$\boldsymbol{u}_S = \boldsymbol{u}_F - \boldsymbol{u}_P. \tag{28}$$

Non-dimensionalising Eqn. (27) using the above substitution alongside the definition of the particle Reynolds number we obtain:

$$Re_P = Re_B d_P^* |\boldsymbol{u}_S^*|. \tag{29}$$

We may now use this to express the drag coefficient as such:

$$C_D = \frac{24}{Re_P} f_D \tag{30}$$

where (Schiller, 1934) and (Clift et al., 2005) offer empirical drag correlations with particle Reynolds number as below:

$$f_D = \begin{cases} 1 & 0 < Re_P \leq 0.5 \\ 1 + 0.15Re_P^{0.687} & 0.5 < Re_P \leq 1000 \\ \frac{0.44}{24} Re_P & 1000 < Re_P \leq 250{,}000 \end{cases} \quad (31)$$

These have been validated via interface tracking techniques (Mark and van Wachem, 2008) and are suggested as the best practice method in various review papers (Loth, 2000; M. Kuerten, 2016). The force equation for drag is hence derived as follows:

$$\boldsymbol{F}_D = m_P \frac{\partial \boldsymbol{u}_P}{\partial t} = \frac{3\rho_F m_P C_D(\boldsymbol{u}_S)|\boldsymbol{u}_S|}{4\rho_P d_P} \quad (32)$$

or,

$$m_P \frac{\partial \boldsymbol{u}_P^*}{\partial t^*}\left(\frac{U_B^2}{\delta}\right) = m_P \frac{3C_D|\boldsymbol{u}_S^*|}{4d_P^*\rho_P^*}\left(\frac{U_B^2}{\delta}\right)\boldsymbol{u}_S^*. \quad (33)$$

The particle equation of motion for solely drag contributions is therefore:

$$\frac{\partial \boldsymbol{u}_P^*}{\partial t^*} = \frac{3C_D|\boldsymbol{u}_S^*|}{4d_P^*\rho_P^*}\boldsymbol{u}_S^*. \quad (34)$$

3.3.5 Saffman slip-shear lift force

Particles are subject to a shear transverse lift force which arises due to local velocity gradients on the particle scale. The strength and direction of the lift force on a small sphere in a slow shear flow was studied by (Saffman, 1965) for low particle Reynolds number. It was observed that the force acts to displace the particle in a direction normal to the local fluid streamlines. Their expressions were later extended by (Mei, 1992) and (Dandy and Dwyer, 1990) for high particle Reynolds number, obtaining the following equation:

$$\boldsymbol{F}_L = \frac{\rho_F}{2}\frac{\pi}{4}\, d_P^2 C_L d_P(\boldsymbol{u}_S \times \boldsymbol{\omega}_F), \tag{35}$$

where

$$C_L = \frac{4.1126}{Re_S^{0.5}} f(Re_P, Re_S), \tag{36}$$

and $\boldsymbol{\omega}_F$ is the vorticity of the fluid, given by:

$$\boldsymbol{\omega}_F = \boldsymbol{\nabla} \times \boldsymbol{u}_F. \tag{37}$$

Here, the Reynolds number of the shear flow around the particle is given as:

$$Re_S = \frac{\rho_F d_P^2}{\mu_F} |\boldsymbol{\omega}_F|, \tag{38}$$

which can be rewritten in terms of non-dimensional parameters as:

$$Re_S = Re_B {d_P^2}^* |\boldsymbol{\omega}_F^*|. \tag{39}$$

The particle Reynolds number scaling for the lift force is as follows:

$$f_L = \begin{cases} \left(1 - 0.3314\beta^{\frac{1}{2}} e^{-\frac{Re_P}{10}}\right) + 0.3314\beta^{\frac{1}{2}} & 0 < Re_P \leq 40 \\ 0.0524(\beta Re_P)^{\frac{1}{2}} & Re_P \geq 40 \end{cases} \tag{40}$$

where

$$\beta = 0.5\frac{Re_S}{Re_P}. \tag{41}$$

The non-dimensional equation for the particle's motion due to solely lift force we choose to use is therefore:

$$\frac{\partial \boldsymbol{u}_P^*}{\partial t^*} = \frac{3}{4}\frac{C_L}{\rho_P^*}(\boldsymbol{u}_S^* \times \boldsymbol{\omega}_F^*). \tag{42}$$

3.3.6 Gravity and buoyancy force

The force due to the influence of gravity upon a spherical mass, m_P, suspended within a fluid with density ratio, ρ_P^*, is as follows:

$$\boldsymbol{F}_G = \boldsymbol{g}(1 - \rho_P^*)m_p, \tag{43}$$

where **g** is the gravitational acceleration vector, which has magnitude 9.8 ms^{-2} and a direction which is geometry dependent. This non-dimensionalizes to:

$$\frac{\partial \boldsymbol{u}_P^*}{\partial t^*} = \frac{1}{Fr}(1 - \rho_P^*)\hat{\boldsymbol{g}}, \tag{44}$$

where $\hat{\boldsymbol{g}}$ is a unit vector in the direction of gravitational attraction and Fr is the Froude number defined by:

$$Fr = \frac{U_B^2}{|\boldsymbol{g}|\delta}. \tag{45}$$

Although implemented, for all simulations presented within this thesis, gravitational forces are not considered due to the focus of the analysis, considered further below.

3.3.7 Local pressure gradient force

The force due to differences in pressure across the local fluid field around the particle is obtained from standard expressions from Newtonian physics wherein a particle subject to a pressure field naturally migrates from a region of high pressure to one of lower pressure. The equation is (neglecting the buoyancy term which has been included in the gravitational term):

$$\boldsymbol{F}_P = \rho_F V_P \frac{D\boldsymbol{u}_F}{Dt}. \tag{46}$$

where $\frac{D}{Dt}$ is the material derivative, given by:

$$\frac{D}{Dt} = \frac{\partial}{\partial t} + \boldsymbol{u}_P \cdot \boldsymbol{\nabla} \tag{47}$$

This can be non-dimensionalized to the form:

$$\frac{\partial \boldsymbol{u}_P^*}{\partial t^*} = \frac{1}{\rho_P^*} \frac{D\boldsymbol{u}_F^*}{Dt^*}. \tag{48}$$

3.3.8 Virtual mass force

The virtual (or added) mass force arises due to consideration of the local accelerating or decelerating fluid field which provides unsteady forces on the submerged particle. It was first observed by Friedrich Bessel and later quantified by (Stokes, 1851). It is expressed as:

$$\boldsymbol{F}_V = \frac{\rho_F}{2} V_P \left(\frac{D\boldsymbol{u}_F}{Dt} - \frac{\partial \boldsymbol{u}_P}{\partial t} \right). \tag{49}$$

By moving the particle velocity term over to the left hand side of the equation, we obtain what appears to resemble an 'added mass' which acts across all force contributions. This can be further be non-dimensionalized and simplified to:

$$\frac{\partial \boldsymbol{u}_P^*}{\partial t^*} = \frac{1}{2\rho_P^*}\left(\frac{D\boldsymbol{u}_F^*}{Dt}\right), \tag{50}$$

where for simulations using virtual mass forces, we ensure that we divide by the 'added mass' in the full equation of motion:

$$M_{VM} = \left(1 + \frac{1}{2\rho_P^*}\right). \tag{51}$$

For simulations where this force is negligible, the above term is set to unity. In general, the force is only relevant for particle-fluid systems with low density ratios. For $\rho_P^* \gg 1$, we observe that $M_{VM} \to 1$ and so this condition is consistent.

3.3.9 Fourth order Runge-Kutta (RK4) algorithm

These equations are solved for each particle after the fluid time stepping has occurred using a 4th-order Runge-Kutta integration algorithm. The algorithm, which is detailed by (Flannery et al., 1992), amongst others, is capable of numerically integrating any differential equation such as those listed above. The method is simple and offers fourth order accuracy with errors on order of $(dt)^4$. It relies on using information about the increments in the timestepped quantity (velocity or position) based on gradients at four regions of the interval. A weighted average is then taken to account for the full step. The solution algorithm is as follows.

We begin with a differential equation of the form:

$$\frac{d\boldsymbol{u}_P(t)}{dt} = \boldsymbol{u}_P'(t) = f(\boldsymbol{u}_P(t), t) \tag{52}$$

with the initial condition:

$$\boldsymbol{u}'_P(t=0) = \boldsymbol{u}_0. \tag{53}$$

Then, performing a Taylor series expansion on $\boldsymbol{u}_P(t+dt)$ we obtain:

$$\boldsymbol{u}_P(t+dt) = \boldsymbol{u}_P(t) + \boldsymbol{u}'_P(t)dt + \frac{1}{2!}\boldsymbol{u}''_P(t)dt^2 \tag{54}$$

$$+\frac{1}{3!}\boldsymbol{u}'''_P(t)dt^3 + \frac{1}{4!}\boldsymbol{u}''''_P(t)dt^4 + \cdots$$

which is of the form:

$$\boldsymbol{u}_P(t+dt) = \boldsymbol{u}_P(t) + f(t,\boldsymbol{u}_P)dt + \frac{1}{2!}f'(t,\boldsymbol{u}_P)dt^2 \tag{55}$$

$$+\frac{1}{3!}f''(t,\boldsymbol{u}_P)t^3 + \frac{1}{4!}f'''(t,\boldsymbol{u}_P)dt^4 + \cdots$$

The RK4 scheme is then as follows:

$$\boldsymbol{u}_P(t+dt) = \boldsymbol{u}_P(t) + \frac{dt}{6}(\boldsymbol{k}_1 + 2\boldsymbol{k}_2 + 2\boldsymbol{k}_3 + \boldsymbol{k}_4) \tag{56}$$

with

$$\boldsymbol{k}_1 = f(t,\boldsymbol{u}_P) \tag{57}$$

$$\boldsymbol{k}_2 = f(t + \frac{dt}{2}, \boldsymbol{u}_P + \frac{\boldsymbol{k}_1 dt}{2}) \tag{58}$$

$$\boldsymbol{k}_3 = f(t + \frac{dt}{2}, \boldsymbol{u}_P + \frac{\boldsymbol{k}_2 dt}{2}) \tag{59}$$

$$\boldsymbol{k}_4 = f(t + dt, \boldsymbol{u}_P + \boldsymbol{k}_3 dt) \tag{60}$$

where each of the above terms represent the slope at different points during the full timestep (dt). Since all particle relaxation times considered are much greater than the relevant fluid time scale, in the present implementation, $dt = dt^*$ in that the particle solver uses the same timestep length as the fluid solver.

3.3.10 Two-way momentum coupling

For increased volume fractions, the forces exerted by the dispersed phase on the carrier fluid must be modelled to ensure accuracy. Each particle's inertial effect on the fluid phase is considered through the inclusion of an additional source term in the NS equations, the acceleration term on cell i is given by:

$$\boldsymbol{f}_{2W}^{*i} = \frac{1}{V_i^*} \sum_j \frac{\partial \boldsymbol{u}_{P_j}^*}{\partial t^*}. \tag{61}$$

Here, V_i^* is the volume of the computational cell and j is an index which runs over the number of particles contained within that cell.

3.3.11 Particle-particle and particle-wall collisions

The LPT also considers particle-particle interactions (or four-way coupling) in the form of hard-sphere elastic collisions in order to more accurately simulate systems with solid-phase volume fractions, $\phi_P \geq 10^{-3}$. Here, we choose to use hard-sphere collision model, as opposed to a full impulse-resolved soft-sphere model, since we assume that the time in which the collision takes place is much lower than the timestep. Furthermore, we

assume that any other interparticle forces acting over the course of the collision are negligible, or in the case of agglomeration will be modelled separately. To reduce computation time, a deterministic binary collision search algorithm based on the work of Breuer et al. (2012) is implemented. This assumes that the particle collision contact time is smaller than the LPT timestep, which is realistic since the particles are rigid and undeformable.

At each timestep, the particles are distributed into cells within a secondary coarse mesh, with the number of cells specified by the user. This is illustrated in the left diagram of Figure 3.4.

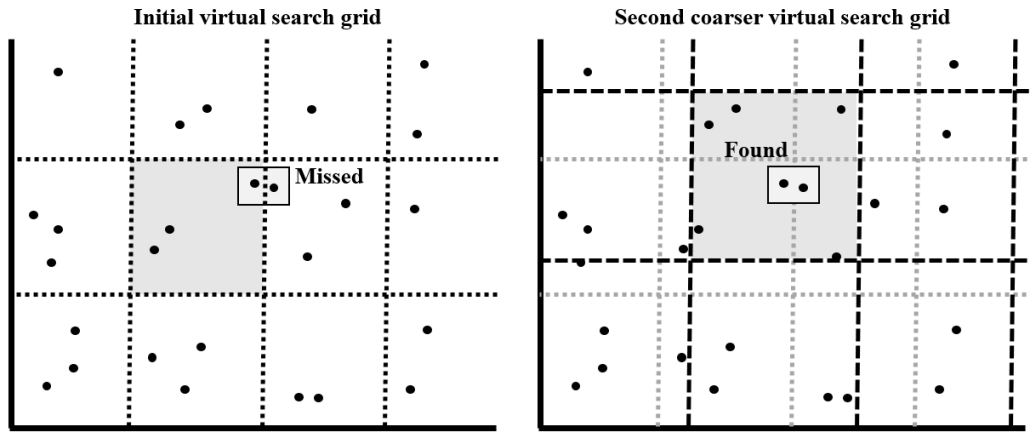

Figure 3.4: Initial (left) and secondary (right) search grids for deterministic binary collision identification.

The collision algorithm is then performed on each individual cell in this new mesh, treating each as a new full domain. The code determines which particles have collided by checking their relative inter-surface displacements and velocities. If both quantities are below zero, the particles collide. This algorithm is performed on all cells and allows for fast collision detection, reducing the computational order from $O(N_P^2)$ to $O(N_P)$. The search is then repeated on a slightly coarser grid, identifying pairs of particles which would have been missed in the initial search. In all simulations considered within this thesis we chose a value of 32^3 equal cells for the initial search and 30^3 cells for the secondary search, which provided the fastest computational time whilst ensuring the initial boxes were large enough to capture most of the collisions. Without this, accurate

collision identification for high particle numbers would be close to impossible with current computational resources.

To perform the collision, standard kinetic energy and momentum conservation arguments are used to determine resultant velocities. Particles are also deflected a distance r_{def} which accounts for the distance they had travelled 'inside' the collision partner. For LPT simulations, particle-particle and particle-wall collisions are assumed to be fully elastic.

Particle wall collisions and periodic boundary reinjection are performed at the end of each timestep (to account for the chance that a particle deflects off another particle and collides with a wall-boundary). For hard walls, particles have the component of velocity normal to the wall surface reflected, and the particles are deflected by the same distance they travelled 'inside' the boundary. For periodic boundaries, particles are reinjected at the appropriate location at the opposite boundary, once again taking into account the distance they penetrated the boundary.

3.3.12 Particle-particle agglomeration model

A particle agglomeration model has also been implemented in the LPT code to predict aggregation events upon particle collisions. In the model, which is based upon the work of Njobuenwu and Fairweather (2015b) we assume that particle agglomeration occurs if, as a particle undergoes a collision, the resulting total kinetic energy is insufficient to overcome the attractive part of the DLVO force between the two colliders. DLVO theory and interparticle forces will be considered in detail later on in the methodology. The requirement is:

$$\boldsymbol{u}^{*2}_{P,rel} < \frac{H^* d_P^*}{12\rho_P^* \delta_0^*}, \tag{62}$$

where $\boldsymbol{u}^*_{P,rel}$ is the relative particle collision velocity, H^* is the non-dimensional Hamaker constant such that $H^* = H/\rho_F U_B^2 \delta^3$ and $\delta_0^* = \delta_0/\delta$ is the minimum contact distance. Although not considered here, the electric double layer repulsive term is examined in more detail in the immersed boundary section of the methodology. For binary particle agglomeration events, its effect on the post-collision result was ignored

since its magnitude for micron-sized particles is much lower than that of the van der Waals attraction, and its effective range is also much smaller.

If the above requirement is met, then the two particles form a new spherical particle with a total volume based on the sum of the volumes of the two original particles. The agglomerate is then given the following velocity, $\boldsymbol{u}^*_{agg}$, and position, $\boldsymbol{r}^*_{agg}$, which derive from momentum conservation arguments:

$$\boldsymbol{u}^*_{agg} = \frac{1}{{d^*_{agg}}^3}({d^*_{p,1}}^3\boldsymbol{u}^*_1 + {d^*_{p,2}}^3\boldsymbol{u}^*_2), \tag{63}$$

$$\boldsymbol{r}^*_{agg} = \frac{1}{2}(\boldsymbol{r}^*_1 + \boldsymbol{r}^*_2) + t_{col}\boldsymbol{u}^*_{agg}, \tag{64}$$

where d^*_{agg} is the non-dimensional diameter of the resulting agglomerate given by:

$$d^*_{agg} = \sqrt[3]{{d^*_{p,1}}^3 + {d^*_{p,2}}^3}. \tag{65}$$

The other terms are as follows: $d^*_{p,1}$ and $d^*_{p,2}$ are the non-dimensional diameter of the first and second colliding respectively, $\boldsymbol{u}^*_1$ and $\boldsymbol{u}^*_2$ are the collision velocities, $\boldsymbol{r}^*_1$ and $\boldsymbol{r}^*_2$ are the collision positions and t_{col} is the collision overlap time.

3.4 Immersed Boundary Method

3.4.1 Introduction

In order to more accurately represent an arbitrary finite-sized particle, of any shape, subject to a flow field, an immersed boundary method (IBM) has been developed to be used concurrently with Nek5000. The original concept is detailed in (Peskin, 2002), wherein the structure is treated as a boundary which is two-way coupled to the flow field. To do this, Peskin imposes forcing conditions on the surface of the boundary through an additional delta function term added to the NS equations. We may extend this idea to a

rigid boundary by reducing the deformability of the elastic fibres forming the boundary, however it is suggested by previous authors (Beyer and LeVeque, 1992) that discrete forcing (as opposed to continuous forcing) approaches are easier to implement when considering arbitrary and rigid particle species.

The solver reads in a structured surface grid corresponding to a particle which consists of vertices and faces. The forcing is carried out using a direct boundary condition imposition method. To do this, cells located just inside the immersed boundary (having neighbouring fluid nodes) are determined to be 'ghost' cells, imposing a trilinear interpolation scheme to determine flow variables just inside the boundary, and the NS equations are solved as normal, using values for velocity obtained from the ghost nodes. Particle advection is performed explicitly using calculations of viscous and pressure forces on each face element of the solid boundary. The method is presented in more detail in the following subsection.

3.4.1 Computational method

The particles used within this project are icospheres, represented by a secondary computational mesh consisting of 320 faces (although other face numbers are explored in the corresponding results chapter), stored in the face-vertex representation. An example of this is presented in Figure 3.5. Each face has an associated centroid position and velocity (where the velocity is derived from the global particle angular velocity).

The immersed boundary (IB) condition is a Dirichlet boundary condition such that $\boldsymbol{u}_F = \boldsymbol{u}_P + \boldsymbol{\omega}_P \times \boldsymbol{r}_F$ on each particle face, F. Here, $\boldsymbol{u}_P$ is the particle linear velocity, $\boldsymbol{\omega}_P$ is the particle angular velocity and $\boldsymbol{r}_F$ is the position vector from the centre of the particle to the centroid of face F.

A second-order accurate ghost cell method is used to ensure the IB condition is met. Every timestep, each cell in the domain (formed by the bisectors between two neighbouring Gauss-Lobatto-Legendre points, which are the fluid interpolation points associated with the SEM) is identified as external fluid, an internal ghost-cell or internal fictitious fluid. A ghost cell is defined such that the IB intersects the cell and contains the cell midpoint. Internal and external fluid cells are those either inside or outside the IB, respectively. This is illustrated in Figure 3.6.

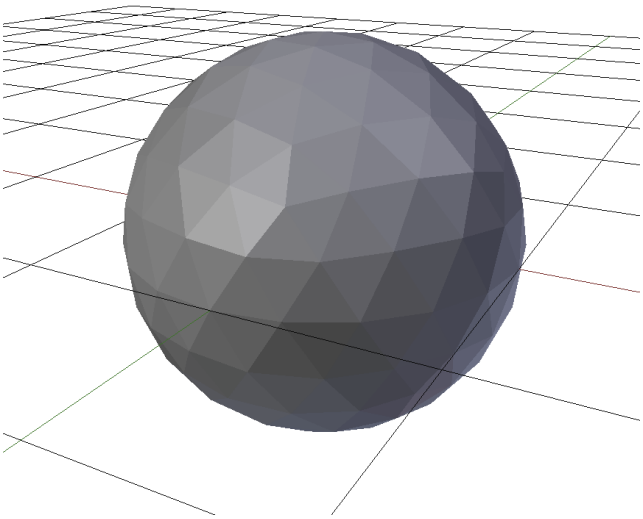

Figure 3.5: Computational icosphere mesh made up of 320 faces representing immersed boundary for spherical particle

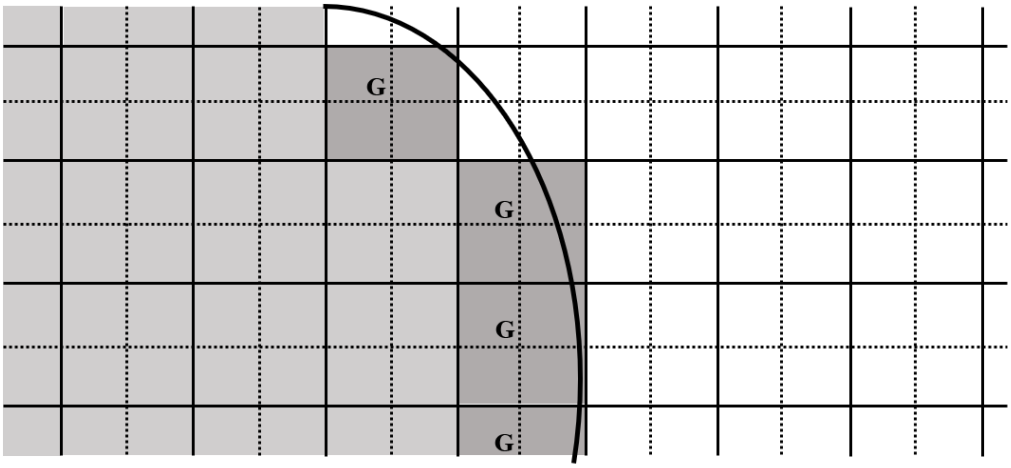

Figure 3.6: Computational domain schematic containing an immersed boundary. The white cells represent the external fluid domain, whilst the light grey cells are interior points. The remaining grey cells identified by ‘G’ represent the ghost cell domain.

The velocities at the ghost-cells are maintained each timestep such that, through trilinear interpolation across the three closest neighbouring cells, the fluid velocity on the boundary is exactly the local face velocity.

To advect the particle, the surface forces (pressure and viscous) are calculated using the following equation:

$$F_j = \sum_{f=1}^{N_f} \left(\underbrace{-P^f \delta_{ij}}_{Pressure} + \underbrace{\tau_{ij}^f}_{Viscous} \right) n_j^f \, dS^f \tag{66}$$

where F is the total translational force on the particle, f refers to the current face in the summation, with N_f being the total number of faces in the particle mesh, P is the pressure interpolated at the face centroid, τ is the viscous stress tensor, n is a unit vector normal to the face, and dS is the surface area of the face. A similar equation is used to calculate the viscous contributions to torque in the off-normal directions, used to update the angular velocity of the particle. The orientation of the mesh is tracked in a quaternion formulation, which is detailed in the next section.

3.4.2 Rotational dynamics

Transitioning between point-like particles and fully-resolved particle meshes involves both changes to translational forces and new degrees of dynamic freedom. At each timestep the extra rotational degrees of freedom must also be updated, hence we have fluid-based torques which either speed up or slow down the angular velocity of the particle. With these extra degrees of freedom, we can also use non-spherical particle meshes. A rotating particle can be fully defined dynamically by its position, orientation, velocity and angular velocity.

We will first consider particle orientation. This can be fully defined by three Euler angles, ϕ, θ and ψ which represent the angles between the co-moving frame (primed) and the particle frame (double-primed) as in Figure 3.7. Following the definition of quaternions (or Euler parameters) as given by (Mortensen et al., 2008), we are able to construct a full orientation state (q_0, q_1, q_2, q_3) as follows:

$$q_0 = cos\left(\frac{1}{2}(\psi + \phi)\right) cos\left(\frac{\theta}{2}\right) \tag{67}$$

$$q_1 = cos\left(\frac{1}{2}(\psi - \phi)\right) sin\left(\frac{\theta}{2}\right) \tag{68}$$

$$q_2 = sin\left(\frac{1}{2}(\psi - \phi)\right) sin\left(\frac{\theta}{2}\right) \tag{69}$$

$$q_3 = sin\left(\frac{1}{2}(\psi + \phi)\right) cos\left(\frac{\theta}{2}\right) \tag{70}$$

An orientation matrix, $\boldsymbol{A}$, capable of transforming between the co-moving frame and the particle frame may be constructed:

$$\boldsymbol{A} = \begin{pmatrix} 1 - 2(q_2^2 + q_3^2) & 2(q_1 q_2 + q_0 q_3) & 2(q_1 q_3 - q_0 q_2) \\ 2(q_1 q_2 - q_0 q_3) & 1 - 2(q_1^2 + q_3^2) & 2(q_2 q_3 - q_0 q_1) \\ 2(q_1 q_3 + q_0 q_2) & 2(q_2 q_3 + q_0 q_1) & 1 - 2(q_1^2 + q_2^2) \end{pmatrix} \tag{71}$$

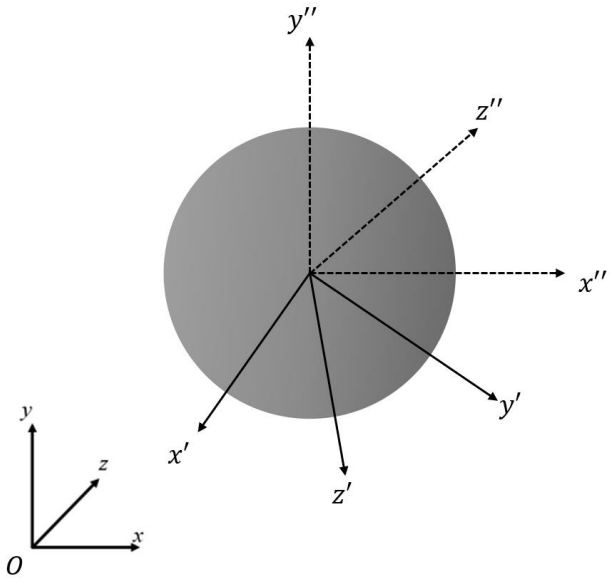

Figure 3.7: Schematic for rotating particle with reference frames.

The corresponding Eulerian torque equation for a non-spherical particle with angular velocity, $\boldsymbol{\omega} = (\omega_x, \omega_y, \omega_z)$ is given by:

$$I\frac{d\boldsymbol{\omega}}{dt} = \boldsymbol{T}_{visc}, \tag{72}$$

where I represents the moment of inertia of the rotating particle, and $\boldsymbol{T}_{visc} = \sum_{\boldsymbol{j}} \boldsymbol{r}_{F,j} \times \boldsymbol{F}_j$ represents the total off-normal torque contribution from the viscous force calculation. For spheres, $I = I_{sphere} = \frac{1}{10} m_p d_p^2$. In general, the moments of inertia may have different components in each dimension depending on the geometry of the particulate mesh.

To time-evolve the orientation parameters, the following quaternion equation is solved each timestep using the RK4 algorithm:

$$\frac{d\boldsymbol{Q}}{dt} = \begin{pmatrix} \frac{dq_0}{dt} \\ \frac{dq_1}{dt} \\ \frac{dq_2}{dt} \\ \frac{dq_3}{dt} \end{pmatrix} = \begin{pmatrix} q_0 & -q_1 & -q_2 & -q_3 \\ q_1 & q_0 & -q_3 & q_2 \\ q_2 & q_3 & q_0 & -q_1 \\ q_3 & -q_2 & q_1 & q_0 \end{pmatrix} \begin{pmatrix} 0 \\ \omega_{x'} \\ \omega_{y'} \\ \omega_{z'} \end{pmatrix} \tag{73}$$

Due to floating-point precision errors inherent in performing calculations using quaternions, after each timestep, the quaternion is normalized by performing the following operation:

$$\boldsymbol{Q}' = \frac{\boldsymbol{Q}}{\sqrt{q_0^2 + q_1^2 + q_2^2 + q_3^2}}. \tag{74}$$

3.4.3 DLVO interaction force and collisions

In addition, a sphere-sphere DLVO (Derjaguin and Landau, 1941; Verwey and Overbeek, 1955) potential is used to calculate the van der Waals attraction and electric double layer

repulsion between particle-pairs. The equation for the attraction or repulsion caused by a spherical particle, k, on spherical particle, l, is as follows:

$$\boldsymbol{F}_{kl}^{TOTAL} = \boldsymbol{F}_{kl}^{VDV} + \boldsymbol{F}_{kl}^{EDL}. \tag{75}$$

where f_{kl}^{VDV} is the van der Waals attractive term and f_{kl}^{EDL} is the electric double layer term. The van der Waals term, which is of great importance in colloidal chemistry, arises due to the electrostatic attraction induced by London dispersion forces (Stenhammar et al., 2010). The electric double layer term arises due to an interfacial pair of ion layers, the first of which screens the second, which are formed on an object when exposed to fluid. The surface charge potential is hence reduced as one moves away from the surface. These two forces are given as:

$$\boldsymbol{F}_{kl}^{VDV} = \frac{-Ar_P\hat{\boldsymbol{n}}}{12H_{kl}^2}, \tag{76}$$

$$\boldsymbol{F}_{kl}^{EDL} = \frac{64\pi r_P n k_B T_F \Theta^2 e^{-\kappa H_{kl}}}{\kappa}\hat{\boldsymbol{n}}. \tag{77}$$

In the above equations, A is the Hamaker constant, r_P is the particle radius, H_{kl} is the inter-surface distance, n is the number density of electrolyte ions, k_B is Boltzmann's constant, T_F is the fluid temperature, Θ is the reduced surface potential and κ is the inverse Debye length. Note that both of these forces are zero when the intersurfacial distance is less than zero. Finally, $\hat{\boldsymbol{n}}$ is a unit vector pointing from particle k to particle l.

Collisions are performed using the inelastic hard-sphere approach, with varying coefficients of restitution. Since the particle-number is usually very low, there is no need to apply the same collision identification algorithm as was performed with the LPT solver. Hence, all particle pairs are checked for a potential collision event. This time, the sole condition for collision is that their intersurfacial distance, H_{kl}, is less than zero. During the timestep which this occurs, the particles collide inelastically and their resulting velocites ($\boldsymbol{u'}_{P,1}, \boldsymbol{u'}_{P,2}$) and positions ($\boldsymbol{r'}_{P,1}, \boldsymbol{r'}_{P,2}$) are evaluated as:

$$\boldsymbol{u}'_{P,1} = \boldsymbol{u}_{P,1} + \frac{m_{P,2}}{m_{P,1} + m_{P,2}}(1 + e)\left(\left(\boldsymbol{u}_{P,2} - \boldsymbol{u}_{P,1}\right) \cdot \hat{\boldsymbol{n}}\right)\hat{\boldsymbol{n}} \tag{78}$$

$$\boldsymbol{u}'_{P,2} = \boldsymbol{u}_{P,2} + \frac{m_{P,1}}{m_{P,1} + m_{P,2}}(1 + e)\left(\left(\boldsymbol{u}_{P,2} - \boldsymbol{u}_{P,1}\right) \cdot \hat{\boldsymbol{n}}\right)\hat{\boldsymbol{n}} \tag{79}$$

$$\boldsymbol{r}'_{P,1} = \boldsymbol{r}_{P,1} + t_{col}\boldsymbol{u}'_{P,1} \tag{80}$$

$$\boldsymbol{r}'_{P,2} = \boldsymbol{r}_{P,2} + t_{col}\boldsymbol{u}'_{P,2} \tag{81}$$

where e is the coefficient of restitution as specified by the user. The choices of these parameters will be discussed in the corresponding later sections.

Particle-wall collisions are handled such that if any vertex in the particle mesh surpasses the boundary, the particle velocity in the direction normal to the wall is reversed, and the particle deflects by the amount it penetrated the barrier. Periodic boundaries work in a similar manner, in that as soon as a vertex exceeds the boundary, the particle is reinjected in the appropriate location at the opposite side. This means that the particle 'jumps' somewhat, but for low particle size with respect to the geometry, the low occurance of this event means that the error which results from this effect is negligible.

4 THE EFFECT OF STOKES NUMBER ON NEAR-WALL PARTICLE DYNAMICS

4.1 Introduction and background

We begin our investigation into particle dynamics in wall-bounded multiphase turbulent fluid flows by examining the emergent behaviour of the simple one-way coupled particle-laden channel flow with a low concentration of dispersed particles. To accomplish this, we employ the DNS and LPT methods described in the methodology to achieve several initial objectives. This chapter primarily aims to revisit and introduce the relevant flow features and particle behaviour which have been studied in previous literature. Since we choose to consider a system that has been simulated by other authors' before, the DNS and LPT codes can be validated. This is important since the LPT has been developed within this project, and hence is an in-house code which requires testing. Because of this, we choose to investigate multi-phase flow dynamics in the well-studied $Re_\tau = 180$ channel flow.

Beyond this, and to generate new understanding, we aim to extend the current analysis of the behaviour exhibited by the multi-phase system by addressing unexplained phenomena, both in terms of the continuous and solid phase dynamics. Years of study into single-phase wall-bounded turbulent flows has helped develop a fundamental understanding of the continuous phase dynamics. Of particular interest is the categorization of ordered near-wall vortical structures, which has been studied extensively (Dritselis and Vlachos, 2008). Particles entering these regions have been observed to show a wide range of responses based on their size, density and inertia (Marchioli and Soldati, 2002). Despite an increasing number of investigations into particle-laden flows, however, the physics underpinning the motion of inertial particles in these systems is yet to be fully understood.

Of great importance is the phenomenon of turbophoresis which describes the turbulence-induced drift of inertial particles towards a wall. With increased momentum, the trajectories of such particles decouple from local vortex motion (Fessler et al., 1994) and accumulate in certain regions leading to preferential concentration. The extent to which this mechanism occurs in wall-bounded flows has been shown (Crowe et al., 1985) to be governed by the particle viscous Stokes number, explained in previous chapters. This type of system can exhibit a homogeneous concentration profile, and mean particle motion statistics match those of the fluid, particularly at low Stokes numbers. Conversely, for very large Stokes numbers, the particle response time is much greater than that of the associated fluid time scale, so particles decouple from the turbulent fluctuations. These heavy particles migrating towards the near-wall region exhibit behaviour different to that in the bulk flow. For example, studies in channels (Li et al., 2001; Zhao et al., 2015; Rouson and Eaton, 2001) all predict increased particle turbulence intensities close to the wall for high Stokes numbers. However, they lack an explanation as to how this phenomenon arises. Likewise, certain mid-range Stokes number particles in this region are subject to local segregation and accumulation in low-speed streaks (Picciotto et al., 2005; Dritselis and Vlachos, 2008; Marchioli and Soldati, 2002; Lee and Lee, 2015). Studies also indicate that particle positions in the viscous sublayer and the buffer region correlate with the local flow topology for low Stokes numbers (Soldati and Marchioli, 2009). More recent work (Sardina et al., 2012; Sardina et al., 2014) has demonstrated a strong link between the two mechanisms of wall accumulation and local clustering intensity.

Macroscopic quantities of the particle-fluid system (concentration profiles, mean velocity profiles, etc.) are directly related to the microscopic trajectories of individual particles, which are further governed by the interaction between particles and turbulent structures. Therefore, by attempting to establish a relationship between the topology of the system with reference to particle behaviour in particular regions of the flow, it is possible to build up understanding of how the macroscopic behaviour is shaped by the presence of particles. The second half of this chapter therefore aims to elucidate the dynamics surrounding particle motion in each region of the turbulent channel flow. In the literature, little explanation is offered for the existence of enhanced particle root-mean-square (rms) velocity fluctuations within the buffer layer and viscous sublayer for particles with high Stokes numbers. This chapter also addresses this issue by analyzing high accuracy simulations of particle motion in those regions. Primarily, the effect of Stokes number on

macroscopic system properties will be discussed. Secondly, we will focus on specific wall-normal regions of the channel and attempt to provide evidence for particle transport mechanisms. This will be established by correlating local mean particle statistics and probability density functions (PDFs) with local flow topologies, following a similar classification to that used by (Blackburn et al., 1996).

Furthermore, we will study Stokes numbers outside the range usually considered by previous work (obtained by varying the particle-fluid density ratio, ρ_P^*, whilst maintaining constant particle diameter). However, consideration will also be given to the behaviour of previously studied mid-range viscous Stokes numbers ($St_\tau = 1, 5, 25$) in the form of a validation of the LPT solver.

4.2 Single-phase turbulent channel flow

4.2.1 Simulation mesh parameters and setup

The computational domain for the channel flow has been detailed in the previous chapter. Dimensions, element number and distribution, and discretisation order were chosen to closely replicate the cell sizes of the previous work of Kim et al. (1987), referred to from hereon as KMM, who obtained very good results when compared with experimental data.

Table 3: Single-phase channel flow grid comparisons between present work and Kim et al. (1987) for DNS simulations.

Simulation	**Present work**	**KMM**
$E_X \times E_Y \times E_Z$	$27 \times 18 \times 23$	-
$n_x \times n_y \times n_z$	$192 \times 127 \times 162$	$192 \times 129 \times 160$
$L_x^* \times L_y^* \times L_z^*$	$14 \times 2 \times 6$	$4\pi \times 2 \times 4\pi/3$
dy_{min}^+	0.33	0.05
dx_{avg}^+	13.13	17.7
dz_{avg}^+	6.67	5.9

Due to the nature of the spectral element method (SEM), comparative cells are based on the boundaries between Gauss-Lobatto-Legendre points within each element. Using

these, we can obtain a comparison between the mesh used in the present work, and that used in KMM. This is presented in Table 3.

In the table, n_i represents the number of cells (or equivalent cells for the SEM) in spatial dimension, i. Clearly, the number of elements in each direction has been chosen to match as closely as possible the number of cells in the validation mesh. The calculated dy^+_{min} represents the minimum cell spacing in the wall-normal direction. Since the turbulence intensity and kinetic energy dissipation rate increases in the wall-region, it is important that the grid-spacing is lower in these regions, to resolve small turbulent structures. Although our minimum grid-spacing is larger than that of KMM, it will be seen in the validation that this is sufficient to obtain very good agreement with the previous simulation, performed with even greater fidelity.

The flow is initialized using the following velocity field condition, which is an approximate solution for the mean flow profile with added noise to encourage the onset of turbulence:

$$u_x^* = \frac{5}{4}\left(1 - y^{*4}\right) + 0.3\cos(12z^*)\, e^{0.5-32.4(1-|y^*|)^2}(1 - |y^*|), \tag{82}$$

$$u_y^* = 0, \tag{83}$$

$$u_z^* = 21.6\sin(12x^*)\, e^{0-32.4(1-|y^*|)^2}(1 - |y^*|). \tag{84}$$

From this initial condition, the flow was allowed to develop until it reached steady state, using a constant SEM timestep of $\delta t^* = 0.01$. In general, this was achieved by $t^* = 150$, but continuous phase statistics were gathered over $200 \leq t^* \leq 500$ to ensure the mean profiles were temporally stationary.

4.2.2 Instantaneous flow analysis

In this subsection we shall introduce snapshots of the settled, steady turbulent channel flow by considering instantaneous distributions of various observables in different regions of the system.

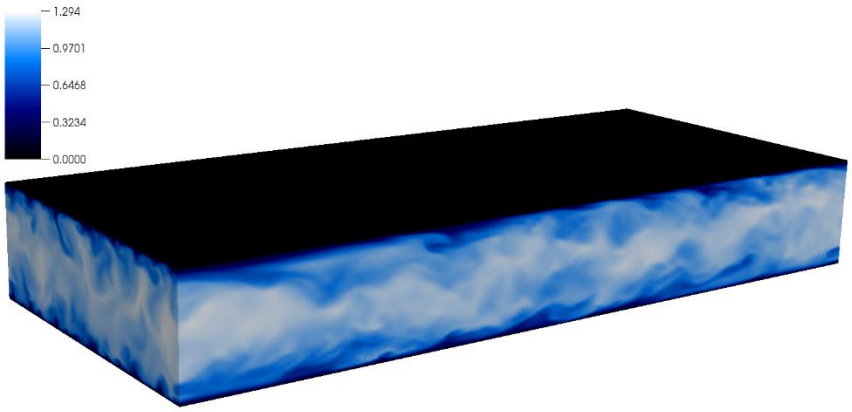

Figure 4.1: Three-dimensional pseudocolour plot of instantaneous streamwise velocity over entire domain for $Re_\tau = 180$ turbulent channel flow.

Figure 4.1 is a three-dimensional pseudocolour plot overview of the statistically settled turbulent channel flow, considered in detail throughout this section. Here, the flow is driven by a fixed pressure gradient as outlined in the methodology section. It is clear that turbulence is exhibited, particularly close to the walls in the lower velocity regions, based on the observed swirling motion.

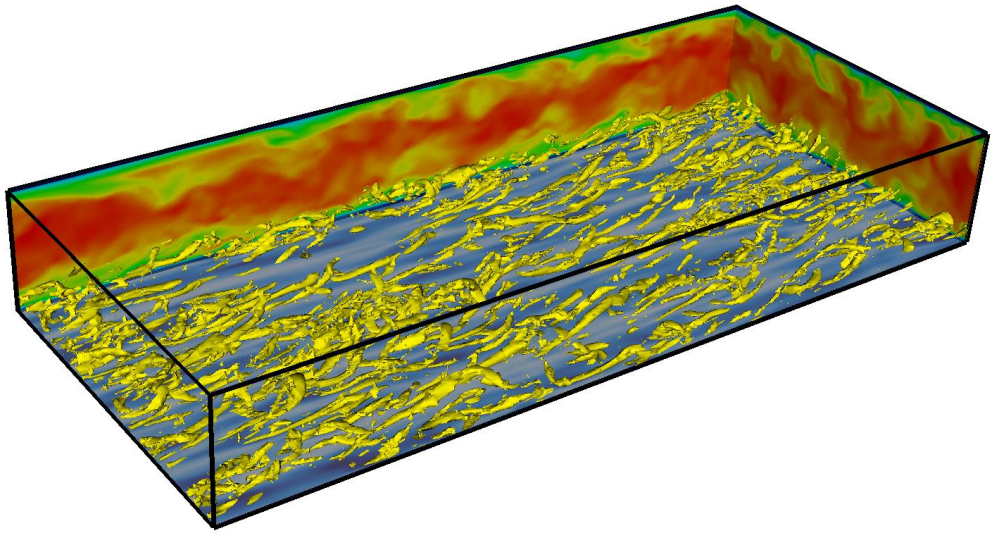

Figure 4.2: Three-dimensional Q-criterion isosurface plot over entire domain for $Re_\tau = 180$ turbulent channel flow. Periodic boundaries are plotted with pseudocolour representations of streamwise velocity. Wall-boundary is a pseudocolour plane cut at $y^+ = 5$ of streamwise velocity.

To further illustrate turbulence in turbulent channel flows, we can use a vortex identification technique to help resolve turbulence structures within the system. These usually use some identifier based on velocity gradients, since shear is inherent in vortex motion. The velocity gradient tensor, D_{ij}, is given by:

$$D_{ij} = \frac{\partial u_i}{\partial x_j}. \tag{85}$$

One method is to use the concept of 'Q-criterion' which defines a vortex as a 'connected fluid region with a positive second invariant of ∇u_F^*' (Holmén, 2012). Here:

$$Q = \frac{1}{2}|tr(D)^2 - tr(D^2)| = \frac{1}{2}\left(||\Omega||^2 - ||S||^2\right) \tag{86}$$

where,

$$\Omega_{ij} = \frac{1}{2}\left(\frac{\partial u_i}{\partial x_j} - \frac{\partial u_j}{\partial x_i}\right), \tag{87}$$

and

$$S_{ij} = \frac{1}{2}\left(\frac{\partial u_i}{\partial x_j} + \frac{\partial u_j}{\partial x_i}\right), \tag{88}$$

which are the symmetric (vorticity magnitude) and skew-symmetric (shear strain rate) parts of the velocity gradient tensor, respectively. The Q-criterion definition then requires that $Q > 0$ in order for a particular region of fluid to be defined as vortex-like. In other words, the vorticity magnitude must be greater than the local shear strain rate.

Isosurfaces of the Q-criterion condition are plotted in Figure 4.2, which depicts coherent turbulence structures in the boundary layer in close proximity to wall, most prevalent in

the buffer region. These are examples of hairpin vortices which are vortical structures which are orientated downstream. The effect of these on particles subject to their influence will be discussed later in the chapter. Another feature of Figure 4.2 is the presence of low speed streaks at $y^+ = 5$, very close to the wall.

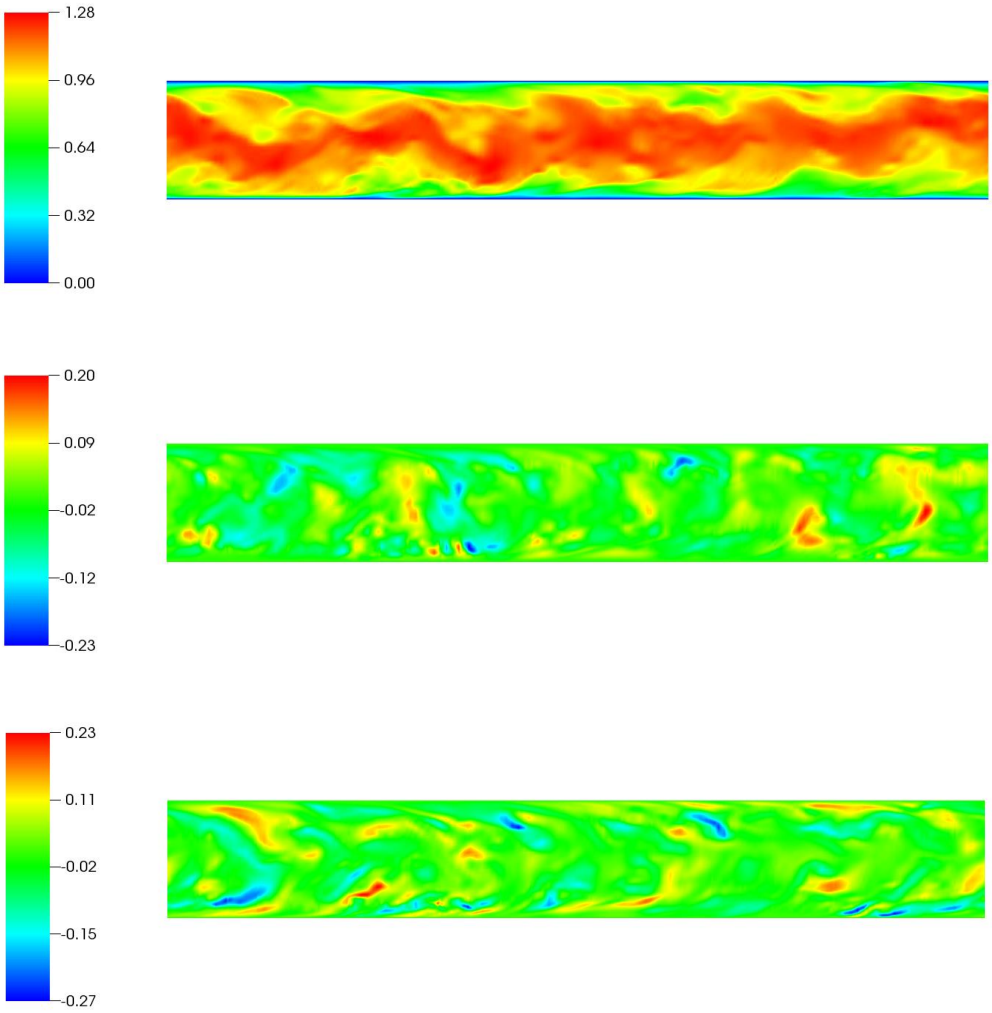

Figure 4.3: Instantaneous fluid velocity contours along spanwise-cut ($z^* = 0$) for streamwise (upper), wall-normal (middle) and spanwise (lower) components.

We will now consider all three components of the velocity vector in planar cuts orientated perpendicular to various directions. This will allow us to visualise a full picture of the turbulence field present in the channel flow. Figure 4.3 illustrates all three components of the fluid velocity for a spanwise cut at $z^* = 0$. Clearly, the strongest motion is in the positive streamwise direction, whilst the wall-normal and spanwise components show both positive and negative motions. It appears also that the spanwise velocity is greatest

in localised regions which are closer to the wall, whilst the wall-normal velocity patches seem more homogeneous.

This variation of behaviour with wall-normal location is very important in understanding turbulence dynamics in a turbulent channel flow. In order to further establish and understand the instantaneous behaviour close to the wall, we will take slices of velocity component pseudocolour plots at different wall-normal locations. It is sensible to consider the classical regions of the boundary layer which are presented in Table 4.

Table 4: Turbulent boundary layer region classification.

Region	**Start y^***	**Midpoint y^***	**End y^***
Viscous sublayer	0	0.0135	0.027
Buffer layer	0.027	0.0965	0.166
Log-law	0.166	0.183	0.2
Bulk flow	0.2	1	1.8

These are based on the historic work of Moser and Moin (1984), who discovered patterns in the mean streamwise velocity distributions in turbulent boundary layers. We will discuss these regions further when considering mean quantities associated with the present flow. Using information from Table 4, slices through the channel are taken at the midpoint of each region.

Figure 4.4 illustrates the instantaneous streamwise velocity throughout each region. At the centre of the channel, the flow is homogeneous in direction and magnitude, with small patches of lower velocity regions also apparent. It is clear that as the wall boundary is approached, there appears to be more emphasized narrow low-speed streaks orientated in the direction of the flow. The greatest contrast in speed in relation to these streaks appears in the buffer layer, where velocity gradients are very high.

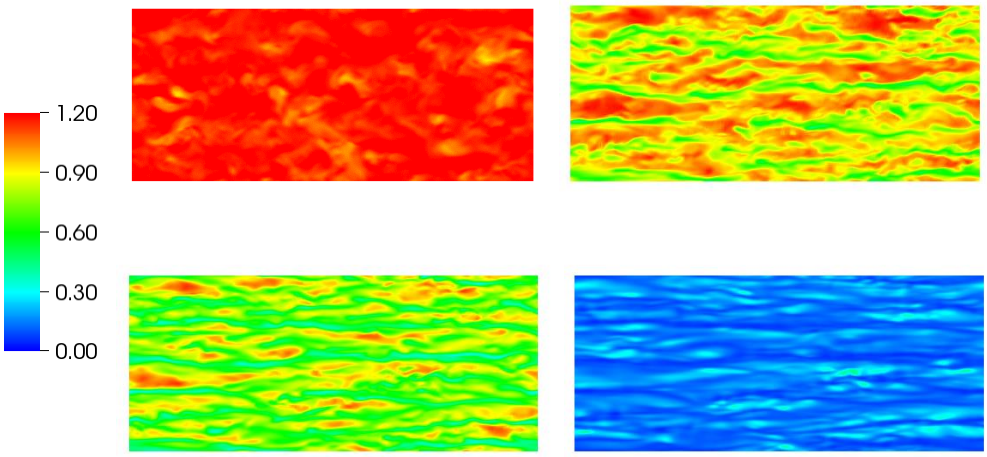

Figure 4.4: Instantaneous streamwise fluid velocity contours along *y*-slices in bulk flow region (upper-left), log-law region (upper-right), buffer layer (lower-left) and viscous sublayer (lower-right)

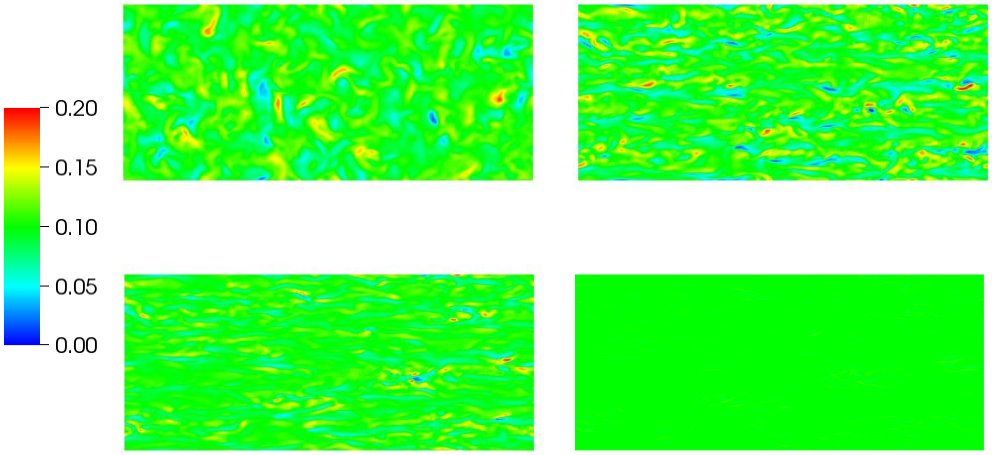

Figure 4.5: Instantaneous wall-normal fluid velocity contours along *y*-slices in bulk flow region (upper-left), log-law region (upper-right), buffer layer (lower-left) and viscous sublayer (lower-right).

Figure 4.5 and Figure 4.6 depict the wall-normal and spanwise velocity components. The same behaviour in terms of contrasting speeds is observed as the wall is approached, but the length of the regions previously associated with ‘streaks’ are much shorter, albeit still orientated in the streamwise direction. Rather than streaks, the patterns look more like oval flecks of positive or negative motion. The greatest density of these specks appears to be in the buffer and log-law regions for the spanwise component of fluid velocity,

which agrees with Figure 4.3 which demonstrated the greatest contrast in velocities in those zones.

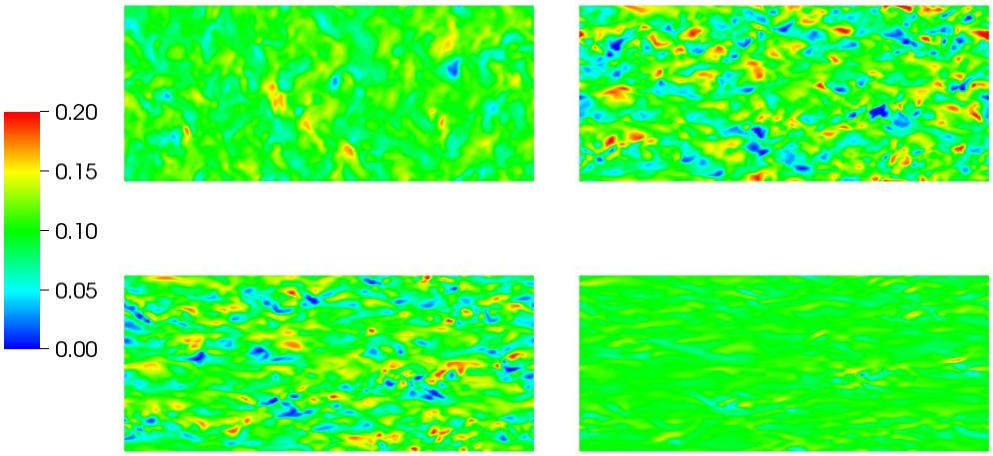

Figure 4.6: Instantaneous spanwise fluid velocity contours along *y*-slices in bulk flow region (upper-left), log-law region (upper-right), buffer layer (lower-left) and viscous sublayer (lower-right).

4.2.3 Mean flow analysis and continuous phase validation

We begin by ensuring that the discretization chosen for the continuous phase grid are sufficient to predict a fluid flow field with similar accuracy to previous DNS cases. The single-phase predictions for the present study at $Re_\tau = 180$ are compared to the previous DNS benchmark results of Vreman and Kuerten (2014) in Figure 4.7 to Figure 4.9. Their work aimed to assess the reproducibility of turbulence statistics using fundamentally different DNS codes to examine identical channel flows. Relative deviations between methods were observed to be very low, with the greatest deviation occurring in the turbulent dissipation components, but even in this case the deviation was below 2%. For validation, our results have been compared with the S2 database (Vreman and Kuerten, 2014), which used a spectral element solver on the most enhanced grid resolution of all the datasets.

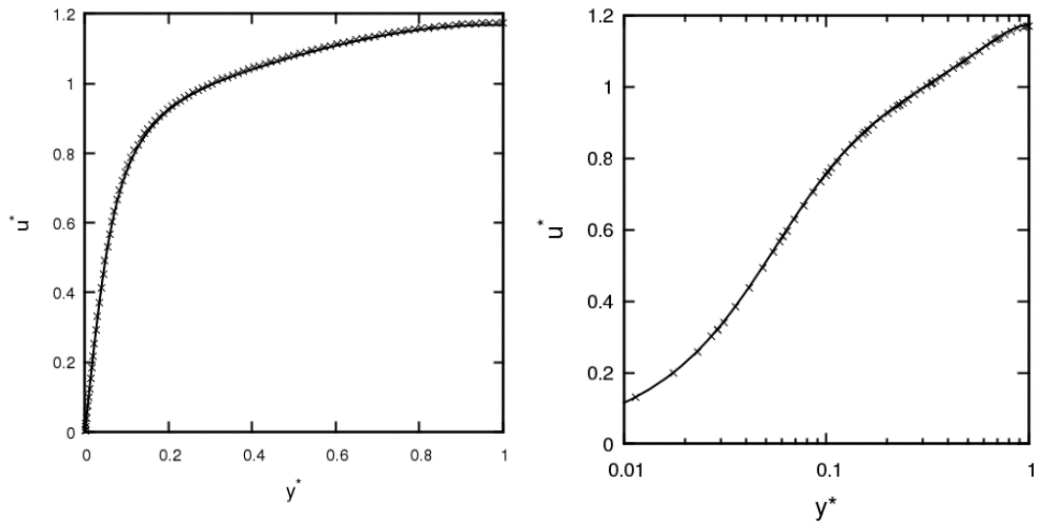

Figure 4.7: DNS validation of turbulent channel flow at $Re_\tau = 180$. Profiles of mean streamwise velocity. Righthand plot is on a log scale. Present work (crosses) and Vreman and Kuerten (2014) (solid line) are compared.

The mean streamwise velocity of the fully developed turbulent channel flow in each simulation is first compared in the left plot of Figure 4.7. This quantity is a spatially (across planes at each y^* node) and temporally (between $200 \leq t^* \leq 500$) averaged streamwise velocity plotted against distance from the wall, where $y^* = 1$ represents the channel centreline. These show excellent agreement when compared with existing DNS. Figure 4.7 also illustrates the same quantity on a logarithmic scale, providing more information surrounding the mean streamwise velocity profile close to the wall.

Similar comparisons can be made for the rms of the velocity fluctuations and the mean turbulence kinetic energy, which are plotted in Figure 4.8 and Figure 4.9. These are obtained using the definition of velocity fluctuation:

$$u'^* = u^* - \bar{u}^*, \tag{89}$$

which is squared on each grid node, then spatially and temporally averaged as with the mean streamwise velocity. The final quantity is then square rooted to obtain a value for u'^*_{RMS}. The turbulent kinetic energy is then calculated using Eq. (4).

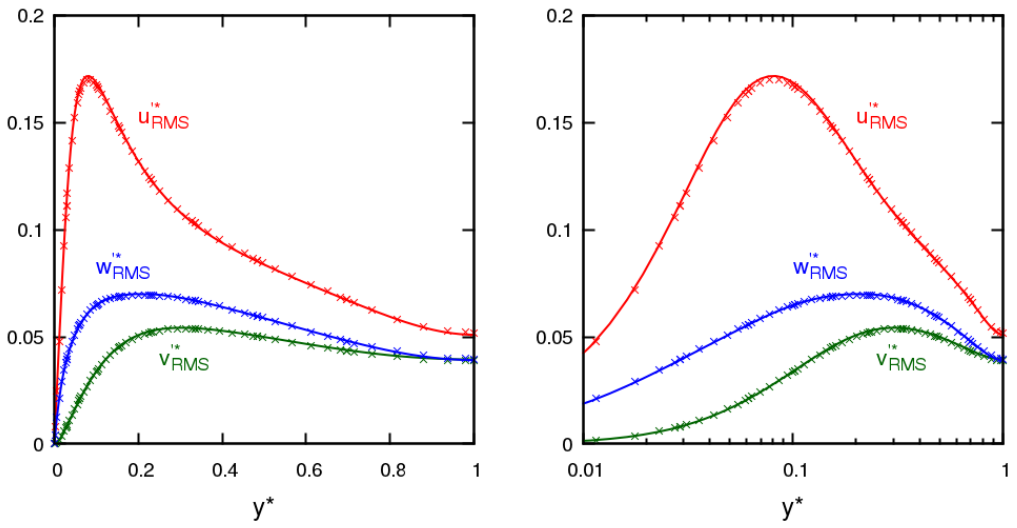

Figure 4.8: DNS validation at $Re_\tau = 180$. Profiles of root mean square of velocity fluctuations. Righthand plot is on a log scale. Present work (crosses) and Vremen and Kuerten (2014) (solid line) are compared.

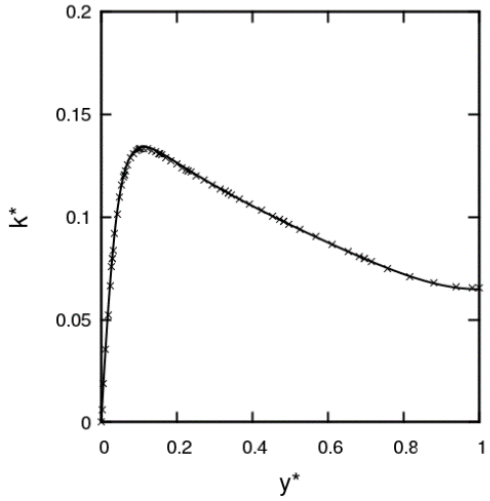

Figure 4.9: DNS validation of turbulent channel flow at $Re_\tau = 180$. Profile of turbulence kinetic energy. Present work (crosses) and Vreman and Kuerten (2014) (solid line) are compared.

These expressions help quantify how much the local fluid velocities are deviating from the mean flow field, and hence can be used as a measure of the local turbulence. As expected, the turbulence levels are greatest in the near-wall region, and suddenly drop to zero as the wall is approached due to low velocities as a result of the no-slip condition on the boundary. In comparison, the only region where there is very slight disagreement is at the peak of the streamwise rms of velocity fluctuations, however the validation

predictions were taken from a database comparing a variety of DNS implementations where the strongest deviation between methods was observed in this region. Despite this, a near-perfect agreement indicates that the present flow-field can be used with confidence.

Another statistical quantity of interest is the mean turbulence kinetic energy dissipation rate, which is illustrated in Figure 4.10. It is given by (in non-dimensional units):

$$\epsilon^* = \frac{1}{Re_B}\overline{\left(\frac{\partial u_i'^*}{\partial x_k^*}\frac{\partial u_i'^*}{\partial x_k^*}\right)}, \tag{90}$$

where $\epsilon^* = \epsilon\delta/U_B^3$.

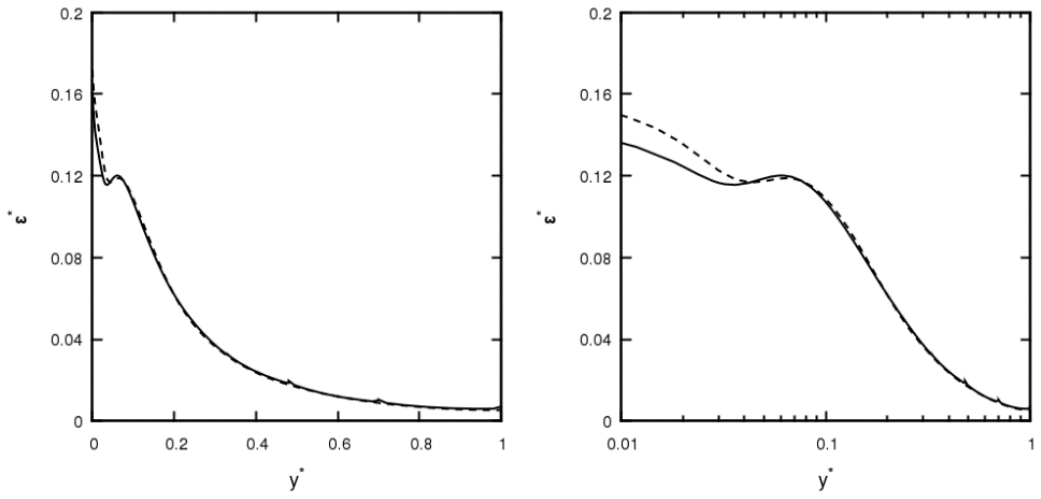

Figure 4.10: DNS validation of turbulent channel flow at $Re_\tau = 180$. Profile of turbulence kinetic energy dissipation rate. Right-hand plot is on a log scale. Present work (solid line) and Vreman and Kuerten (2014) (dashed line) are compared.

Clearly, the rate at which turbulence energy is dissipated is greatest in the turbulent region, and actually peaks on the wall boundary. Some discrepancies are observed between the present and compared simulations in the region $y^* < 0.03$ when considering the same data on a logarithmic scale, but the other turbulence statistics are all very close to those predicted in the same region, and so this is attributed to the way in which the statistics were sampled very close to the wall.

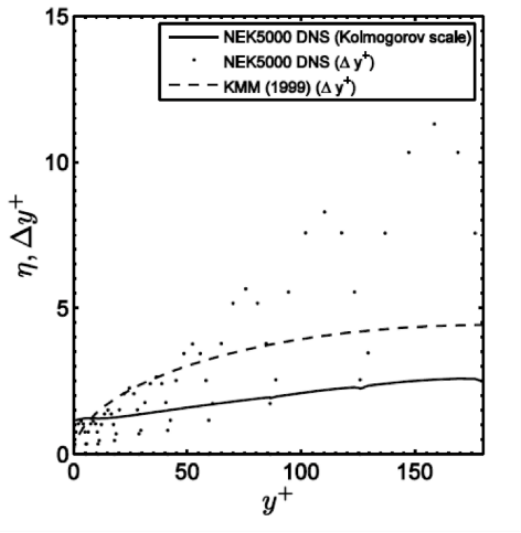

Figure 4.11: Kolmogorov length scale and mesh discretisation length scale comparison for turbulent channel flow at $Re_\tau = 180$.

Using the kinetic energy dissipation rate, we can also obtain the corresponding Kolmogorov scale using the following expression:

$$\eta = \left(\frac{\nu^3}{\epsilon}\right)^{\frac{1}{4}}, \tag{91}$$

or in non-dimensional units:

$$\eta^* = \left(\frac{1}{Re_B^3 \epsilon}\right)^{\frac{1}{4}}. \tag{92}$$

In Figure 4.11, we compare the calculated Kolmogorov scale (in viscous wall units) with the local grid spacing for the present simulation, and the grid spacing used by KMM. Despite it appearing that the resolution is insufficient to resolve the Kolmogorov scale everywhere throughout the channel, previous work carried out by (Moser and Moin, 1984) suggests that grid sizes within a few Kolmogorov length scales will still capture all the small energy scales. In the present simulation, the grid spacing is sufficient such that all cells distances are within $4\eta^+$.

Within this section, a spectral element-based DNS code has been used to predict the turbulent statistics of a settled turbulent channel flow at $Re_\tau = 180$. When compared with a high-accuracy dataset generated by Vreman and Kuerten (2014) excellent agreement was obtained for the mean streamwise velocity and rms velocity fluctuation profiles. A slight discrepancy was observed in the near-wall region for the kinetic energy dissipation rate profile, but in this region, the Kolmogorov length scale was resolved completely, and all other quantities compared very well. This deviation is attributed to either differing statistic gathering methods, or slight deviations in the single-phase solver. Despite this, we are confident that injected particles will be subject to a realistic, accurate and well-understood flow field. In the next section, we shall extend the simulation to a multiple particle-laden flows by utilising the Lagrangian particle tracking (LPT) method.

4.3 Particle-laden turbulent channel flow

4.3.1 Discrete phase validation

To validate the particle solver, a separate simulation was performed using the same mesh for the fluid, but this time at $Re_\tau = 150$. The change in Reynolds number was chosen to be able to compare directly with a database which was the result of work by (Marchioli et al., 2008). Their work compared a variety of computational methods to simulate particle-laden turbulent channel flows, but solely the drag force was used when calculating particle trajectories. Here, the dispersed phase statistics from the TUE dataset Marchioli et al. (2008) for particles with shear Stokes numbers St^+ = 1, 5 and 25 are compared with those obtained using the present solver. The same particle parameters and forces are used in both cases and each system is one-way coupled. More information about the simulation is provided in Table 5.

Table 5: Particle phase parameters for validation simulation at $Re_\tau = 150$.

Parameter	$\boldsymbol{St^+ \approx 1}$	$\boldsymbol{St^+ \approx 5}$	$\boldsymbol{St^+ \approx 25}$
Particle diameter, d_P^*	0.001	0.002	0.005
Particle diameter, d_P^+	0.15	0.3	0.75
Number of particles, N_P	300,000	300,000	300,000
Shear Stokes number, St_τ	1.000	4.998	25.010
Bulk Stokes number, St_B	0.093	0.467	2.334
Density ratio, ρ_P^*	769	769	769
Volume fraction, Θ_P	10^{-6}	10^{-5}	10^{-4}
Particle and fluid timestep, Δt^*	0.01	0.01	0.01
Particle and fluid timestep, Δt^+	0.12	0.12	0.12

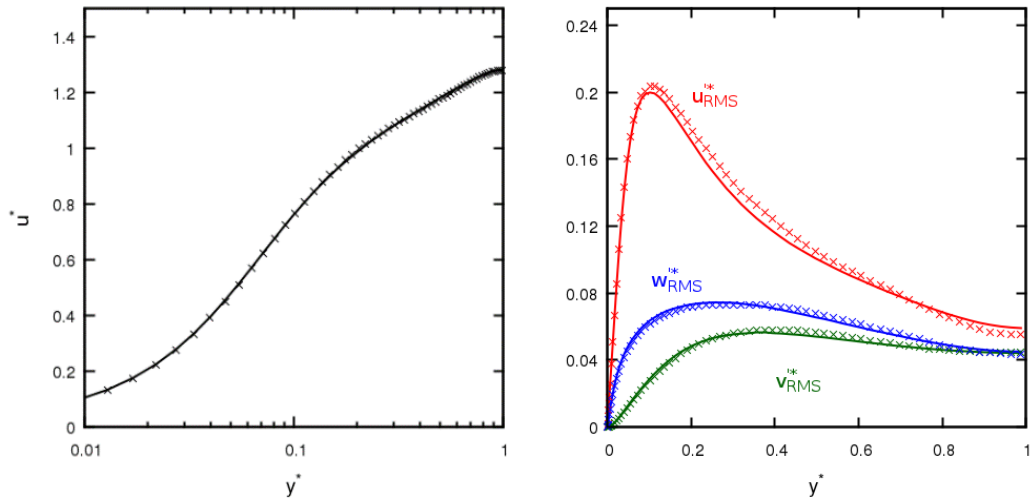

Figure 4.12: LPT validation at Re_τ = 150. Profiles of mean streamwise velocity (left) and rms of velocity fluctuations (right), for St^+= 1. Present work (crosses) and TUE group from Marchioli (2008) (solid line) are compared.

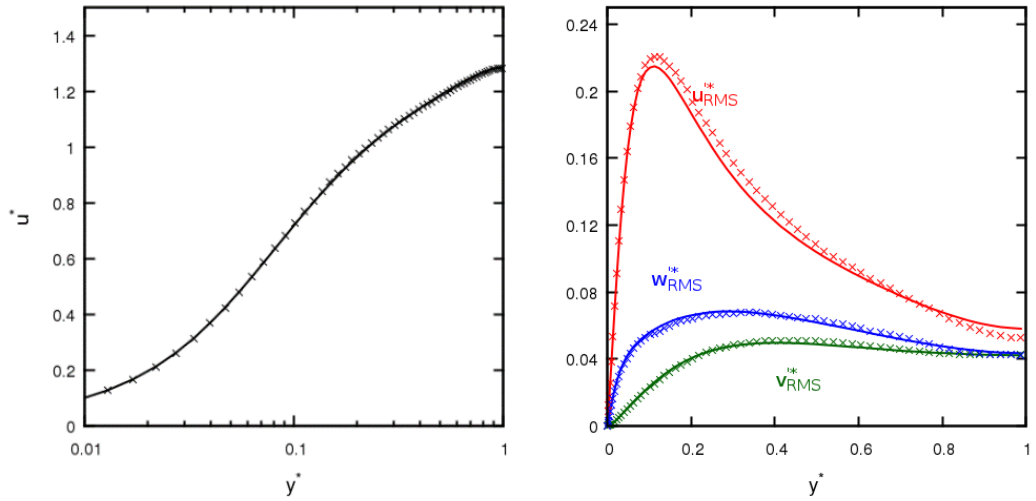

Figure 4.13: LPT validation at Re_τ = 150. Profiles of mean streamwise velocity (left) and rms of velocity fluctuations (right), for St^+= 5. Present work (crosses) and TUE group from Marchioli (2008) (solid line) are compared.

From Figure 4.12 to Figure 4.14, the mean streamwise velocity profiles show very good agreement for all three Stokes numbers. The rms velocity profiles also show very good agreement in the wall-normal and spanwise directions, but there is a slight overprediction (near-wall) and underprediction (bulk flow region) by the present approach for the streamwise direction. However, this quantity had a high spread of values between the simulations considered in the database (Marchioli et al., 2008), and so some deviation is

to be expected. Overall, the agreement is very good and builds confidence in the results obtained at the higher Reynolds number.

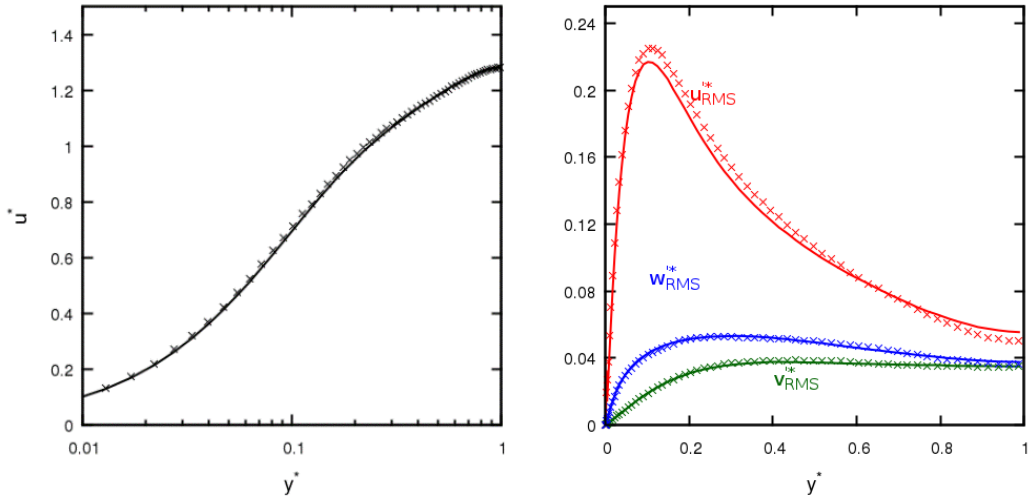

Figure 4.14: LPT validation at Re_τ = 150. Profiles of mean streamwise velocity (left) and rms of velocity fluctuations (right), for St^+ = 25. Present work (crosses) and TUE group from Marchioli (2008) (solid line) are compared.

4.3.2 Macroscopic particle behaviour

This section explores the effect of Stokes number on the macroscopic particle behaviour by studying mean particle statistics in the wall-normal direction across the length of the channel. This time, three different Stokes numbers are simulated, which are obtained by choosing a fixed diameter ($d_P^* = 0.005$) whilst varying the density ratio, ρ_P^*. These have been chosen not only such that they lie beyond the boundaries of standard investigations, but also such that their properties match real-world systems of interest. At $St^+ = 0.1$, the analogous system is for 100 μm diameter glass particles in water, with $St^+ = 92$ representing 100 μm glass particles in air. The final value of $St^+ = 50$ is chosen at the approximate mid-point between the other values considered. Each of these corresponds to the case of a $\delta = 0.02$m channel. More information on the simulation is provided in Table 6.

Table 6: Particle phase parameters for analysis simulation at $Re_\tau = 180$.

Parameter	$\boldsymbol{St^+ \approx}$ **0.1**	$\boldsymbol{St^+ \approx}$ **50**	$\boldsymbol{St^+ \approx}$ **92**
Particle diameter, d_P^*	0.005	0.005	0.005
Particle diameter, d_P^+	0.9	0.9	0.9
Number of particles, N_P	300,000	300,000	300,000
Shear Stokes number, St_τ	0.113	49.995	91.845
Bulk Stokes number, St_B	0.01	4.321	7.937
Density ratio, ρ_P^*	2.5	1111	2041
Volume fraction, Θ_P	10^{-4}	10^{-4}	10^{-4}
Particle and fluid timestep, Δt^*	0.02	0.02	0.02
Particle and fluid timestep, Δt^+	0.23	0.23	0.23

Simulations were monitored as for the validation exercise described earlier to observe whether a statistically steady state had been reached before mean statistics began being sampled. To obtain these, the channel domain was divided across the wall-normal direction into 128 regions, with endpoints given by the following equation: $s_f^i = -cos(\pi i/128)$, thereby ensuring thinner regions in the areas of greater turbulence and eventual particle concentration. Each timestep, averages of quantities presented below were calculated and updated for each region.

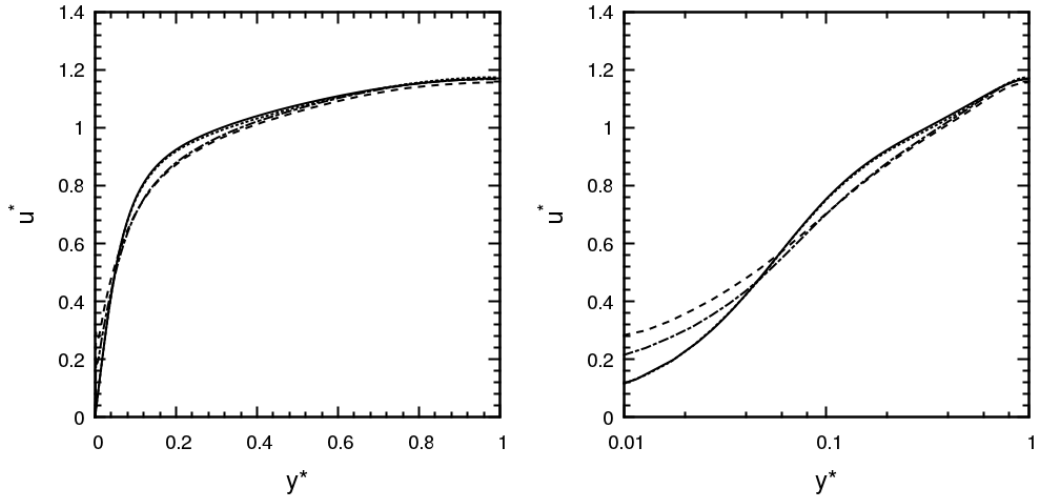

Figure 4.15: Comparison of mean streamwise particle velocity profiles. Solid line: unladen flow; dashed: St^+= 92; dot-dashed: St^+= 50; dotted: St^+= 0.1. The right-hand graph is plotted on a logarithmic scale.

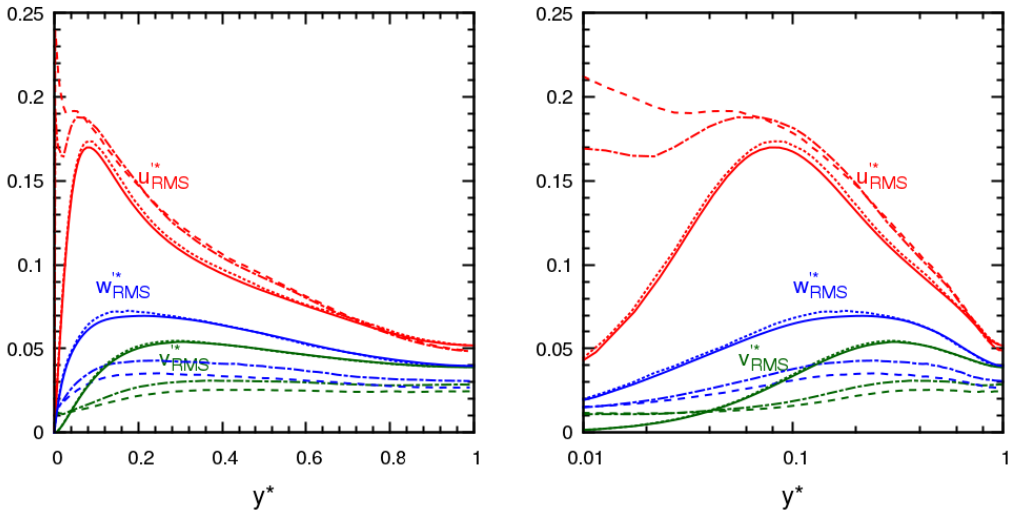

Figure 4.16: Comparison of mean particle rms velocity fluctuation profiles. Solid line: unladen flow; dashed: St^+= 92; dot-dashed: St^+= 50; dotted: St^+= 0.1. The right-hand graph is plotted on a logarithmic scale.

Figure 4.15 compares the mean streamwise velocity profiles of each particle set with that of the unladen fluid. Clearly, the $St^+ = 0.1$ particles follow the fluid streamlines very closely and act as tracers. As the Stokes number increases, the deviation increases such that particles in the bulk and log-law regions lag behind the fluid, whilst particles in the viscous sublayer and buffer layer overtake the fluid, with particles entering these regions taking longer to relax to the local fluid velocities. The rms velocity fluctuations for both the unladen fluid and each particle set are presented in Figure 4.16. Here, we observe a similar tracer effect at St^+= 0.1, although there are slight deviations in the turbulent region.

At higher Stokes numbers, the spanwise and wall-normal components are dampened when compared to the unladen flow. This effect is most apparent in the turbulent region and scales with Stokes number. Conversely, the streamwise rms profiles are greatly enhanced everywhere aside from at the central plane of the channel, and this effect is strongest near the wall boundary. The fact that these rms profiles do not go to zero at the wall is an interesting feature which is only exhibited at very high Stokes numbers. We will discuss the reasons for this effect later in the chapter.

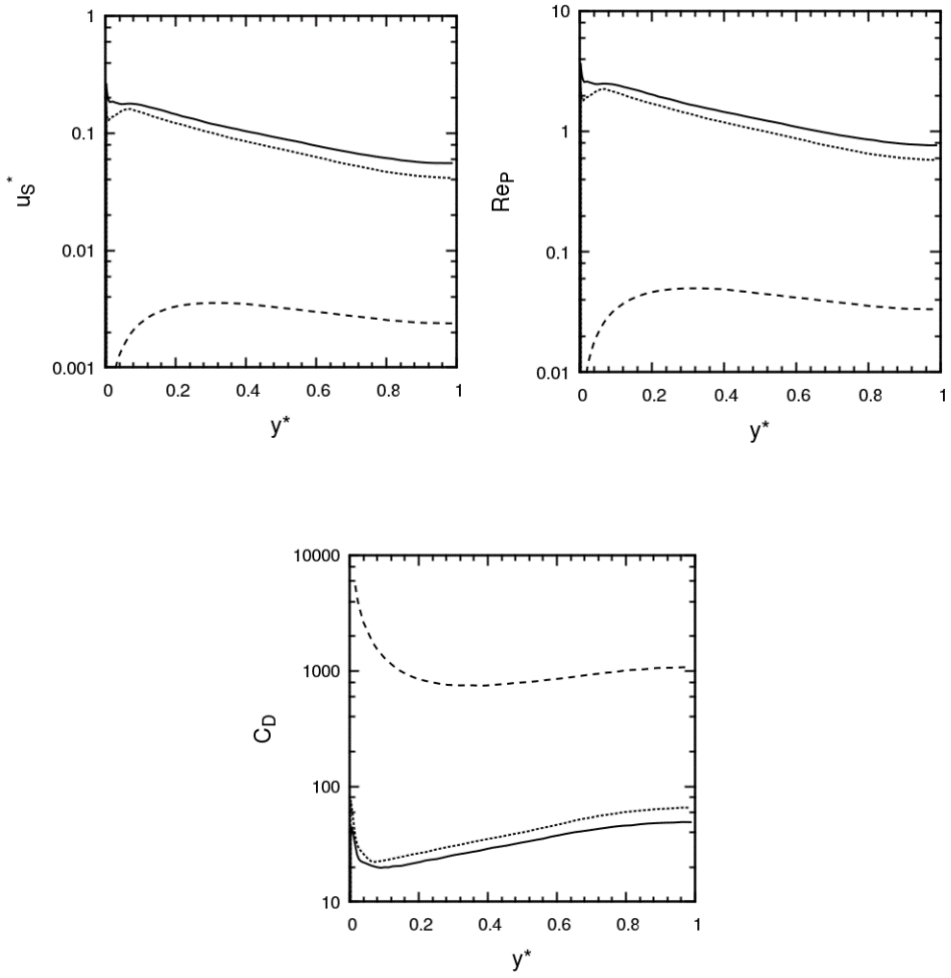

Figure 4.17: Comparison of profiles of mean particle slip velocity (upper-left), particle Reynolds number (upper-right) and drag coefficient (lower). Solid line: St^+= 92; dotted: St^+= 50; dashed: St^+= 0.1.

Other particle properties of interest which help ascertain the dynamics particles are being subjected to in each region of the flow are the slip velocity, the particle Reynolds number, and the calculated drag coefficient. Each of these is plotted across the wall-normal axis of the channel for each Stokes number in Figure 4.17. Slip velocities and the particle Reynolds numbers are directly related and therefore exhibit the same qualitative behaviour. They can both be used to measure the extent to which the particles follow the fluid. It is observed that for St^+ = 0.1, these quantities are very small throughout, indicating tracer-like behaviour. They fall off to zero close to the wall, but peak between the turbulent region and the bulk flow. Because the drag coefficient is inversely proportional to the particle Reynolds number, very close to the wall this quantity is very large. For the two higher Stokes numbers, the slip velocity and particle Reynolds number

exhibit a steady increase as the wall is approached, indicating maximum decoupling from the fluid in the turbulent region. In these cases, the drag coefficient remains relatively steady (between 10 and 100) throughout the domain, where its maxima are located at the channel centreline and at the wall.

Figure 4.18 demonstrates the evolution of near-wall particle concentration over time, which was monitored for each particle set to determine whether the dispersed system had reached a statistically steady state. To generate this quantity, the number of particles at position $y^* < 0.1$ was recorded each timestep and divided by the volume of the enclosed regions to generate a concentration C. This was then divided by the mean initial concentration measured across the entire channel after injection, C_i, to obtain a relative concentration. It is observed here that the statistically steady state has a very slight constant drift of particles towards the wall, but the flux (or the time derivative of concentration) remained stable. The other plot in Figure 4.18 depicts the mean concentration profile across the channel, with statistics gathered after $t^* > 100$. It is apparent from this plot that the maximum near-wall concentration was actually obtained from the St^+ = 50 particle set. This is likely due to particle entrainment in low speed streaks close to the wall, the effect of which is greatest for midrange particle Stokes numbers as we shall see later.

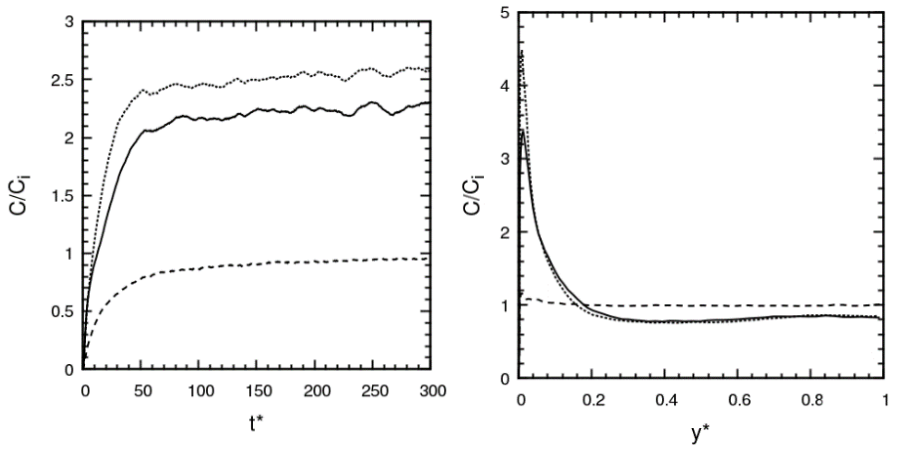

Figure 4.18: Near-wall particle concentration normalised by the initial bulk concentration over time (left) and particle concentration normalised by initial bulk concentration across the channel (right). Solid line: St^+= 92; dotted: St^+= 50; dashed: St^+= 0.1.

The contributions to acceleration from drag and lift in Eq. (5) are plotted in Figure 4.19 and Figure 4.20, respectively, for each particle Stokes number. The streamwise drag force at St^+ = 0.1 is homogeneous in the bulk of the channel. In the turbulent region, the magnitude peaks and the force is negative. The wall-normal drag force varies across the channel. In the bulk, the particles are carried away towards the turbulent region. A pair of stable fixed points in the wall-normal force plot is observed at $y^* = \pm 0.7$. Away from these points, the particles are subject to large forces in all directions aside from spanwise, which is a result of chaotic fluid velocities in that region. The mean spanwise forces are negligible due to the homogeneity associated with that direction.

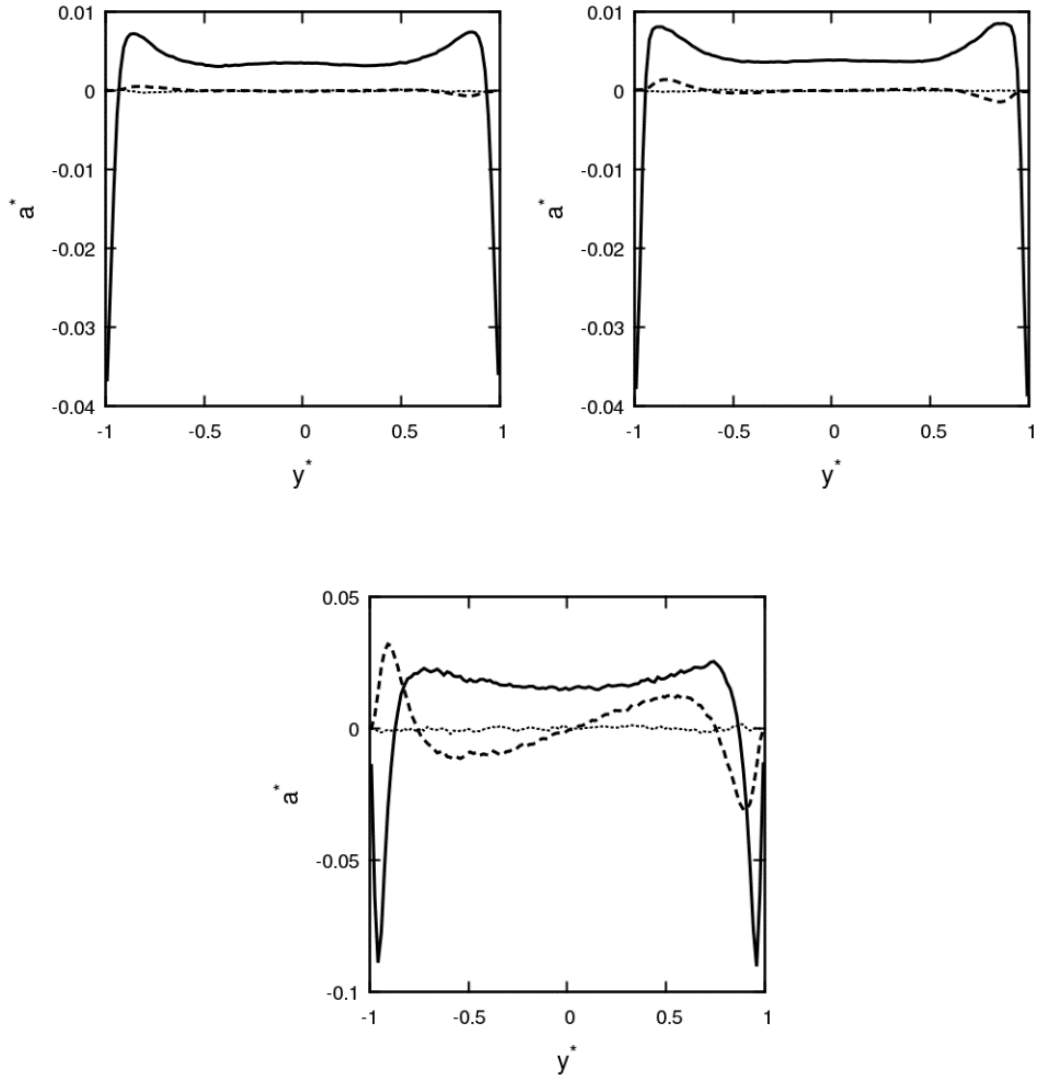

Figure 4.19: Mean non-dimensionalized drag force components per particle across the channel at St^+= 92 (upper-left), St^+= 50 (upper-right) and St^+= 0.1 (lower). Solid line: streamwise; dashed: wall-normal; dotted: spanwise.

Figure 4.19 also illustrates the average drag force per particle across the channel for the two higher Stokes numbers. In contrast with St^+ = 0.1, the mean accelerations are generally much lower due to the inverse scaling with the density ratio. The streamwise force now deviates even within the bulk of the flow, and the extent of the region of the channel where the particles are subject to large forces downstream is much greater. In the wall-normal direction, the force is only relevant in the turbulent region and is still small compared to the streamwise drag force.

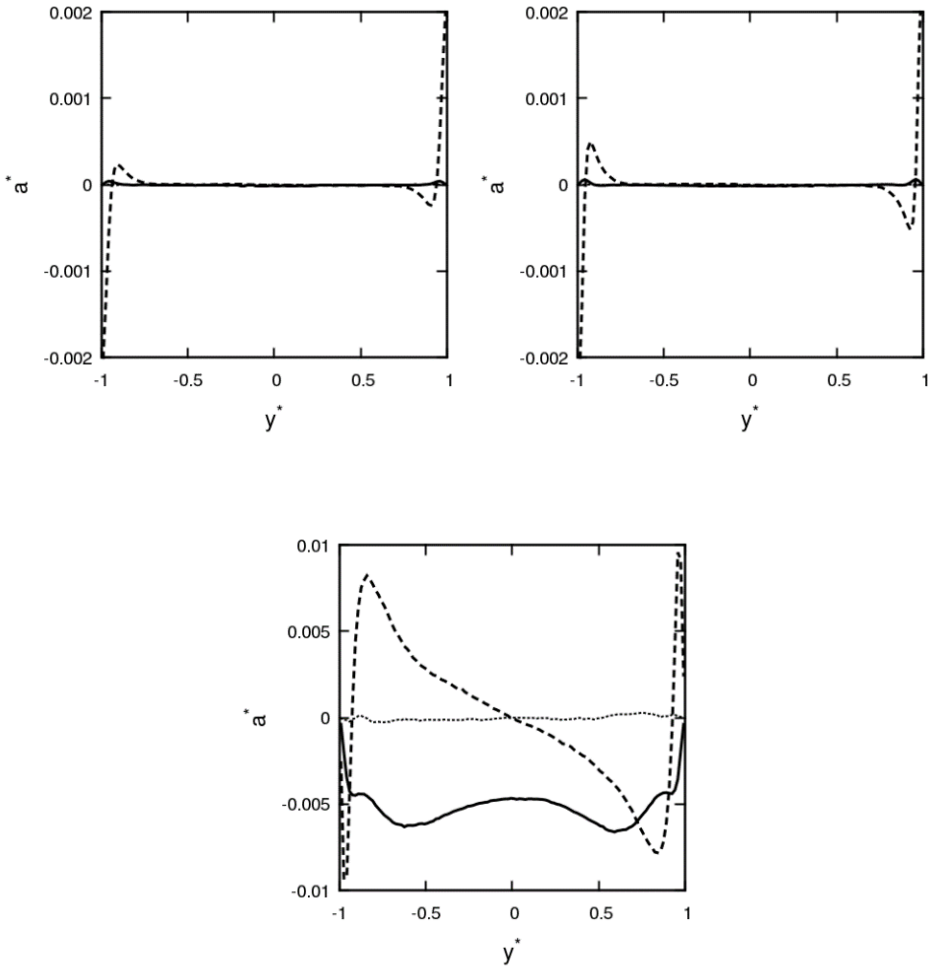

Figure 4.20: Mean non-dimensionalized lift force components per particle across the channel at St^+= 92 (upper-left), St^+= 50 (upper-right) and St^+= 0.1 (lower). Solid line: streamwise; dashed: wall-normal; dotted: spanwise.

Again, this component demonstrates a slight tendency to push the particles back towards the bulk. At lower particle densities, the inclusion of the lift force significantly alters the motion of particles moving in the turbulent flow field, therefore this parameter is considered for each Stokes number in Figure 4.20. At St^+= 92 and St^+= 50, the lift force

is negligible when compared with drag, but becomes relevant for the St^+= 0.1 particles. The streamwise component acts to decelerate the particles in the bulk, whereas the wall-normal component pushes particles back towards the bulk, and scales with distance from the centreline.

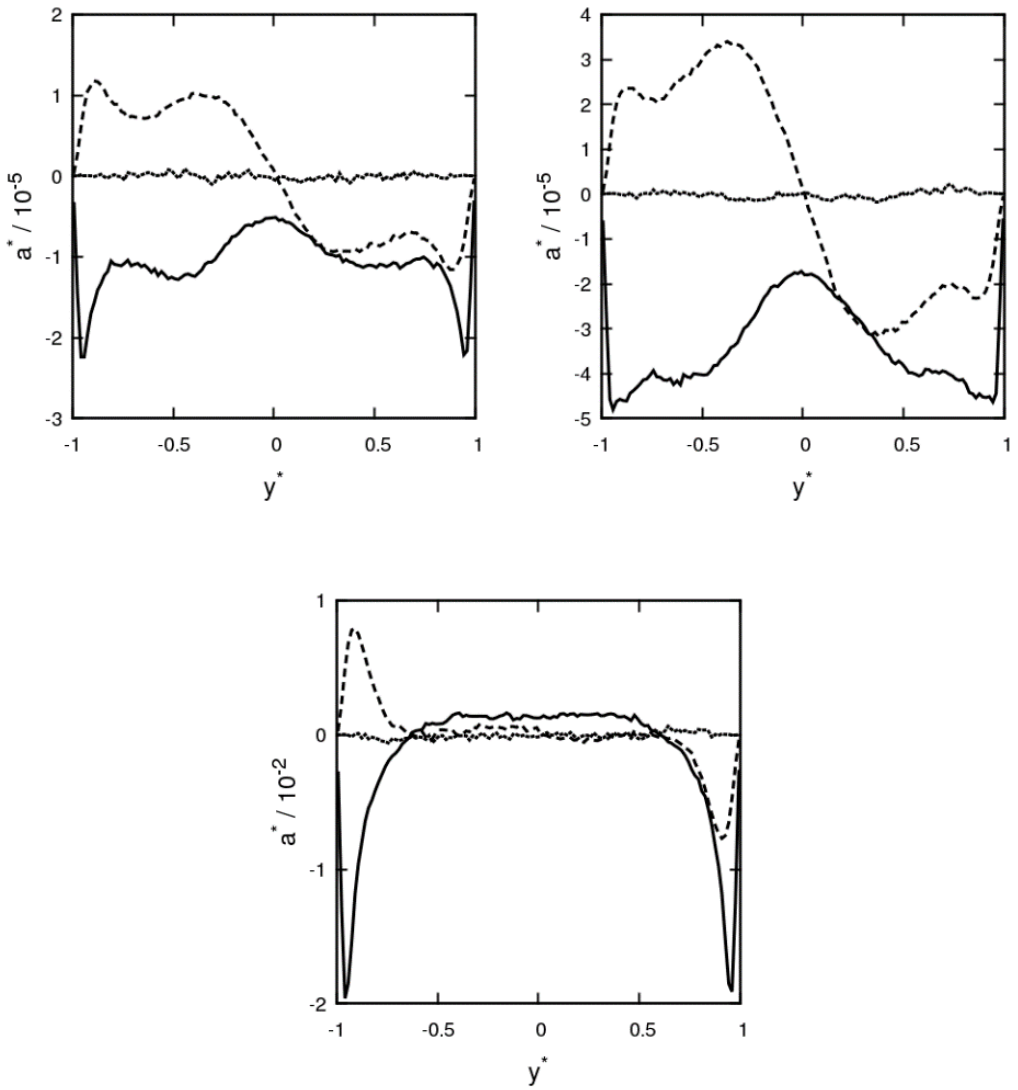

Figure 4.21: Mean non-dimensionalized pressure gradient force components per particle across the channel at St^+= 92 (upper-left), St^+= 50 (upper-right) and St^+= 0.1 (lower). Solid line: streamwise; dashed: wall-normal; dotted: spanwise.

Figure 4.21 and Figure 4.22 illustrate the average pressure gradient and virtual mass forces across the channel. For the two higher Stokes numbers, contributions from these terms are very low when compared to the drag force (~0.1%). Due to the inverse scaling with density ratio, the contribution from these terms becomes very significant for the $St^+ = 0.1$ particles. Their magnitudes are comparable with the lift force in the near-wall

region. Since $u_F \approx u_P$ at low Stokes numbers, the material derivatives used to calculate these terms are approximately equivalent. Hence, the only difference is a factor of two, indicated by comparing Figure 4.21 and Figure 4.22 for the $St^+ = 0.1$ particle set. Here, both of these forces act to accelerate particles in the bulk, and decelerate particles in the near-wall regions. Their wall-normal components also act to reintroduce particles from the wall regions back into the outer layer.

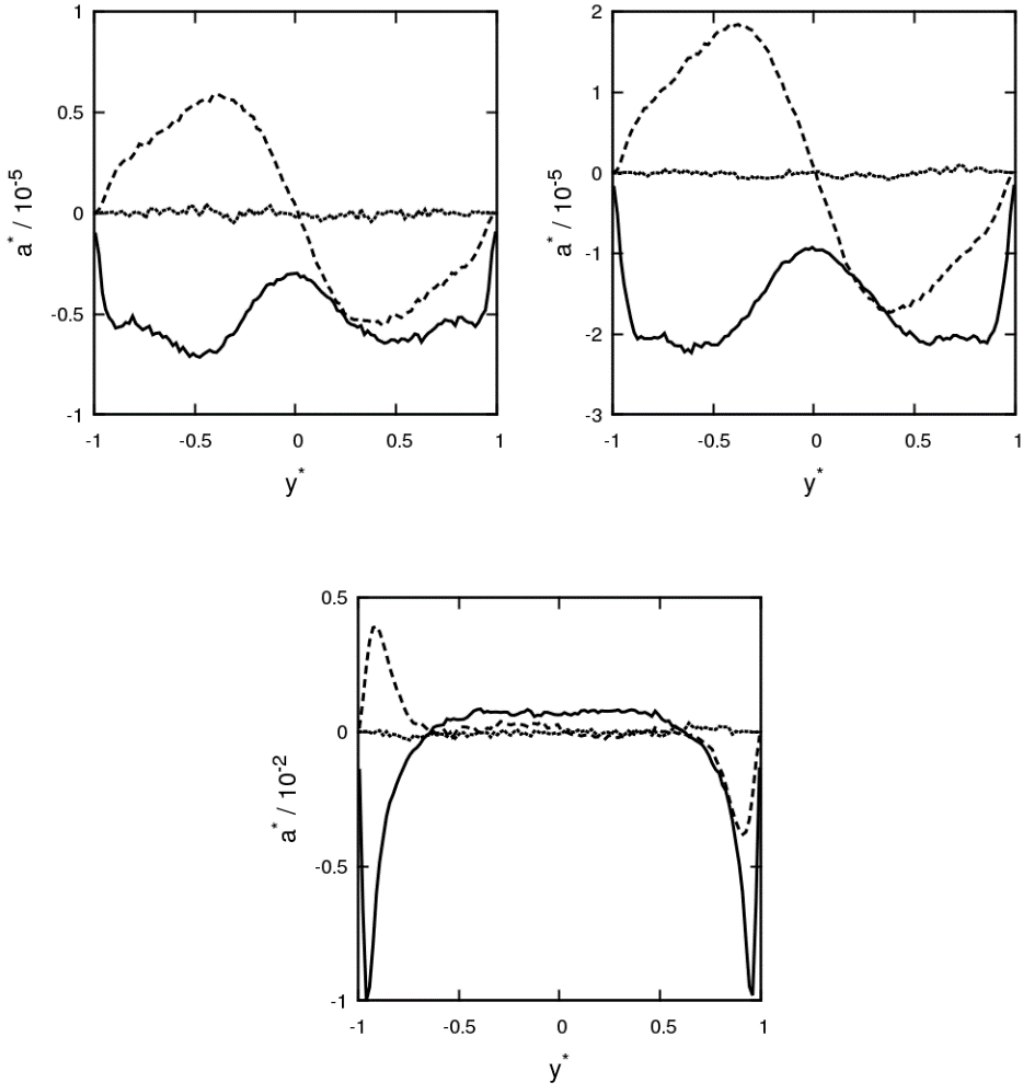

Figure 4.22: Mean non-dimensionalized virtual mass force components per particle across the channel at St^+= 92 (upper-left), St^+= 50 (upper-right) and St^+= 0.1 (lower). Solid line: streamwise; dashed: wall-normal; dotted: spanwise.

4.3.3 Region-based particle dynamics

This section focuses on identifying the key particle dynamics associated with each layer of the turbulent channel flow. The four layers are (with y^* now indicating the distance from the wall): the viscous sublayer ($0 \leq y^* < 0.027$), the buffer layer ($0.027 \leq y^* < 0.166$), the log-law region ($0.166 \leq y^* \leq 0.2$) and the bulk flow region ($0.166 \leq y^* \leq 1$). The layers are mirrored about the channel centre ($y^* = 1$).

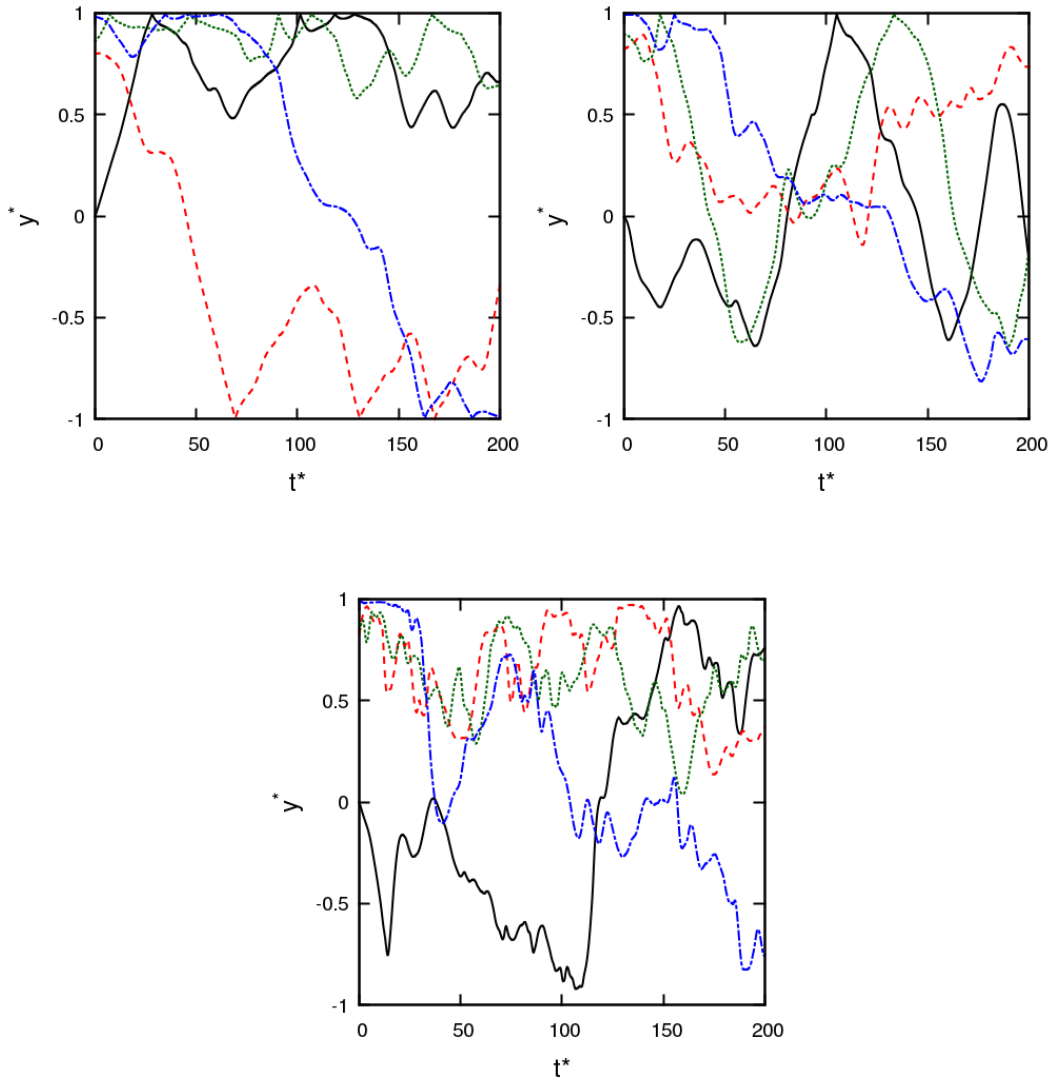

Figure 4.23: Particle trajectories in the wall-normal direction for particles released in different regions at $St^+ = 92$ (upper-left), $St^+ = 50$ (upper-right) and $St^+ = 0.1$ (lower). Solid line: viscous sublayer; dashed: buffer layer; dotted: log-law region; dot-dashed: bulk flow.

Sample trajectories in the wall-normal direction for particles released in each of regions are depicted in Figure 4.23. These plots help determine the microscopic motion of single particles, and aid in visualizing the differences associated with particles of low and high inertia. For instance, it is indicated that particles at $St^+ = 92$ exhibit more wall collisions than those at $St^+ = 50$. Furthermore, the $St^+ = 0.1$ particles sampled indicate no wall collisions at all. There also seems to be a broad trend in that the particles with higher Stokes numbers change their wall-normal direction much less frequently than those with lower values. For $St^+ = 92$, wall collisions tend to account for most of the changes in direction.

Probability density functions of various dynamic quantities were gathered for each region to obtain more information surrounding the local behavior of many particles. These will later be correlated with the flow topology for each layer. Figure 4.24 shows the streamwise particle velocity PDFs in each region for all three Stokes numbers. It is evident in all cases that as the channel centre is approached, the distribution of velocity increases. It is also apparent that the bulk distribution is very similar for all three Stokes numbers. A feature of interest occurs for the $St^+ = 92$ case, where there appears to be a secondary distribution of streamwise velocities in the viscous sublayer around $u_{p,x} = 0.6$. This indicates two regimes of particle transport very close to the wall. The fact that the secondary peak matches the distribution in the buffer layer could indicate fast transfer of particles from that region, where particles do not have enough time to lose their momenta upon entering the viscous sublayer.

PDFs of wall-normal velocities in each layer are shown in Figure 4.25. Aside from in the bulk, samples were only taken in the upper wall-normal region to provide more information surrounding motion towards and away from the boundary. In the case of $St^+ = 0.1$, each region has a symmetric distribution such that there are an equal number of particles with positive and negative velocities. This indicates strong homogenous mixing. Here, particles in the viscous sublayer have very particular wall-normal velocities, the range of which increases as they approach the bulk flow region, which is in agreement with the results of Figure 4.16. For the higher Stokes numbers, particles have a tendency to favour negative wall-normal velocities. Since these samples were gathered after the near-wall concentration had stabilised, the mean wall-normal velocity is zero in all regions.

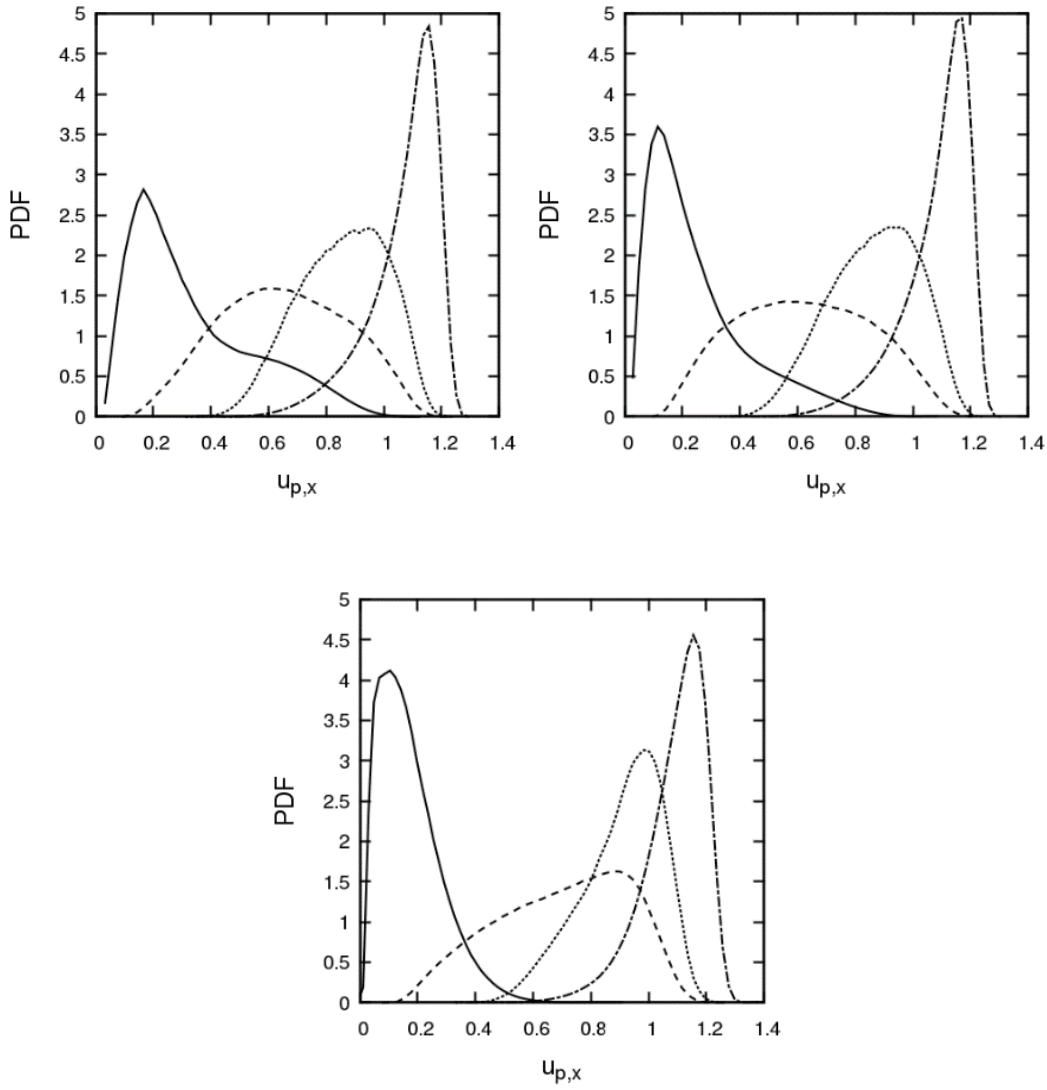

Figure 4.24: Probability density function for the particle streamwise velocity in each region of the channel at St^+= 92 (upper-left), St^+= 50 (upper-right) and St^+= 0.1 (lower). Solid line: viscous sublayer; dashed: buffer layer; dotted: log-law region; dot-dashed: bulk flow.

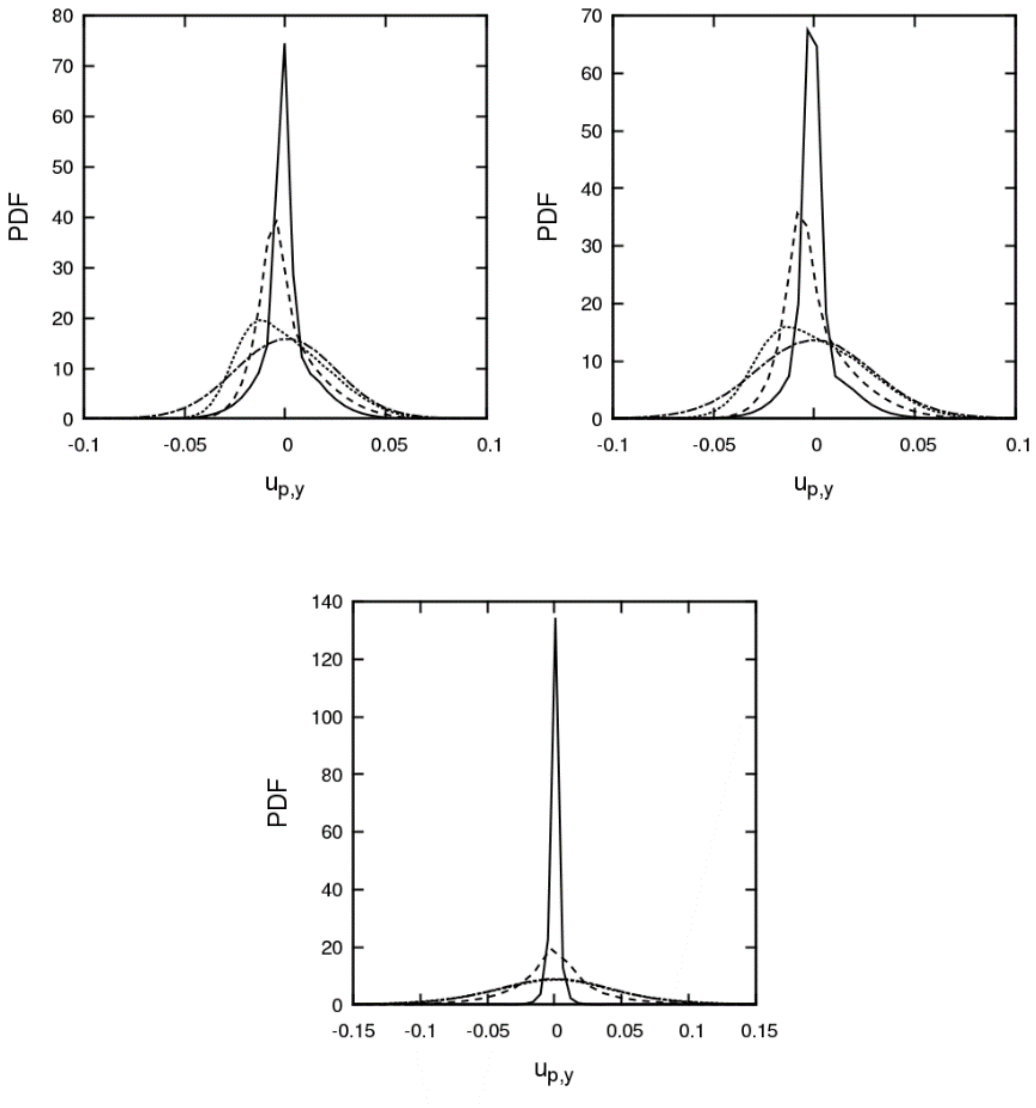

Figure 4.25: Probability density function for the particle wall-normal velocity in each region of the channel at St^+= 92 (upper-left), St^+= 50 (upper-right) and St^+= 0.1 (lower). Solid line: viscous sublayer; dashed: buffer layer; dotted: log-law region; dot-dashed: bulk flow.

Figure 4.26 shows region-based PDFs of the spanwise velocity for each Stokes number. Evidently, all distributions are symmetric due to the periodicity and homogeneity in that direction. As indicated by the velocity fluctuations in Figure 4.16, the range of spanwise velocities increases as Stokes number decreases. Furthermore, for St^+= 0.1, the greatest spanwise motion is located in the buffer layer, and not the bulk flow region as for the inertial particles.

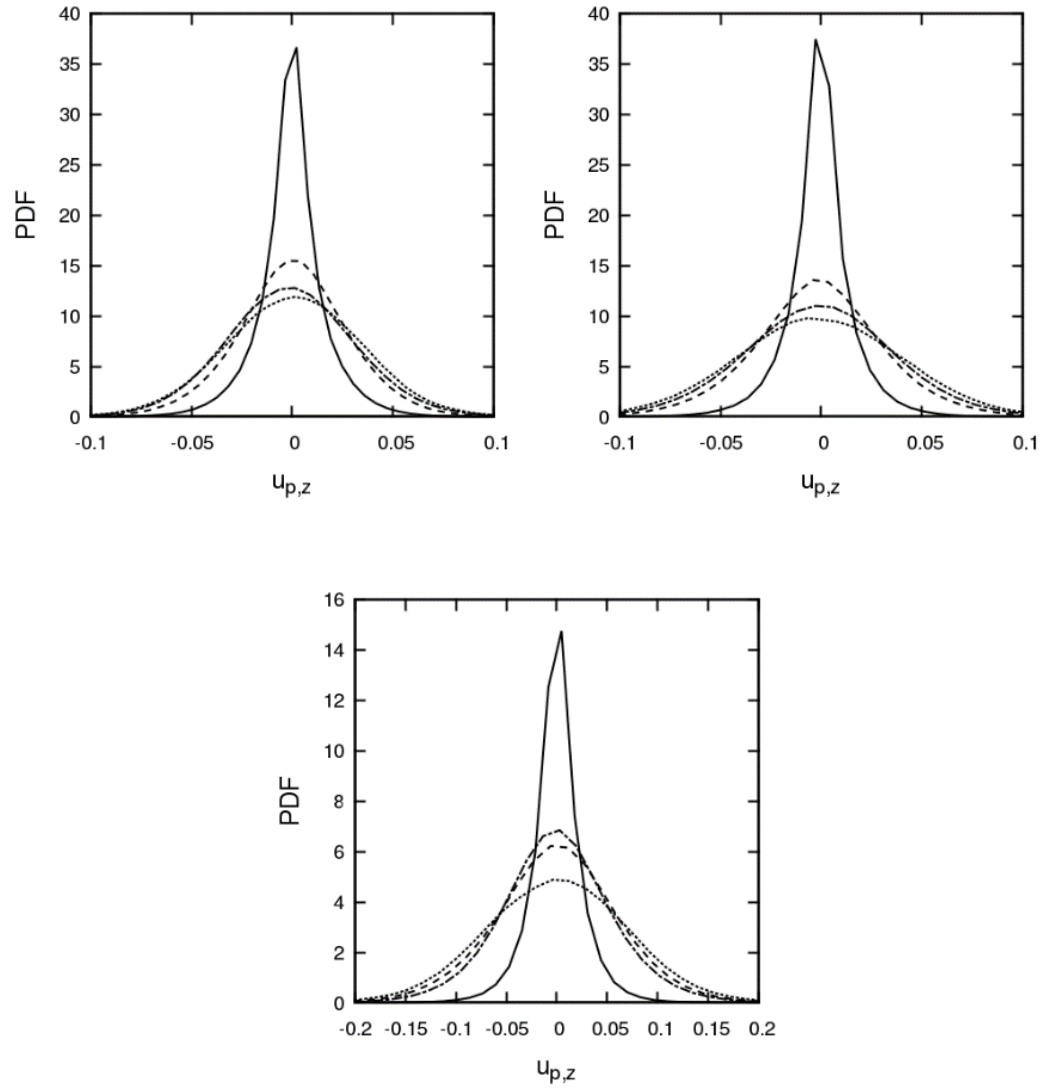

Figure 4.26: Probability density function for the particle spanwise velocity in each region of the channel at St^+= 92 (upper-left), St^+= 50 (upper-right) and St^+= 0.1 (lower). Solid line: viscous sublayer; dashed: buffer layer; dotted: log-law region; dot-dashed: bulk flow.

PDFs of region-based particle Reynolds number (Re_P) are presented in Figure 4.27. For the two larger Stokes numbers, there is not a great difference between the various layers, other than that the viscous sublayer has a larger range which seems to stretch far beyond that of the other three layers. Conversely, for St^+= 0.1, particles in the viscous sublayer have very low Reynolds numbers, which increase as the bulk is approached.

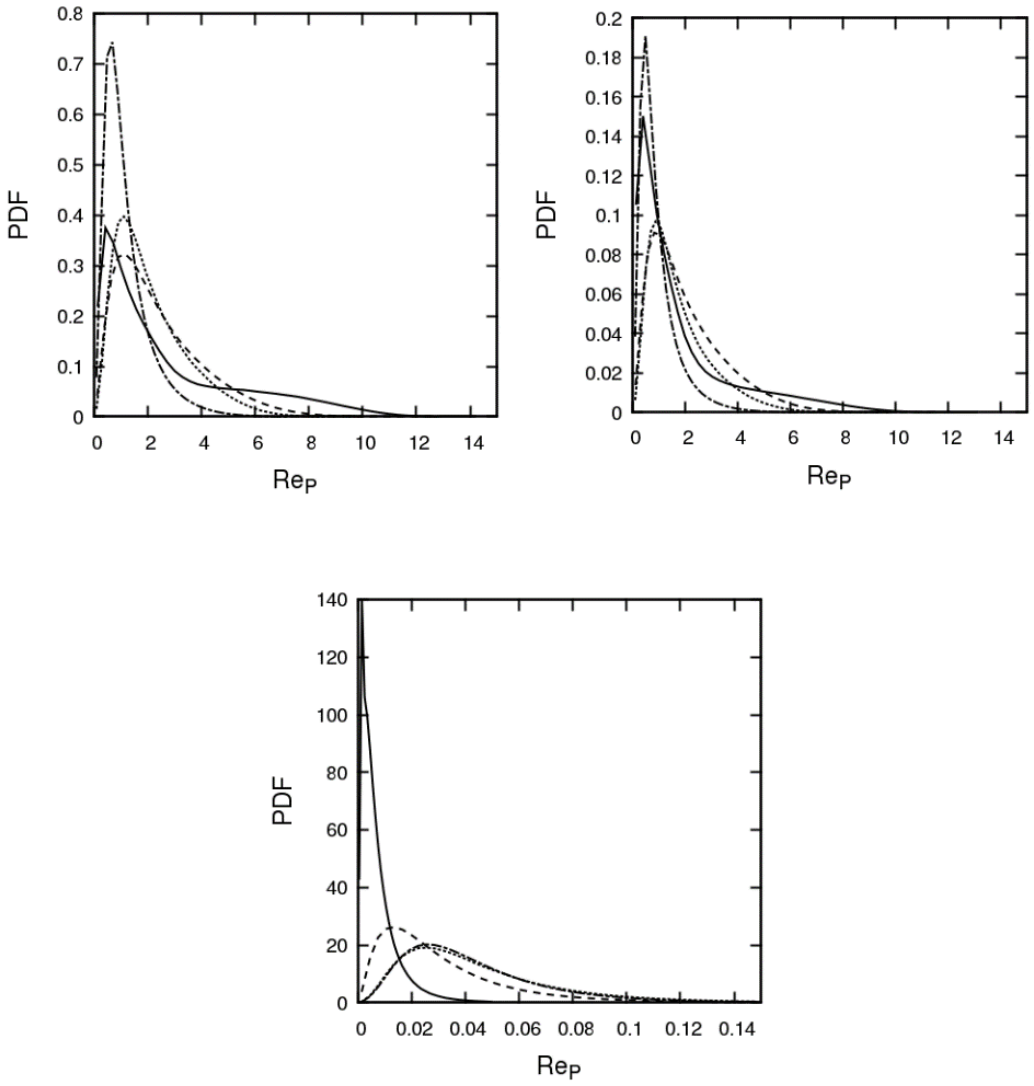

Figure 4.27: Probability density function for the particle Reynolds number in each region of the channel at St^+ = 92 (upper-left), St^+ = 50 (upper-right) and St^+ = 0.1 (lower). Solid line: viscous sublayer; dashed: buffer layer; dotted: log-law region; dot-dashed: bulk flow.

Lastly, Figure 4.28 illustrates the drag coefficient (C_D) distributions in each region for the three Stokes numbers. Qualitatively, the two higher Stokes number particles exhibit similar characteristics, with peaks for most regions residing around $C_D = 10$. At St^+= 0.1, due to the low particle Reynolds numbers, drag coefficients are much higher, and are distributed over a much larger range. In the viscous sublayer, particles are observed to possess drag coefficients greater than 10,000. From Figure 4.27 and Figure 4.28, it is evident that in all cases, the greatest range of particle dynamics is found within the viscous sublayer.

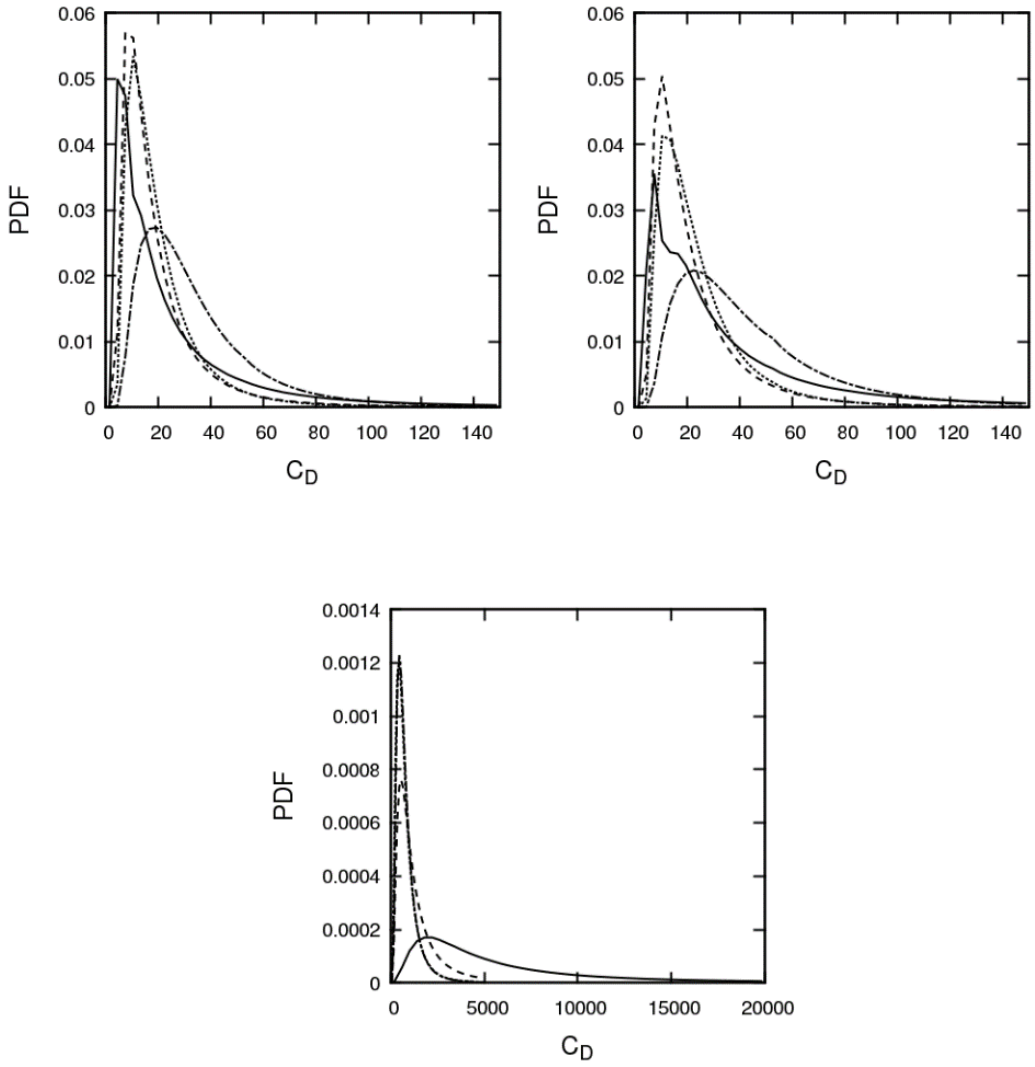

Figure 4.28: Probability density function for the particle drag coefficient in each region of the channel at St^+= 92 (upper-left), St^+= 50 (upper-right) and St^+= 0.1 (lower). Solid line: viscous sublayer; dashed: buffer layer; dotted: log-law region; dot-dashed: bulk flow.

4.4 Particle dynamics and flow topology

In this section, the behaviour of particles in each near-wall region is related to their interaction with local coherent flow structures. To classify structures within each region, we use the scheme of Blackburn et al. (1996). Using the latter approach, each fluid field point can be categorised into one of four topology types, illustrated in Figure 4.29. These are (in regular quadrant ordering): unstable focus / compressing, stable focus / stretching, stable node / saddle / saddle and unstable node / saddle / saddle. Fluid points representing vortices have Q-R space points in the first two regions, and the last two regions represent

convergence zones, where Q and R are, respectively, the second and third invariants of the velocity gradient tensor. The four regions identified in the previous section are used to compare Q-R values computed on the fluid grid points with Q-R values computed at particle locations for snapshots of the statistically converged simulations. Each of these calculations is illustrated as a two-dimensional PDF with contoured regions representing equivalent ranges of Q-R point density. By performing this analysis, we are able to determine the type of turbulence structures the particles are likely to encounter, and whether they show any preference to a particular classification of structure.

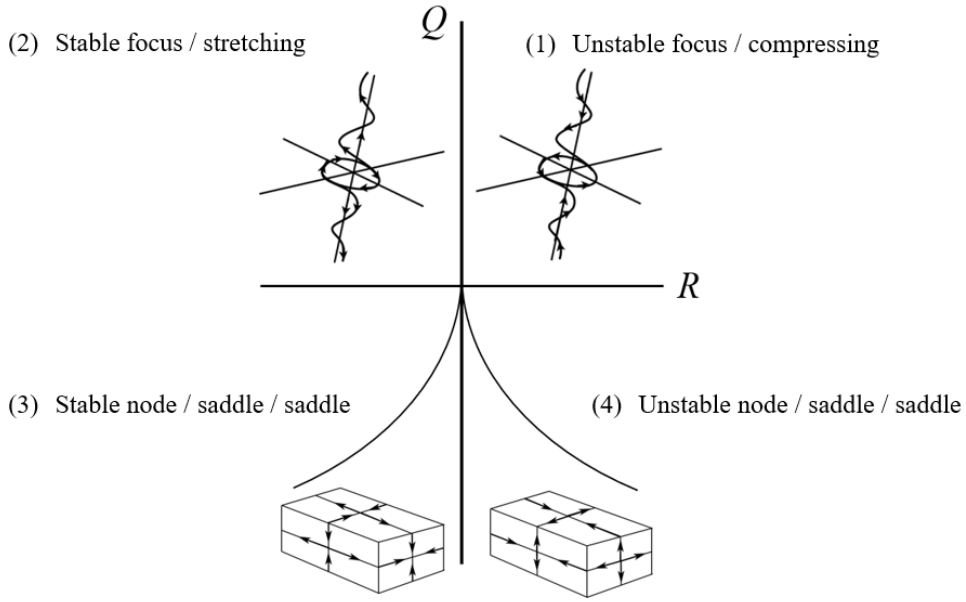

Figure 4.29: Q and R tensor invariants for incompressible flow topology classification. Solid curved lines represent $D = \left(\frac{27}{4}\right) R^2 + Q^3 = 0$. After (Blackburn et al., 1996), region terminology is that of Chong et al. (1990).

Figure 4.30 compares PDFs at the fluid grid points with those at particle positions for the St^+ = 0.1 and St^+ = 92 simulations, using solely points sampled from the viscous sublayer. Fluid node values indicate almost isotropy in radial preference, with a slight lean towards the fourth quadrant, which corresponds to unstable node / saddle / saddle type points. Considering particle position-based sampling, both exhibit a greater preference towards the convergence zones, which are areas where particles are likely to congregate. However, it appears that at St^+ = 92, the particles still sample the vortical

regions as seen by the fluid grid points. Similar findings were observed in (Rouson and Eaton, 2001).

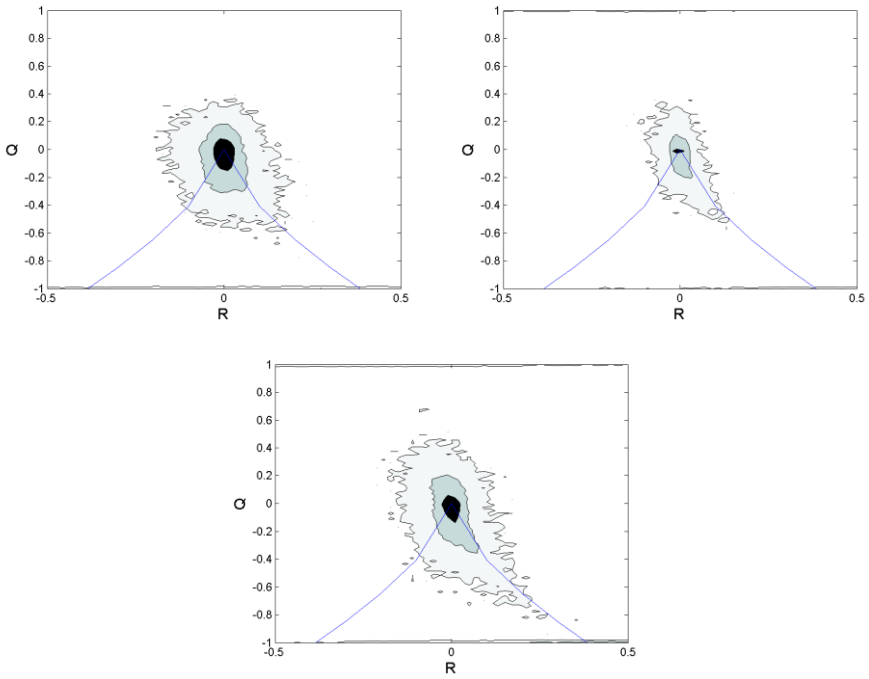

Figure 4.30: PDF of invariants of the velocity gradient tensor, Q and R, sampled at fluid nodes and particle positions in the viscous sublayer at fluid nodes (upper-left), and for St^+= 0.1 (upper-right) and St^+= 92 (lower) particles.

Figure 4.31 illustrates the same PDFs, this time sampled in the buffer layer. Moving away from the wall, the fluid grid points now exhibit a much more pronounced preference for stable focus / stretching vortices and the unstable node / saddle / saddle topologies. Comparing the two particle sets, the St^+= 92 particles sample more of the strongest stretching vortical regions than the St^+ = 0.1 particles, which is similar to the type of sampling occurring for the former particles in Figure 4.30. This could provide an explanation and mechanism for the buffer layer to viscous sublayer transfer phenomenon mentioned earlier since particles avoid these regions in the viscous sublayer, hence it appears that particles encountering vortex cores are ejected in the direction of the wall.

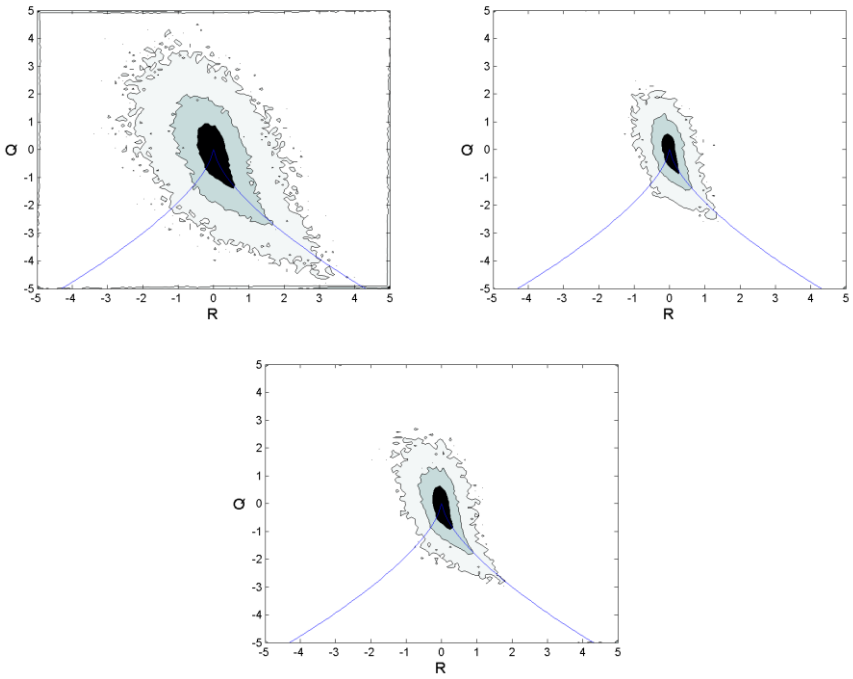

Figure 4.31: PDF of invariants of the velocity gradient tensor, Q and R, sampled at fluid nodes and particle positions in the buffer layer at fluid nodes (upper-left), and for St^+= 0.1 (upper-right) and St^+= 92 (lower) particles.

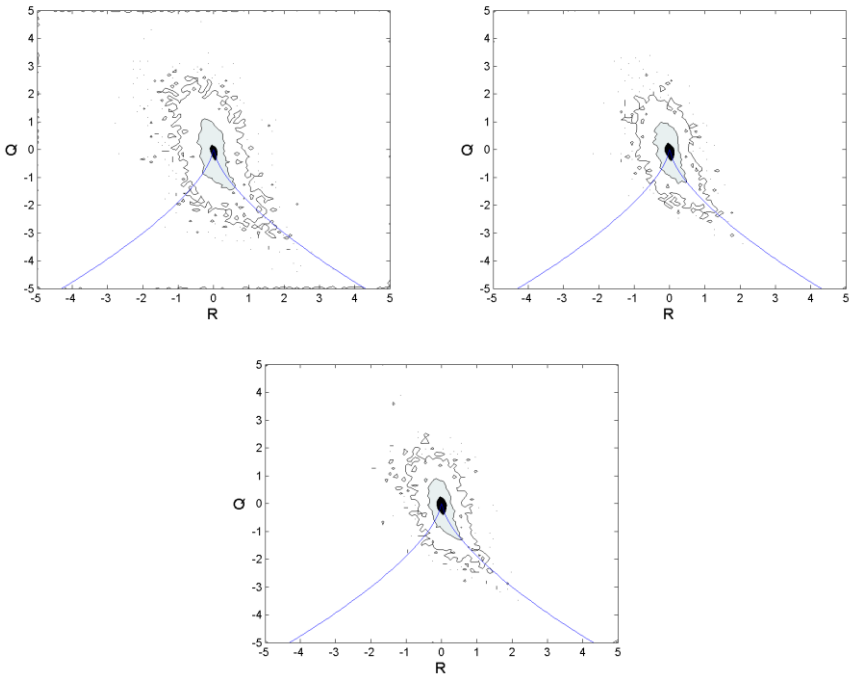

Figure 4.32: PDF of invariants of the velocity gradient tensor, Q and R, sampled at fluid nodes and particle positions in the log-law region at fluid nodes (upper-left), and for St^+= 0.1 (upper-right) and St^+= 92 (lower) particles.

Figure 4.32 and Figure 4.33 compare Q-R PDFs for the log-law region and the bulk flow. In each case, there is very little effect of Stokes number on the resulting distributions. Furthermore, the particles exhibit no obvious preferential concentration in these regions when compared to the fluid.

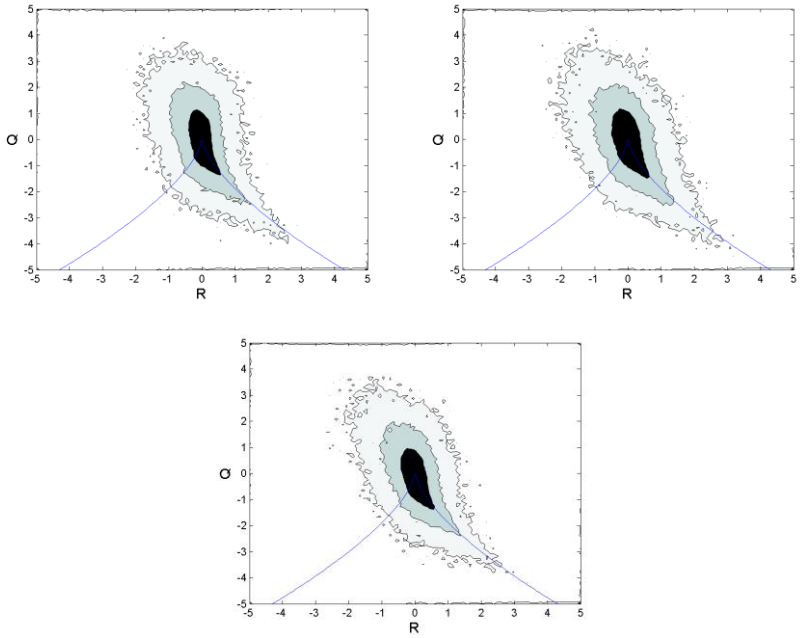

Figure 4.33: PDF of invariants of the velocity gradient tensor, Q and R, sampled at fluid nodes and particle positions in the bulk flow region at fluid nodes (upper-left), and for St^+= 0.1 (upper-right) and St^+= 92 (lower) particles.

Instantaneous particle distributions near the channel boundary were obtained from the final timestep of each simulation and are presented in Figure 4.34. Results from the validation runs have been included here to provide a more in-depth overview of the response of near-wall particle segregation to Stokes number, however, it should be emphasised that results at $St^+ = 1, 5$ and 25 were obtained at a slightly lower Reynolds number, and with an absence of lift, pressure gradient and virtual mass forces. Therefore, the extent of preferential concentration is likely to vary slightly at $Re_\tau = 180$.

Despite this, the overall trend is clear; particles at very low Stokes numbers are homogenously distributed near the wall, showing very little indication of their location within low speed streaks. As the Stokes number increases, the level of order increases likewise, and the results indicate a maximum level of order by inspection at $St^+ = 25$.

Above this value, the streaks begin to become much less clear, as the particles begin to decouple from the fluid motion.

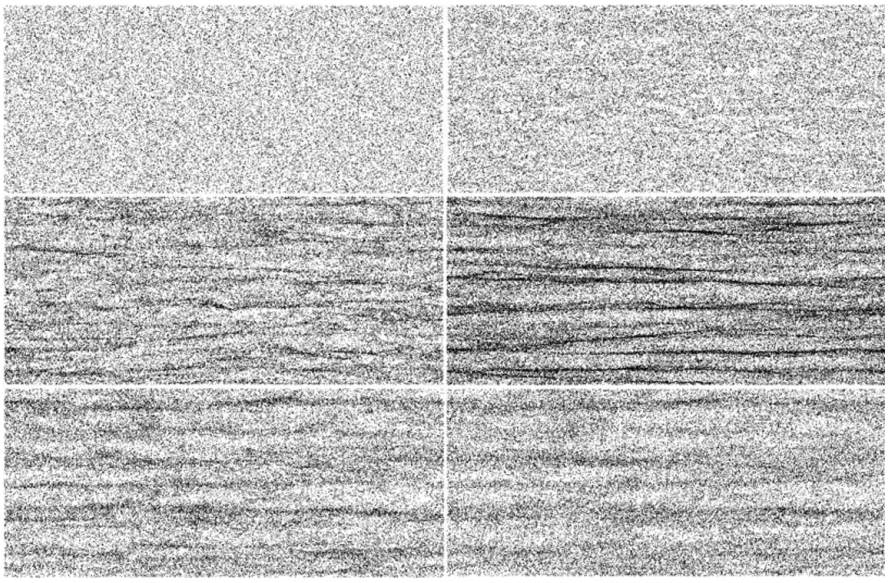

Figure 4.34: Instantaneous near-wall particle distributions at $y^* = 0.9$ for $St^+ = 0.1,\ 1,\ 5,\ 25,\ 50$ and 92 starting at top-left and ending at lower-right (moving left to right). $St^+ = 1, 5$ and 25 were taken from the validation simulations at a slightly lower Reynolds number, $Re_\tau = 150$.

Lastly, to determine the effect of Stokes number on particle mixing, mean fluxes were calculated through the boundaries between each region between t^* = 200 and t^* = 300 to ensure the statistics were stationary. The results of this investigation are presented in Table 7. Here, F+ represents the flux towards the wall, and F- represents the flux away from the wall. It is evident that in all cases, the net flux through each plane is approximately zero, with a slight preference for turbophoresis at St^+ = 92. At St^+ = 0.1, the greatest mixing occurs between the bulk region and the log-law / buffer layer regions. Low Stokes number particles travelling from the buffer layer to the viscous sublayer are limited due to low velocities and large forces influencing them back towards the bulk. In the case of St^+ = 92 particles, the strongest mixing effect actually occurs between the buffer layer and the viscous sublayer. Since particles are likely ejected into this region, they reach the wall with high velocities and so elastic wall reflections likely remove particles from this region at the same rate that they enter. The significance of this is that the wall acts to filter high wall-normal particles back into the buffer layer.

Table 7: Inter-region mean particle fluxes in particle-laden turbulent channel flow.

Region	**Start** (y^*)	**End** (y^*)	**F+** ($St^+ = 0.1$)	**F+** ($St^+ = 92$)	**F-** ($St^+ = 0.1$)	**F-** ($St^+ = 92$)
Bulk flow	0.200	1.000	-	-	994	449
Log-law	0.166	0.200	994	456	914	458
Buffer layer	0.027	0.166	914	463	137	576
Viscous sublayer	0.000	0.027	136	576	-	-

4.5 Conclusions

Lagrangian particle tracking and direct numerical simulation have been used throughout this chapter to study three sets of particles in a multi-phase turbulent channel flow at $Re_\tau = 180$ to determine the effect of Stokes number on near-wall particle dynamics. Parameters have been chosen to augment and expand upon existing work in this area by performing simulations at Stokes numbers outside the range usually considered. Furthermore, continuous-phase topology analysis techniques have been performed to correlate particle behaviour with local turbulent structures.

Turbulent channel flow results obtained using the continuous phase solver, Nek5000, at a shear Reynolds number of 180 exhibited excellent agreement with those of previous high accuracy DNS studies. Furthermore, the particle simulation technique described in this thesis validated very well against the work of Marchioli et al, using a separate simulation performed at $Re_\tau = 150$.

Results indicate that particles with larger Stokes numbers tend to overtake the fluid flow near the wall, and lag behind the flow in the bulk flow region. Moreover, the high Stokes particles exhibit increased rms velocity fluctuations very close to the wall, implying strong decoupling from local flow velocity fields. This is in agreement with previous work both at similar and increased fluid Reynolds numbers (Li et al., 2001; Zhao et al., 2015; Rouson and Eaton, 2001). Other components of the rms velocity fluctuations were suppressed. All of these near-wall effects scale with Stokes number. Other particle properties such as slip velocities, Reynolds numbers and drag coefficients indicate large differences in mean behaviour between low and high Stokes number particles. Concentration profiles indicate rapid near-wall accumulation for the $St^+ = 50$ and $St^+ =$

92 particle sets. In all cases, the near-wall concentration reached an approximately statistically steady state after $t^* > 100$, however, this period still exhibited a slow and uniform particle accumulation rate. Acceleration terms due to drag and lift forces were analysed across the channel and the necessity for the inclusion of the lift term was confirmed for the low particle Stokes number, accounting for large wall-normal velocities pushing particles back into the bulk of the flow. This effect was observed to be greatest at the boundary between the log-law region and the bulk flow, and could explain the increased mixing effect inherent in the $St^+ = 0.1$ system.

A novel analysis technique involving region-based particle dynamical property PDFs was employed throughout the channel to determine local behaviour. For the first time, it was observed that at large Stokes numbers, particles in the viscous sublayer seemingly exhibit two streamwise velocity regimes, the greater of which coincides with the peak of the velocity distribution in the buffer layer. This indicates that particles from the buffer layer are entering the viscous sublayer, whilst retaining their higher streamwise velocity. A consequence of this is that the streamwise rms velocity fluctuations will be greater in this region, since the velocities of the migrating particles will differ from those of the surrounding flow. Furthermore, the rapid movement of a particle into a region of low fluid streamwise velocity in turn produces a high 'slowing' drag force (see Figure 4.19), which it scales with, and is highly sensitive to the distance from the wall. A spread of particle velocities is therefore generated as the particle traverses this region and decelerates with the particles closest to the wall experiencing the greatest force. This important effect has consequences for the deposition behaviour and wall accumulation of particles, but is much less pronounced for lower Stokes numbers. In the case of previous studies (Marchioli et al., 2008), which regularly use $St^+ < 25$, this effect was not observed. Other interesting results from the PDF-based analysis include increased wall-normal velocities in the viscous sublayer for higher Stokes number particles (hence increased wall collision velocities) and greater spanwise motion in the log-law region for $St^+ = 0.1$ particles (as opposed to inertial particles where it is greatest in the bulk).

The fluid topology classification scheme of Blackburn et al. (1996) was also used to determine the types of flow structures each set of particles were likely to sample for each region. In the viscous sublayer, it was observed that high Stokes number particles were located in regions similar to that of the fluid in the buffer layer, implying a coupling between the two layers. It is suggested that this could provide an additional mechanism

by which inertial particles migrate laterally to the viscous sublayer whilst retaining streamwise velocities similar to those present in the buffer layer.

5 TWO-WAY MOMENTUM COUPLING AND PARTICLE-PARTICLE INTERACTION

5.1 Introduction and background

In the previous chapter, we considered the direct numerical simulation of one-way coupled particle-laden turbulent flows in order to elucidate the dynamics associated with particle-turbulence interaction, with a primary focus on how the particles respond to different regions of turbulence. Due to the nature of the coupling, momentum transfer to the fluid and particle-particle interactions were ignored, which is accurate for low volume fractions ($\phi_P \leq 10^{-6}$) as shown by Elghobashi (2007). For flows with greater concentrations, accurate simulation requires further considerations.

Since the interaction between a particle and its surrounding fluid entails a two-way exchange of momentum, it is also important to consider the effect that the dispersed-phase has on the fluid phase, which has been shown in previous studies to modulate the turbulence (Crowe, 2000). Gas-solid flows have been examined experimentally (Lee and Durst, 1982; Tsuji and Morikawa, 1982; Varaksin and Polyakov, 1998; Gore and Crowe, 1989) and it was observed that for particles with small diameter the fluid turbulence intensities are attenuated. Conversely, when considering suspensions with large particles, the turbulence is enhanced. The mechanisms by which the turbulence is modified by particles dispersed within the flow are of great importance to industries interested in predicting multi-phase flows. The most accurate way to model such phenomena would be to directly track the surface of each solid, imposing no-slip boundary conditions and this technique will be considered in the following chapter. For large numbers of particles, however, this is unrealistic due to the large computer run times involved and, in general, a point-force approximation is used to estimate the coupling between the fluid and solid phases.

Furthermore, and to carry out more realistic simulations, particle-particle interactions must also be accounted for in dense flows. It has previously been experimentally observed by Bäbler et al. (2010) that flows possessing turbulent properties are capable of encouraging particle aggregation, which can arise due to attractive electrostatic forces exerted when the particles move close to one another and collide.

Direct numerical simulation (DNS) coupled with Lagrangian particle tracking (LPT) has been shown (Dritselis and Vlachos, 2011) to be more reliable than large eddy simulation when examining the induced effects of coupling on turbulence intensities. Previous simulation work of this nature has been carried out in recent years (Squires and Eaton, 1990; Sundaram and Collins, 1999; Li et al., 2001). Important findings indicate that turbulence intensities become more anisotropic as the particle mass loading is increased. Furthermore, qualitative descriptions have been offered (Vreman et al., 2009) concerning the way particles affect the continuous phase at high concentrations.

This chapter aims to expand on the recent work by more realistically investigating the effect that the presence of a solid, spherical particle phase has on the carrier fluid by considering two-way and four-way coupling mechanisms at low and high particle-fluid density ratios, matching those of the previous chapter. Lagrangian particle tracking is again used in conjunction with a high order spectral element method fluid solver to investigate turbulence modulation in a channel to a good degree of accuracy. Furthermore, a deterministic particle-particle agglomeration model is introduced and demonstrated which uses the DLVO (Derjaguin and Landau, 1941; Verwey and Overbeek, 1955) potential energy barrier model to determine collision events which result in aggregation.

The work performed provides both a more in-depth understanding of particle-fluid and particle-particle interaction in different turbulent regions within a channel flow, as well as laying the foundations for investigating particle agglomeration at a more fundamental level, as will be carried out in the following chapter.

5.2 Two-way coupling

5.2.1 Response and transition to steady state

For this section, the effect of two-way momentum coupling shall be considered at both low ($\rho_P^* = 2.5$) and high ($\rho_P^* = 2041$) density-ratios, whilst preserving the particle size. This is equivalent to examining the effects of particle-fluid interaction of identical particles dispersed in two fluids with different densities. As before, these are chosen to represent typical situations of relevance to the nuclear industry, whilst being at opposite ends of the tracer-inertial density ratio spectrum. Knowledge from this type of study could then be obtained surrounding how particles affect the turbulence properties of water (in such system as a waste slurry) or air (in thermal hydraulics). We first examine the temporal effects which occur upon enabling two-way coupling from an initial statistically settled particle-laden flow. The simulation parameters used throughout this chapter are presented in Table 8. The primary difference between the simulations performed here and those in the previous chapter is in the number of particles and hence, the volume fraction. This value ($\Theta_P = 10^{-3}$) has been chosen because it resides on the boundary between flows where two-way coupling must be considered and those where four-way coupling becomes important.

Table 8: Particle phase parameters for two- and four-way coupled simulations at $Re_\tau = 180$.

Parameter	$\boldsymbol{St^+ \approx 0.1}$	$\boldsymbol{St^+ \approx 92}$
Particle diameter, d_P^*	0.005	0.005
Particle diameter, d_P^+	0.9	0.9
Number of particles, N_P	2,567,400	2,567,400
Shear Stokes number, St_τ	0.113	91.845
Bulk Stokes number, St_B	0.01	7.937
Density ratio, ρ_P^*	2.5	2041
Volume fraction, Θ_P	10^{-3}	10^{-3}
Particle and fluid timestep, Δt^*	0.02	0.02
Particle and fluid timestep, Δt^+	0.23	0.23

In Figure 5.1 and Figure 5.2 we observe the effect of two-way coupling on the temporal evolution of the mean streamwise velocity in both the low and high Stokes number channel flows. At $St^+ = 0.1$ there is negligible response in this quantity. This is expected since the particles are tracer-like and the forces exerted by the fluid on these are very small. Hence, the two-way feedback is also very low. Conversely, for the $St^+ = 92$

particles, the mean streamwise velocity initially increases over the first $t^* = 50$, before decreasing slightly throughout the bulk flow region. The initial increase is likely due to the flow responding to the initial presence of the particles which are decorrelated with the local velocity field. From Figure 4.15 we know that the inertial particles are travelling slower than the surrounding fluid. After a short time, the particle-fluid feedback allows the flow to readjust, decreasing the mean flow velocity, particularly in the outer layer.

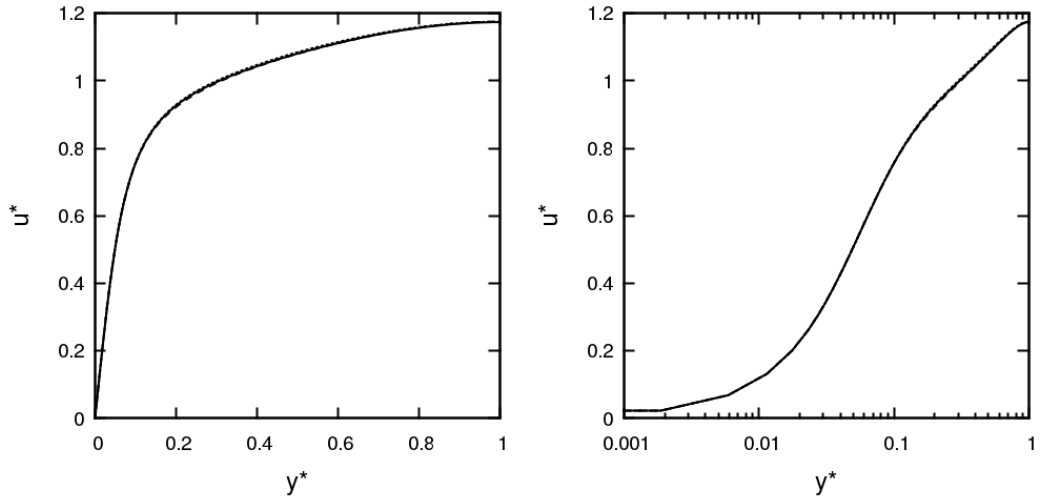

Figure 5.1: Temporal evolution of mean fluid streamwise velocity profile at $t^* = 0$ (solid), $t^* = 50$ (dashed) and $t^* = 100$ (dotted) after onset of two-way coupling in $St^+ \approx 0.1$ flow. Right plot is on a log scale.

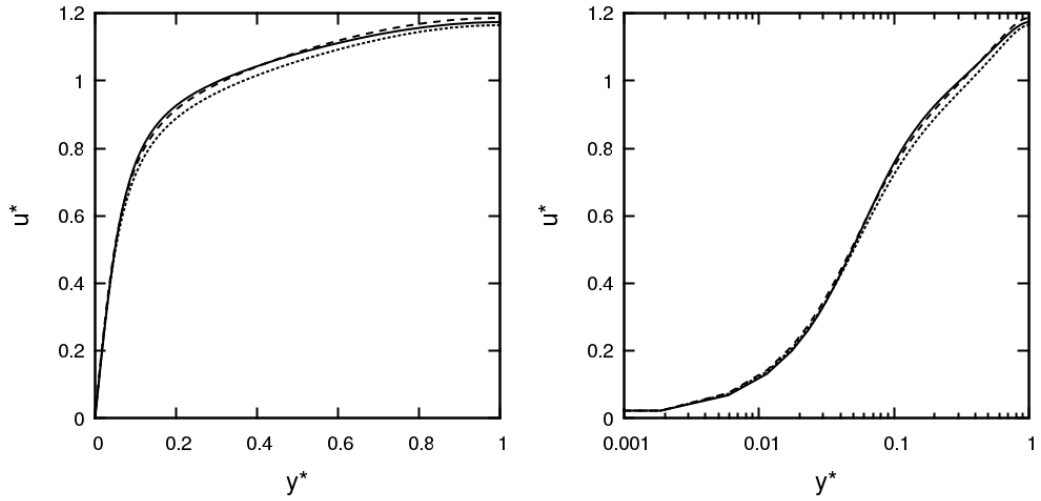

Figure 5.2: Temporal evolution of mean fluid streamwise velocity profile at $t^* = 0$ (solid), $t^* = 50$ (dashed) and $t^* = 100$ (dotted) after onset of two-way coupling in $St^+ \approx 92$ flow. Right plot is on a log scale.

Figure 5.3 and Figure 5.4 illustrate the time evolution of the mean fluid rms streamwise velocity fluctuations for both particle sets. Again, for the $St^+ = 0.1$ particles there is very little response in this quantity, although a slight decrease may be observed at the channel centreline during the transition period.

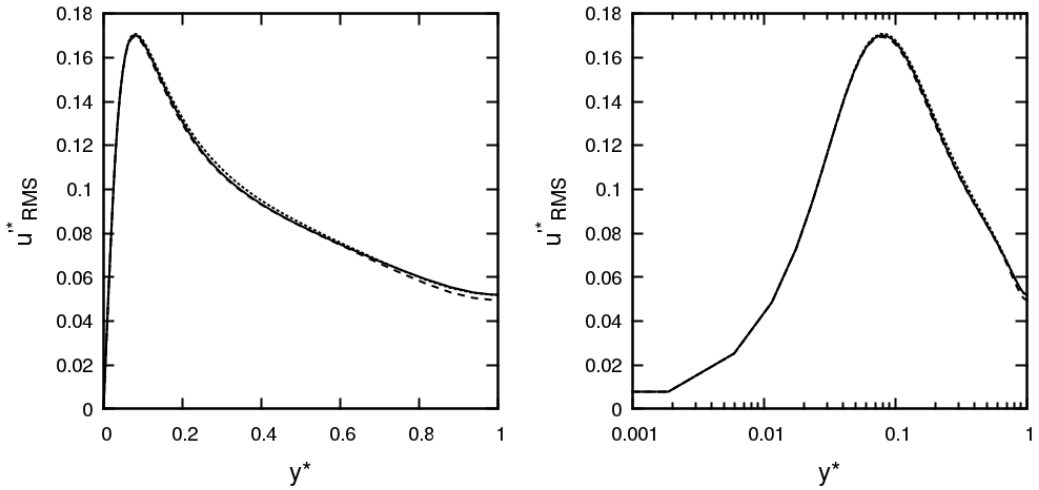

Figure 5.3: Temporal evolution of mean fluid rms streamwise velocity fluctuations profile at $t^* = 0$ (solid), $t^* = 50$ (dashed) and $t^* = 100$ (dotted) after onset of two-way coupling in $St^+ \approx 0.1$ flow. Right plot is on a log scale.

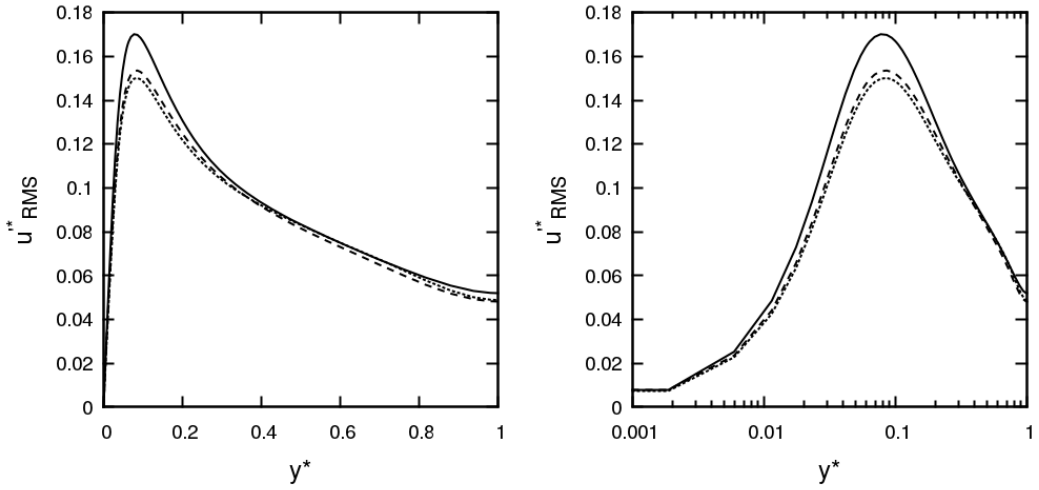

Figure 5.4: Temporal evolution of mean fluid rms streamwise velocity fluctuations profile at $t^* = 0$ (solid), $t^* = 50$ (dashed) and $t^* = 100$ (dotted) after onset of two-way coupling in $St^+ \approx 92$ flow. Right plot is on a log scale.

For the inertial particles, the streamwise turbulence is reduced, particularly in the buffer layer and slightly at the channel centreline. It has already been discussed in the previous chapter that inertial particles travel with high speeds throughout the near-wall region. This means that their velocities will be highly decorrelated from the local fluid velocities, even more so due to the large velocity gradients in this region which arise due to the no-slip condition at the wall. According to the work of Eaton and Segura (2006), this is to be expected due to the particle diameter with respect to the Kolmogorov length scale being similar, albeit smaller. Particles show a slow response to the turbulent eddies in these region, which damps their associated turbulence.

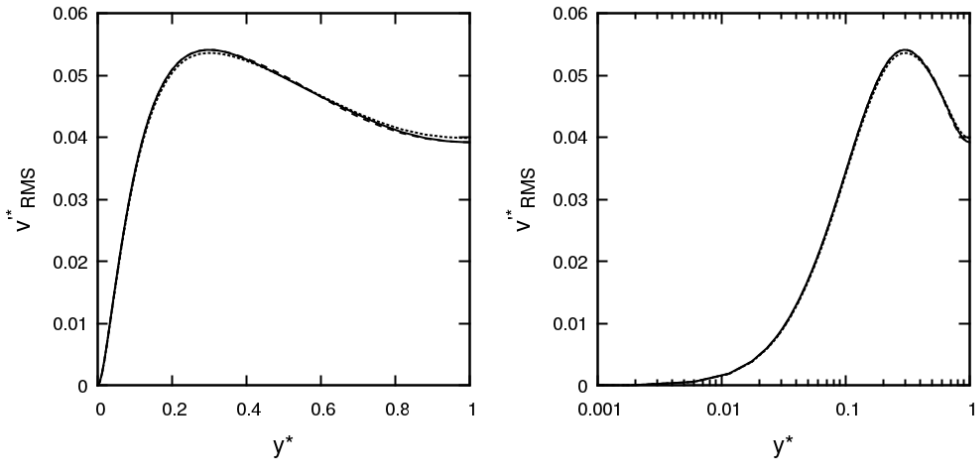

Figure 5.5: Temporal evolution of mean fluid rms wall-normal velocity fluctuations profile at $t^* = 0$ (solid), $t^* = 50$ (dashed) and $t^* = 100$ (dotted) after onset of two-way coupling in $St^+ \approx 0.1$ flow. Right plot is on a log scale.

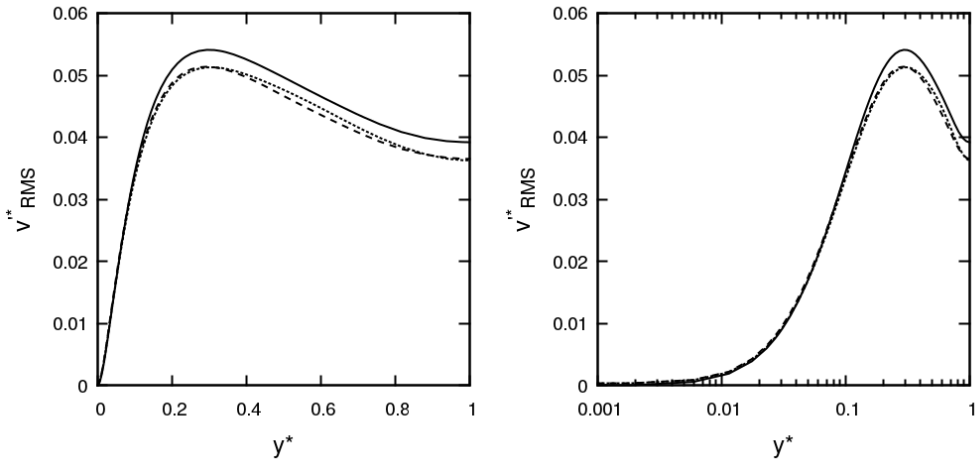

Figure 5.6: Temporal evolution of mean fluid rms wall-normal velocity fluctuations profile at $t^* = 0$ (solid), $t^* = 50$ (dashed) and $t^* = 100$ (dotted) after onset of two-way coupling in $St^+ \approx 92$ flow. Right plot is on a log scale.

Figure 5.5 and Figure 5.6 illustrate the same quantity, this time in the wall-normal direction. The same trend is observed, in that particles at low Stokes number have minimal effect on the fluid, whilst particles of increased Stokes number attenuate the turbulence. This time, the greatest attenuation is exhibited in the bulk flow region, with negligible effects occurring close to the wall. Most of the transition occurs during the first $t^* < 50$, with only slight changes occurring thereafter.

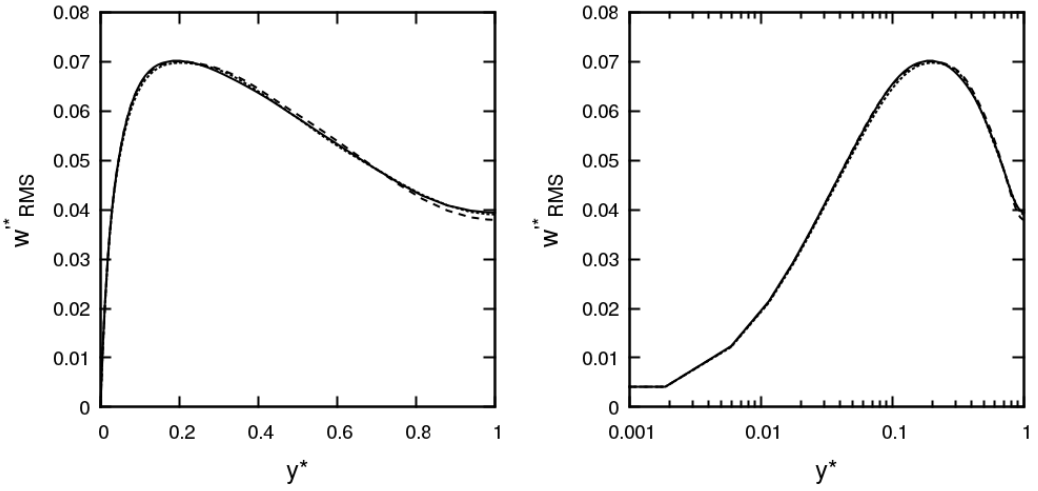

Figure 5.7: Temporal evolution of mean fluid rms spanwise velocity fluctuations profile at $t^* = 0$ (solid), $t^* = 50$ (dashed) and $t^* = 100$ (dotted) after onset of two-way coupling in $St^+ \approx 0.1$ flow. Right plot is on a log scale.

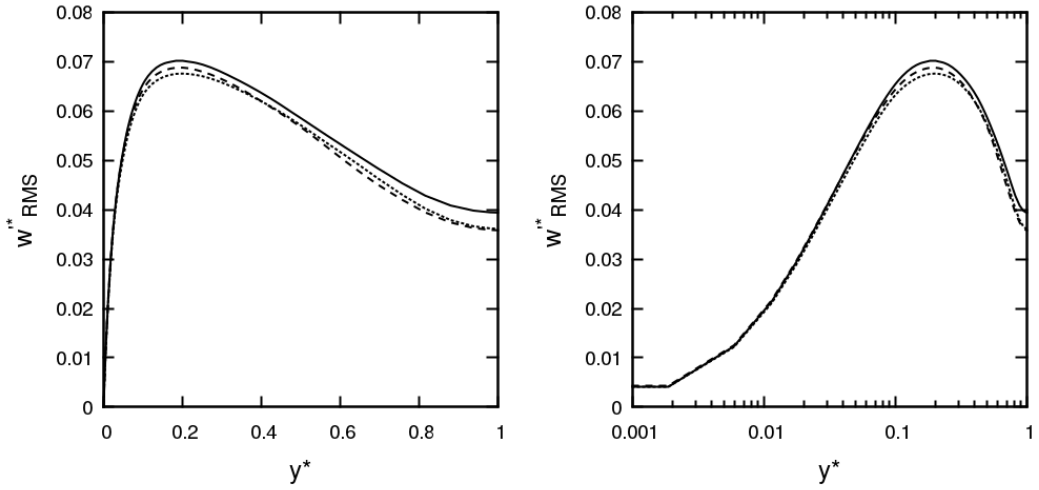

Figure 5.8: Temporal evolution of mean fluid rms spanwise velocity fluctuations profile at $t^* = 0$ (solid), $t^* = 50$ (dashed) and $t^* = 100$ (dotted) after onset of two-way coupling in $St^+ \approx 92$ flow. Right plot is on a log scale.

A similar trend is observed in the spanwise components, which are presented in Figure 5.7 and Figure 5.8. In both cases, inertial particles are unable to quickly adjust to deviations of the velocity field and produce a delay, attenuating the turbulence intensities.

Similar studies on the temporal development of key turbulence properties have been performed in isotropic turbulence for (Druzhinin, 2001) for microparticles ($\tau_P^* \ll \tau_K^*$) and those with finite inertia ($\tau_P^* \approx \tau_K^*$), where τ_K^* is the Kolmogorov time scale in bulk units, calculated using $\tau_K^* = (Re_B \epsilon^*)^{-\frac{1}{2}}$. For information, the time scale ratios τ_P^*/τ_K^* of the glass-air and glass-water systems are, respectively, 132 and 0.17. It was observed in that study that as the inertia was increased particles cause a reduction the turbulent kinetic energy (TKE) of the fluid over the course of the simulation, for particles with diameters below the Kolmogorov scale, in agreement with which we observe. Other studies for very inertial particles were carried out by Boivin et al. (1998) and indicated mechanisms by which particles increasingly dissipate TKE at high mass loadings.

5.2.2 Effect of two-way coupling and Stokes number on turbulence statistics

In this subsection we shall compare both the low and high density ratio two-way coupled flows with the unladen flow, focusing on the modification of turbulence statistics due to Stokes number. It is important to underline that the only difference between these two simulations is the density ratio, and so the comparison is equivalent to examining the turbulence statistics of identical glass particles dispersed in both water ($St^+ = 0.1$) and air ($St^+ = 92$).

Figure 5.9 compares the mean streamwise velocity for each system at a statistically settled state ($t^* = 150$). It is clear here that the particles in water ($St^+ = 0.1$) have very little effect on the profile, whereas identical particles in air ($St^+ = 92$) cause a reduction in the region of $0.08 \leq y^* \leq 1$ which is largest around $y^* = 0.2$. The same trend is observed for all three components of the turbulence intensities presented in Figure 5.10, Figure 5.11 and Figure 5.12. In summary, low density ratio particles act as tracers, closely following the fluid streamlines and experiencing very low forces due to low slip velocities. This means that the momentum feedback is also very low and so the laden flow statistics are unchanged. Conversely, particles in air are inertial due to the high density ratio, and so with greater slip velocities these particles exhibit a strong momentum coupling with the fluid. Further to this, the particle length scale is very close to the

Kolmogorov length scale and when interacting with turbulent eddies of similar size their energy is dampened, reducing the turbulence intensity.

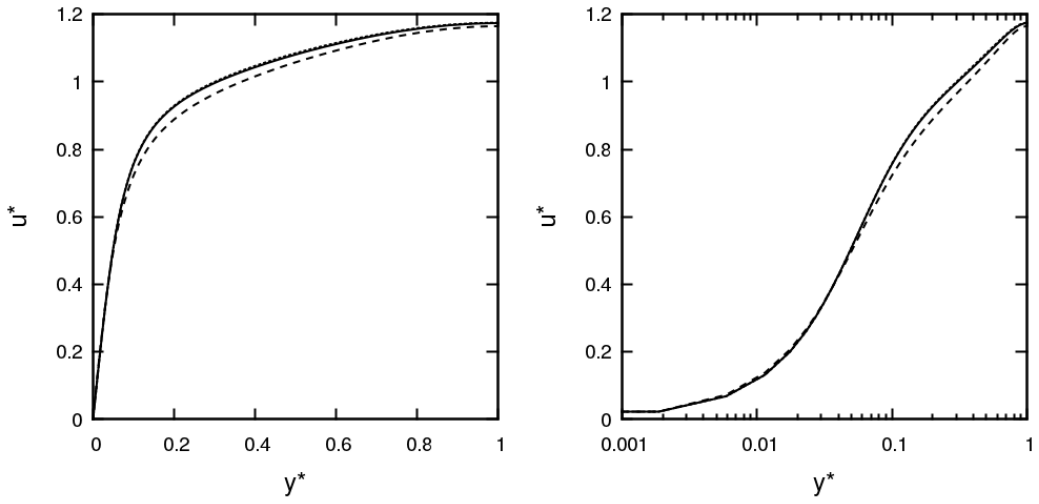

Figure 5.9: Effect of Stokes number on the two-way coupled mean streamwise fluid velocity profile at $t^* = 150$. Solid: unladen flow; dashed: $St^+ \approx 92$; dotted: $St^+ \approx 0.1$. Right plot is on a log scale.

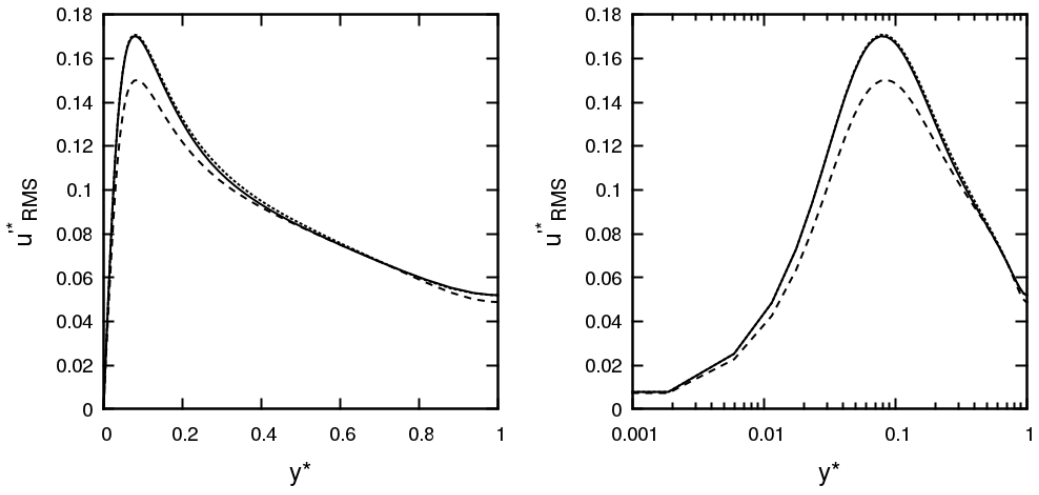

Figure 5.10: Effect of Stokes number on the two-way coupled mean fluid rms streamwise velocity fluctuations profile at $t^* = 150$. Solid: unladen flow; dashed: $St^+ \approx 92$; dotted: $St^+ \approx 0.1$. Right plot is on a log scale.

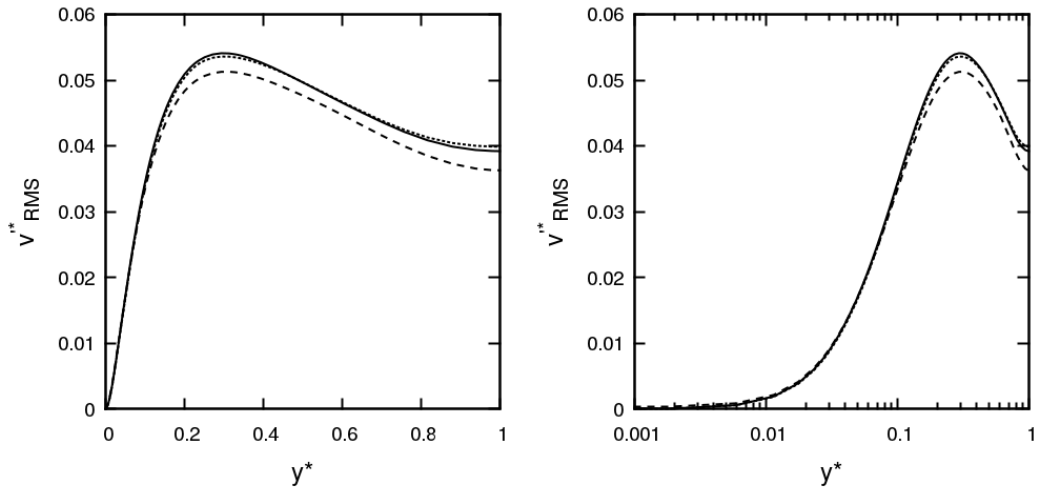

Figure 5.11: Effect of Stokes number on the two-way coupled mean fluid rms wall-normal velocity fluctuations profile at $t^* = 150$. Solid: unladen flow; dashed: $St^+ \approx 92$; dotted: $St^+ \approx 0.1$. Right plot is on a log scale.

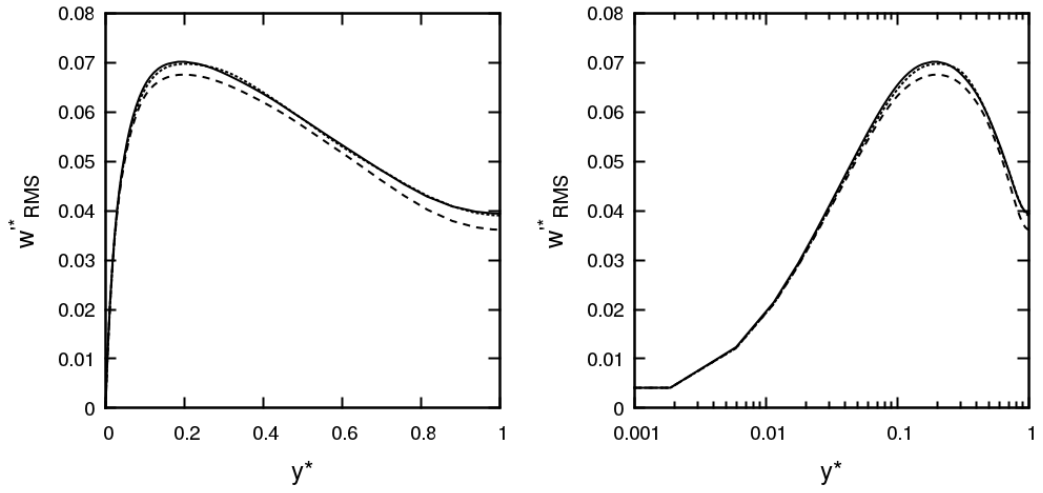

Figure 5.12: Effect of Stokes number on the two-way coupled mean fluid rms spanwise velocity fluctuations profile at $t^* = 150$. Solid: unladen flow; dashed: $St^+ \approx 92$; dotted: $St^+ \approx 0.1$. Right plot is on a log scale.

Similar studies (Kulick et al., 1994; Paris, 2001) both predict turbulence attenuation for particles with large Stokes numbers, which is greatest at the channel centreline. Kussin and Sommerfeld (2002) actually predicted turbulence augmentation however the particles which caused this effect were larger than the Kolmogorov length scale, in contrast with the particles studied here. Having obtained results in agreement with other

authors, we now extend the study to determine how the modified turbulence effects the particulate trajectories.

5.2.3 Effect of two-way coupling on particle phase statistics

In this subsection we shall examine the effect of introducing two-way coupling on the particle phase statistics. As before, the time evolution of each statistic shall be presented for both the low and high Stokes number system. Once the turbulence statistics of the single-phase flow were settled, particle statistics were allowed slightly longer to settle since, particularly for the inertial particles, they must now respond to the changes in the flow field.

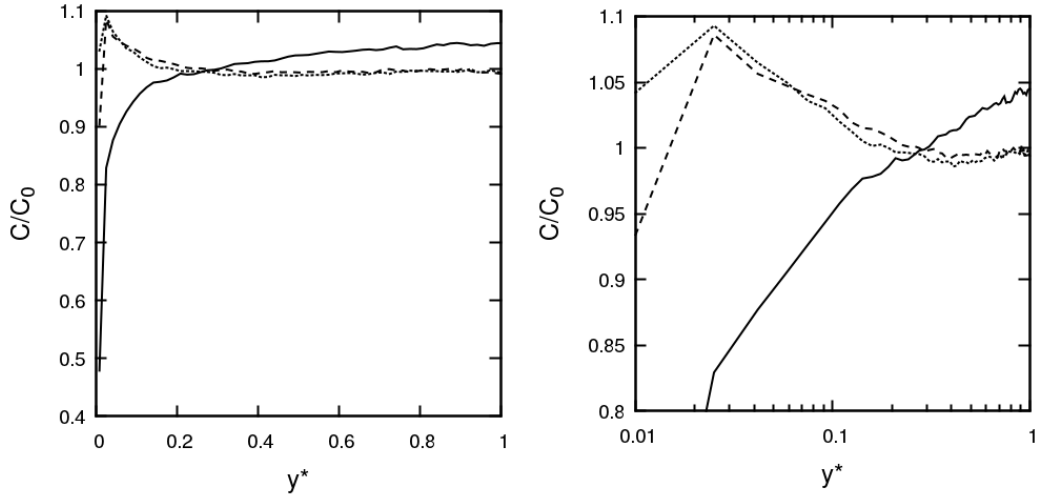

Figure 5.13: Temporal evolution of particle concentration profile at $t^* = 0$ (solid), $t^* = 50$ (dashed) and $t^* = 100$ (dotted) after onset of two-way coupling in $St^+ \approx 0.1$ flow. Right plot is on a log scale.

Figure 5.13 and Figure 5.14 illustrate the time evolution of the particle concentration profile with t^* (non-dimensional time units) after the onset of two-way coupling. The particles in water exhibit the same eventual state as they did in the one-way coupled system, where there is a slight peak in concentration in the viscous sublayer around $y^* = 0.025$, which soon falls off as the wall is approached. This is likely due to nature of the tracer-like particles. Since they follow the fluid streamlines very closely, and wall-normal rms velocity fluctuations are very small in this region, there are unlikely to be events where particles are travelling towards the wall beyond this point. This is in agreement

with Figure 4.23 which demonstrated no wall collisions for the particle trajectories studied.

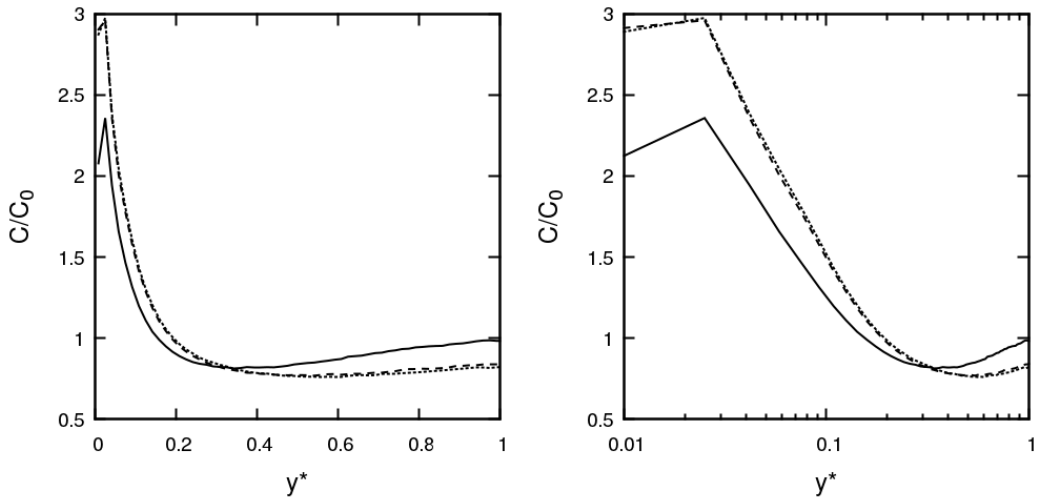

Figure 5.14: Temporal evolution of particle concentration profile at $t^* = 0$ (solid), $t^* = 50$ (dashed) and $t^* = 100$ (dotted) after onset of two-way coupling in $St^+ \approx 92$ flow. Right plot is on a log scale.

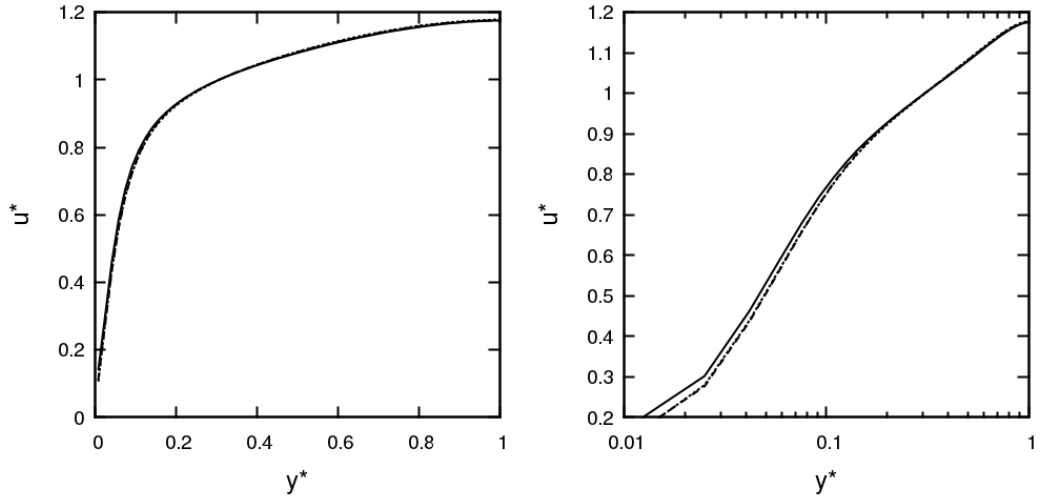

Figure 5.15: Temporal evolution of mean particle streamwise velocity profile at $t^* = 0$ (solid), $t^* = 50$ (dashed) and $t^* = 100$ (dotted) after onset of two-way coupling in $St^+ \approx 0.1$ flow. Right plot is on a log scale.

The inertial particles in Figure 5.14 exhibit an increase in the near-wall concentration before settling after $t^* > 100$. The fact that the concentration profile settles during this time period is significant, because turbophoresis should promote a slow increase in

concentration over time, as was observed in the one-way coupled system (Figure 4.18). This implies that the addition of two-way coupling creates a mechanism to limit the concentration of particles at the wall, which shall be investigated further later on in the analysis.

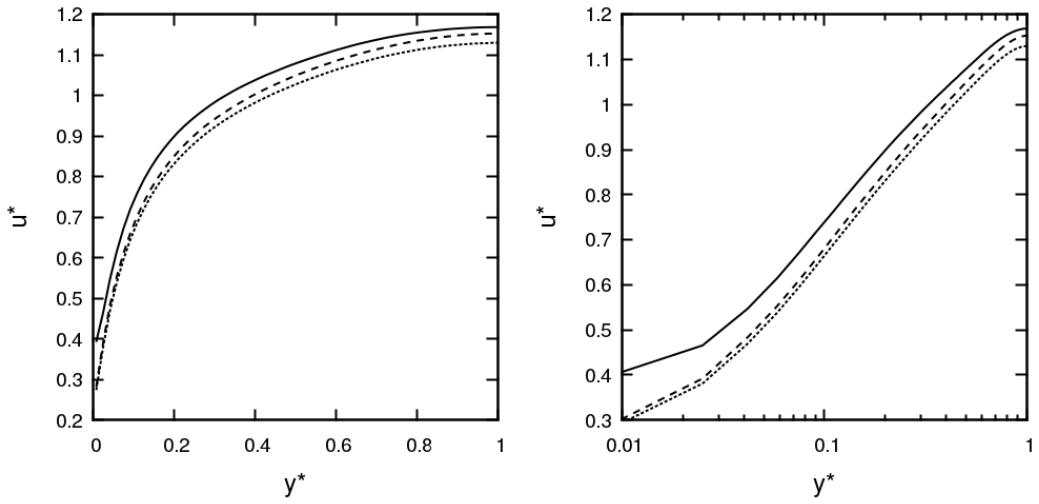

Figure 5.16: Temporal evolution of mean particle streamwise velocity profile at $t^* = 0$ (solid), $t^* = 50$ (dashed) and $t^* = 100$ (dotted) after onset of two-way coupling in $St^+ \approx 92$ flow. Right plot is on a log scale.

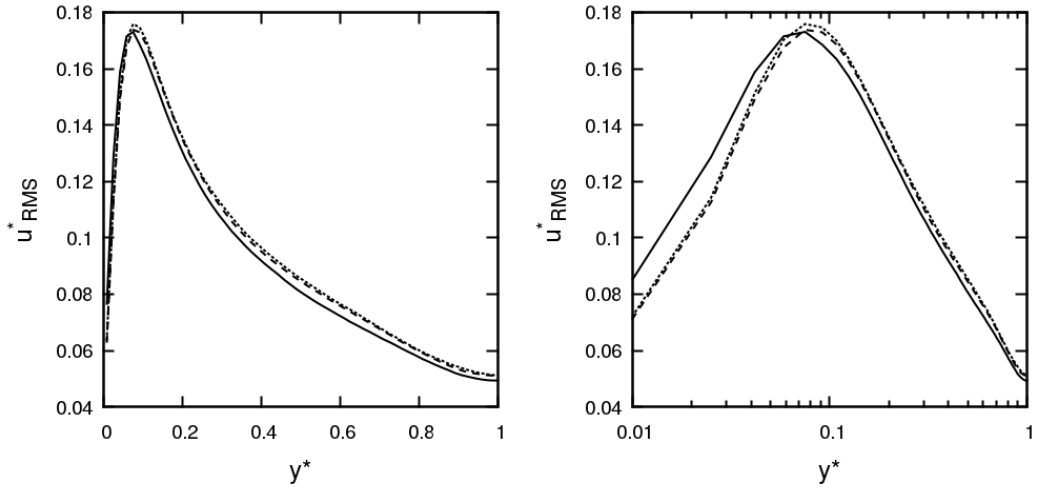

Figure 5.17: Temporal evolution of mean particle rms streamwise velocity fluctuations profile at $t^* = 0$ (solid), $t^* = 50$ (dashed) and $t^* = 100$ (dotted) after onset of two-way coupling in $St^+ \approx 0.1$ flow. Right plot is on a log scale.

Figure 5.15 and Figure 5.16 illustrate the time evolution of the particle mean streamwise velocity over time. In water, there is very little effect other than a slight decrease in velocity very close to the wall. This is likely due to the particles adjusting to match the streamwise velocity in this region. The inertial particles exhibit a much greater response, and show a homogeneous decrease in all regions, lagging behind the fluid. This decorrelation with the local fluid mean velocity explains the momentum coupling effect on the mean streamwise fluid velocity profile in Figure 5.2.

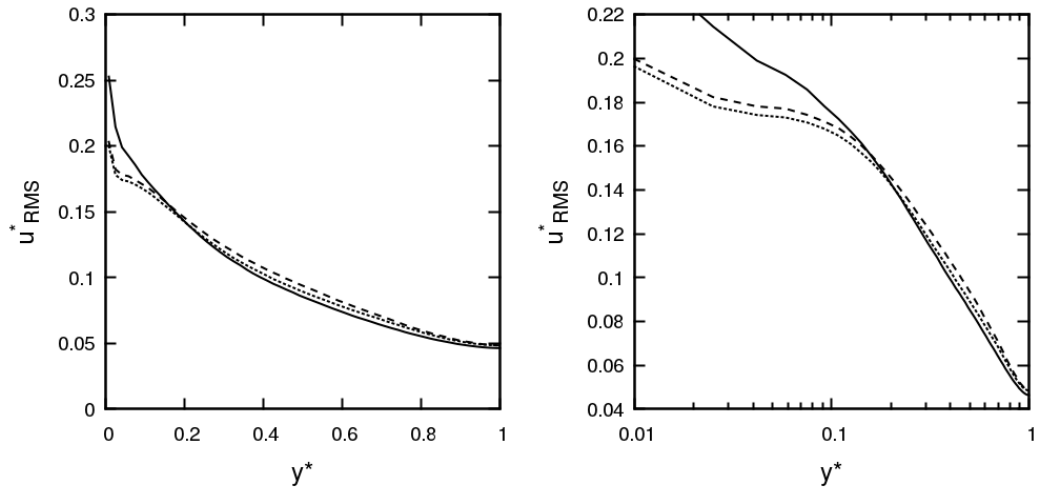

Figure 5.18: Temporal evolution of mean particle rms streamwise velocity fluctuations profile at $t^* = 0$ (solid), $t^* = 50$ (dashed) and $t^* = 100$ (dotted) after onset of two-way coupling in $St^+ \approx 92$ flow. Right plot is on a log scale.

Figure 5.17 and Figure 5.18 consider the time evolution of the mean particle streamwise rms velocity fluctuations. In water, there is a very slight reduction in the turbulent region and increase in the outer layer, taking place over the first $t^* < 50$ which quickly settles. This is likely due to the particles readjusting to minor fluctuations in the fluid field due to the onset of two-way coupling. An observation is that the onset of two-way coupling seems to shift the peak closer to the channel centreline slightly, meaning the particles are seeing the same turbulence field, but spatially translated by a small amount.

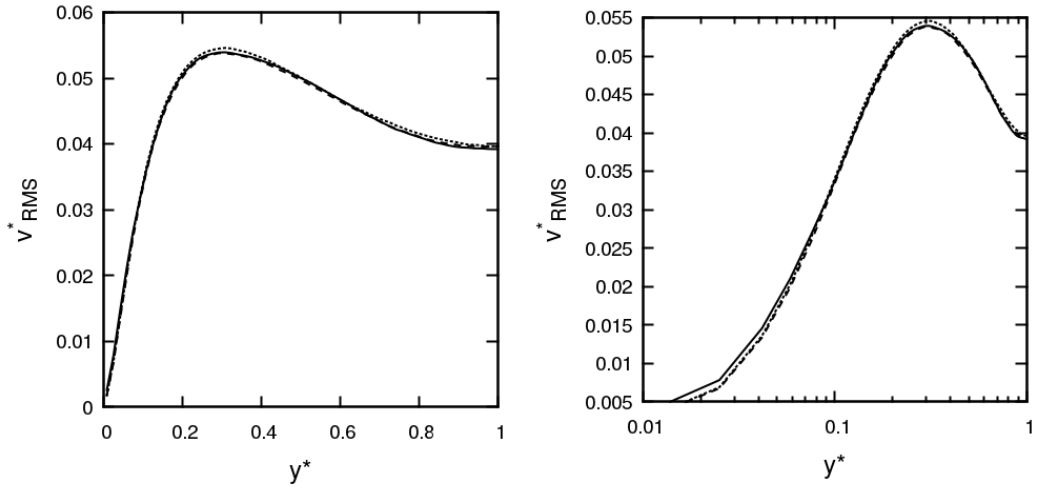

Figure 5.19: Temporal evolution of mean particle rms wall-normal velocity fluctuations profile at $t^* = 0$ (solid), $t^* = 50$ (dashed) and $t^* = 100$ (dotted) after onset of two-way coupling in $St^+ \approx 0.1$ flow. Right plot is on a log scale.

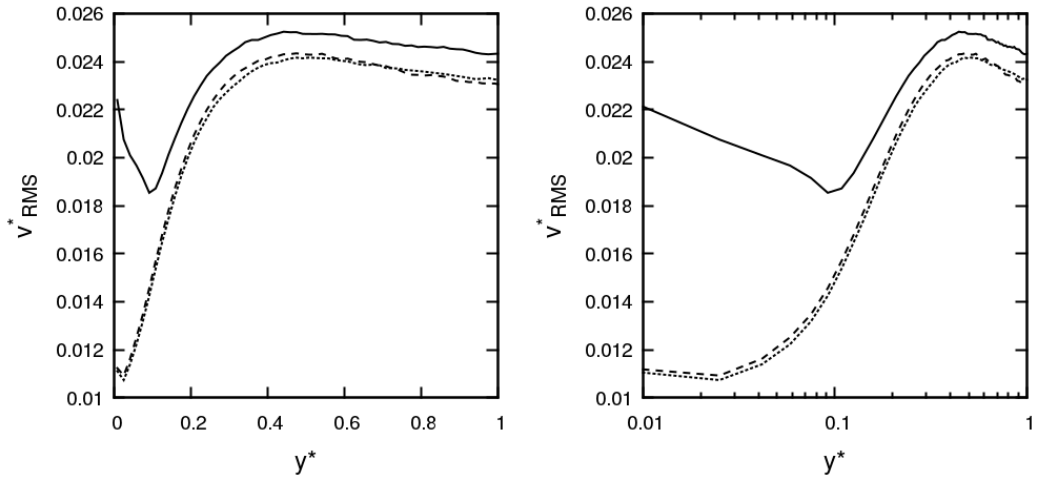

Figure 5.20: Temporal evolution of mean particle rms wall-normal velocity fluctuations profile at $t^* = 0$ (solid), $t^* = 50$ (dashed) and $t^* = 100$ (dotted) after onset of two-way coupling in $St^+ \approx 92$ flow. Right plot is on a log scale.

The inertial particles behave similarly but to a greater extent. In the bulk flow region, the turbulence they exhibit is slightly increased whereas close to the wall their streamwise rms velocity fluctuations are attenuated, similar to the fluid phase.

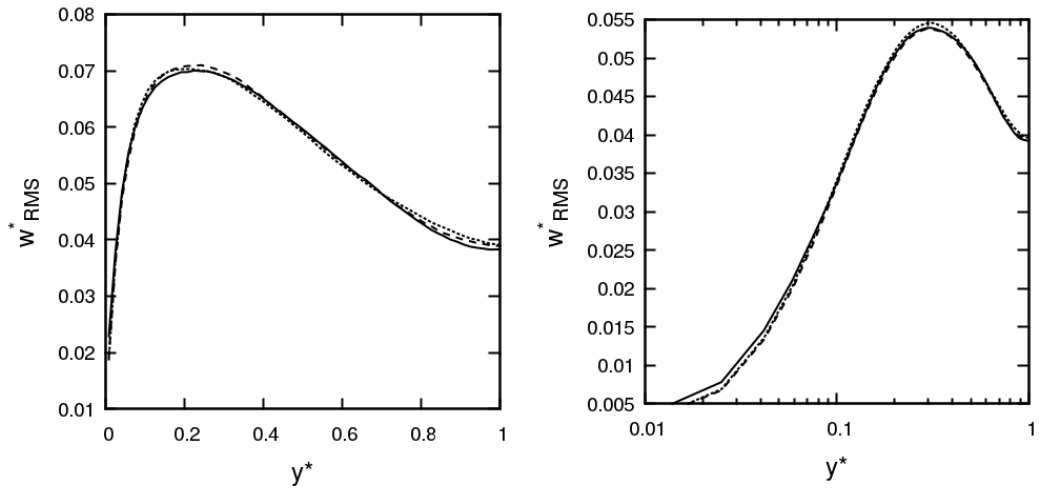

Figure 5.21: Temporal evolution of mean particle rms spanwise velocity fluctuations profile at $t^* = 0$ (solid), $t^* = 50$ (dashed) and $t^* = 100$ (dotted) after onset of two-way coupling in $St^+ \approx 0.1$ flow. Right plot is on a log scale.

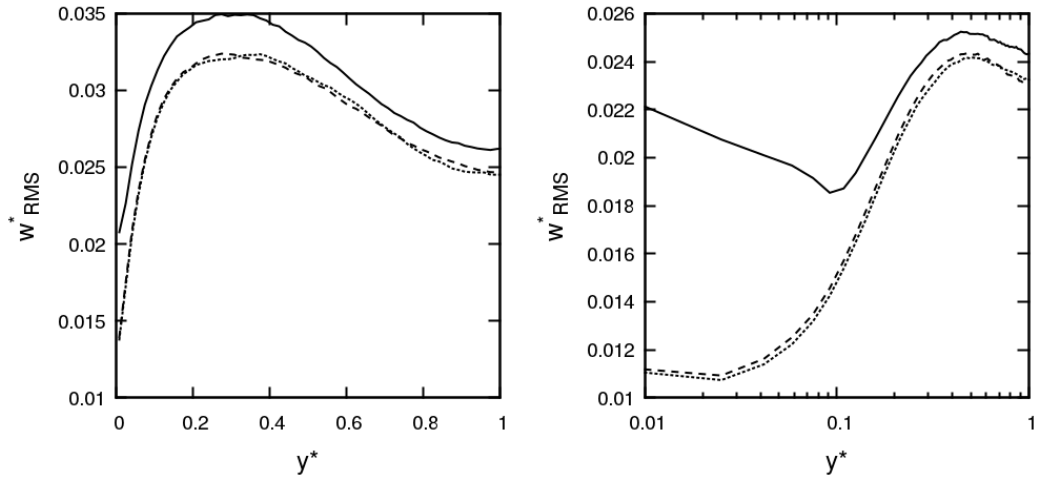

Figure 5.22: Temporal evolution of mean particle rms spanwise velocity fluctuations profile at $t^* = 0$ (solid), $t^* = 50$ (dashed) and $t^* = 100$ (dotted) after onset of two-way coupling in $St^+ \approx 92$ flow. Right plot is on a log scale.

The wall-normal and spanwise rms velocity fluctuations for both systems are presented in Figure 5.19, Figure 5.20, Figure 5.21 and Figure 5.22. The particles in water all exhibit very small deviations in these quantities due to the onset of two-way coupling, whereas the inertial particles (in air) exhibit attenuation, which is greatly emphasized in the turbulent region, $y^* < 0.1$.

An interesting observation is that in water, despite the fluid barely responding to two-way coupling, the particles seem to show a different behaviour. An explanation for this is that, since the particles are approximately the same length as the Kolmogorov scale, their initial response to the eddies present in turbulent regions is similar to that in air.

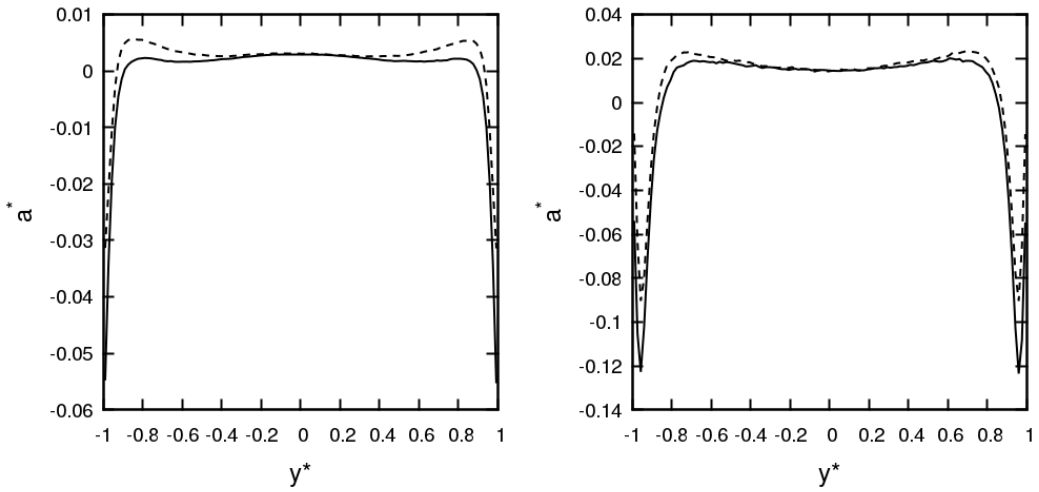

Figure 5.23: Effect of two-way coupling on the acceleration due to streamwise drag force for $St^+ \approx 92$ flow (left) and $St^+ \approx 0.1$ flow (right). Solid: unladen flow; dashed: particle-laden flow.

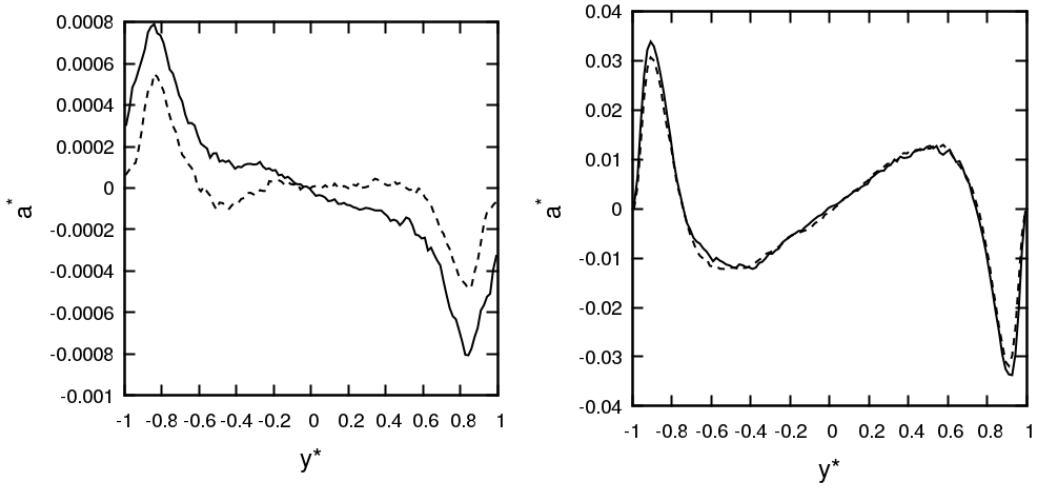

Figure 5.24: Effect of two-way coupling on the acceleration due to wall-normal drag force for $St^+ \approx 92$ flow (left) and $St^+ \approx 0.1$ flow (right). Solid: unladen flow; dashed: particle-laden flow.

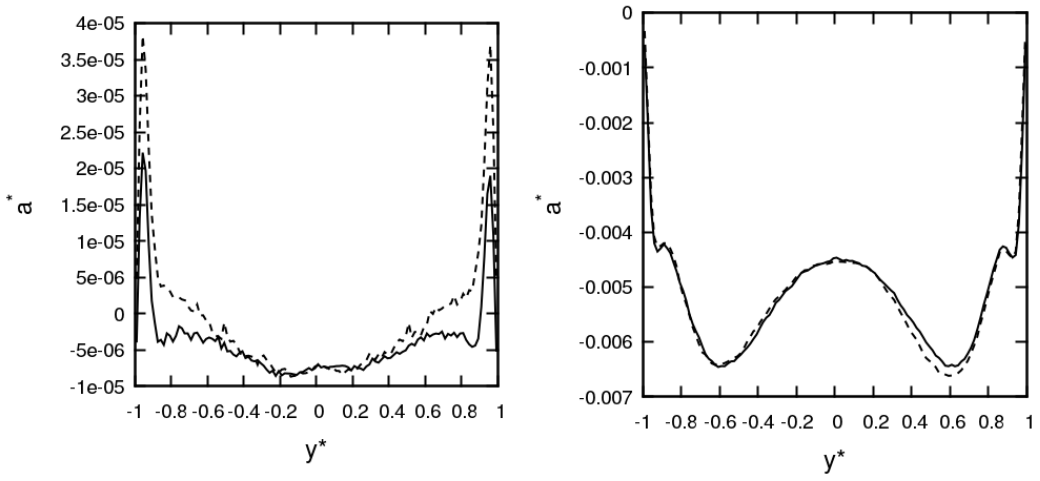

Figure 5.25: Effect of two-way coupling on the acceleration due to streamwise lift force for $St^+ \approx 92$ flow (left) and $St^+ \approx 0.1$ flow (right). Solid: unladen flow; dashed: particle-laden flow.

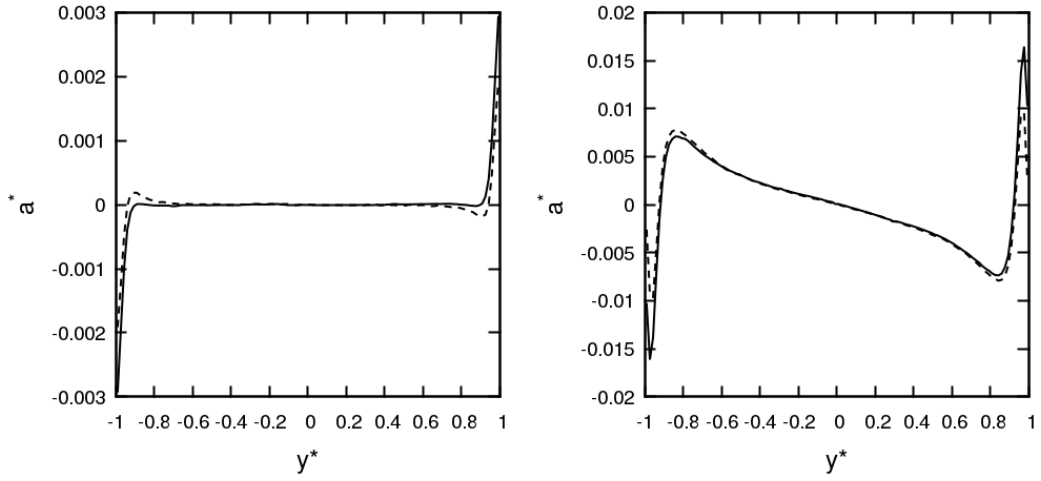

Figure 5.26: Effect of two-way coupling on the acceleration due to wall-normal lift force for $St^+ \approx 92$ flow (left) and $St^+ \approx 0.1$ flow (right). Solid: unladen flow; dashed: particle-laden flow.

The nature of the momentum coupling term in the Navier-Stokes equations is such that it relates directly back to the calculated acceleration of each particle, a^*, therefore it is natural to consider the deviations in these terms due to the onset of two-way coupling. In all cases, the spanwise contributions average out to zero, due to the symmetry of that direction, and so only streamwise and wall-normal contributions shall be considered.

Figure 5.23 compares the modification to the streamwise drag contribution on both systems. Here, both systems show a slight increase in the drag term between the log-law region and the bulk flow region, and a slight decrease in the magnitude of the 'slowing' drag force very close to the wall. As the most dominant forcing term, the effect of this is such that the flow will be hindered by the particles in the bulk flow region, whilst particles close to the wall will actually exert forwards momentum on the surrounding fluid close to the wall. The wall-normal drag component is compared in Figure 5.24. For the inertial particles, the onset of two-way coupling actually reduces this component homogeneously throughout the channel, whereas it remains unchanged for the low Stokes number particles. However, in air this component is very small, with most of the drag being orientated downstream, and so this change has little effect on the resulting motion of both the fluid and the particles. The streamwise acceleration due to the lift force is compared in Figure 5.25. Again, the tracer particle profile remains largely unchanged, which is a trend observed for the remaining force contributions analysed and so we shall focus the remaining discussion on the inertial particles. Despite the lift contribution being small compared to the drag force, the region where wall-orientated lift and bulk flow orientated lift act is shifted further towards the channel centreline. This has consequences for turbophoresis in that particles need only travel a shorter distance in the bulk before they are encouraged towards the wall by the lift force.

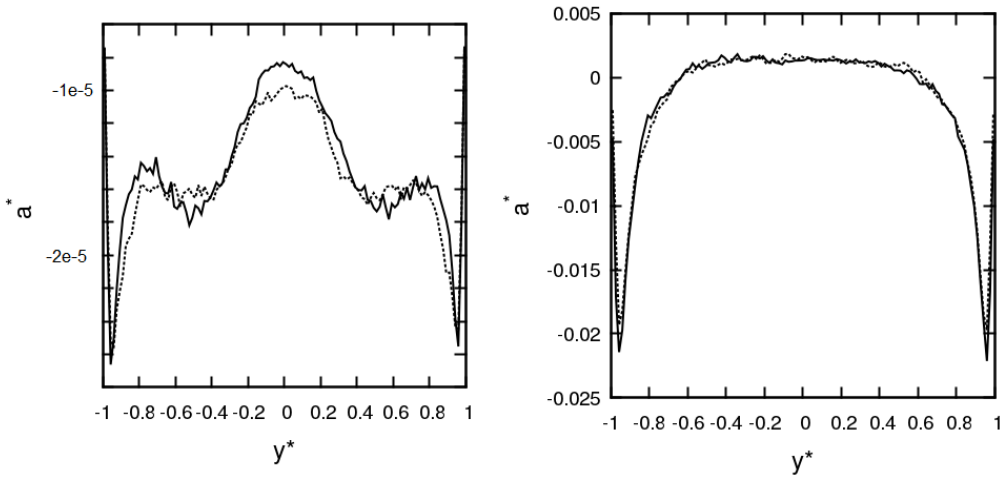

Figure 5.27: Effect of two-way coupling on the acceleration due to streamwise pressure gradient force for $St^+ \approx 92$ flow (left) and $St^+ \approx 0.1$ flow (right). Solid: unladen flow; dashed: particle-laden flow.

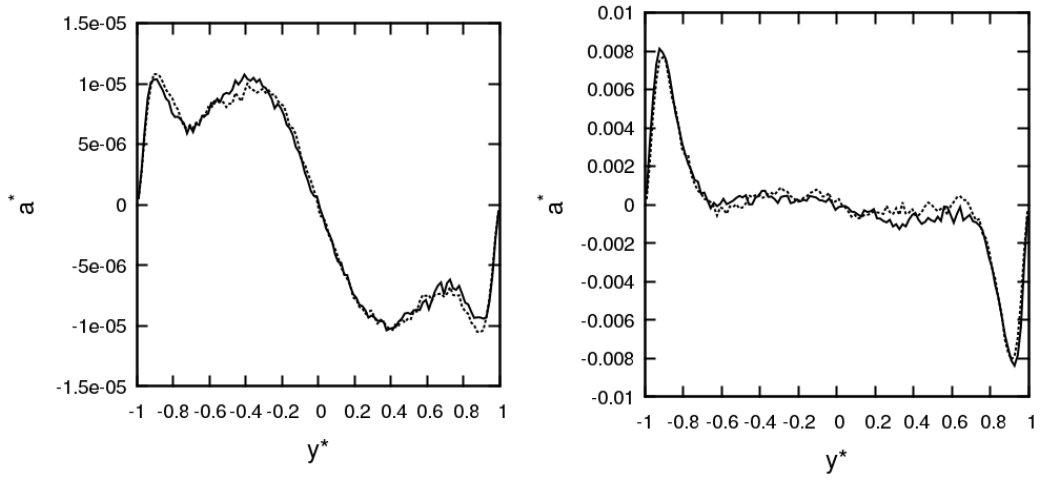

Figure 5.28: Effect of two-way coupling on the acceleration due to wall-normal pressure gradient force for $St^+ \approx 92$ flow (left) and $St^+ \approx 0.1$ flow (right). Solid: unladen flow; dashed: particle-laden flow.

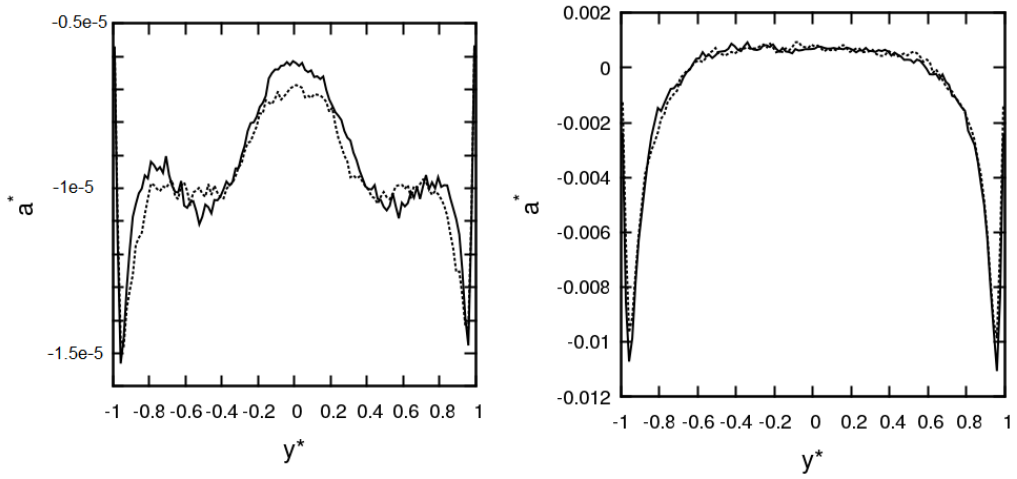

Figure 5.29: Effect of two-way coupling on the acceleration due to streamwise virtual mass force for $St^+ \approx 92$ flow (left) and $St^+ \approx 0.1$ flow (right). Solid: unladen flow; dashed: particle-laden flow.

The remaining force contributions in Figure 5.26, Figure 5.27, Figure 5.28, Figure 5.29 and Figure 5.30 are negligible compared to the drag and lift forces and are seemingly unchanged by the onset of two-way coupling in both Stokes number systems.

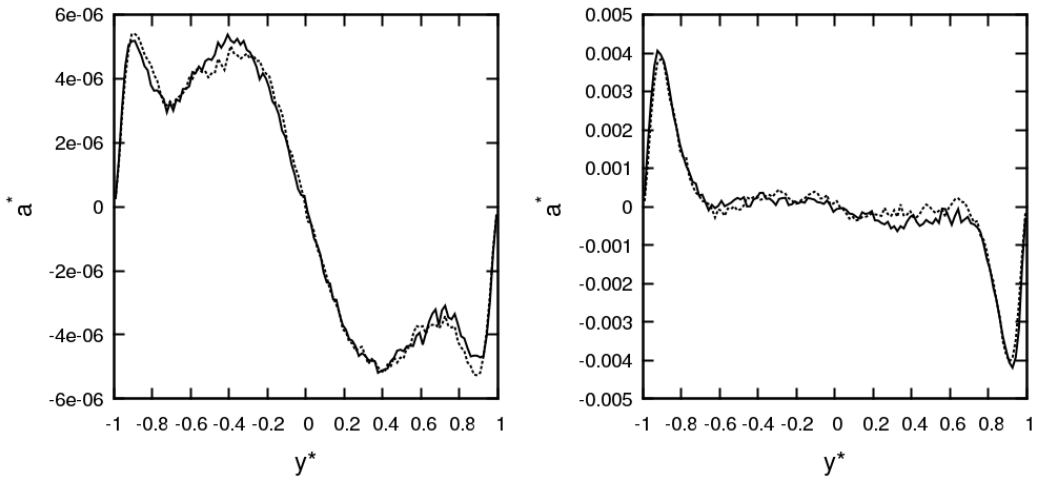

Figure 5.30: Effect of two-way coupling on the acceleration due to wall-normal virtual mass force for $St^+ \approx 92$ flow (left) and $St^+ \approx 0.1$ flow (right). Solid: unladen flow; dashed: particle-laden flow.

5.3 Four-way coupling

In a particle-fluid system of volume fraction $\Theta_P = 10^{-3}$, previous work (Elghobashi, 2007) suggests that particle-particle collisions must also be considered in the model to provide accurate simulation. This is because at this volume fraction, the collision density is large enough that the trajectorial motion of the particles will be altered significantly by post-collision rebounds. The simulations presented here were restarted from particle injection with the collision mechanism switched on, making sure no particles were overlapping at $t^* = 0$, and were run until $t^* = 150$ with statistics gathered over $100 \leq t^* \leq 150$. Throughout, elastic collisions were assumed in that the coefficient of restitution, e, was equivalent to one.

5.3.1 Effect of four-way coupling on turbulence statistics

The further modification to the fluid phase statistics due to the effects of collisions shall first be considered. Figure 5.31 compares the three coupling regimes (one-way, two-way and four-way) and their effect on the mean streamwise fluid velocity profiles for the inertial particle system ($St^+ \approx 92$). Interestingly, the onset of four-way coupling provides a slight increase in streamwise velocity in the bulk, as compared to the two-way coupled system. This will be discussed further later on when analysing collision density profiles, but the reason is likely due to increased spanwise and wall-normal motion due to

transverse interactions in the bulk flow. For the tracer-like particles in Figure 5.32 ($St^+ \approx$ 0.1), there is little difference when compared with the one- and two-way coupled system.

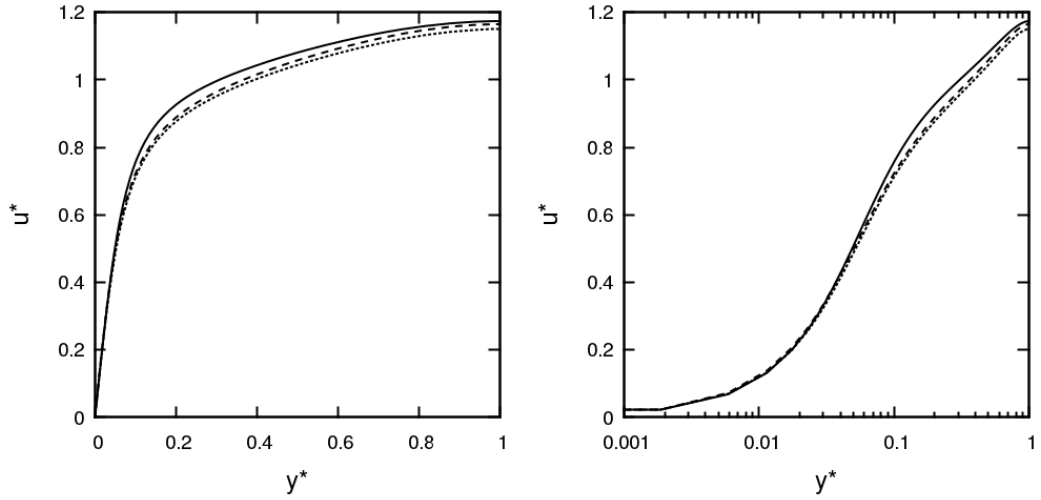

Figure 5.31: Effect of coupling on the $St^+ \approx 92$ system mean streamwise fluid velocity profile at $t^* = 150$. Solid: unladen flow; dashed: two-way coupled; dotted: four-way coupled. Right plot is on a log scale.

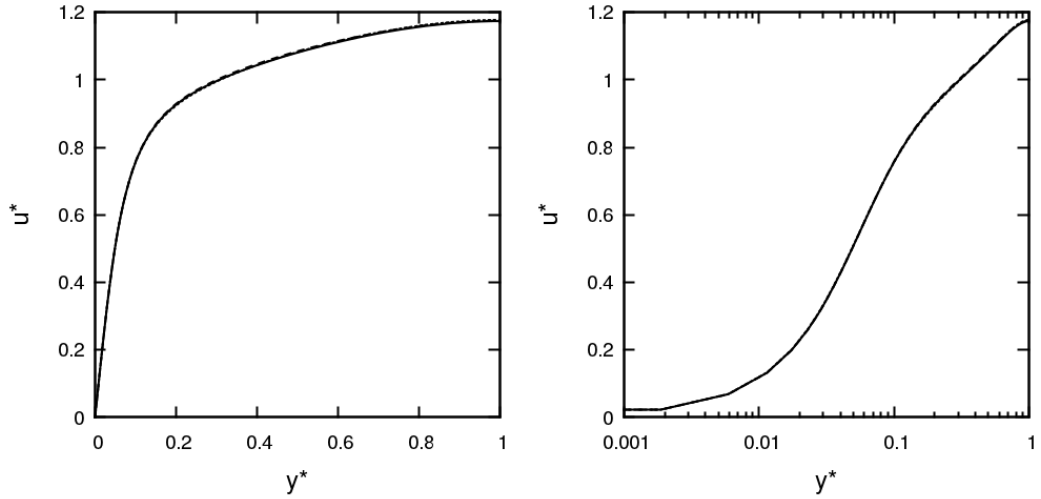

Figure 5.32: Effect of coupling on the $St^+ \approx 0.1$ system mean streamwise fluid velocity profile at $t^* = 150$. Solid: unladen flow; dashed: two-way coupled; dotted: four-way coupled. Right plot is on a log scale.

Comparisons of streamwise rms velocity fluctuations for each coupling regime are plotted in Figure 5.33 and Figure 5.34. In a similar manner to before, the inclusion of four-way coupling provides an increase in this quantity for the inertial particles. This is to be expected, since the interparticle collisions decorrelate the particles further with the local fluid velocity. As before, the inclusion of this mechanism has little effect on the $St^+ \approx 0.1$ particles. Similar observations can be made for the wall-normal and spanwise components presented in Figure 5.35 to Figure 5.38.

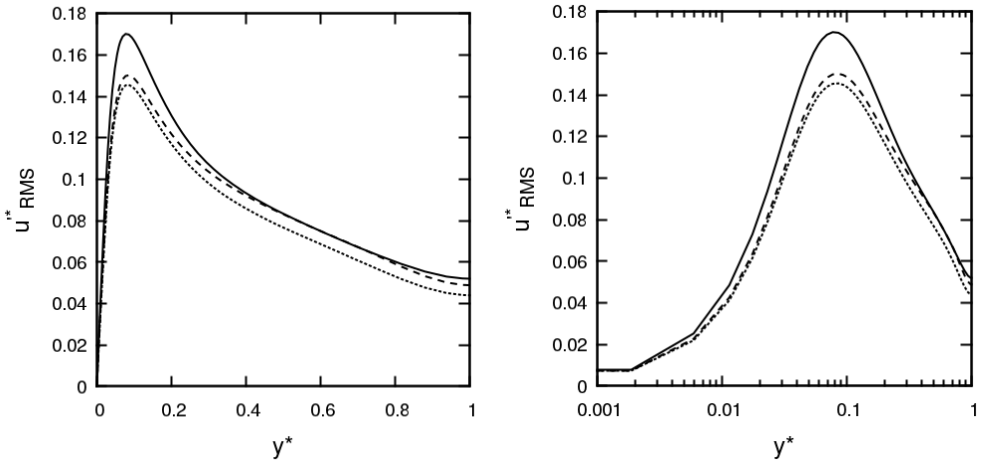

Figure 5.33: Effect of coupling on the $St^+ \approx 92$ system mean streamwise fluid rms velocity fluctuations profile at $t^* = 150$. Solid: unladen flow; dashed: two-way coupled; dotted: four-way coupled. Right plot is on a log scale.

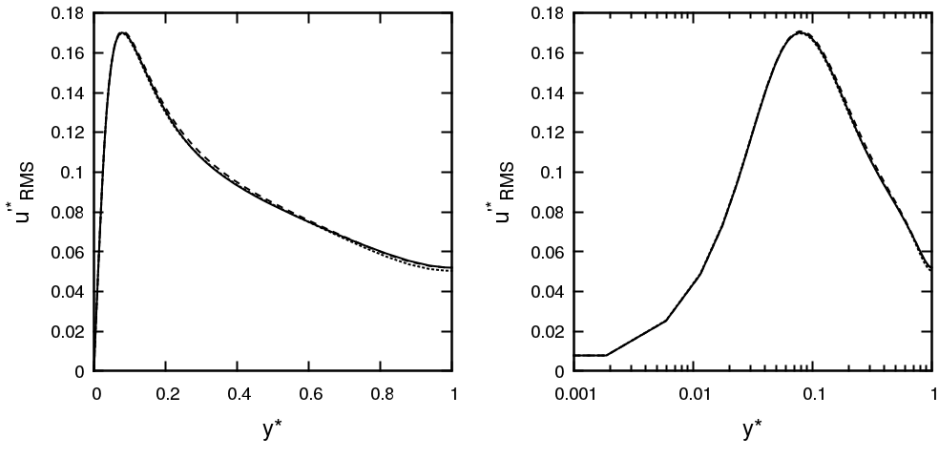

Figure 5.34: Effect of coupling on the $St^+ \approx 0.1$ system mean streamwise fluid rms velocity fluctuations profile at $t^* = 150$. Solid: unladen flow; dashed: two-way coupled; dotted: four-way coupled. Right plot is on a log scale.

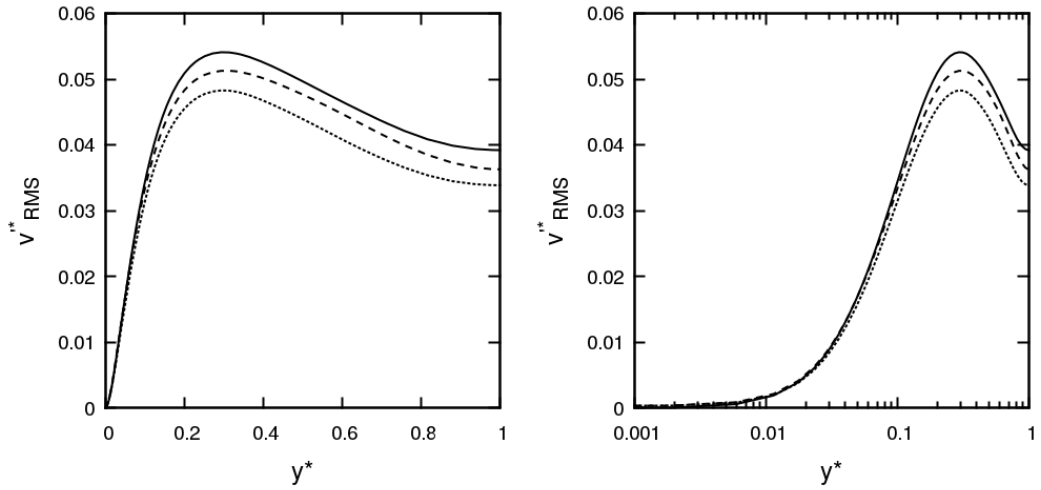

Figure 5.35: Effect of coupling on the $St^{+}\approx 92$ system mean wall-normal fluid rms velocity fluctuations profile at $t^{*}=150$. Solid: unladen flow; dashed: two-way coupled; dotted: four-way coupled. Right plot is on a log scale.

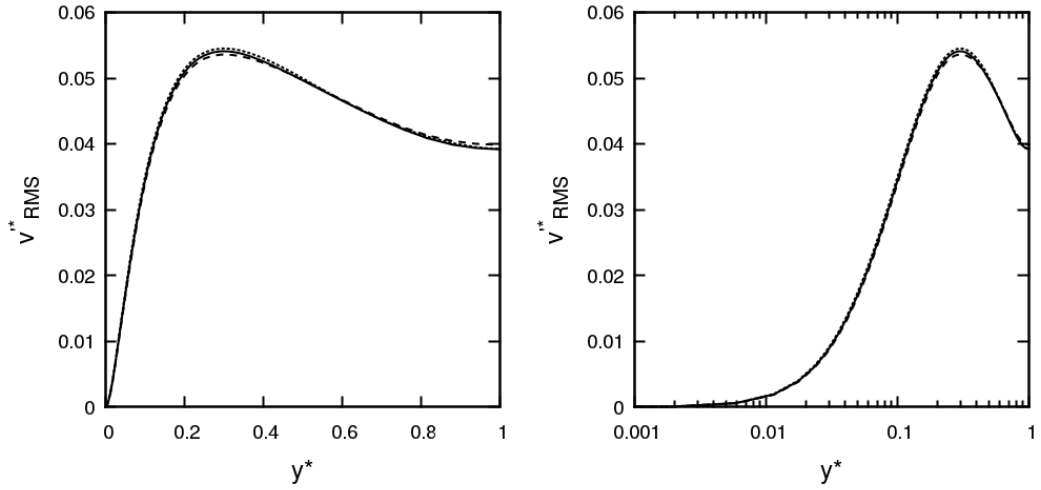

Figure 5.36: Effect of coupling on the $St^{+}\approx 0.1$ system mean wall-normal fluid rms velocity fluctuations profile at $t^{*}=150$. Solid: unladen flow; dashed: two-way coupled; dotted: four-way coupled. Right plot is on a log scale.

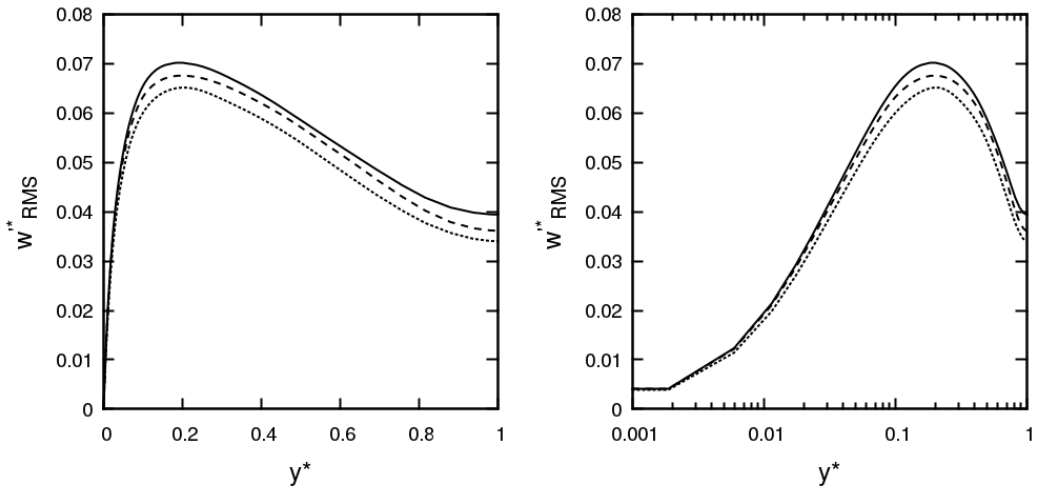

Figure 5.37: Effect of coupling on the $St^{+}\approx 92$ system mean spanwise fluid rms velocity fluctuations profile at $t^{*}=150$. Solid: unladen flow; dashed: two-way coupled; dotted: four-way coupled. Right plot is on a log scale.

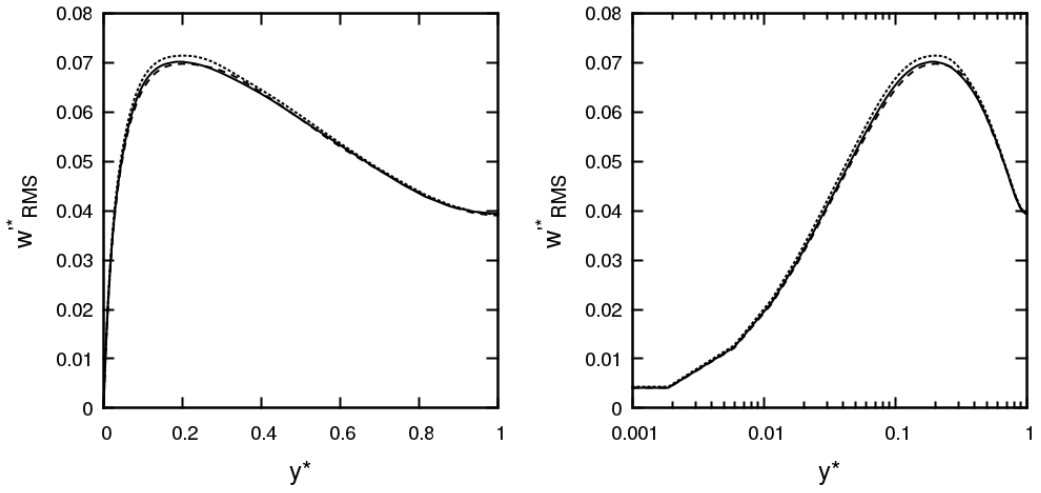

Figure 5.38: Effect of coupling on the $St^{+}\approx 0.1$ system mean spanwise fluid rms velocity fluctuations profile at $t^{*}=150$. Solid: unladen flow; dashed: two-way coupled; dotted: four-way coupled. Right plot is on a log scale.

5.3.2 Effect of Stokes number on four-way coupled particle phase statistics

This subsection compares the particle behaviour of both the glass-air ($St^{+}\approx 92$) and glass water ($St^{+}\approx 0.1$) realistic flows by analysing particle statistics from high accuracy, fully coupled simulations. Figure 5.39 compares the normalized concentration (relative to the initial concentration) profiles of both flows. Here there are substantial differences in the

overall behaviour. For the inertial particles, there is a build-up of particles both in the centre and very close to the wall ($y^*\sim0.05$), whereas in the tracer-like case, the greatest concentration is at the channel centreline and there is a falloff in concentration as the wall is approached. In the case of low Stokes number particles, the slight turbophoretic effects observed in the one- and two-way coupled flows are dampened (or at least occur at a reduced rate) by the inclusion of collisions, and particles actually migrate towards the channel centreline.

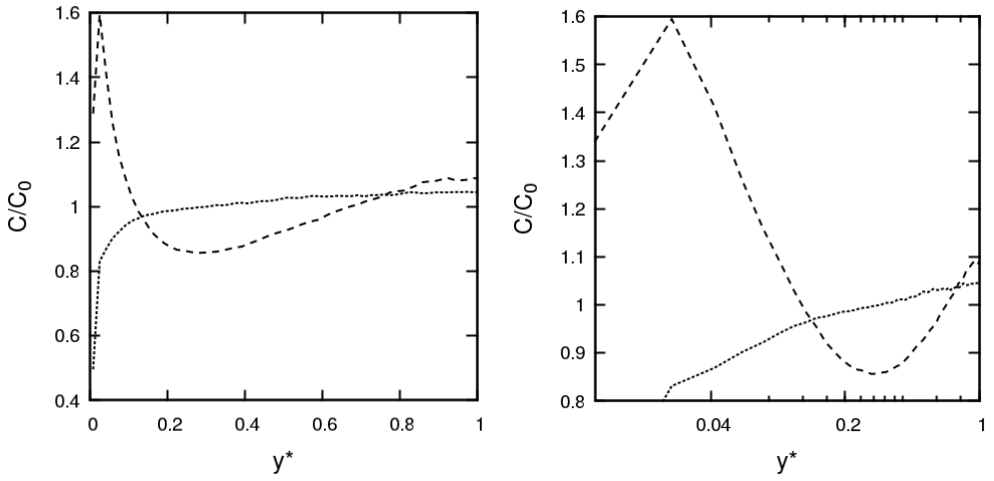

Figure 5.39: Effect of Stokes number on the four-way coupled mean particle concentration profile at $t^* = 150$. Dashed: $St^+\approx 92$; dotted: $St^+\approx 0.1$. Right plot is on a log scale.

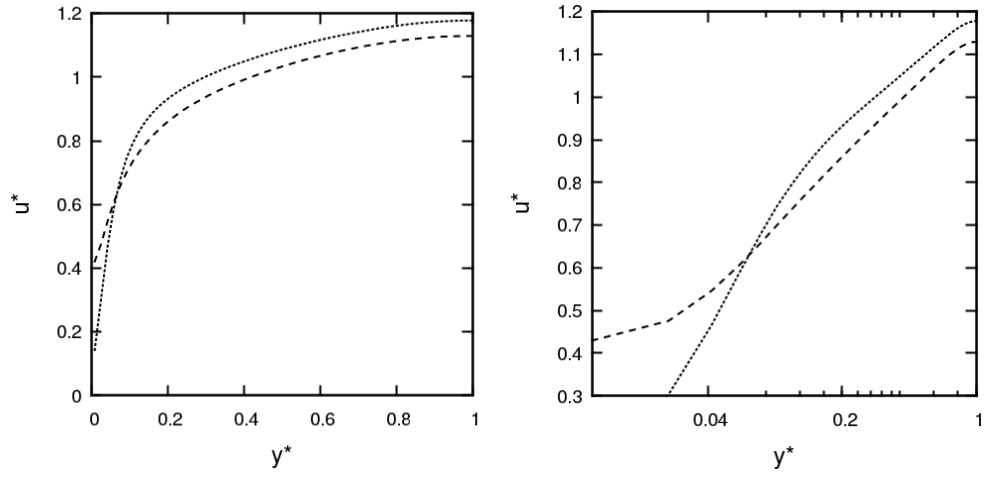

Figure 5.40: Effect of Stokes number on the four-way coupled mean particle streamwise velocity profile at $t^* = 150$. Dashed: $St^+\approx 92$; dotted: $St^+\approx 0.1$. Right plot is on a log scale.

Figure 5.40 compares the mean streamwise velocity of both flows. It is observed that particles with a low-Stokes number travel faster in the bulk flow, while inertial particles travel faster in the near-wall region. This is likely due to particles migrating from regions of high velocity in the lateral direction whilst retaining their increased speed, as was observed in the one-way coupled regime.

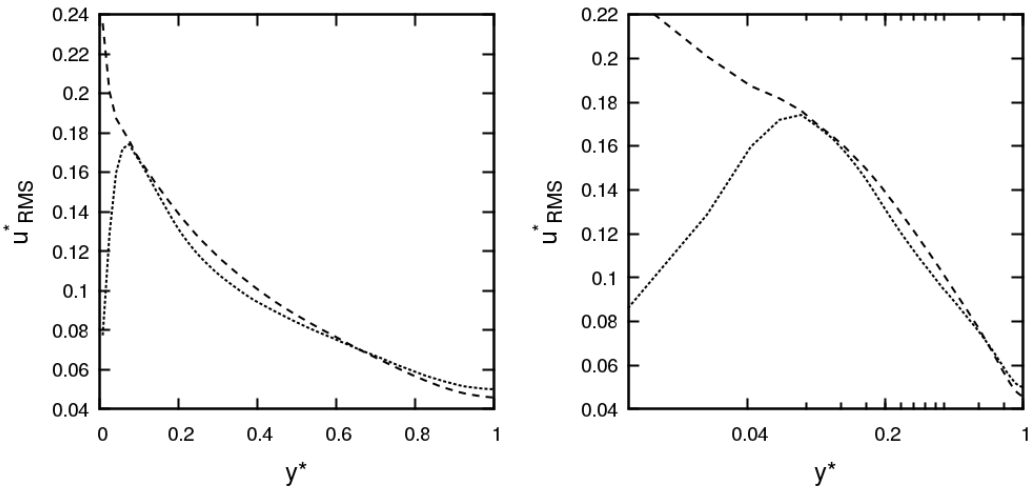

Figure 5.41: Effect of Stokes number on the four-way coupled mean particle streamwise rms velocity fluctuations profile at $t^* = 150$. Dashed: $St^+ \approx 92$; dotted: $St^+ \approx 0.1$. Right plot is on a log scale.

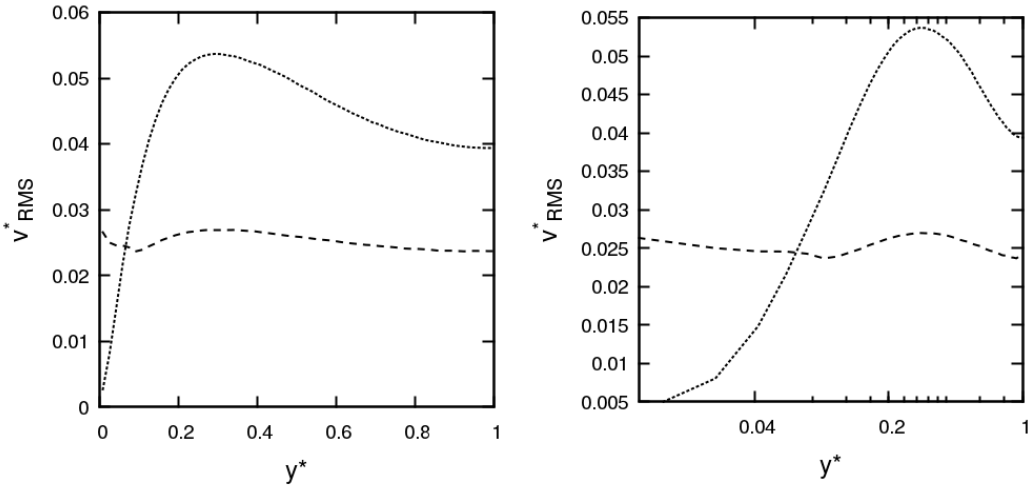

Figure 5.42: Effect of Stokes number on the four-way coupled mean particle wall-normal rms velocity fluctuations profile at $t^* = 150$. Dashed: $St^+ \approx 92$; dotted: $St^+ \approx 0.1$. Right plot is on a log scale.

This argument is also strengthened by Figure 5.41 which depicts increased streamwise rms velocity fluctuations for inertial particles in the near-wall region, implying a significant decorrelation from the local fluid velocity field. Comparing those particles with the tracer-like particles, the streamwise fluctuations are similar in the bulk of the flow. Figure 5.42 compares the wall-normal rms velocity fluctuation profiles for both systems. This time, the inertial particle behaviour differs greatly from that of the tracer-like particles. For the $St^+ \approx 92$ particles, the fluctuations are homogeneous throughout the channel, indicating that wall-normal motion is dominated by collisions. Since inertial particle concentrations are higher close to the wall, it is easy to see how frequent collisions in this region led to increased fluctuations.

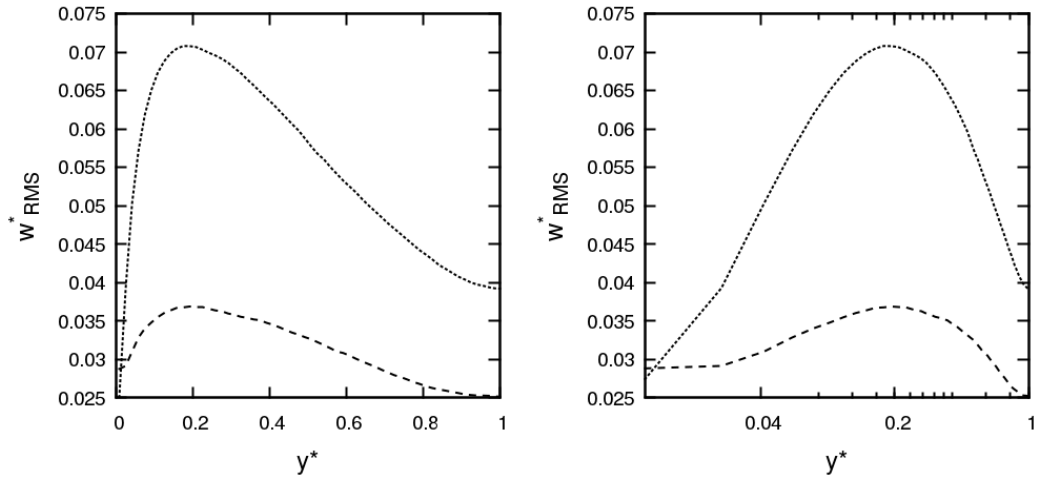

Figure 5.43: Effect of Stokes number on the four-way coupled mean particle spanwise rms velocity fluctuations profile at $t^* = 150$. Dashed: $St^+ \approx 92$; dotted: $St^+ \approx 0.1$. Right plot is on a log scale.

In Figure 5.43 we compare the spanwise rms velocity fluctuations. This time, those belonging to the inertial particles are strongly dampened when compared to the tracer-like particles, particularly in the bulk flow region. They are also homogenous and of similar magnitude to the wall-normal component. This implies that, for the inertial particle collisions, decorrelation from the local flow velocities takes place in all three dimensions, and the interactions are comparable with, and compete with, turbulence interaction for dominance over particle trajectories.

To summarise, and to draw analogies with real-world systems, high concentrations of glass particles in air appear highly decorrelated from local flow velocities, whilst on

average retaining just slightly lower than the fluid mean velocity. Systems of this kind will also exhibit increased wall-collision rates, due to the large wall-normal fluctuations in the near-wall region. Furthermore, collisions with the wall will be high-energy due to particles with increased velocities travelling towards the wall from the bulk flow region and retaining their velocity. High concentrations of glass particles in water still very closely follow the fluid streamlines, with collisions resulting in small deviations in trajectories upon which particles quickly readjust due to their low Stokes number. These systems will exhibit very few wall collisions and those which do occur will be low in energy. Concentration profiles indicate that inertial particles still undergo substantial turbophoresis, resulting in high densities of particles close to the wall, potentially promoting increased collision rates. This shall be investigated and discussed in the following subsection.

5.3.3 Particle-particle collision dynamics

In this subsection, statistics surrounding collision events were obtained in an effort to elucidate the way in which collisions occur throughout each region of the channel. In Figure 5.44, we compare the mean number of collisions occurring per timestep across the channel between $100 \leq t^* \leq 150$. Information from the inertial particle system indicates increase collision rates in the wall regions ($|y^*| > 0.8$), whilst the peak collision rate density for the tracer particles is at the channel centreline.

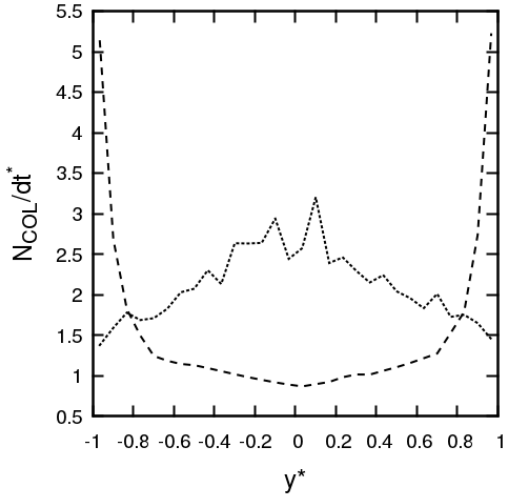

Figure 5.44: Effect of Stokes number on the four-way coupled mean collision density profile between $100 \leq t^* \leq 150$. Dashed: St^+=92; dotted: St^+= 0.1.

For the analysis presented below, collisions occurring within four distinct regions of the channel were considered. As a reminder to the reader, the four regions are: the viscous sublayer ($0 \leq y^* < 0.027$), the buffer layer ($0.027 \leq y^* < 0.166$), the log-law region ($0.166 \leq y^* \leq 0.2$) and the bulk flow region ($0.2 \leq y^* \leq 1$). These layers are mirrored about the channel centreline ($y^* = 1$).

The relative concentrations in each region are important since the local volume fraction in the near-wall region will increase for the larger Stokes number particles. This means inter-particle collisions will be more likely to affect the fluid and solid phase flow properties. Since turbophoresis encourages particles in the direction of decreasing turbulence kinetic energy, a slight increase in the bulk is observed at high Stokes number for particles remaining close to the channel centre.

Figure 5.45, Figure 5.46 and Figure 5.47 illustrate probability density functions (PDFs) of particle velocity components before a collision takes place. These were gathered after the system reached a statistically steady state, based on averaged flow properties such as those demonstrated in the validation.

Figure 5.45 (streamwise velocity of colliders) indicates that the greatest spread of collision velocities is within the buffer layer for both low and high Stokes numbers. An interesting observation is that particles with low Stokes numbers have much more well defined streamwise velocities in the viscous sublayer, whereas the range is almost doubled for highly inertial particles. This can be explained by the fact that particles at St^+=92 are highly decorrelated from the turbulence field, and so have an increased chance of inter-region migration whilst retaining their velocity. This mechanism would indeed increase the spread of velocities, particularly in the near-wall regions. On the other hand, streamwise collision velocities in the bulk are very similar.

Considering wall-normal particle velocities (Figure 5.46), the greatest spread in this quantity is in the bulk and log-law regions for low Stokes number particles, whereas collisions closer to the wall are more defined. The opposite is true for inertial particles, where the greatest spread lies within the near-wall regions. Given the increased concentration and turbulence decorrelation in this region, and increased likelihood of wall collisions due to particle inertia, this observation is unsurprising.

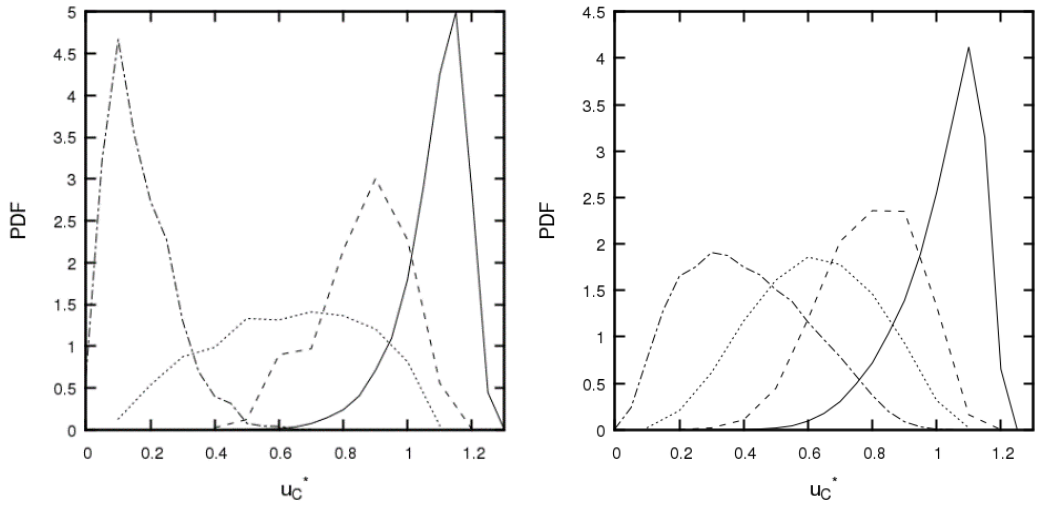

Figure 5.45: PDFs of collider streamwise velocity at $St^+ = 0.1$ (left) and $St^+ = 92$ (right). Solid line: bulk flow; dashed: log-law region; dotted: buffer layer; dot-dashed: viscous sublayer.

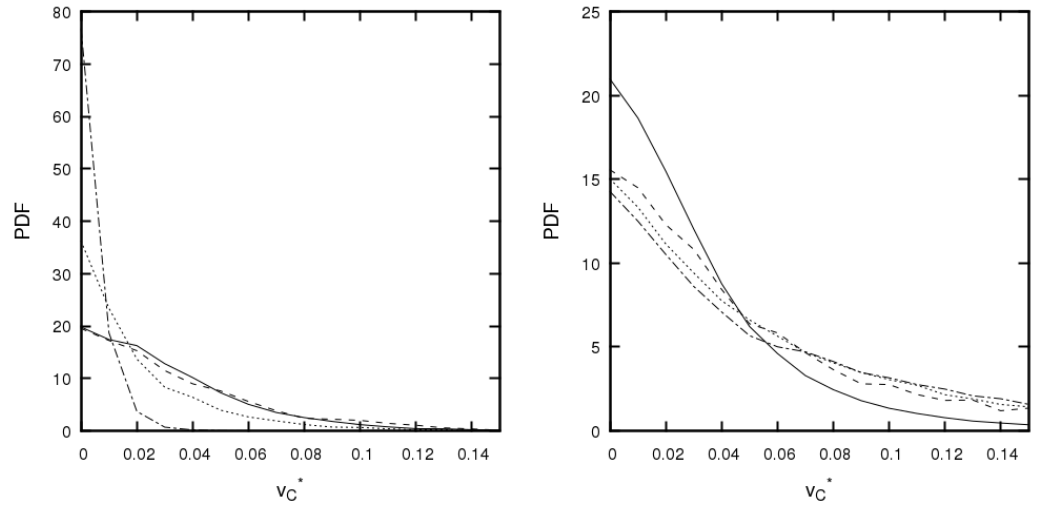

Figure 5.46: PDFs of collider wall-normal velocity at $St^+ = 0.1$ (left) and $St^+ = 92$ (right). Solid line: bulk flow; dashed: log-law region; dotted: buffer layer; dot-dashed: viscous sublayer.

Figure 5.47 shows the relative spanwise velocities between the colliding particle and that of its neighbour before the collision takes place. For the larger Stokes number, the behaviour is similar to that of the wall-normal component, whereby the three regions nearest the wall have particles colliding with a very similar distribution of velocities. Again, bulk flow collisions favour lower spanwise velocities. For low Stokes number

particles, the greatest spread of spanwise velocities is in the log-law region, whilst particles in the viscous sublayer have more well defined spanwise velocities.

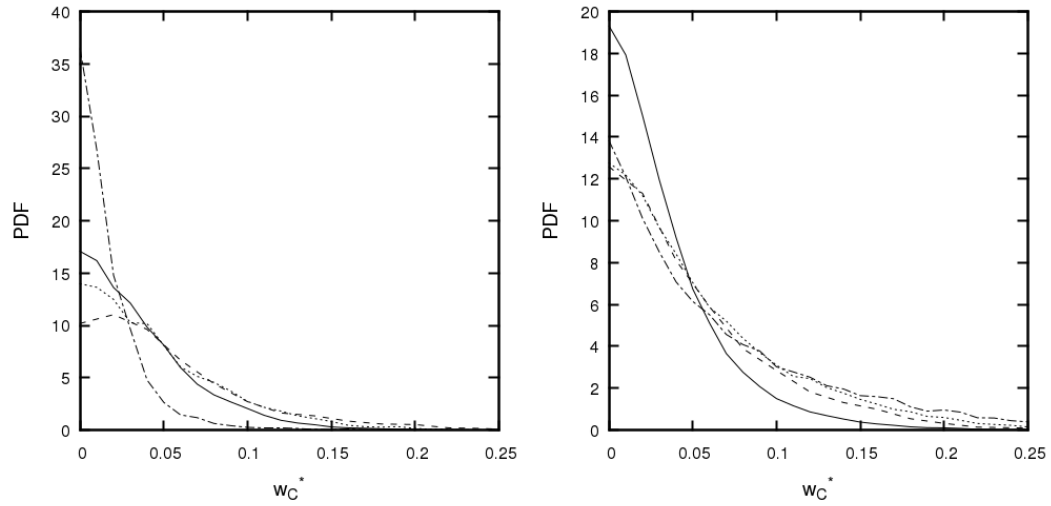

Figure 5.47: PDFs of collider spanwise velocity at $St^+ = 0.1$ (left) and $St^+ = 92$ (right). Solid line: bulk flow; dashed: log-law region; dotted: buffer layer; dot-dashed: viscous sublayer.

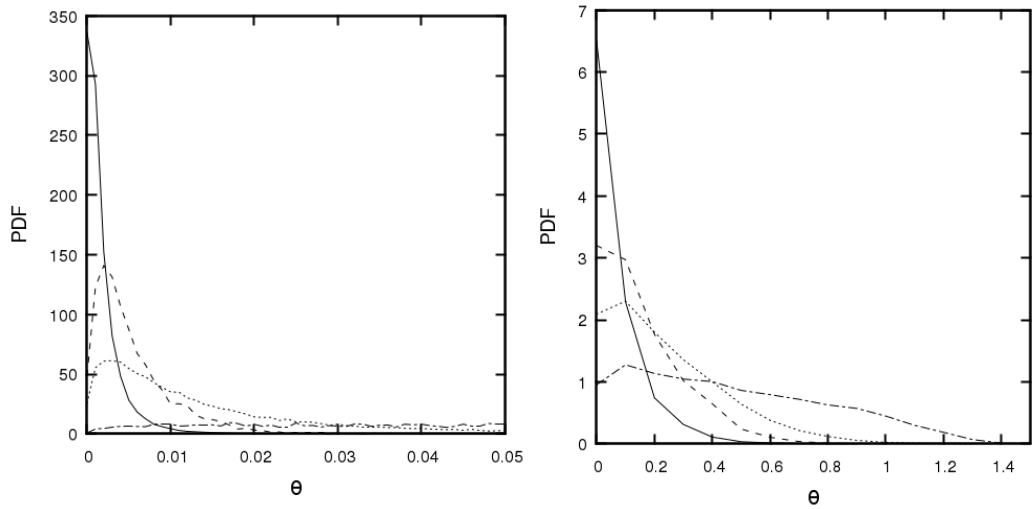

Figure 5.48: PDFs of angle between colliders at $St^+ = 0.1$ (left) and $St^+ = 92$ (right). Solid line: bulk flow; dashed: log-law region; dotted: buffer layer; dot-dashed: viscous sublayer.

Figure 5.48 demonstrates the collision angle (θ) in radians, which is the angle between the colliders' velocity vectors before the collision takes place. In both cases as the wall is approached, the spread and mean collision angle increases. This suggests more chaotic

and head-on collisions in those regions. At $St^+ = 0.1$, most of the collisions in the system are due to small deviations from the streamlines (which are locally parallel), and so the likelihood of collision is low. When they do occur, it is a glancing interaction and the exchange of momentum is most likely perpendicular to the direction of motion. Moving towards the wall, the most likely collision angle begins to increase, if only slightly. At the high Stokes number, the probability of more head-on collisions is increased. This is mostly true in the viscous sublayer, very close to the channel boundary. In this region, the distribution of collision angles is wide and fairly flat, indicating chaotic interactions in that zone. Moving away from the wall, the collision angles become more well defined and the mean is lowered. In all regions, the mean and spread of angles are much larger than those of the $St^+ = 0.1$ simulation. This is because the trajectories are now governed mainly by particle inertia, and so approach the limit where collision angles are arbitrary. These findings agree with those of Choi et al. (2016) who studied particle collisions in isotropic turbulence.

One final quantity of importance is the collision rate. The nature of this study is such that collision behaviour in different channel flow regions is compared, and so the collision frequency within each of these was calculated and compared. Because each region has a different volume, we have normalised by the length of the region to obtain a collision rate density, defined as $f_C = N_C(r)/(N_{\Delta t^*} L_R^*)$. Here, f_C is the collision rate density, $N_C(r)$ the total number of collisions across the averaging period in a particular region, $N_{\Delta t^*}$ the number of averaging timesteps ($N_{\Delta t^*} = 10^4$) and L_R the width of the region.

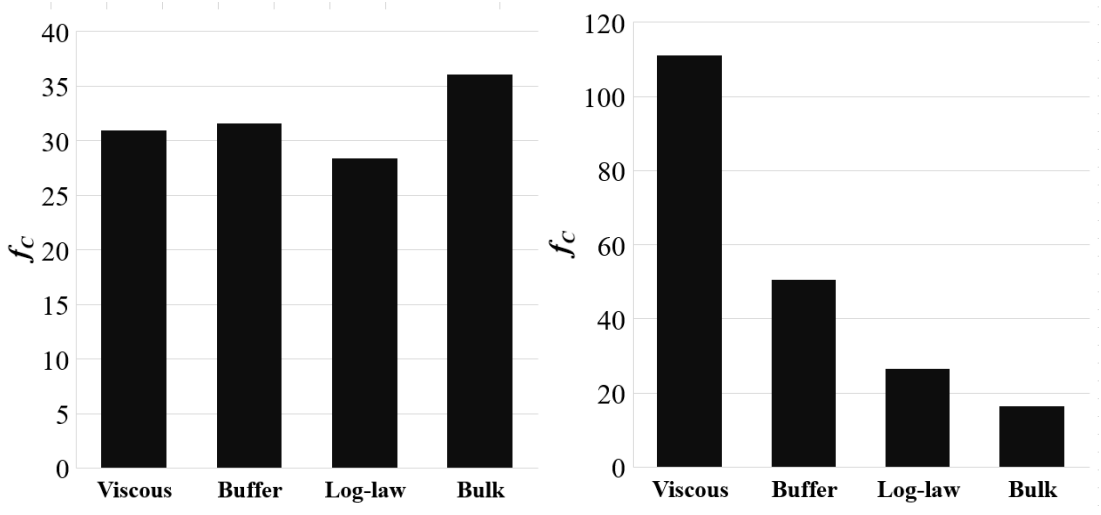

Figure 5.49: Mean collision rate density (f_C) at $St^+ = 0.1$ (left) and $St^+ = 92$ (right) for each channel flow region.

The results of this analysis are presented in Figure 5.49. Evidently, for $St^+ = 0.1$ the collision rate density is relatively homogenous across the four regions, with a slight increase in the bulk. This is expected, given the evenly distributed particle concentration. The $St^+ = 92$ particle set displays an obvious skew towards collisions taking place in the near-wall regions, with most collisions occurring in the viscous sublayer. Here, since particles are driven to these locations due to turbophoresis, increased local concentration and turbulence levels encourage more particle interactions. Another interesting observation is that in the bulk flow region, particles with $St^+ = 0.1$ undergo more collisions than those with $St^+ = 92$. This is likely due to the reduced concentrations in this region for the inertial particles.

5.4 Particle-particle agglomeration

Due to time constraints and long simulation times, a single run for $t^* = 30$ with 300,000 particles was performed to examine particle agglomerations. The mechanisms included four-way coupling with agglomeration, and this was implemented using the $St^+ = 0.1$ system in order to determine whether the inclusion of this extra mechanism would impact the turbulence field. For this simulation, the Hamaker constant, Debye screening length and reduced surface potential were chosen to approximate 100 μm diameter calcite (Sadowski, 1994) particles in water. This particle material was chosen as it is used as a simulant for nuclear waste in industrial investigations. These parameters are presented in Table 9.

Table 9: Parameters for agglomerating particle-laden turbulent channel flow at $St^+ = 0.1$

Parameter	Value
ρ_P^*	2.71
A	22.3 zJ
n	1×10^{-3} M
Θ	20 mV
κ	0.1 nm^{-1}
T_F	300 K

The time evolution of the number of agglomerates of constituents, *N*, present in the system is presented in Figure 5.50. It is clear that it would have taken just slightly longer than the simulation time $t^* = 30$ for 1/3 of the particles to form agglomerates, and the number of agglomerates formed per second appears linear in this period. The rate at which *N*=2 agglomerates are formed decreases over time, with a sharp increase during the first third of the simulation. The higher order agglomerates actually accelerate in formation over time, however, their overall totals remain few in number.

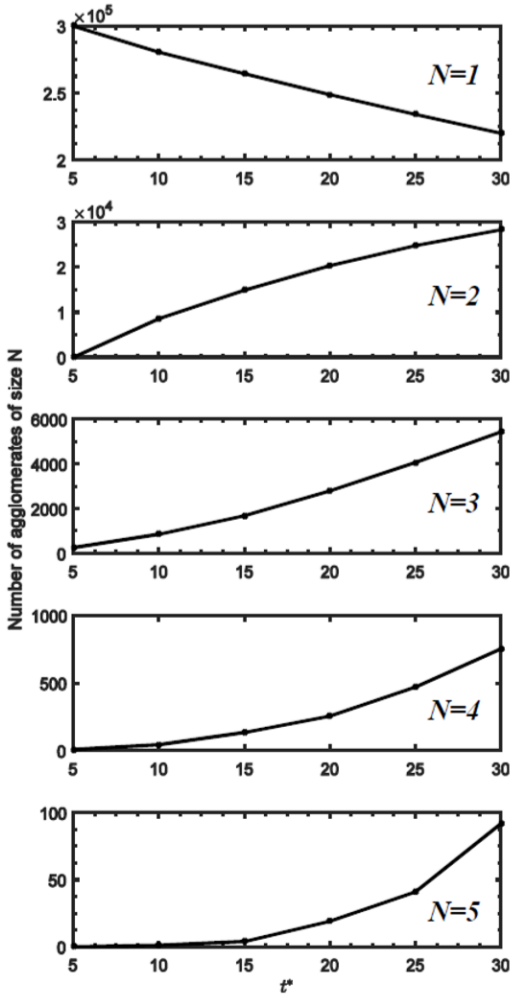

Figure 5.50: Time evolution of the number of agglomerates with *N* constituent particles in the $St^+ = 0.1$ flow.

With the addition of this mechanism, and for the duration of simulation time studied, the particle statistics did not change, implying that their local concentration and impact on the turbulence field was mostly unaffected, but further simulation time would be required to verify this.

5.5 Conclusions

This chapter has considered the effect that two-way and four-way coupling has on the turbulence and particle statistics associated with a multi-phase channel flow at a Reynolds number (based on the shear velocity) of 180. Direct numerical simulations have been carried out at two particle-fluid density ratios, corresponding to that of glass particles in both water and air. The volume fraction is chosen to study flows which are modified by both two- and four-way coupling as indicated by (Elghobashi, 2007). Throughout, we have demonstrated that the introduction of two and four-way coupling shows some modification to the fluid and particulate motion, with inertial particles showing a more enhanced response.

The time evolution of fluid turbulence statistics was first considered for each case in order to determine what effect the inclusion of two-way coupling had on these quantities. It was observed that momentum coupling reduced the mean streamwise velocity and worked to attenuate the turbulence intensities over time for the inertial particles, whilst the flow remained largely unchanged for the tracer-like particles. When two-way coupled, particle concentration statistics indicated turbophoretic effects for the inertial particles and a slight increase in the near-wall concentration profile for the tracer-like particles, with this shift in distribution taking place during the first 50 non-dimensional time units. The fluctuating velocities associated with the inertial particles were also dampened slightly in the wall region, adjusting to the local reduced streamwise turbulence intensities.

At high Stokes number (air), a greater qualitative difference is observed wherein the inclusion of coupling reduces the turbulence intensities, particularly in the streamwise direction. This is explicable by considering the increased slip velocities due to greater particle inertia. It is also observed that the inclusion of particle collisions has a greater impact on these statistics. Acceleration contributions from all particle force components were also considered in the analysis. When compared to the unladen flow, the main differences were that the streamwise drag term was increased in the wall region for both low and high density-ratio systems, whereas the wall-normal drag contributions were dampened for the inertial particles. Other force contributions remained unchanged. It is important here to underline the significance of varying density-ratio here in order to obtain different Stokes numbers. The lack of observable two-way coupling effects in the case of low Stokes is likely due to low mass loading, which is a result of low density-

ratio, despite volume fractions still being within the range suggested by Elghobashi (1994). Further work at increased mass loadings should be carried out to fully determine the effect of two-way coupling in low density-ratio flows.

Four-way coupling the flow led to further differences in both the fluid and particle statistics. For the fluid, the inclusion of interparticle collisions led to increased mean streamwise velocities in the bulk flow region when compared to the two-way coupled flow, however these were still not as high as the original unladen flow. This was also observed in all three components of the fluctuating velocities, enhancing the inertial particle-laden turbulence intensities but still leading to an overall reduction when compared to the unladen flow. Four-way coupling had little effect on the statistics associated with the tracer-like particles.

Comparing the particle statistics in both cases, there are very distinct differences in the way the particles behave when dispersed throughout the two systems. In terms of concentration, particles in air migrate towards the wall region, whilst spending most of the time either near the channel centreline or very close to the wall. In other regions, turbophoresis and particle-particle collisions encourage the particles either closer to the wall or back towards the centreline. Particles in water are discouraged away from the wall region, with particles more likely to be reintroduced back into the flow. Inertial particles were observed to travel faster than tracer-like particles in the wall region, whereas in the bulk the opposite was true. Whereas particles in water possess turbulence intensity profiles similar to those of the unladen fluid, the corresponding profiles in air are homogeneous across the channel, indicating that four-way coupling causes interparticle collisions to reduce the correlation with local turbulence.

In general, inertial particles are much more likely to collide with each other close to the wall (partly due to the increased concentration in that region), whereas tracer-like particles collide more frequently in the bulk. A novel method of analysing particle-particle collision dynamics was introduced wherein collisions in each of four channel regions are considered separately. The greatest spread of streamwise velocities was found to be in the buffer layer in both particle cases, but tracer particles in the viscous sublayer were observed to have much more well-defined pre-collision velocities than the inertial particles. This is to be expected as the inertial particles travel from higher layers into this region, but retain their increased velocities. This is not the case with tracer particles which

have very low slip velocities. For the wall-normal component, the two particle sets had opposite behaviours. Inertial particles possess a spread of velocities in the near-wall regions, whereas in the bulk flow velocities are more well-defined. For the tracer-like particles, their behaviour was found to be most well-defined close to the wall. Similar observations were made for the spanwise component; for the low Stokes number particles the greatest spread of spanwise velocities was observed to be in the log-law region. Collision angles were found to be more representative of head-on collisions for inertial particles, and more glancing collisions for tracer-like particles. In both cases, these angles were larger and more widely distributed closer to the wall. Collision rate densities for each region were also compared, the greatest being found for the $St^+ = 92$ case in the viscous sublayer. This is expected due to the increased particle concentration, number of wall collisions and turbulence in that region. The collision data obtained here will be used in the following chapter to determine typical collision events used to simulate binary particle-particle interactions in various regions of turbulence.

Lastly, the deterministic agglomeration mechanism as proposed in the methodology was tested on the low Stokes number flow. The system exhibited reasonable agglomerate formation in the time simulated, however, the turbulence statistics were unresponsive to the introduction of this phenomena and so more work should be carried out to determine the influence of agglomeration on the flow field.

6 FULLY RESOLVED BINARY PARTICLE INTERACTIONS IN TURBULENCE

6.1 Introduction and background

In the previous chapters, we have studied particle-laden turbulent flows by considering the solid particulate phase as point-like particles. With recent advances in computational power, providing the capability to obtain greater levels of accuracy with high fidelity techniques, understanding multiphase systems on a more fundamental level has become of great interest in the recent literature. Whilst the combination of direct numerical simulation (DNS) of the continuous phase with Lagrangian particle tracking (LPT) of the discrete phase is frequently used to simulate such systems, in this approach, despite all relevant length-scales being resolved in the Eulerian phase, the point-like constraint on the particulate phase means that information surrounding the small-scale fluid-structure interactions is lost. Instead, models based on both empirical observation and higher fidelity simulations are used to provide, for example, such quantities as the drag and lift coefficients which estimate the influence of the local fluid field on the particle. This approach is highly effective in studying large ensembles of particles as we have seen in previous chapters, where mean quantities can be studied to understand macroscopic behaviour. However, to fully determine the dynamics of small-scale motion and interaction (which are fundamental to and underpin the large scales), the flow field surrounding the particle must be fully resolved. Approaches which allow this are commonly referred to as interface tracking techniques, and various methods of performing such computations have been developed in recent years (Mark and van Wachem, 2008; Tseng and Ferziger, 2003; Peskin, 2002; Hu, 1996), all of which offer a trade-off between accuracy and computational cost/complexity.

The work presented within this chapter uses an immersed boundary method (IBM) coupled to a spectral element method (SEM) based DNS solver to fully resolve the flow

around dynamic particle meshes. The aim is to study the effect of turbulence on particle-particle interactions at turbulence intensities based on those present at varying wall-normal distances in the $Re_\tau = 180$ turbulent channel flow. By analysing the resulting trajectories and dynamic properties of these two-particle systems, understanding can be developed on how (and under what conditions) particle collisions or agglomerations occur, at levels of detail which greatly surpass those of LPT-based studies.

We will begin this chapter by revisiting the turbulent channel flow, analysing the relevant fluid scales throughout the geometry in order to determine the structure and intensity of the turbulence which the IBM particles should be exposed to. Based on this analysis, periodic boxes of isotropically forced homogeneous turbulence will be obtained via the linear forcing method, with properties matching those in the various regions of the channel flow. A validation of the IBM is also offered, using simulations of the flow around a sphere to calculate drag coefficients for different particle Reynolds numbers.

The remainder of this chapter considers DNS-IBM simulations of typically occurring binary particle interactions in the periodic boxes of turbulence. From these we are able to probe deeper into the fundamental dynamic nature of particle-particle agglomeration, taking into account both the roles of turbulence and chemistry in why particles either aggregate or are driven apart beyond the collision event. Finally, by studying small ensembles of interaction events, we determine the effect that varying certain chemical and mechanical properties has on the resulting interaction dynamics. Suggestions are also offered for realistic behavioural modification techniques, taking the knowledge obtained within this chapter and using it to propose novel techniques to improve current solid-fluid processing methods.

6.2 Turbulence scales in the $Re_\tau = 180$ channel flow

To consider regions of turbulence similar to those present in the channel flow, we must first analyse the relevant length scales associated with the turbulent eddies. An intermediate length scale which is suitable is the Taylor microscale which lies between the Kolmogorov length scale and the integral scale. This is also the length scale at which fluid viscosity has a significant contribution to the behaviour and dynamics of the turbulent eddies. Furthermore, previous work (Boivin et al., 1998; Rosales and Meneveau, 2005) on both turbulence modulation and isotropic forcing uses this parameter

to classify systems of this nature. Based on information obtained from the single phase turbulent channel flow at $Re_\tau = 180$, this microscale was computed as a function of wall distance using the following equation:

$$\lambda^* = \sqrt{\frac{\overline{u'^* u'^*}}{\overline{\left(\frac{du'^*}{dx^*}\right)^2}}} \tag{93}$$

The Taylor microscale for the streamwise direction is presented in Figure 6.1, with λ^* peaking in the turbulent region. In the outer layer, the profile is fairly constant indicating a similar turbulence structure throughout this region.

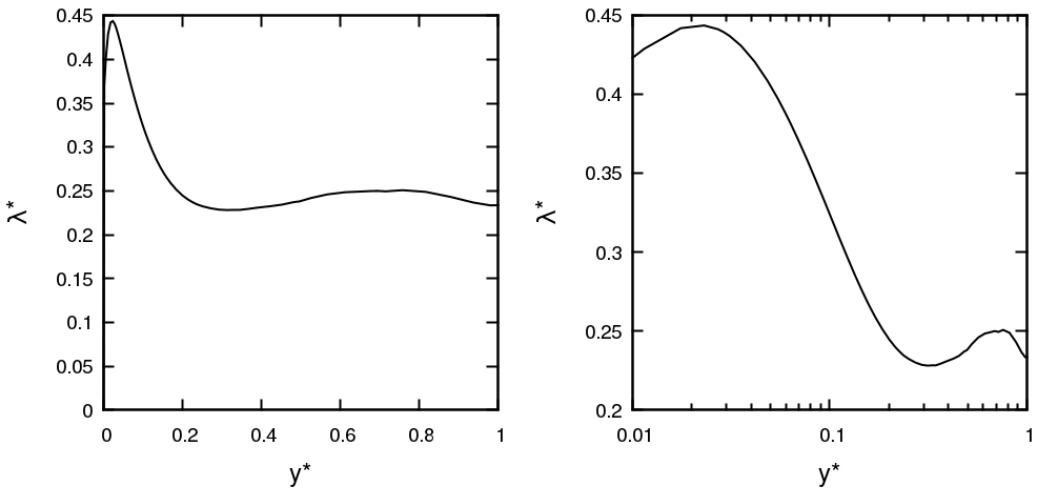

Figure 6.1: Profiles of streamwise Taylor microscale in turbulent channel flow at $Re_\tau = 180$. Righthand plot is on a log scale.

From these results we can obtain an equivalent Reynolds number based on the Taylor microscale, which can be calculated using the following equation:

$$Re_\lambda = \frac{\lambda u'_{RMS}}{\nu_F}. \tag{94}$$

This quantity is plotted in Figure 6.2. We can use this information to determine the range of turbulence levels and eddy length scales of interest associated with each region of the channel flow.

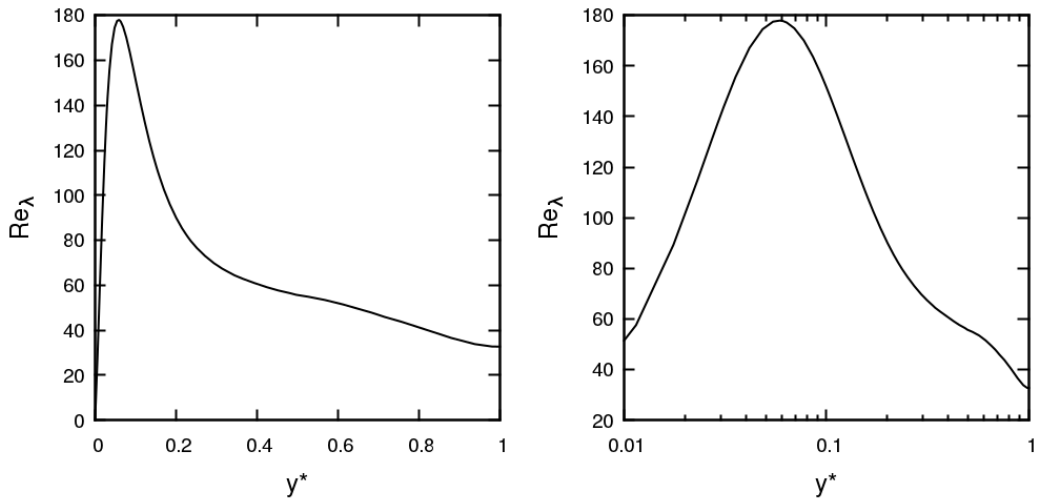

Figure 6.2: Profiles of Reynolds number based on the streamwise Taylor microscale in turbulent channel flow at $Re_\tau = 180$. Righthand plot is on a log scale.

The values for the Taylor microscale Reynolds number chosen to represent the entire range of turbulence levels encountered with the channel flow are presented in Table 10. Note that each of these has been assigned to a typical region within the flow, with each region having a turbulence level roughly represented by the Re_λ value chosen. Additionally, however, the range of Reynolds numbers chosen was primarily decided upon to encompass the range of turbulence levels within the flow as a whole, whilst also matching Reynolds numbers which have been studied before, particularly in the work of Rosales and Meneveau (2005).

Table 10: Representative Reynolds number based on the Taylor microscale for each region of the $Re_\tau = 180$ turbulent channel flow.

Representative region	**Start y^+**	**End y^+**	**Start y^***	**End y^***	**Re_λ**
Viscous sublayer	0	5	0.000	0.027	197
Buffer layer	5	30	0.027	0.166	120
Log-law region	30	36	0.166	0.200	51
Bulk flow	36	180	0.200	1.000	29

6.3 Homogeneous isotropic turbulence

6.3.1 Linear forcing method

This section discusses how simulated statistically stationary periodic boxes of homogeneous, isotropic turbulence were computed using the linear forcing method, as described by (Lundgren, 2003). By homogeneous we mean that the turbulence structure enforced must be similar in all directions within a box. RMS velocity fluctuations may therefore be randomly distributed, but a suitably time-averaged velocity sample should be constant everywhere. By isotropic we enforce that the fluctuations are direction-independent and therefore $u' = v' = w'$ where $u' = \sqrt{\overline{u^2}}$, $v' = \sqrt{\overline{v^2}}$ and $w' = \sqrt{\overline{w^2}}$.

The linear forcing method is suggested as an ideal solution to the above in place of low wave-number forcing (Doering and Petrov, 2005) as it removes the necessity to transform from physical space to Fourier-space in order to force the correct computational nodes. The 'linear' term refers to a global node forcing proportional to the velocity vector at each grid-point. (Rosales and Meneveau, 2005) conclude that the linear forcing method provides the same results as the Fourier-space forcing regime. They also determined that the system convergence depends on domain size and Reynolds number but not the initial velocity distribution. Hence, we choose to pursue this method in order to obtain a suitable continuous phase for use with the IBM.

The simulation parameters used to obtain the correct Reynolds numbers based on the Taylor microscale are presented in Table 11.

Table 11: Simulation parameters for periodic boxes of isotropic turbulence

Re_λ	**29**	**51**	**120**	**197**
N_E	48^3	48^3	48^3	48^3
A	0.0667	0.2	1.0	0.1667
ρ_F	1	1	1	1
ν_F	4.491×10^{-3}	4.491×10^{-3}	1.272×10^{-2}	3.256×10^{-4}

Here, N_E is the number of elements in the system, and A is the linear forcing coefficient, defined below. ρ_F and ν_F have their usual meanings. For the IBM simulations, in all cases we set the density of the fluid phase equal to unity whilst modifying the viscosity and the

linear forcing coefficient in order to obtain the desired Reynolds number based on the Taylor microscale. These have been chosen to match various systems with Reynolds numbers comparable to those present in the different channel regions, each of which were considered by (Rosales and Meneveau, 2005). The forcing function we supply as a force term in the Navier-Stokes equation is as follows:

$$\boldsymbol{F} = A\boldsymbol{u}_F, \tag{95}$$

where the linear forcing coefficient, A, is determined based on the desired energy dissipation rate per unit mass in relation to the velocity fluctuations. The following relation holds:

$$A = \frac{\epsilon}{3u_{F,RMS}^2}, \tag{96}$$

which for constant A indicates a turnover time scale. Here:

$$u_{F,RMS}^2 = \frac{1}{3}(\overline{\boldsymbol{u}_F \cdot \boldsymbol{u}_F}) = \frac{1}{3}\left(\overline{\boldsymbol{u}_x^2 + \boldsymbol{u}_y^2 + \boldsymbol{u}_z^2}\right), \tag{97}$$

6.3.2 Computational domain and initial conditions

As outlined in the methodology chapter, we construct the mesh and provide the simulation parameters in Table 11 in order to obtain the continuous phase predictions as obtained by (Rosales and Meneveau, 2005). Since the latter authors demonstrated a lack of reliance on the spectral state of the initial condition, the continuous phases for all four box systems are developed from the Arnold-Beltrami-Childress flow, a steady solution to the Euler equations with a well-defined turbulence energy spectrum. The initial conditions are:

$$u_x = \sin(z) + \cos(y)$$
$$u_y = \sin(x) + \cos(z). \quad (98)$$
$$u_Z = \sin(y) + \cos(x)$$

Figure 6.3 illustrates the evolution of the mean of the three rms velocity fluctuation components, $\langle u'^2_{rms} \rangle$, with time. Note that here the non-dimensional time scale, $t' = t/\tau$, ranges from $\tau = l/u'_{rms} = 4.97$ for $Re_\lambda = 29$ to $\tau = 2.05$ for $Re_\lambda = 197$. Here, l represents the turbulence length scale, $l = u'^3_{rms}/\epsilon$, where ϵ is the viscous energy dissipation rate. One consequence of linear forcing is that this scale converges on $l \sim 0.19L$, where $L = 2\pi$ is the domain length.

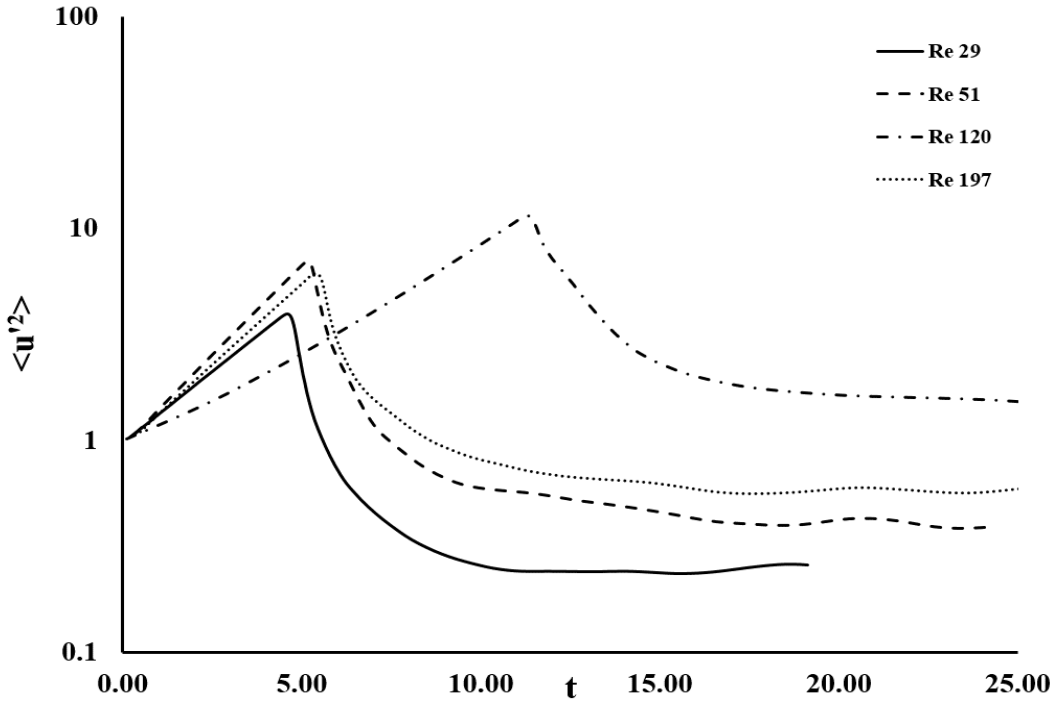

Figure 6.3: Time evolution of rms velocity fluctuation components.

In all cases, the initial transient period involves an increase in kinetic energy as the dissipation associated with the initial solution is greatly outweighed by the forcing's energy injection. At around $t' = 6$, the systems with low viscosity undergo a sudden transition into turbulence. The dissipation from thereon works to reduce the kinetic energy of the system until a statistically stationary state is reached where the forcing injection and turbulence energy dissipation are approximately equivalent.

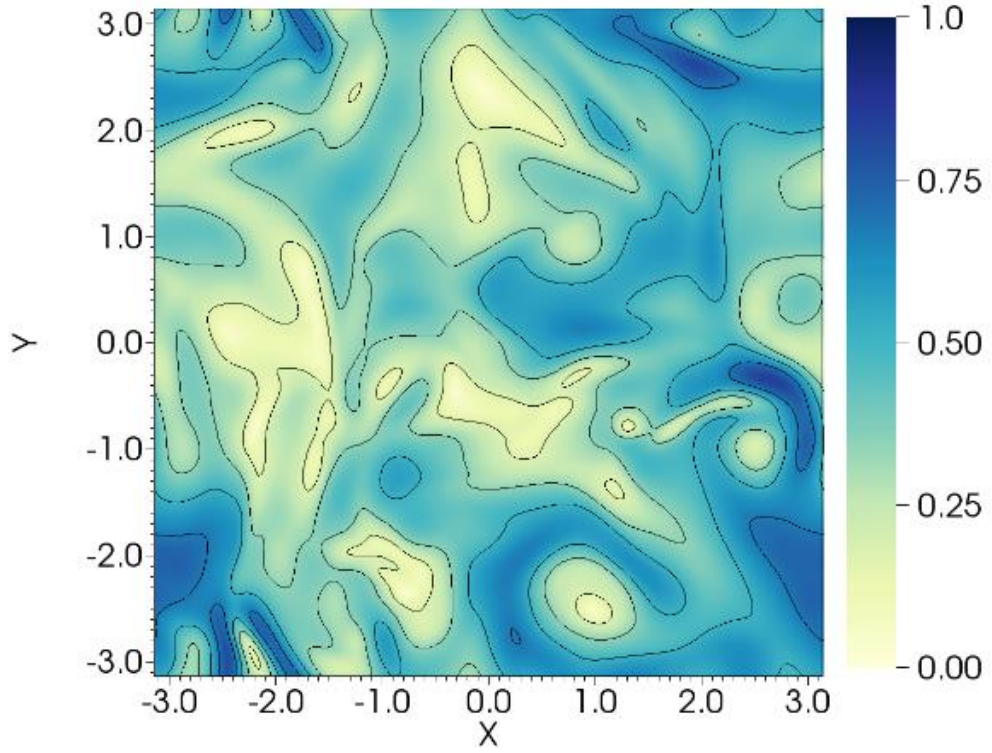

Figure 6.4: Contour plot of velocity magnitude (ms^{-1}) for $Re_\lambda = 29$.

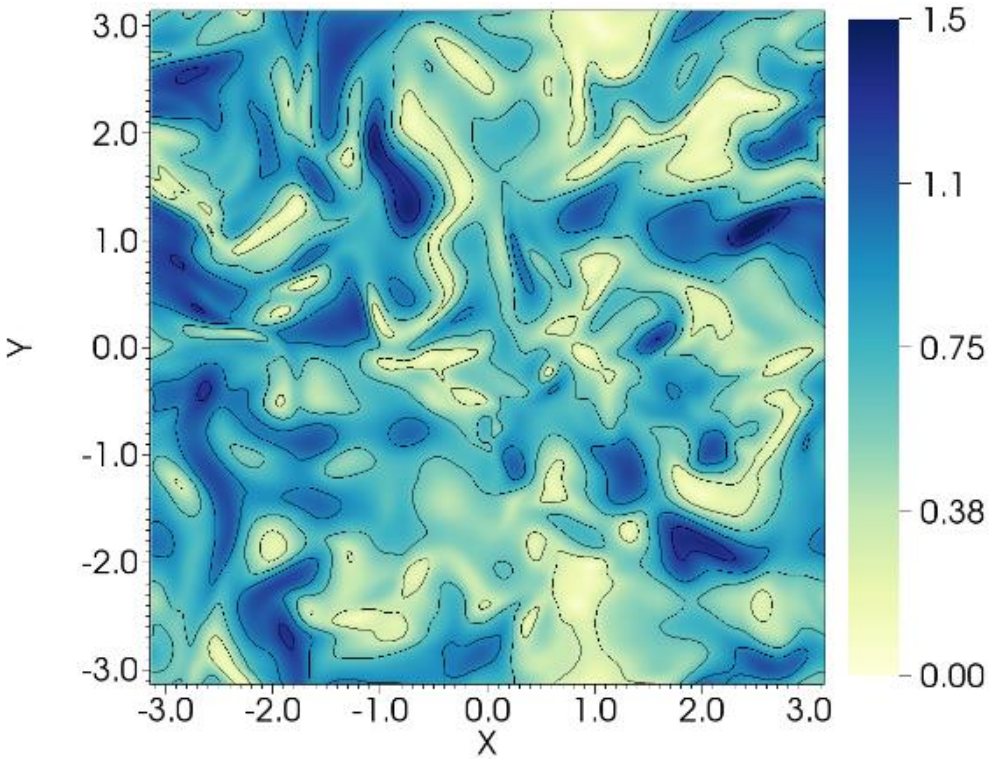

Figure 6.5: Contour plot of velocity magnitude (ms^{-1}) for $Re_\lambda = 51$

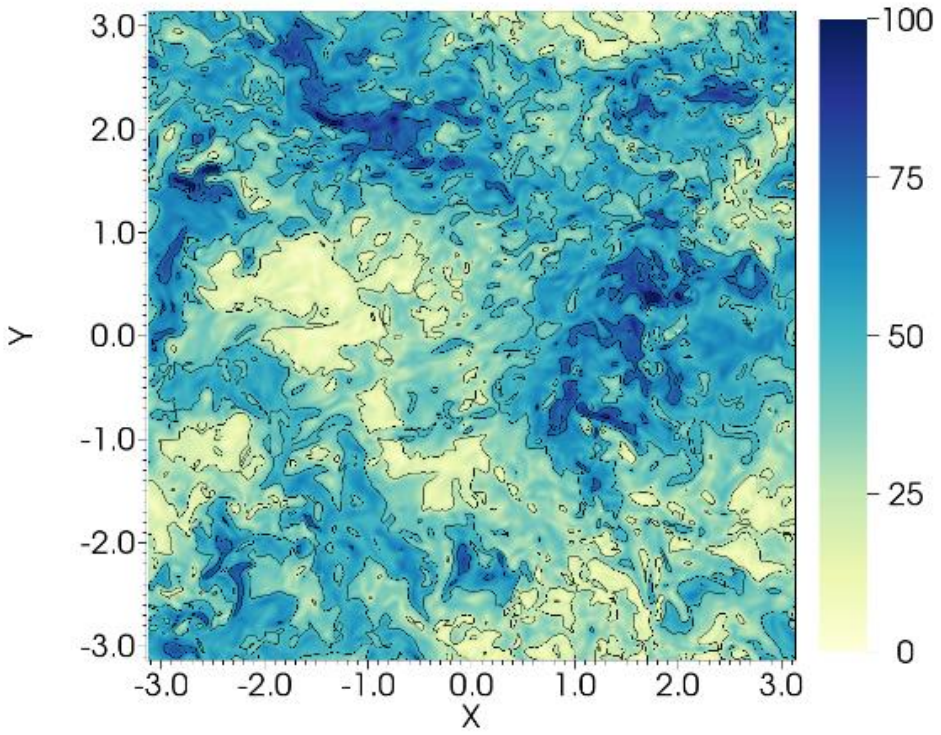

Figure 6.6: Contour plot of velocity magnitude (ms^{-1}) for $Re_\lambda = 120$

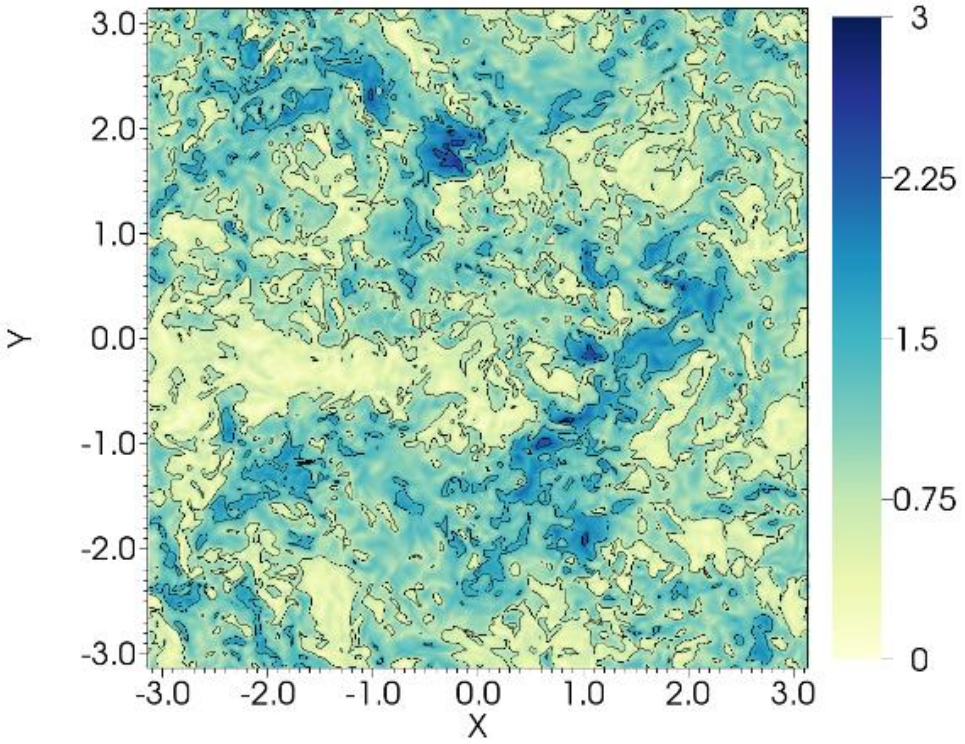

Figure 6.7: Contour plot of velocity magnitude (ms^{-1}) for $Re_\lambda = 197$

It is from time varying solutions of this final state ($t' > 15$) that particle simulations are performed. The $Re_\lambda = 120$ system takes slightly longer to reach this state and so the injection point for particles for this system begins at $t' > 25$. Figure 6.4, Figure 6.5, Figure 6.6 and Figure 6.7 present contour plots sampled at the statistically stationary state for each box system illustrating the instantaneous velocity magnitude of the resulting turbulence field.

6.4 Immersed boundary method validation

To determine the validity of the employed immersed boundary method, various simulations of immersed spheres at different Reynolds numbers were performed to compare calculated drag coefficients to those obtained by empirical investigations.

This validation is similar to that carried out by (Mark and van Wachem, 2008), however it should be noted that in the case of the present work, a much smaller equivalent grid spacing was employed. In our case, the mesh used to predict isotropic turbulence in the previous subsection was used, whilst the physical length of the box (relative to the particle) was modified in each case to ensure the cell spacings were sufficient to resolve the flow around the sphere, particularly for increased particle Reynolds numbers.

In each case the sphere diameter was fixed at $d_P = 1.0m$ whilst the geometry length varied between $5m$ and $20m$. The density of the fluid was $1.0kgm^{-3}$ and the kinematic viscosity was $0.1\ Nsm^{-2}$. The boundary conditions were set such that all boundaries of the box, aside from the outlet, were set to a particular velocity, u_∞(which was varied to obtain different Reynolds numbers). The outlet used a Neumann boundary condition with zero fluid pressure. Simulations were performed using three icosphere subdivision levels in order to determine the effect of this on the accuracy of the predicted drag coefficient. These subdivisions corresponded to $N_F = 20, 80$ and 320, where N_F is the number of triangular faces within the IB mesh.

Fixing the spheres in place, the simulations were allowed to run until the pressure and viscous forces were statistically stationary. These were then used to generate a drag force using the following equation:

$$\boldsymbol{F}_D = \boldsymbol{F}_{viscous} + \boldsymbol{F}_{pressure}. \tag{99}$$

Upon obtaining the drag force, the drag coefficient could be calculated using the equation:

$$C_D = \frac{2}{\rho_F u_\infty^2 \pi r_P^2} |F_D|, \tag{100}$$

which is compared below against the proposed relations based on empirical observations of Stokes (1851) and Schiller (1934):

$$C_D = \begin{cases} 24/Re_P & 0 < Re_P \leq 0.5 \\ \frac{24}{Re_P}(1 + 0.15Re_P^{0.687}) & 0.5 < Re_P \leq 1000, \end{cases} \tag{101}$$

with the particle Reynolds number Re_P being calculated using:

$$Re_P = \frac{u_\infty d_p}{\nu_f}. \tag{102}$$

The results of these simulations are presented in Figure 6.8. Throughout, the lowest subdivision level particles have their drag coefficients severely underpredicted. This is likely due to the resolution of the mesh and its lack of resemblance to a smooth sphere (for which we are comparing against in the equation for drag coefficient). Due to the increase in reference area, these underpredictions are to be expected. As the subdivisions in the mesh are increased, we obtain better accuracy when compared to empirical correlations, particularly for lower particle Reynolds numbers.

It is suggested in the literature (Mark and van Wachem, 2008) that deviations at higher Reynolds numbers could be due to the particle to domain size ratio, and further studies should be carried out should this method be used to predict the motion of particles at very high Reynolds numbers. In previous channel studies from the first results chapter, we

observed that particle Reynolds numbers are such that $Re_P < 10$ in all regions of the flow, and so the current validation is sufficient to verify the correct calculation of the drag coefficient for the type of motion we are interested in.

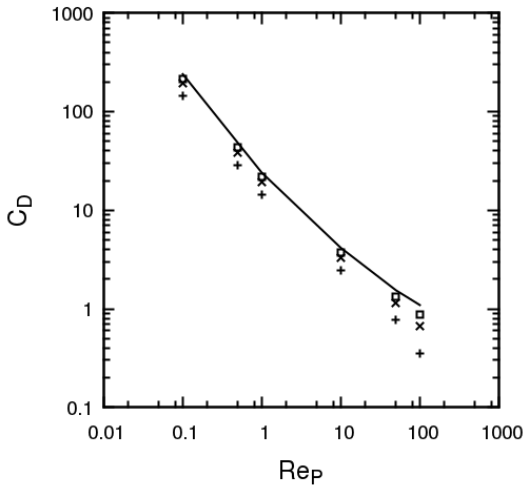

Figure 6.8: Simulated drag coefficient at icosphere face subdivision $N_F = 20$ (+), $N_F = 80$ (×), and $N_F = 320$ (□) compared against empirical values (solid line).

6.5 Effect of turbulence on binary particle interaction

After having obtained suitable continuous phases and verified the accuracy of the solid-phase solver, two identical particles are injected into each box system with relative initial velocity vectors matching those most commonly occurring from collision events sampled in the equivalent region of the four-way coupled multi-phase channel flow simulations from the previous chapter. In these prior simulations, particle streamwise velocities have the mean particle streamwise velocity at their corresponding wall-normal distance subtracted from them, to account for the shift to isotropic turbulence in the present work. This is allows us to approximate particle collisions in a reference frame moving with the fluid downstream inside the channel flow.

The simulation parameters for each of these studies are presented in Table 12. Here, l is the turbulence length scale, u'_{rms} is the statistically stationary state root-mean-squared velocity fluctuation averaged over the three co-ordinate directions, λ is the Taylor microscale, d_P and r_P are the particle diameter/radius with reference to the size of the box, N_N is the number of equivalent grid nodes in a given direction, ρ_N is the density of grid nodes per unit distance in the box and N/N_P is the number of nodes across the

particle within the box. Table 13 provides the material and chemical parameters associated with the DLVO and collision equations. These parameters, as in the previous chapter, have been chosen to represent a simulant for nuclear waste material. Specifically, these are based upon a 100μm calcite particle suspension in water.

Table 12: Simulation parameters for binary particle interactions using immersed boundary method.

Re_λ	**29**	**51**	**120**	**197**
l	1.19381	1.19381	1.19381	1.19381
u'_{rms}	0.24416	0.40213	1.47660	0.58104
τ	4.88947	2.96871	0.80848	2.05460
ν_F	0.00449	0.00449	0.01272	0.00033
λ	0.53342	0.56957	0.64608	0.11039
d_P	0.9068	0.9683	1.0983	0.1877
r_P	0.4534	0.4841	0.5492	0.0938
N_N	336.00	336.00	336.00	336.00
ρ_N	53.48	53.48	53.48	53.48
N_N/N_P	48.49	51.78	58.73	10.04

Table 13: DLVO and collision material and chemical parameters for binary particle interactions using immersed boundary method.

Parameter	**Value**
r'_P	50 μm
e	0.4
ρ_P/ρ_F	2.71
A	22.3 zJ
n	1×10^{-3} M
Θ	20 mV
κ	0.1 nm^{-1}
T_F	300 K

In Table 12, l is the turbulence length scale; u'_{rms} the time and space averaged rms velocity fluctuation within the box; τ the fluid time scale in the box; ν_F the kinematic viscosity of the fluid; λ the Taylor microscale of the fluid, d_P the diameter of the particle in the box; r_P the radius of the particle in the box; N_N the equivalent number of cells across the box in one direction; ρ_N the density of cells and N_N/N_P the number of nodes across a single particle. In Table 13, r'_P is the equivalent particle radius represented in the channel flow; e the coefficient of restitution; ρ_P/ρ_F the particle to fluid density ratio; A the Hamaker constant; n the molarity of the solution; Θ the reduced surface potential; κ the inverse Debye length and T_F the fluid temperature.

In the following subsections we shall explore a particle-particle interaction event taking place in each turbulence region (aside from the $Re_\lambda = 120$ box which shall be considered later in greater detail, and since all particle-particle interaction outcomes were manifest in the $Re_\lambda = 29$, 51 and 197 boxes). In each case, particles are injected into randomly chosen locations throughout the box domain with a constant separation distance of 2 box distance units. The simulation is then performed for 50 non-dimensional box time units and information surrounding the instantaneous fluid field and particle location, orientation, velocity and angular velocity are recorded at each timestep over the course of the interaction.

6.5.1 Particle-particle interaction at $Re_\lambda = 29$

We first examine a typical interaction event occurring at low Reynolds number, typical of the bulk flow region in the turbulent channel flow.

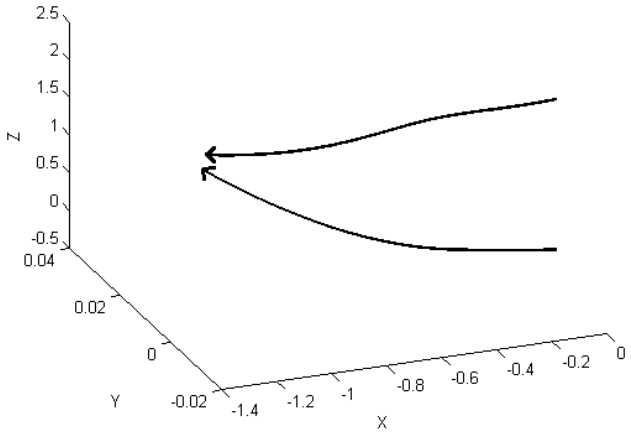

Figure 6.9: Typical three-dimensional interaction trajectories during $t' < 25$, lines represent the particle motion, plotted at particle centres. Arrows indicate direction.

Figure 6.9 illustrates a typical trajectory of the binary particle system occurring in the low turbulence box. It appears that over the course of the motion, the particles are attracted towards each other whilst also being carried in directions due to the influence of the surrounding fluid. From this perspective, it does not appear that there are any significant turbulent fluctuations leading to large deviations from streamlines, and that particle inertia as well as the van der Waals attraction are dominant.

Figure 6.10 shows these trajectories in more detail, with each component for position plotted separately. It is clear here that there is a slight drift in the x and y directions, whilst in the z direction the particles are brought close to one another until $t' = 25$ where they agglomerate. This is more closely observed in the lower right plot of separation distance, which shows that the attraction takes place over $t' < 25$, after which the particles stick together, with no indication of bouncing or break up.

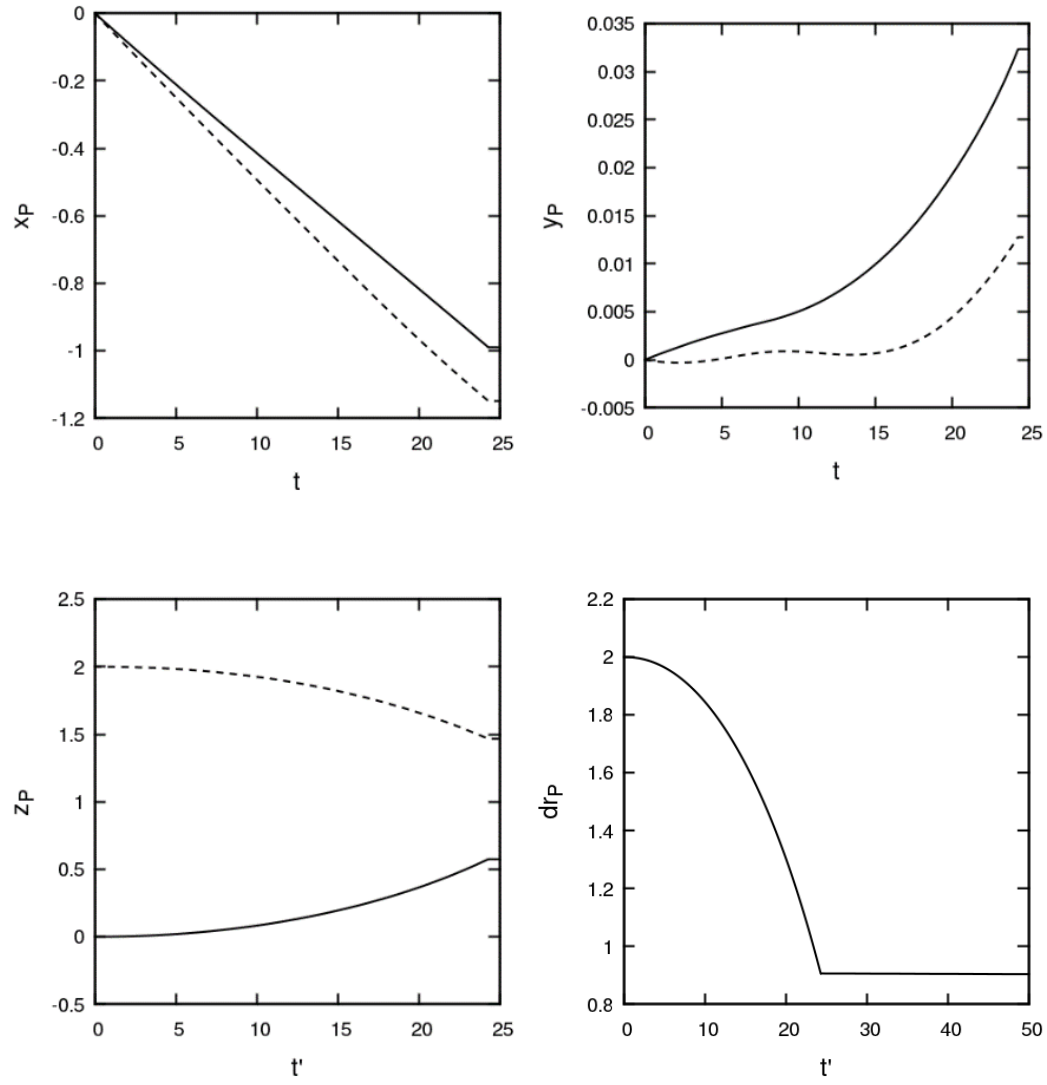

Figure 6.10: Centroid position components of each particle in the $Re_\lambda = 29$ binary interaction over time. Lower-right demonstrates the evolution of interparticle distance.

Figure 6.11 illustrates the three components of linear velocity belonging to both interacting particles. These indicate that upon injection, the particles rapidly obtain a velocity in the negative x direction, with an increase in relative velocity over time caused by the van der Waals attraction (in this case the relative velocity was due to the particles travelling towards each other). After $t' > 25$ it is clear that both particles share very similar velocities upon aggregation with each other.

Angular velocities are plotted in Figure 6.12. In all components, each particle obtains a small amount of rotational motion during the agglomeration time. After the particles undergo agglomeration, their relative angular velocity remains approximately constant.

This is likely due to the fact that they are experiencing very similar local velocity fields and their rotational motion is hence coupled.

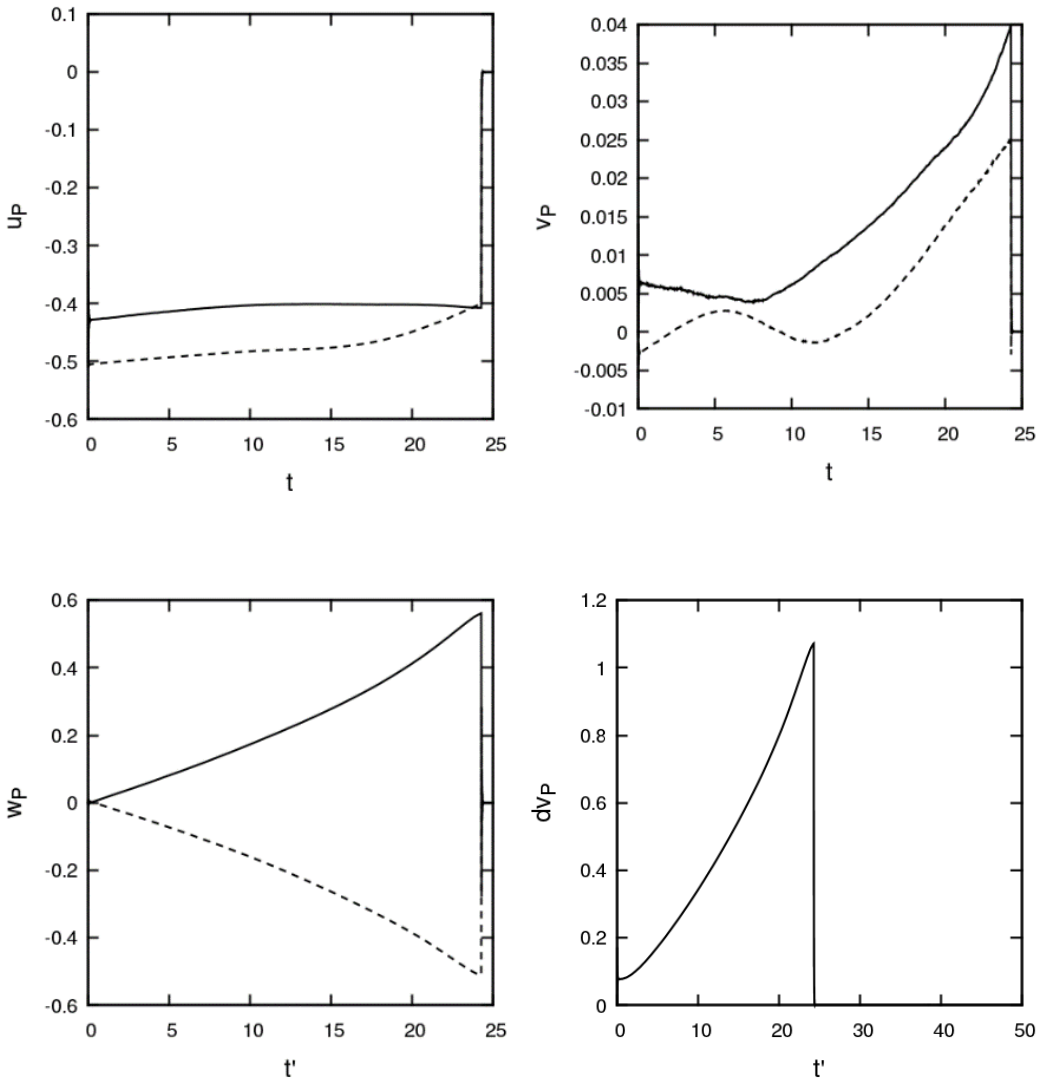

Figure 6.11: Linear velocity components of each particle in the $Re_\lambda = 29$ binary interaction over time. Lower-right demonstrates the evolution of relative velocity.

Figure 6.13 compares the hydrodynamic force components over the course of the interaction. Clearly this quantity is very responsive to minute fluctuations in the flow field, which leads to a lot of variability in their values during each calculation timestep. The x and y components fluctuate around zero, whilst the z (direction of separation) component increases as the particle velocity increases. This is likely due to the drag force being proportional to the local slip velocity, which becomes large when the van der Waals attraction decouples the particle motion from that of the surrounding fluid velocity. The relative force indicates that once the particles agglomerate, they eventually experience a

similar hydrodynamic force, which is expected because they are in contact with each other and so experience similar surrounding fluid characteristics.

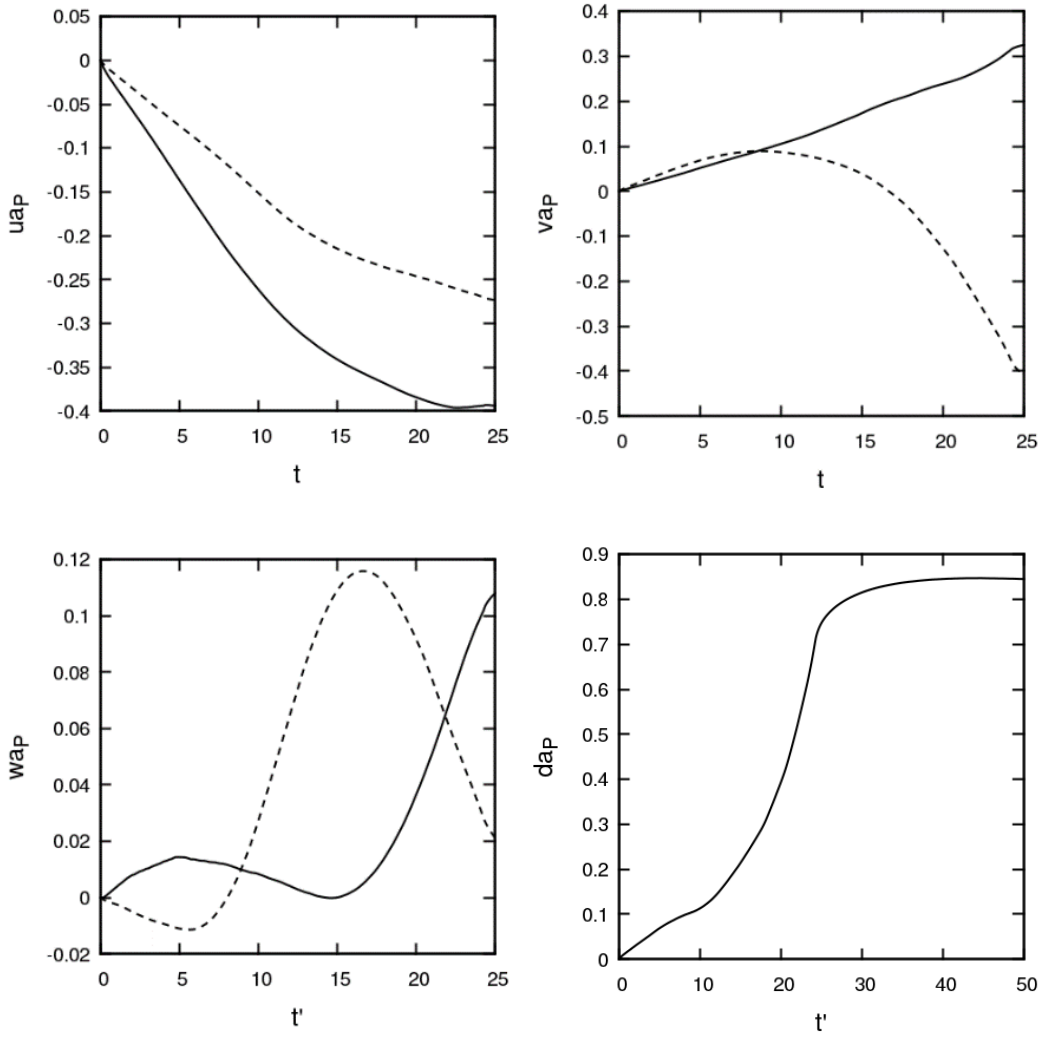

Figure 6.12: Angular velocity components of each particle in the $Re_\lambda = 29$ binary interaction over time. Lower-right demonstrates the evolution of relative angular velocity.

Figure 6.14 compares the DLVO forces between the particles. As expected, these increase with decreasing separation distance and are in general more dominant than the hydrodynamic forces, particularly at very close interparticle distances. This indicates that the DLVO attraction is the primary mechanism behind the motion caused by the interaction event.

Finally, Figure 6.15 gives the angular torque components over the course of the interaction event. Agreeing with earlier observations, the relative torque increases over

time causing the particles to build up a rotation speed prior to colliding. Once the collision occurs, the relative torque soon falls to zero.

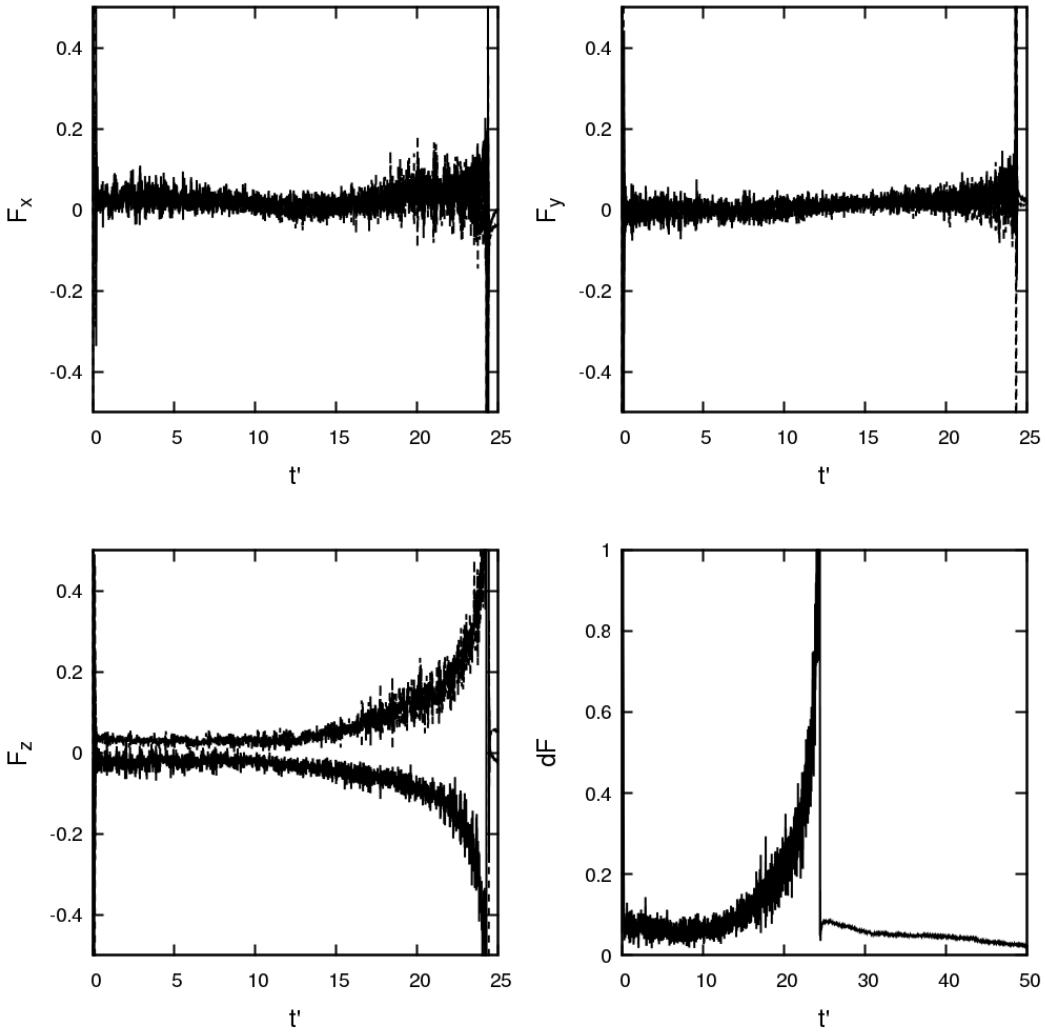

Figure 6.13: Hydrodynamic forces of each particle in the $Re_\lambda = 29$ binary interaction over time. Lower-right demonstrates the evolution of relative hydrodynamic force.

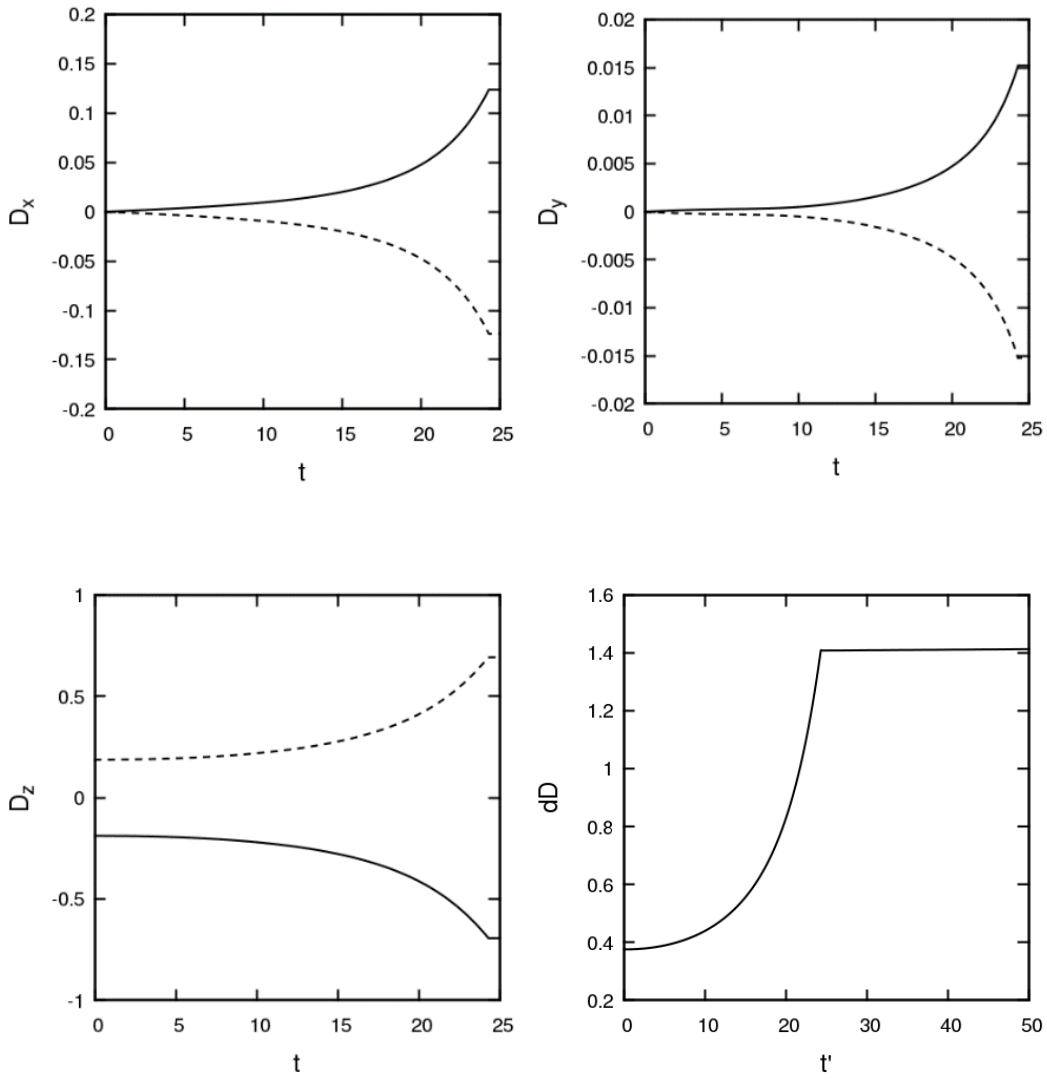

Figure 6.14: DLVO forces of each particle in the $Re_\lambda = 29$ binary interaction over time. Lower-right demonstrates the evolution of relative hydrodynamic force.

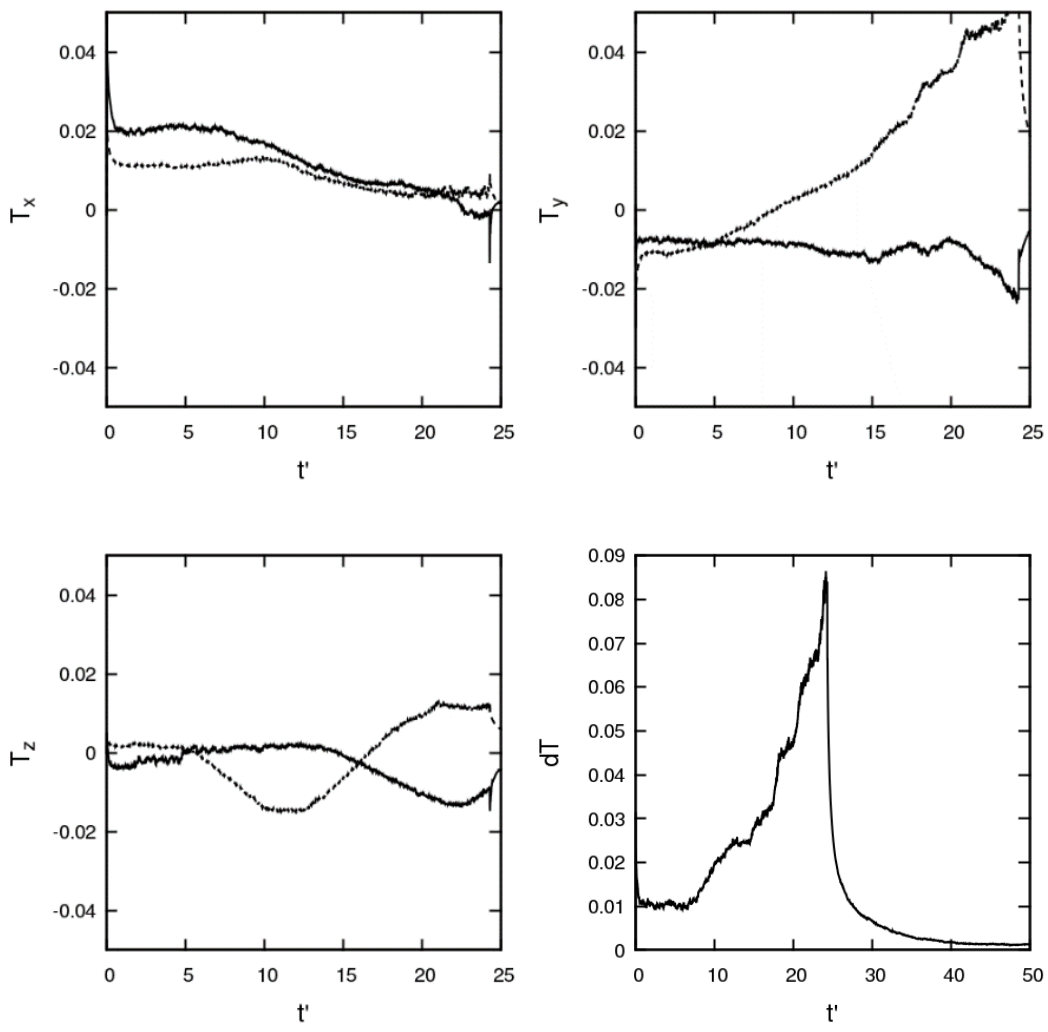

Figure 6.15: Torque due to hydrodynamic shear of each particle in the $Re_\lambda = 29$ binary interaction over time. Lower-right demonstrates the evolution of relative hydrodynamic force.

6.5.2 Particle-particle interaction at $Re_\lambda = 51$

Increasing in Reynolds number slightly, we now observe a binary particle collision taking place in the $Re_\lambda = 51$ box which resembles the turbulence characteristics present in the log-law region of the turbulent channel flow. In Figure 6.16 we observe a three-dimensional overview of the interaction event taking place. As before, the trajectory to collision appears smooth and without indication of fluctuations.

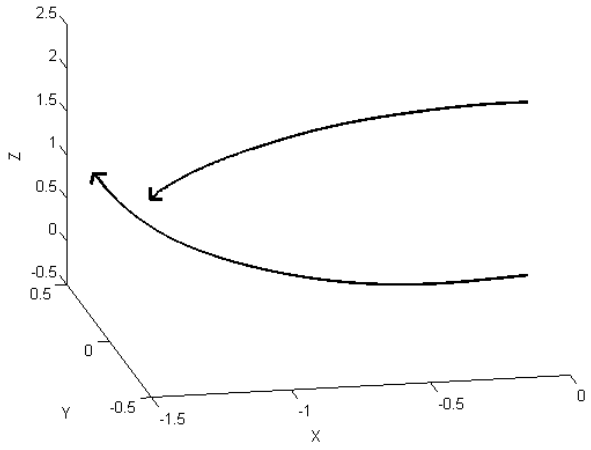

Figure 6.16: Typical three-dimensional interaction trajectories during $t' < 25$, lines represent the particle motion, plotted at particle centres. Arrows indicate direction.

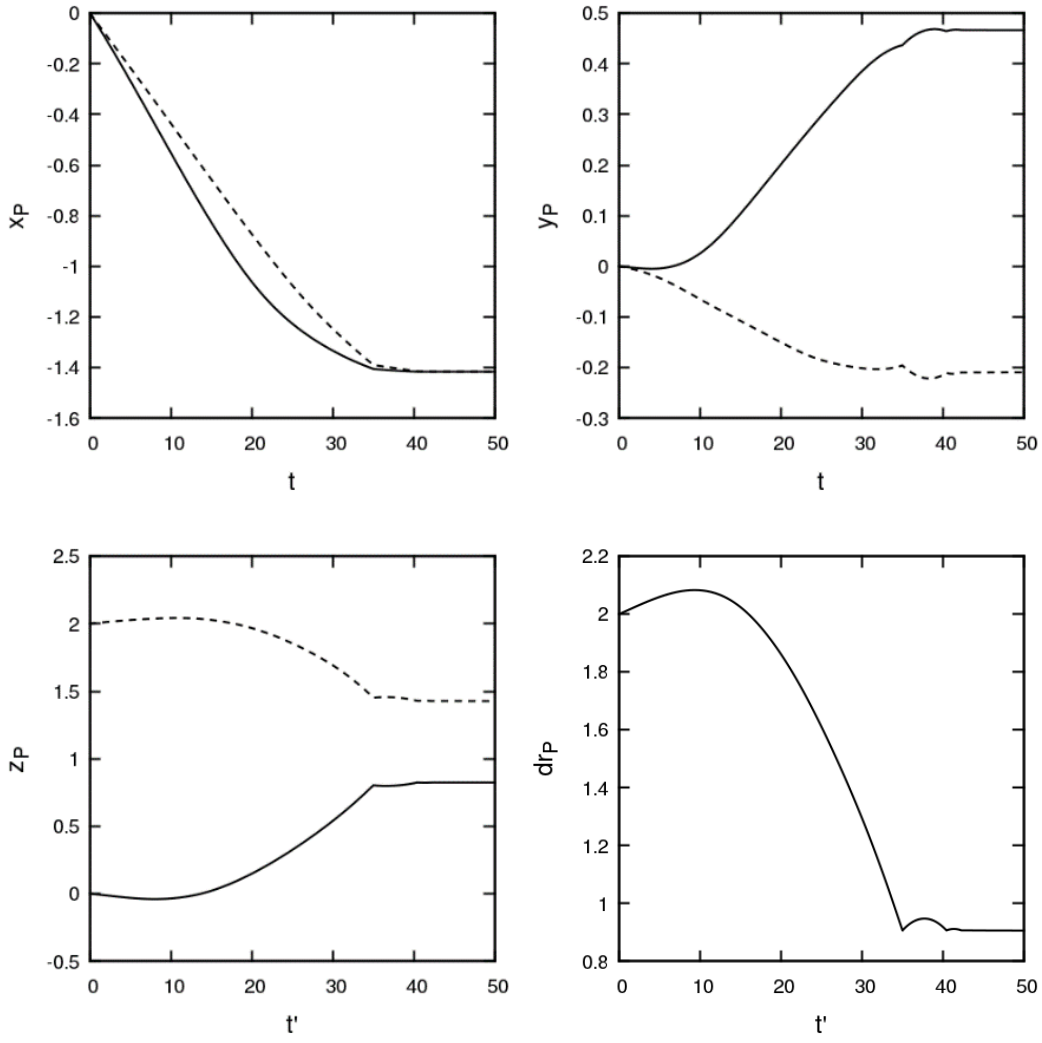

Figure 6.17: Centroid position components of each particle in the $Re_\lambda = 51$ binary interaction over time. Lower-right demonstrates the evolution of interparticle distance.

Figure 6.17 illustrates the various components of each particle's position vector during the interaction. Interestingly, in this case, the particles initially move away from each other, likely due to the fluid providing them with opposite velocities close to the start of the event. At around $t' = 10$ the particles begin moving towards each other until an initial collision occurs at $t' = 35$. After this, the particles undergo a small bounce which was never observed at lower Reynolds numbers. Despite the bounce, the particles eventually undergo agglomeration and remain together as before.

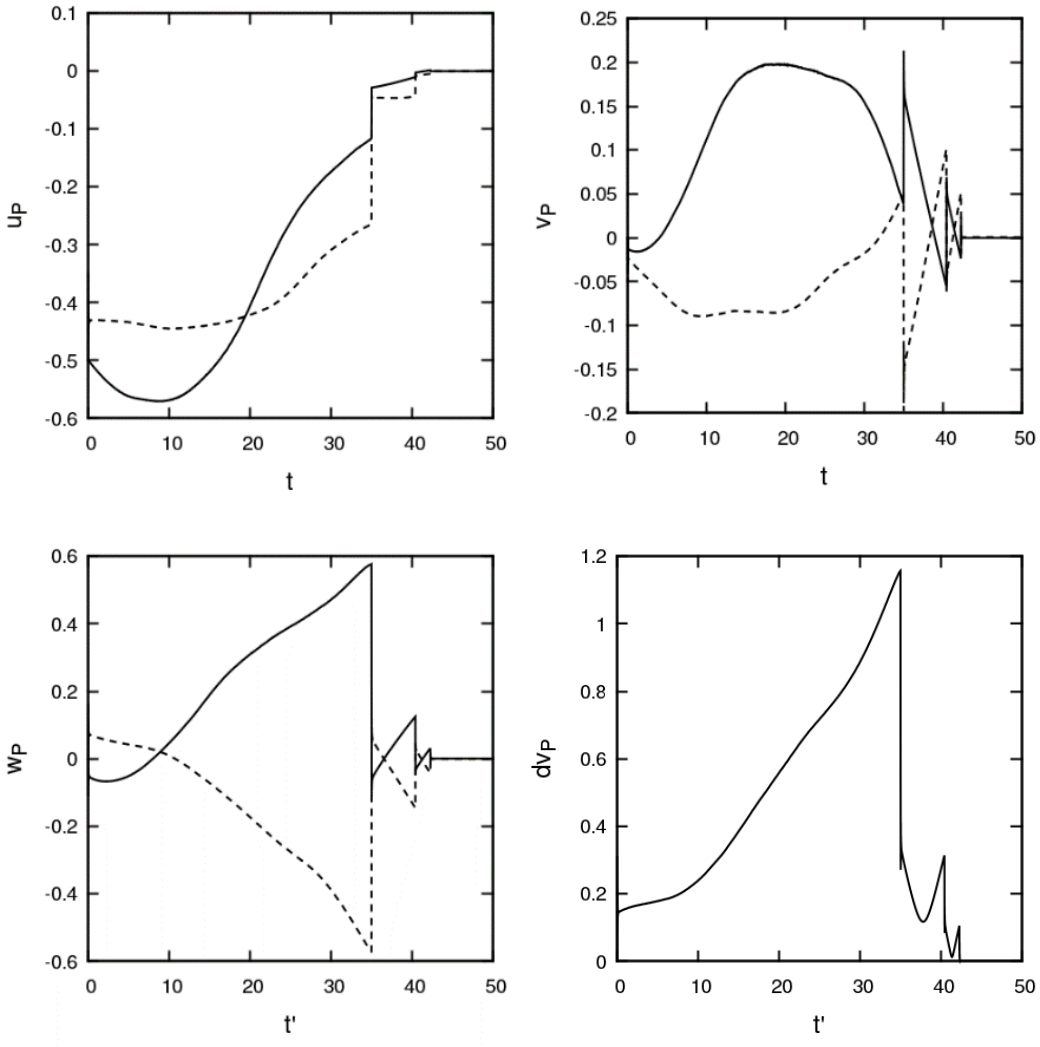

Figure 6.18: Linear velocity components of each particle in the $Re_\lambda = 51$ binary interaction over time. Lower-right demonstrates the evolution of relative velocity.

Figure 6.18 illustrates the linear velocity components for this event. It is observed here that the turbulence starts to play a role in altering the trajectories and the velocities of motion up until the first collision. In comparison to Figure 6.11, there now appears to be

small bumps in the velocity which is likely due to hydrodynamic forces altering the acceleration vector (which before was dominated by the van der Waals component). After the initial collision, the particles reverse their velocities and it is evident here that two further collisions take place before the particle relative velocity reaches zero. It is implied here that the increase in turbulence allows for the particles to move away from each other upon bouncing for a short time before the van der Waals attraction takes over the motion once again.

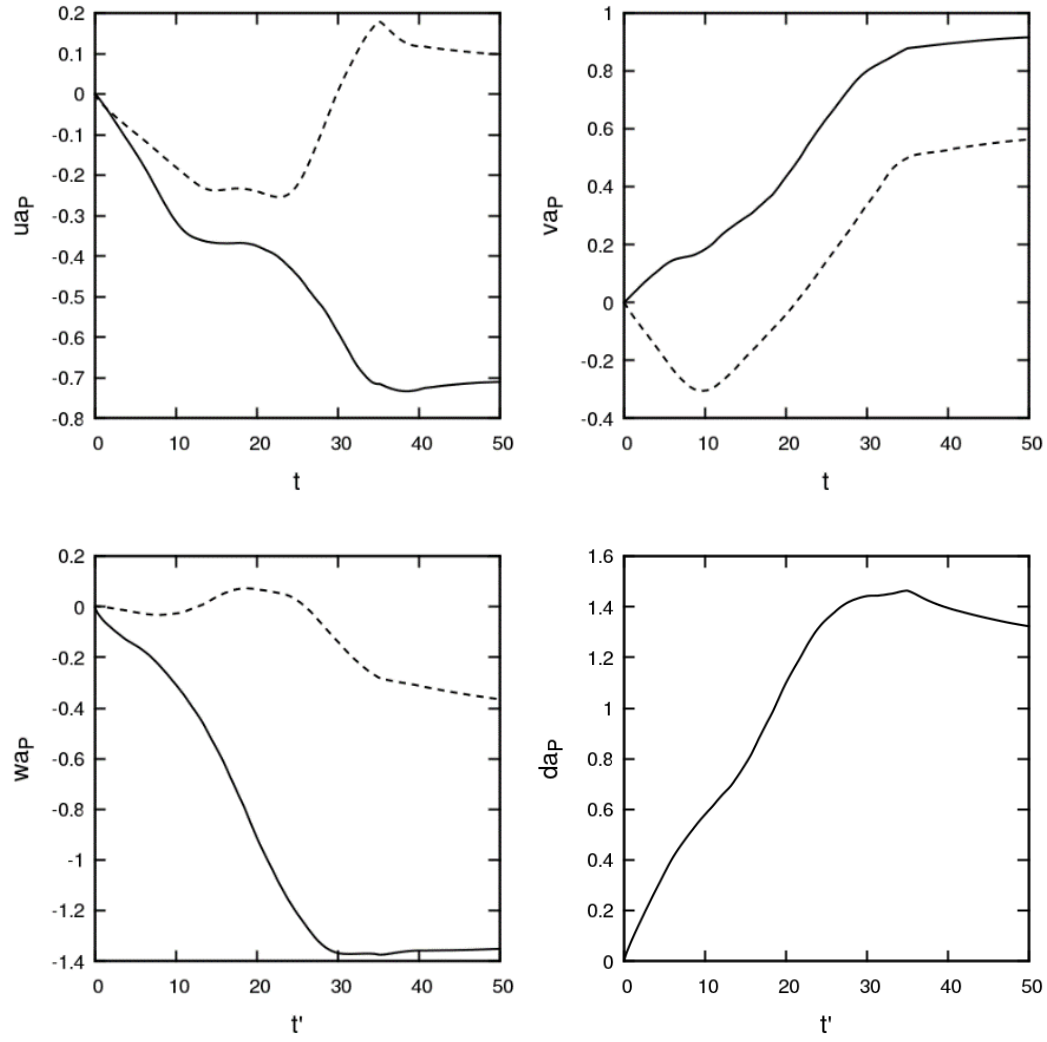

Figure 6.19: Angular velocity components of each particle in the $Re_\lambda = 51$ binary interaction over time. Lower-right demonstrates the evolution of relative angular velocity.

Figure 6.19 shows the temporal evolution of angular velocity over the trajectories during the collision event. The rotational motion is largely the same as before, with the bouncing

event seemingly having no effect on the angular velocities after the collision has taken place.

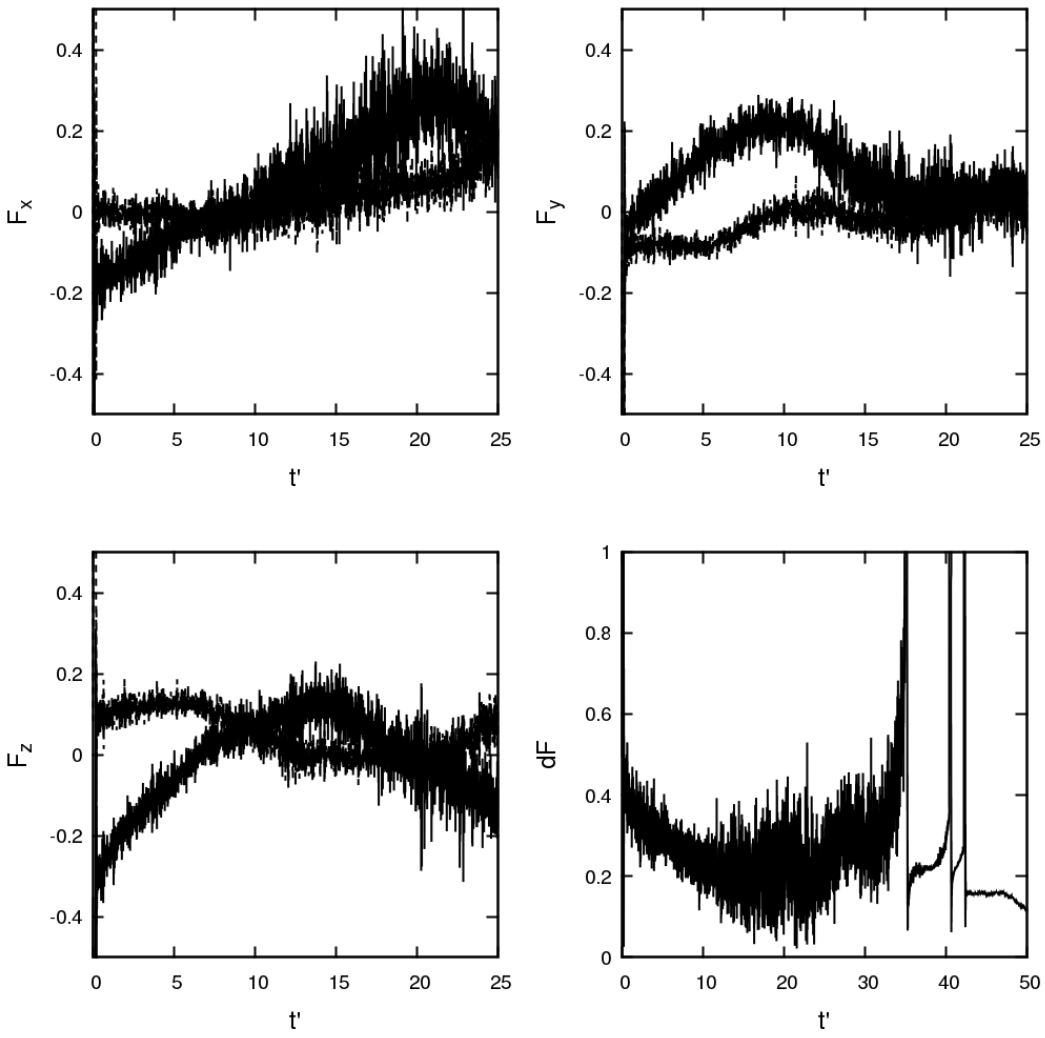

Figure 6.20: Hydrodynamic forces of each particle in the $Re_\lambda = 51$ binary interaction over time. Lower-right demonstrates the evolution of relative hydrodynamic force.

The hydrodynamic forces are plotted in Figure 6.20. As expected, we now observe much greater hydrodynamic forces in all three directions when compared to those seen at $Re_\lambda = 29$, with the forces increasing greatly as each collision occurs. Again, after the collision takes place, the particle relative hydrodynamic force begins to drop to zero.

Figure 6.21 shows the DLVO forces over the course of the trajectory. These are largely unaltered from before since the force calculation is solely a function of interparticle distance, however we see that during the 'bouncing' period ($30 < t' < 40$), the relative DLVO forces are comparable in magnitude to the peaks in the hydrodynamic forces,

which provides a mechanism for allowing the particles to bounce rather than simply stick together. From here it is theorised that in higher turbulence levels, the particles may have increased hydrodynamic forces after a bounce and could free themselves from the potential well caused by the van der Waals attraction.

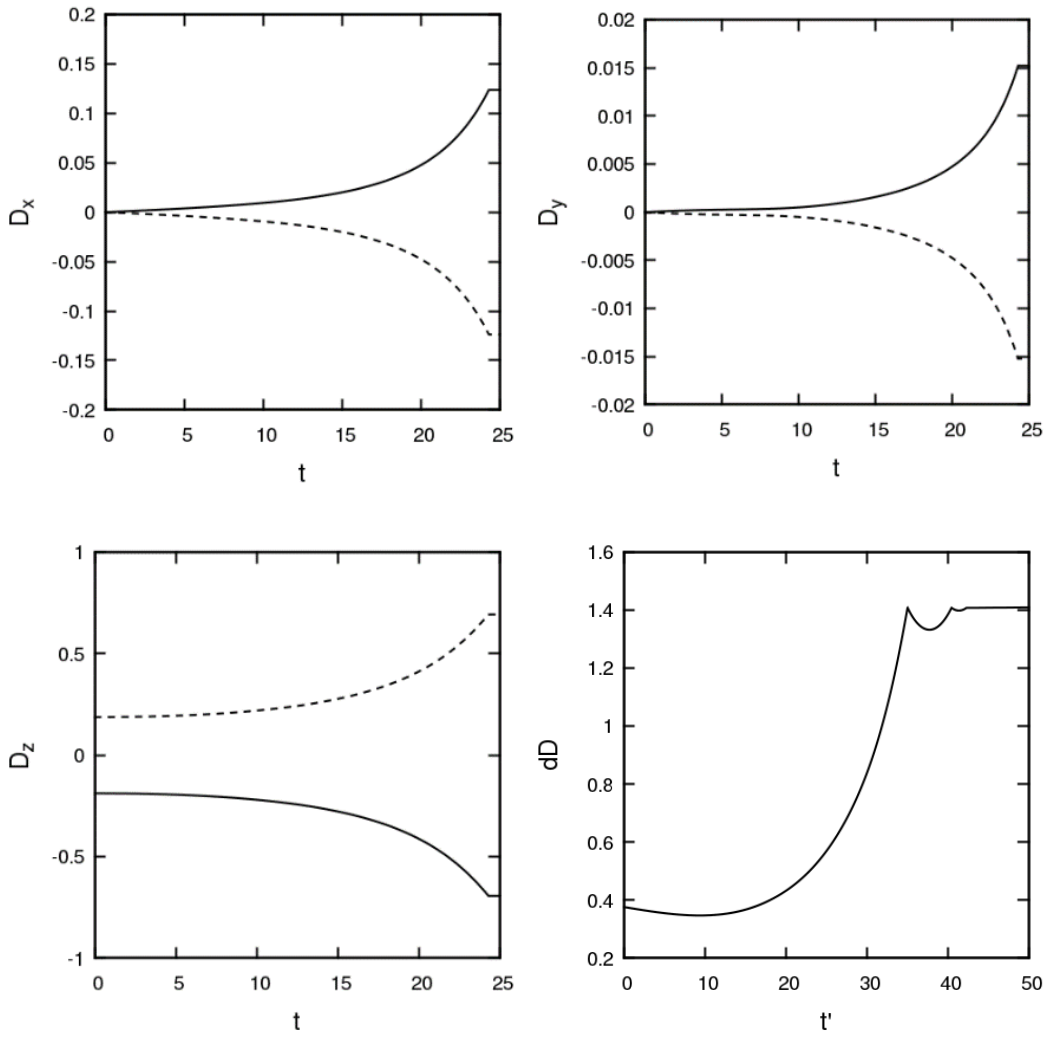

Figure 6.21: DLVO forces of each particle in the $Re_\lambda = 51$ binary interaction over time. Lower-right demonstrates the evolution of relative hydrodynamic force.

Finally, Figure 6.22 demonstrates the relative torque across the trajectories of the particles. A feature of interest is that after the collision, despite travelling away from each other, both particles experience similar torque forces which results in similar angular acceleration. This is likely due to the local fluid field encompassing both particles and providing approximately the same level of shear, but it also provides some justification for using models which approximate agglomerates as single particles, where all constituents observe the same local velocity field.

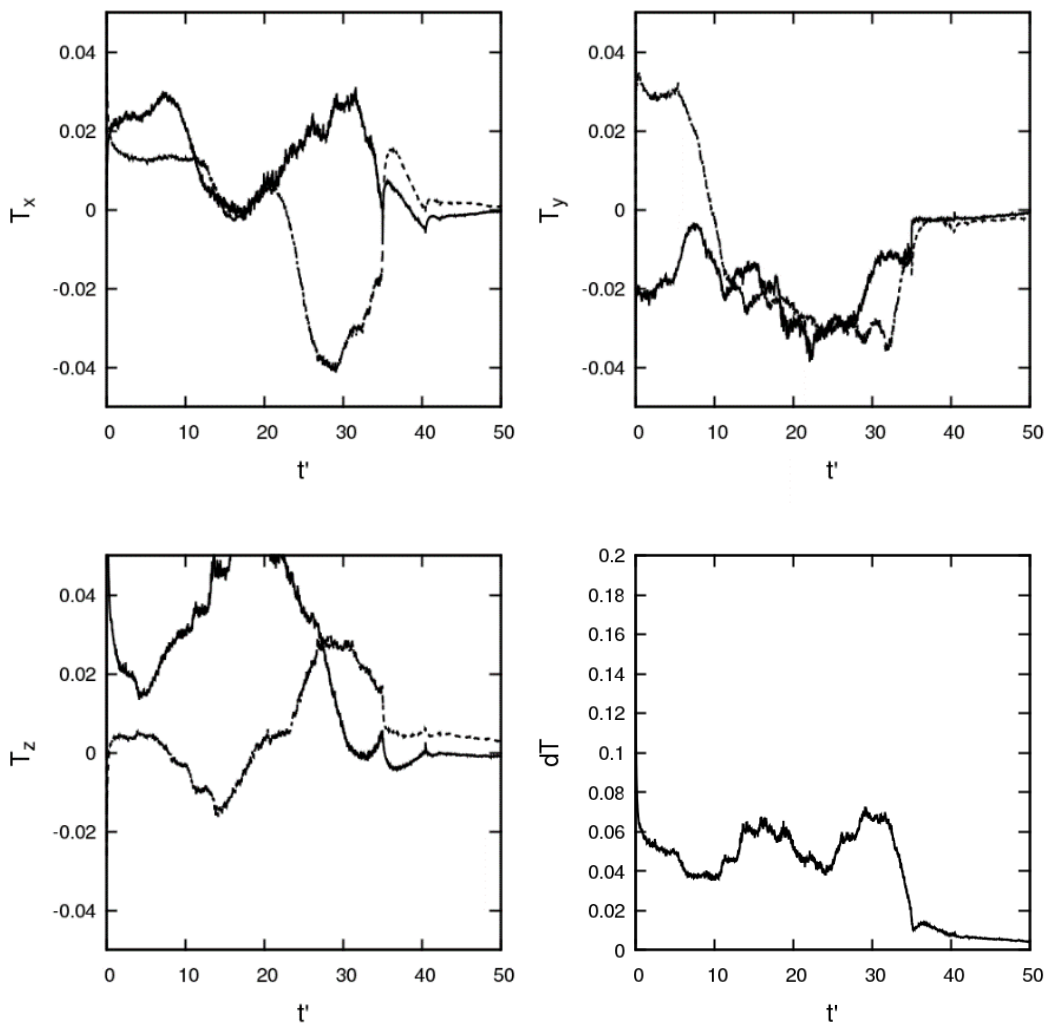

Figure 6.22: Torque due to hydrodynamic shear of each particle in the $Re_\lambda = 29$ binary interaction over time. Lower-right demonstrates the evolution of relative hydrodynamic force.

6.5.3 Particle-particle interaction at $Re_\lambda = 197$

Here we perform the same binary particle interaction simulations at $Re_\lambda = 197$, which is of the order of the highest turbulence level associated with the $Re_\tau = 180$ turbulent channel flow. In Figure 6.23 we observe the three-dimensional interaction trajectories associated with a typical event. It is clear that in this case, the two particles do not collide, despite their initial velocity vectors being orientated towards each other. It is also clear that the particles exhibit much more chaotic motion, appearing to change direction multiple times over the course of the interaction event.

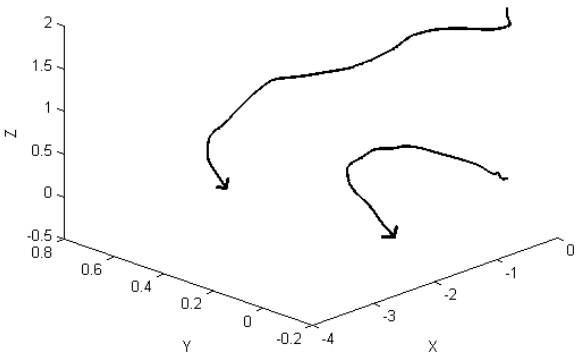

Figure 6.23: Typical three-dimensional interaction trajectories during $t' < 25$, lines represent the particle motion, plotted at particle centres. Arrows indicate direction.

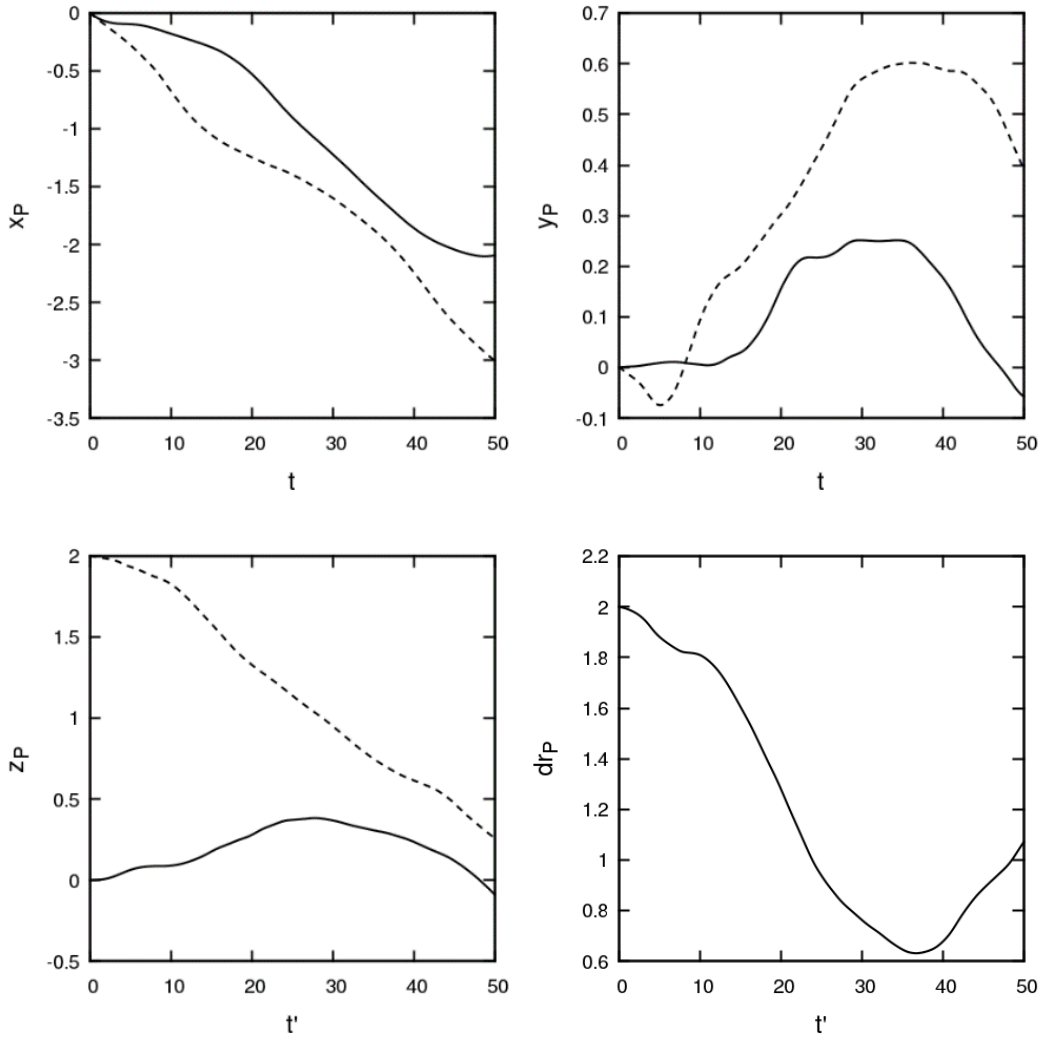

Figure 6.24: Centroid Position components of each particle in the $Re_\lambda = 197$ binary interaction over time. Lower-right demonstrates the evolution of interparticle distance.

Figure 6.24 demonstrates the position vector components over the course of the simulation. In all cases, the particles' motion is chaotic, and from the lower right plot we observe that the particles never collide with each other, even moving away from each other towards the end of the sample time.

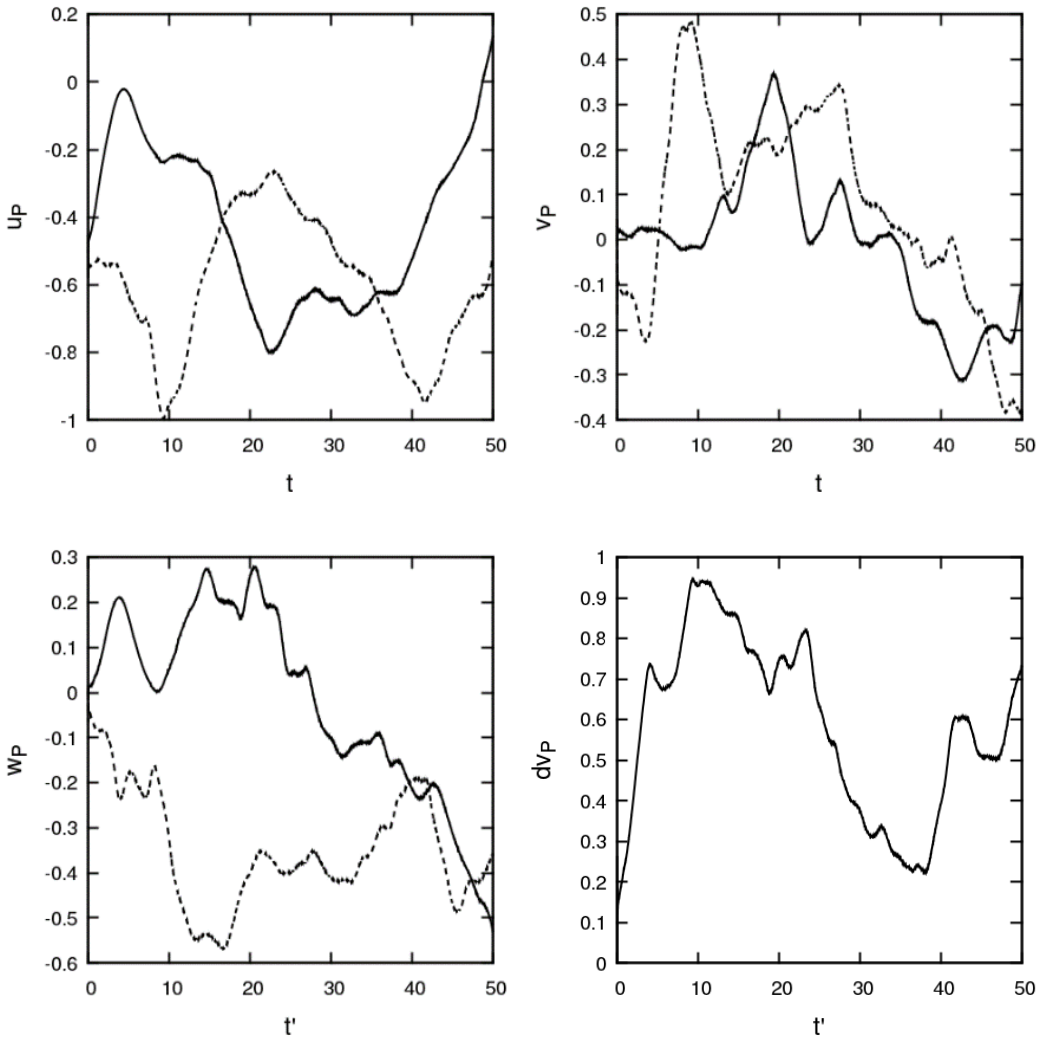

Figure 6.25: Linear velocity components of each particle in the $Re_\lambda = 197$ binary interaction over time. Lower-right demonstrates the evolution of relative velocity.

Figure 6.25 confirms the chaotic nature of the particle trajectory, with an indication that the calculated acceleration vector is frequently changing direction. In this case each particle shows no dependence on the location of the other, with relative velocities fluctuating throughout the entire sample time. Similar observations can be made for the evolution of angular velocity, presented in Figure 6.26, with the relative angular velocity actually increasing towards the end of the simulation.

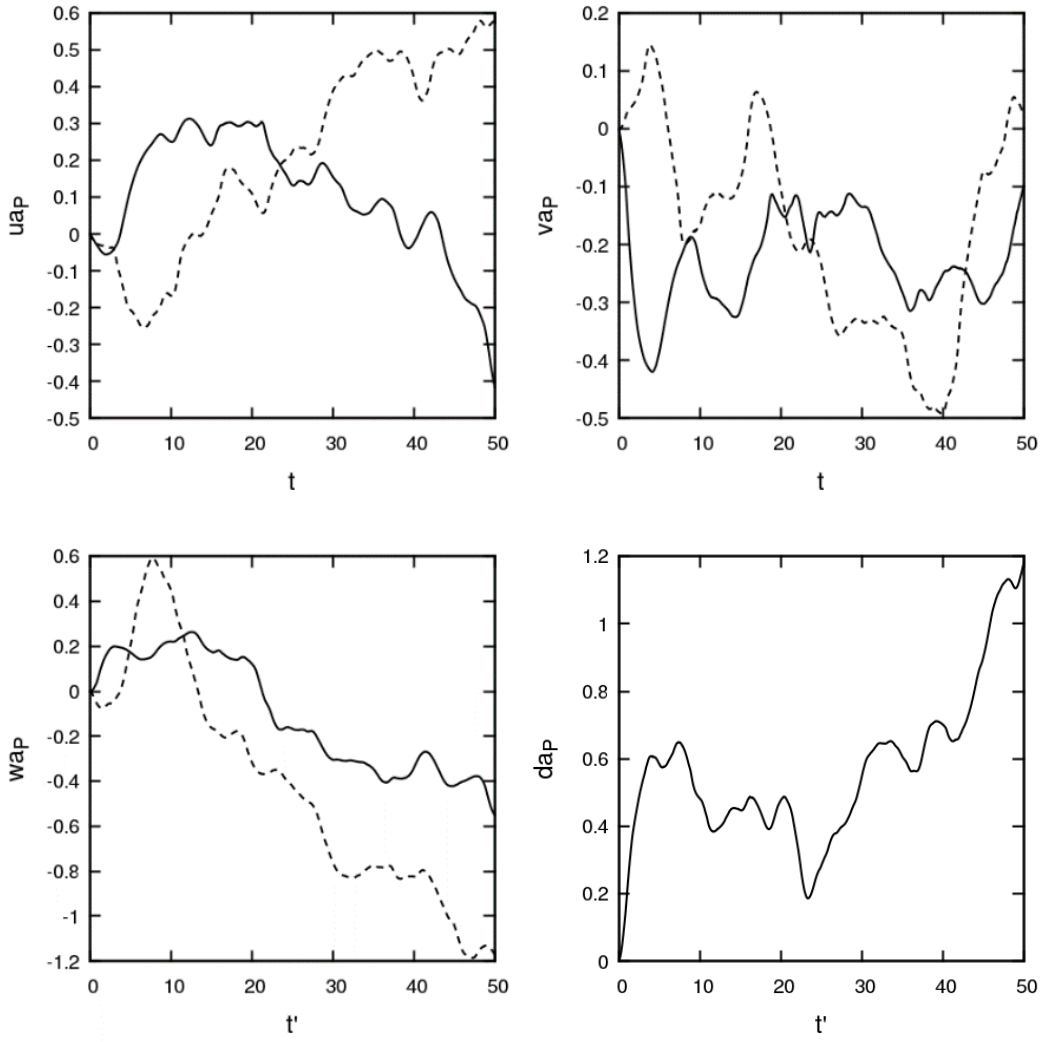

Figure 6.26: Angular velocity components of each particle in the $Re_\lambda = 197$ binary interaction over time. Lower-right demonstrates the evolution of relative angular velocity.

Figure 6.27 illustrates the hydrodynamic forces exerted on each particle over the course of their motion. Clearly these forces are far greater than at previous Reynolds numbers, with the particles travelling through eddies and turbulent regions of different magnitudes leading to fluctuating accelerations throughout the event. Since the mean of the plots is approximately zero in all three components, this indicates that the particles are experiencing isotropic influences from the turbulence.

We can also compare the hydrodynamic forces to those exerted between the particles due to DLVO forces (primarily attraction due to van der Waals) by contrasting the results of Figure 6.27 and Figure 6.28. In the latter figure, and for the majority of the motion, the attraction force is much less than that exerted by the hydrodynamic forces, but as the

particles approach one another, they are subject to increased attraction. This interaction causes the particles to travel towards each other but never hit, taking a roughly parabolic orbit. The built-up velocity and kinetic energy allows the particles to separate and, due to the lack of any collision, travel back to a regions where the turbulence once again dominates. This type of 'interaction with no collision' was found to be typical in regions of high turbulence since the particles already have increased relative velocities before any attraction takes place.

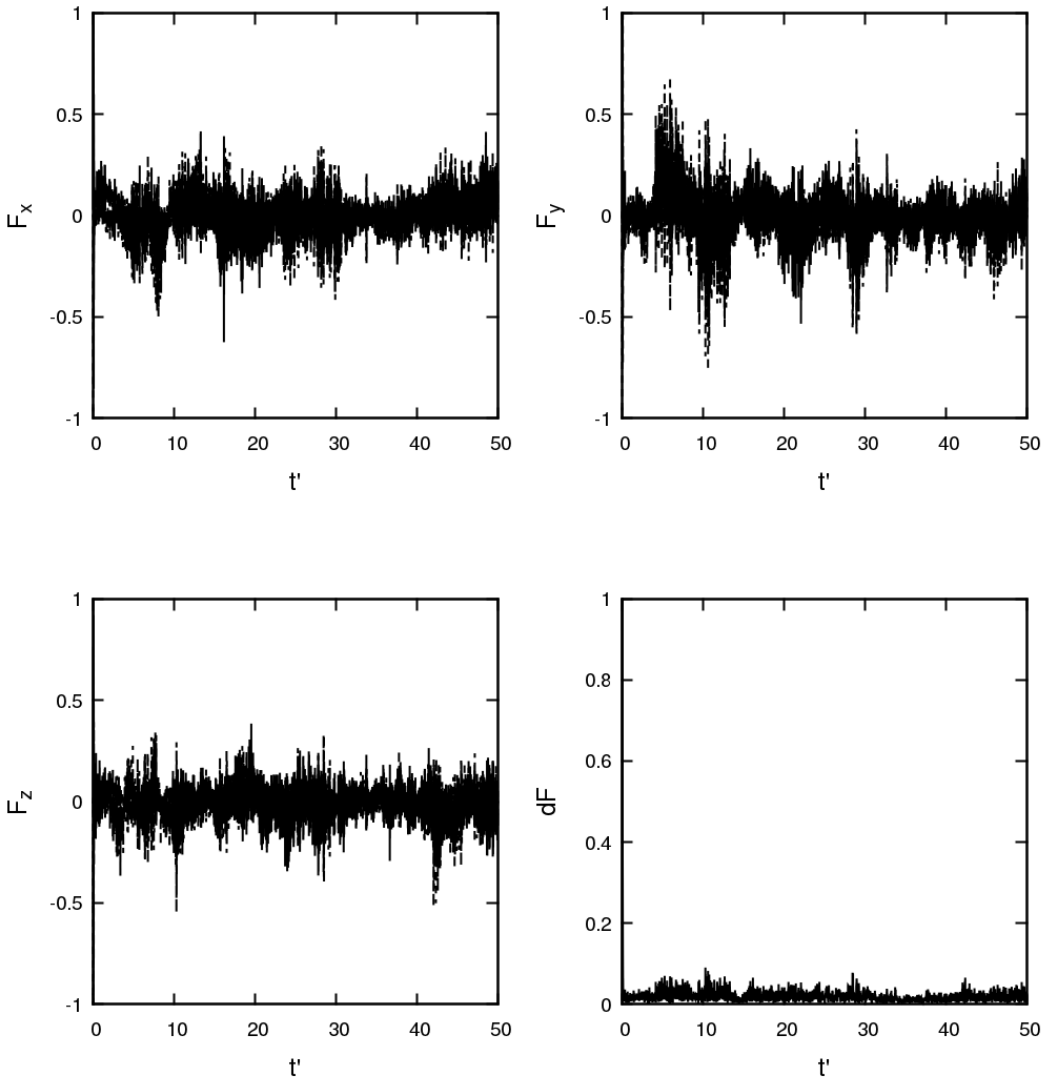

Figure 6.27: Hydrodynamic forces of each particle in the $Re_\lambda = 197$ binary interaction over time. Lower-right demonstrates the evolution of relative hydrodynamic force.

Finally, Figure 6.29 demonstrates the torque exerted on each particle over the course of the simulation. An interesting observation is that their magnitudes are very small but, despite this, we still observe rotational motion of the particles. However, this does

increases over time and if we take the example of the angular velocity about the z axis, the torque is almost always negative, so the particle can slowly build up a spin about that axis over the course of the sample time.

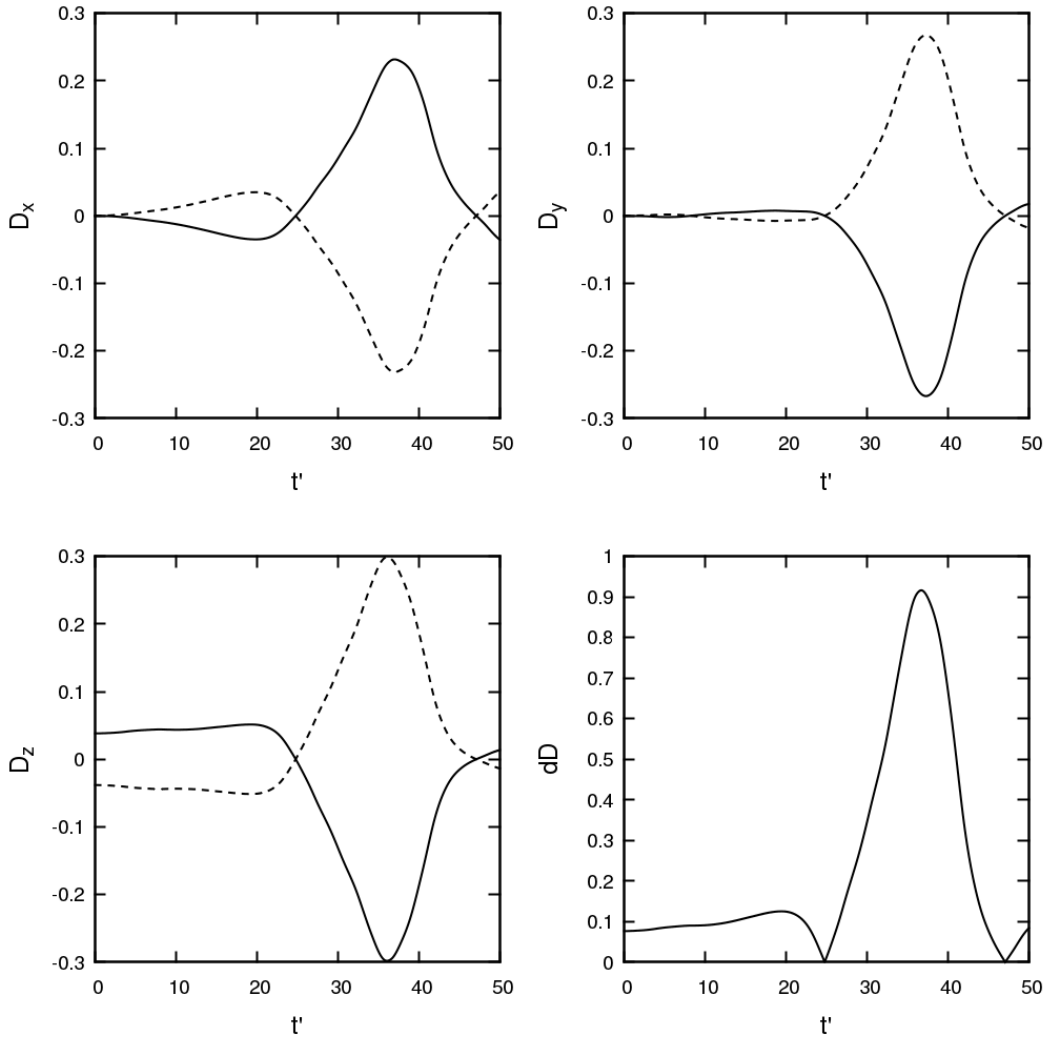

Figure 6.28: DLVO forces of each particle in the $Re_\lambda = 197$ binary interaction over time. Lower-right demonstrates the evolution of relative hydrodynamic force.

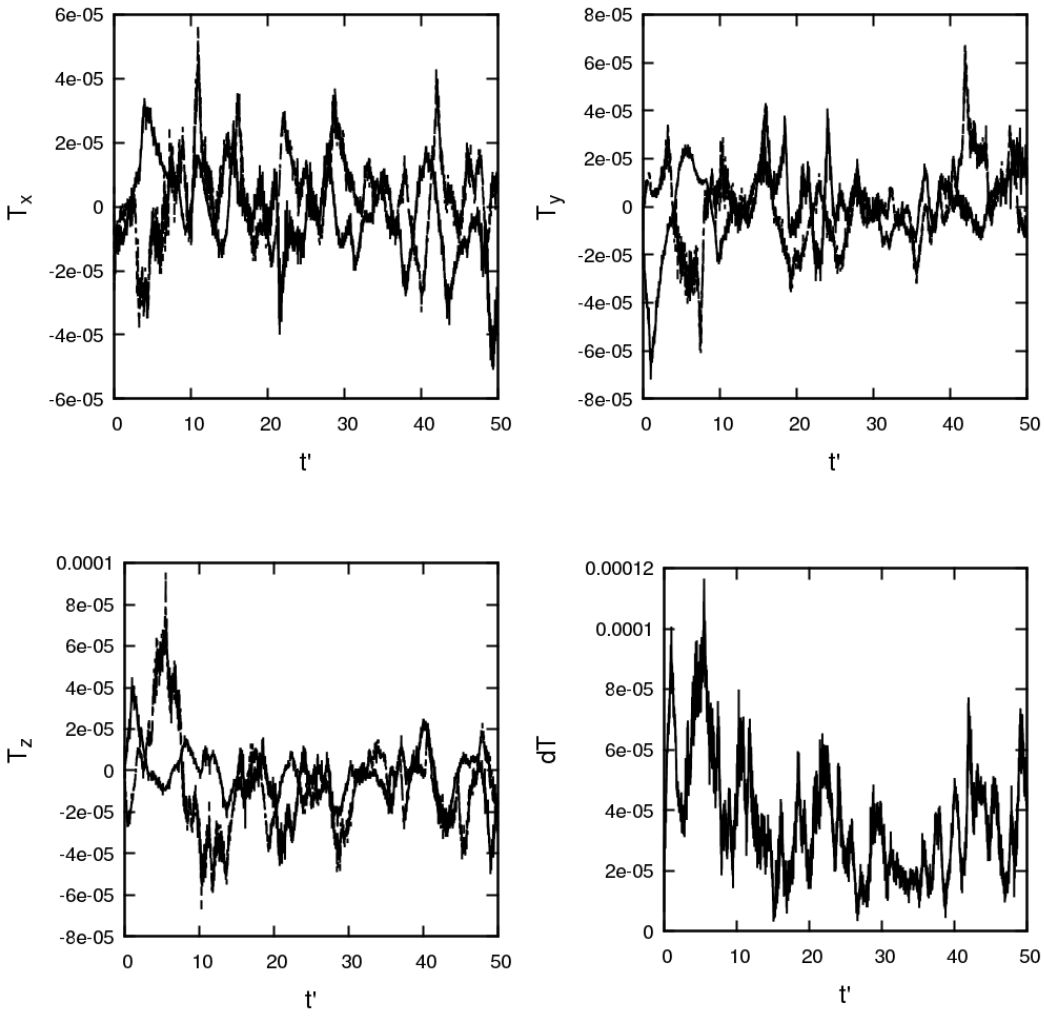

Figure 6.29: Torque due to hydrodynamic shear of each particle in the $Re_\lambda = 197$ binary interaction over time. Lower-right demonstrates the evolution of relative hydrodynamic force.

6.5.4 Effect of turbulence on particle interaction

To summarise and draw conclusions from the work reported in the previous subsections, we shall compare some of the above observed quantities in order to determine the effect which turbulence (specifically Reynolds number based on the Taylor microscale) has on the resulting particle motion. We have studied three boxes of periodic isotropic turbulence containing identical pairs of particles which were injected with initial velocity vectors matching those present in the previously studied turbulent channel flow at $Re_\tau = 180$.

The left plot in Figure 6.30 gives the relative separation for both particles at all three Reynolds numbers. Clearly, for the low Reynolds number turbulence field, the dominant force is van der Waals attraction which encourages the particles together. After this point they remain at constant separation, indicative of an agglomeration event. Conversely, as the Reynolds number increases, the particle pair moving in the $Re_\lambda = 51$ turbulence field collides and undergoes multiple bounces before they agglomerate. The particles in the high turbulence field do not collide despite moving close to one another, after which they are carried away by the hydrodynamic forces caused by the turbulence.

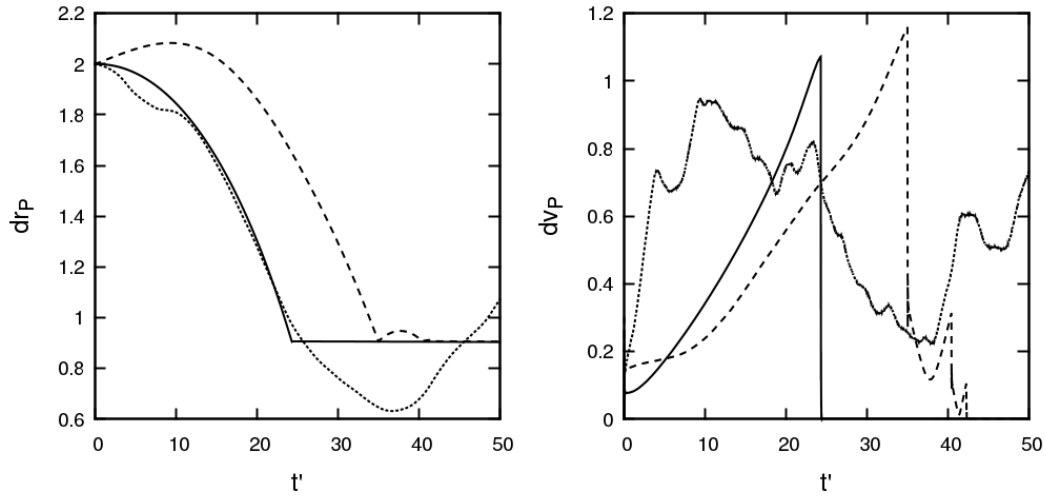

Figure 6.30: Effect of turbulence on interparticle distance (left) and relative velocity (right). Solid: $Re_\lambda = 29$; dashed: $Re_\lambda = 51$; dotted: $Re_\lambda = 197$.

The right-hand plot in Figure 6.30 illustrates the relative velocity magnitude for both particles over the course of their interaction. For the low Reynolds number turbulence field, one particle undergoes acceleration towards the second particle before coming to an almost instantaneous stop. Close inspection of the $Re_\lambda = 51$ trajectory confirms a very short period of time during which the particles 'bounce', however, the combination of strong attraction and a low coefficient of restitution (Table 13) ensures the relative distance remains low. After agglomeration, the particle's relative velocity is zero indicating that they travel together. The particles in the high Reynolds number turbulence field undergo much more chaotic motion, showing an increased response to the turbulent fluctuations they encounter. The motion and velocity of the particles in this case is governed by the turbulence field rather than the attraction from van der Waals forces.

6.6 Sensitivity studies on chemical properties

In this section we shall study the effect of varying mechanical and chemical parameters for particle interactions in the $Re_\lambda = 120$ box. Each simulation was initialized with particles separated and given a velocity equivalent to a typical pre-collision event in the buffer layer of the channel flow, obtained in the previous chapter. Statistics were gathered over 40 instances of one typical interaction setup, with random injection locations within the isotropic turbulence. These were run for 50 non-dimensional time units, which was enough time in all three previous boxes for the system to exhibit interaction dynamics (either agglomeration, bouncing or turbulent motion).

Simulation parameters are presented in Table 14, where e is the coefficient of restitution, A the Hamaker constant, and Θ the electric double layer potential. Simulation 0 represents 'standard' parameters, whilst 1, 2 and 3 are varying e, A and Θ, respectively.

Table 14: Sensitivity study simulation mechanical and chemical properties.

Parameter	**0**	**1a**	**1b**	**2a**	**2b**	**3a**	**3b**
r_P	50 μm	50 μm	50 μm	50 μm	50 μm	50 μm	50 μm
e	0.4	0.4	0.4	0.2	0.6	0.4	0.4
ρ_P/ρ_F	2.71	2.71	2.71	2.71	2.71	2.71	2.71
A	22.3 zJ	17.84 zJ	26.76 zJ	22.3 zJ	22.3 zJ	22.3 zJ	22.3 zJ
n	1×10^{-3} M	1×10^{-3} M	1×10^{-3} M	1×10^{-3} M	1×10^{-3} M	1×10^{-3} M	1×10^{-3} M
Θ	20 mV	20 mV	20 mV	20 mV	20 mV	16 mV	24 mV
κ	0.1 nm^{-1}	0.1 nm^{-1}	0.1 nm^{-1}	0.1 nm^{-1}	0.1 nm^{-1}	0.1 nm^{-1}	0.1 nm^{-1}
T_F	300 K	300 K	300 K	300 K	300 K	300 K	300 K

Figure 6.31 illustrates a typical event where two particles meet and where the surrounding turbulence field reacts to the collision. Note that the slice is through the particle on the right, indicated by the local velocity matching the velocity of the particle as per the immersed boundary condition. In the following subsections we shall examine the effect that modifying the restitution coefficient, the Hamaker constant and the electric double layer potential has on the resulting interaction dynamics.

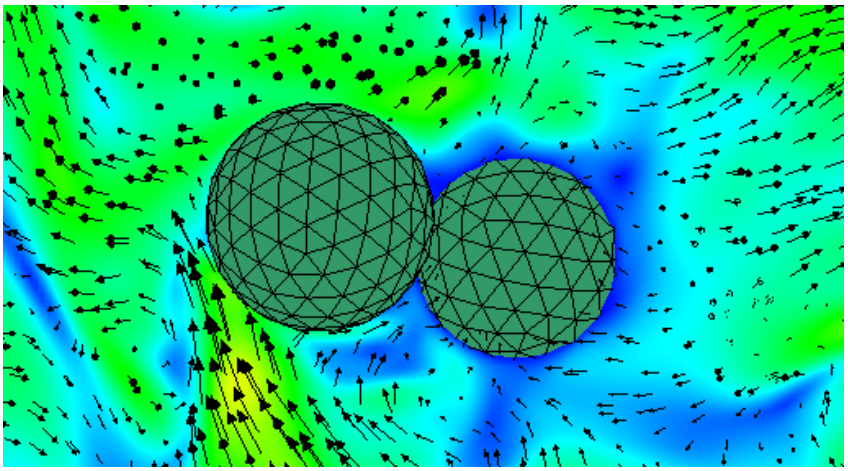

Figure 6.31: Typical binary particle interaction event with pseudocolour to represent fluid velocity magnitudes plotted alongside fluid velocity vectors.

6.6.1 Sensitivity to resitution coefficient

Figure 6.32 indicates the sensitivity of particle interactions events to the restitution coefficient by considering the mean relative displacement and mean relative velocity between the two particles sampled over 40 instances. Clearly this property has a strong effect on collision dynamics. A high *e* means that particles spend less time in close proximity to each other, which is a result of their retention of kinetic energy, allowing them to overcome the van der Waals attraction, and return back to a region where turbulence dominates.

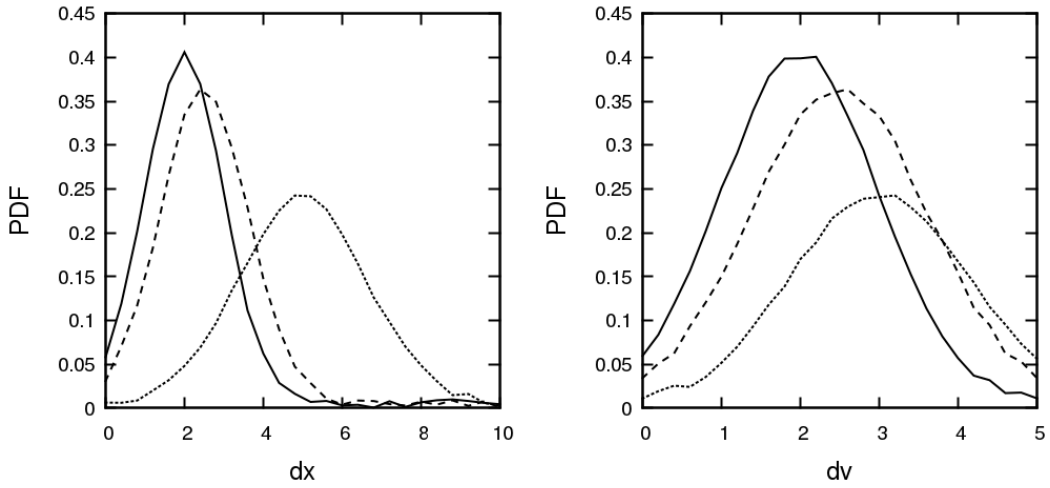

Figure 6.32: PDFs of relative displacement (left) and relative velocity (right) for *e*=0.2 (solid), *e*=0.4 (dashed) and *e*=0.6 (dotted).

The plot of relative velocity magnitude indicates a larger spread in velocities for increased e, which suggests a greater variety of events where particles frequently change their velocity. In practice, there are certain procedures which could modify this parameter such as pre-coating the particles with viscous films (Gollwitzer et al., 2012).

6.6.2 Sensitivity to Hamaker constant

The Hamaker constant directly modulates the attraction term in the DLVO potential equation, and as such should, it would be expected, govern the agglomeration rate. In Figure 6.33 we observe that actually the Hamaker constant has little effect on the resulting PDF of relative displacement. This implies that, for the range of values studied, the amount of time particles spend close to each other is actually independent of the strength of the attraction. An explanation for this is likely that the particles are undergoing near-hits but then travelling past each other and being carried away by turbulence once they overshoot the attractive region. This would make the agglomeration mechanism less sensitive to the Hamaker constant, since the agglomeration would only depend on the velocity vectors of the particles at the start of the event.

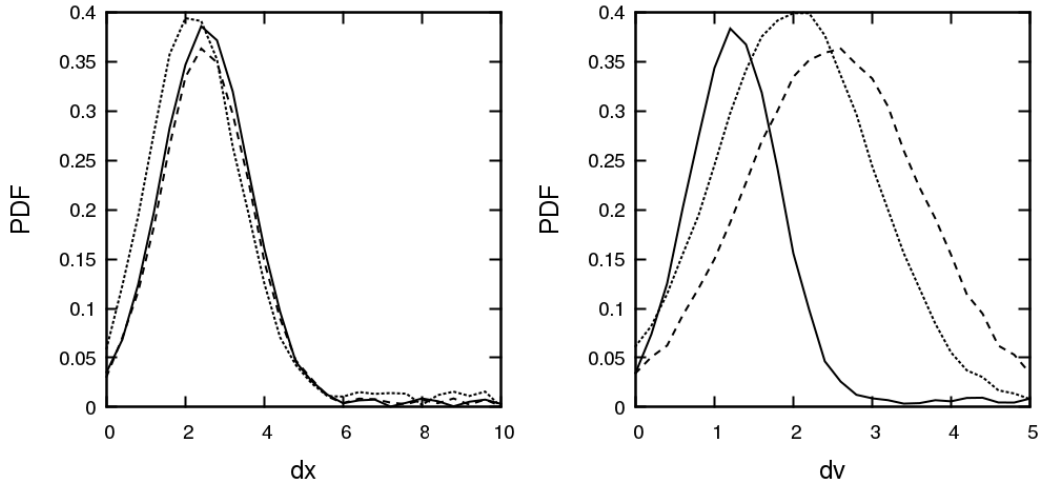

Figure 6.33: PDFs of relative displacement (left) and relative velocity (right) for A=17.84 zJ (solid), A=22.3 zJ (dashed) and A=26.76 zJ (dotted).

The above explanation is reinforced by the plot of relative velocity. Despite the particles not spending different amounts of time close to each other, they differ quite extensively in velocity, with high Hamaker constants meaning the particles travel faster and at a greater range of speeds. If the particles are shooting past each other then this would be

the case since the acceleration and subsequently range of velocities would depend primarily on the attraction strength. This behaviour implies that in high concentration fluid-particle dispersions, the Hamaker constant would also have an effect on decoupling the particles from local flow velocities, particularly for inertial particles. For low Stokes number particles, or tracers, the forces may cause additional collisions since the attractive forces may cause particle motion to deviate away from the fluid flow streamlines, which could lead to increased agglomeration rates, particularly in the bulk flow region.

In practice, the Hamaker constant has been shown to be adjustable by adding salt to the fluid (Shahidzadeh et al., 1998) and has also been shown to be temperature dependent (Bergström, 1997). By tuning this parameter, one has control over dispersion, collision rate and aggregation of particles in the flow.

6.6.3 Sensitivity to electric double layer

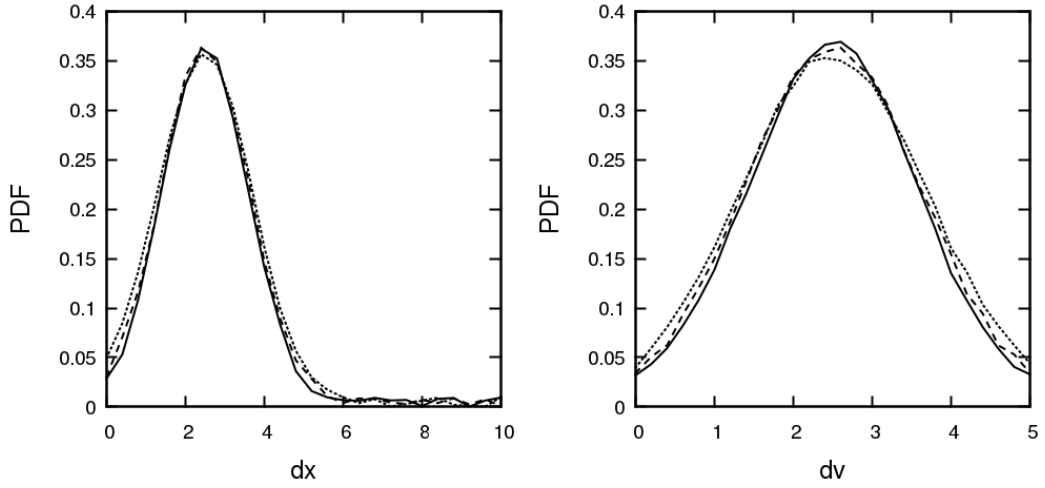

Figure 6.34: PDFs of relative displacement (left) and relative velocity (right) for Θ=16 mV (solid), Θ=20 mV (dashed) and Θ=16 mV (dotted).

Figure 6.34 illustrates the sensitivity of the relative displacement and relative velocity to the strength of the electric double layer. In both plots, it is evident that for the range of parameters considered, there is little effect on the resulting dynamics. This is due to the very short range associated with this force, which is negligible when compared to the length scales associated with both the particles and the turbulence. In order for this to have an effect on particle-scale motion, the size of the particles would need to be in the nano-size range.

6.7 Conclusions

A novel second-order accurate IBM has been implemented in the spectral element-based DNS code, Nek5000. The ghost-cell method is used to ensure the no-slip condition on the particle surface is met. For the first time, this has been used to predict binary particle interaction events at fine particle and turbulence scales using DLVO forcing. Periodic boxes of isotropic turbulence at four different Reynolds numbers based on the Taylor microscale have been obtained using the linear forcing method to resemble the regions of turbulence studied in previous chapters of this thesis. Slices of velocity magnitude contour plots are presented for all levels of turbulence, with each possessing their own eddy length spectra and range of velocities. The transition from initial conditions to steady state isotropic turbulence is also demonstrated, with temporal plots of the mean velocity fluctuation throughout the box.

A validation of the IBM has been performed which considers the drag force on a stationary spherical particle subject to flow fields with differing Reynolds numbers. For a high degree of mesh subdivisions on the particle, the calculated drag coefficients agree very well with frequently used empirical correlations. Particle-particle interactions have also been simulated in all four boxes of isotropic turbulence using the IBM solver. Particles were injected with initial conditions matching those present in pre-collision events sampled from the four-way coupled turbulent channel flow performed with identical dispersed, but point, particles at $Re_\tau = 180$.

For three of the systems, the trajectories, velocities, angular velocities, hydrodynamic and DLVO forces and torques are monitored and illustrated. It is evident that agglomeration takes place in the low Reynolds number system, whereas for the high Reynolds number system, the particles are encouraged together only slightly, with turbulent fluctuations dominating the bulk of their motion. This is further confirmed by a force magnitude analysis over the course of each particle's trajectory. As the Reynolds number increases, the particles still undergo collisions but are capable of bouncing, with the fluid forces during a collision competing with the van der Waals attraction. It is indicated that in the high Taylor microscale Reynolds number system, DLVO forces are either very low or comparable when compared to all the forces acting on the particle throughout its entire motion. This is in contrast with the low Reynolds number system, for which the DLVO forces are entirely dominant.

In the final buffer layer periodic box, DNS and the IBM have been used to study the effect of varying certain mechanical and chemical parameters on collision and aggregation dynamics. Here we observe that increasing the coefficient of restitution leads to reduced aggregation. It is also shown that increasing the Hamaker constant increases the mean speed of the interacting particles, but has little effect on the probability of agglomeration, over the range of A studied. We suggest that in this case particles are attracted to each other but often miss, leading to their reintroduction to regions of turbulence where DLVO forces are low. Finally, varying the electric double layer potential has little effect on the resulting statistics since its magnitude is small compared to other forces, and its effective range is also very short.

The work presented here provides a novel basis for the development of behavioural modification techniques which modify the above parameters of interest in order to obtain, or discourage, certain desired flow properties such as agglomeration, collision and deposition rates.

7 CONCLUSIONS

7.1 Conclusions

Motivated by the issues and uncertainties which present themselves within particle-laden flow processes in the nuclear industry, a set of novel multiphase computational fluid dynamic techniques have been developed, tested, validated and employed on multiple scales to further elucidate the relevant dynamics and generate new understanding surrounding multiphase processes. This new knowledge can be used to develop understanding surrounding particle-fluid and particle-particle interaction on a fundamental level. By doing so, we possess the ability to improve current waste-processing techniques and design safer and more efficient processes in the future. This chapter shall summarise the findings in this thesis and provide ideas for the potential further investigation in this field.

With this emphasis on developing our understanding of particle-particle interaction, two different system scales have been studied. The first scale is that of a turbulent channel flow at Reynolds number of 180 based on shear properties, which has been used to examine the macro-scale properties of particle dispersion, turbulence modulation and interaction by simulating thousands or millions of particles simultaneously. The second scale is that of the local turbulent eddy sizes, which has allowed for much more in-depth fundamental studies to be carried out in a box of isotropic homogeneous turbulence, probing the fundamentals of interactions involving very few particles in much more detail than has been performed previously in the literature.

Throughout, to predict the time evolution of the fluid phase velocity and pressure fields, direct numerical simulation (DNS) has been employed. The spectral element method-based solver, Nek5000 has been used extensively throughout this project to provide high-accuracy continuous phase predictions whilst providing the open-source flexibility to allow the coupling of additional components in order to model both the fluid and coupled fluid-solid phases.

In the first results chapter, DNS was used to predict a turbulent channel flow at $Re_\tau = 180$, with comparisons being made throughout with the previous simulation results of Kim et al. (1987) and Vreman and Kuerten (2014). Very good agreement was observed for all statistical quantities obtained, and instantaneous slices of velocity components indicate the various turbulence structures expected of such a system such as low speed streaks and turbulent eddies close to the wall.

A Lagrangian particle tracker (LPT) has been developed which runs concurrently alongside Nek5000, capable of accurately predicting the motion of up to millions of particles dispersed within the flow. The solver considers contributions from drag, shear lift, virtual mass and pressure gradient forces when calculating accelerations and uses non-dimensionalized parameters and variables to provide enhanced flexibility in solution relevancy. The solver uses the fourth order Runge-Kutta algorithm for integration and time-stepping to further provide increased accuracy to the calculated particle trajectories.

The one-way coupled LPT was extended to consider other mechanisms of relevance to flows of increased concentrations. Firstly, a particle-source-in-cell method was employed to two-way couple the particulate phase to the fluid by considering the momentum feedback effect in which the particles exert their force on the local fluid properties. Interparticle collisions (or four-way coupling) were implemented by identifying collision events, and the resulting trajectories were calculated using the elastic hard-sphere model. To reduce computational complexity, the binary particle search algorithm was improved to limit the amount of searches required. Finally, a particle-particle agglomeration model was implemented to determine aggregation events which result from particles colliding with the correct energies. The requirement for two particles to agglomerate is such that the kinetic energy must be insufficient to overcome the attractive potential due to the van der Waals component of the DLVO forces between the two colliders. Agglomerates are assumed to be spherical with total volumes equal to that of the sum of the constituents. The LPT was validated against the benchmark simulation results of Marchioli et al. (2008) with very good agreement obtained.

A particle-laden channel flow simulation was performed at $Re_\tau = 180$ using solid phase Stokes numbers of $St_\tau = 0.1, 50$ and 92. These were chosen to extend previously performed work by using values outside of the range usually considered. Further to this, these were used to further examine an effect in the literature which is not yet understood,

where particles exhibit increased rms velocity fluctuations in the near-wall region. The results of this investigation show that the inertial particles tend to overtake the fluid in the near-wall region, but lag behind the flow elsewhere. The increased near-wall rms velocity fluctuations identified in previous literature were also observed for two larger Stokes numbers, and this effect scaled with particle inertia. The other components of rms velocity fluctuations were suppressed. To further understand the particle dynamics, properties such as slip velocities, Reynolds numbers and drag coefficients were investigated. These indicated very distinct differences between the low Stokes number (tracer-like) particles and the high Stokes number (inertial) particles.

Concentration effects such as turbophoresis were also examined within the $Re_\tau = 180$ channel flow. Rapid near-wall accumulation was observed for particles with increased inertia, a process which reached a statistically steady state for large times ($t^* > 100$). Even after this point, a slow migration of particles towards the wall was identified. A force analysis was also performed indicating drag and lift forces to be the most dominant forces in all cases, with lift forces having a more pronounced effect for tracer-like particles. An interesting observation is that for low particle Stokes numbers, the lift force was responsible for reintroducing particles back into the bulk of the flow, working to reduce turbophoretic effects. This was enhanced at the boundary between the log-law and bulk region, and causes increased mixing.

The way particles behave in different wall-normal regions of the turbulent channel flow was studied by considering PDFs of various particle dynamical properties. For inertial particles, it was observed that those in the viscous sublayer exhibited two streamwise velocity regimes, with the greater coinciding with the peak of the streamwise velocity PDF distribution in the buffer layer. This implies that particles from the buffer layer are migrating towards the wall whilst retaining their increased velocities. A consequence of this is that some particles in the near-wall region are decoupled from the local flow velocities and hence increase the rms velocity fluctuations in that location. The development of high 'slowing' drag forces and increased velocity ranges at distances very near the wall is therefore explained.

These mechanisms have important consequences for processes such as deposition and near-wall particle accumulation. Through generating further understanding of them, we are able to more finely design and improve current multiphase processing systems in

which it may be desirable to encourage or discourage turbophoresis. For instance, by reducing the size of the particles dispersed within the flow, we also reduce the Stokes number, which will promote mixing and reduce the rate of bulk particle migration towards the wall.

To study preferential concentration and particle-turbulence interaction, the fluid topology classification scheme as presented in Blackburn et al. (1996) was employed to provide insight surrounding the types of turbulence structures each particle type was likely to encounter. Similar structures in the buffer and viscous sublayers were identified with particles congregating in these regions providing a turbulence mechanism by which inertial particles could rapidly migrate through the near-wall layers towards the wall.

Similar simulations were carried out at increased concentration, this time using two- and four-way coupling mechanisms to ensure accurate prediction of particle behaviour for higher volume fractions. The effect of introducing the two-way momentum feedback mechanism was first observed by monitoring various statistical quantities over the course of the flow readjustment period. It was observed that the inertial particles caused a reduction in the mean streamwise velocity and induced turbulence attenuation in all three components of the rms velocity fluctuations. The tracer-like particles had very little effect on the flow statistics. Particle statistics indicated increased turbophoresis for the high Stokes number particles and slight near-wall concentration increases for the low Stokes number particles. The turbulence attenuation meant that the particles also exhibited reduced decoupling from the flow, even in the near-wall regions. These results show that even for identical particle sizes, the extent of turbulence attenuation is related to density ratio, rather than solely the particle Stokes number. The previous results of Elghobashi (2007) and related works demonstrate that particle diameter plays a key role in determining the extent of turbulence interaction and modulation, but the current work suggests that the two properties work independently, and so classification should be based on size, density ratio and volume fraction rather than Stokes number and volume fraction.

With the inclusion of four-way coupling we observed further modifications to both the fluid and particle statistics. The consideration of interparticle collisions of inertial particles meant that the fluid streamwise velocity was actually increased slightly when compared to the two-way coupled regime, likely attributable to redistributed streamwise

momentum as a result of chaotic motion due to collisions. This is further demonstrated by the slight increase in turbulence intensities.

The particles in both systems were observed to behave in a very different manner. For the high Stokes number system, some particles would show rapid migration towards the wall whereas others would be influenced back into the bulk flow of the channel, leading to a build-up of particles very close to the wall and also at the channel centre. At low Stokes number, high transverse lift forces meant that particles would often be reintroduced back into the bulk flow, with very few particles even reaching the wall. Comparing speeds, inertial particles would overtake tracer particles close to the wall, but lag behind them in the bulk of the flow. The turbulence intensity profiles indicated that the collisions caused the inertial particles to exhibit isotropic and homogeneous motion throughout the width of the channel, whereas low Stokes number particles displayed similar motion to that of the unladen fluid.

To elucidate further the way in which the particles were interacting with each other in both systems, PDFs of their pre-collision relative velocity and angles were obtained and analysed. The results indicated that the buffer layer particles showed the greatest spread in streamwise velocities in both particle cases. As concluded earlier, inertial particles migrate from the bulk flow region to the near-wall region with a large range of velocities depending on where they migrate from and how long it takes them to reach the wall. This means that collisions in the near-wall regions are much more chaotic and often occur with increased wall-normal velocities, providing a mechanism to transfer wall-normal momentum from the bulk flow particles into those trapped within the wall region. Most of the collisions were also observed to take place very close to the wall, likely due to particle concentration. The collision angles indicated more head-on collisions for inertial particles, whilst the majority of collisions with tracer particles were glancing.

A deterministic agglomeration model based on collision energy and van der Waals attraction was introduced and demonstrated for the low density ratio system. Due to computational cost, the simulation was run for a short time, during which a reasonable amount of agglomeration was observed.

To develop further understanding surrounding the way in which particles interact in turbulence, an interface tracking method was developed and implemented to run

concurrently with Nek5000. The second-order accurate immersed boundary method used the ghost-cell method to ensure the no-slip condition on the particle surface was met. A validation and sensitivity study was performed by varying icosphere subdivision level, which produced very good agreement when calculating drag coefficients for high subdivision levels.

Linear forcing and DNS were used to generate four boxes which varied in Reynolds number based on the Taylor microscale, designed to represent those which might be observed in the $Re_\tau = 180$ turbulent channel flow. Binary particle interactions based on those most commonly occurring in the four-way coupled simulations were simulated and dynamic quantities such as trajectories, velocities, angular velocities, hydrodynamic and DLVO forces and torques were presented and compared. Results indicated that at low Reynolds numbers, particles agglomerate with ease, with very little influence of the turbulence over the course of the trajectories predicted. As the Reynolds number increases, force magnitudes indicate that the fluid influence increases and surpasses that of the van der Waals attractive force, leading to interactions which do not necessarily result in collisions. The interesting indication of this work is that these types of interaction take place in high-concentration regions, which suggests that the reason why we observe more agglomeration close to the wall is more due to the frequency of events which may result in an agglomeration, and not to the initial collision properties and dynamics being biased towards an aggregation result.

Finally, a sensitivity study in the buffer layer turbulent box on chemical and mechanical properties was performed to determine the effect of variation of these parameters on the resulting interaction dynamics. The coefficient of restitution had the greatest effect, since most collisions in the buffer layer led to at least one bounce, and so the trajectory is very responsive to the extent of retained kinetic energy. Here we determined that by increasing this parameter, interactions were less likely to result in particles remaining bound to each other. Increases in the Hamaker constant mean that the interaction has more energy, but sometimes such increases resulted in the particles missing each other and ending up at separation distances where they were carried away by the turbulence. The electric double layer potential had very little influence on the interaction, since the particles were on the micron scale and the range of interaction was only on the nanometer scale.

This thesis provides novel methods and analyses which have been developed to target the generation of new understanding of the dynamics underpinning particle-laden flows and particle-particle interaction. For the first time, new ways of analysing multiphase flows have provided explanations for phenomena which have not been provided elsewhere in the literature, such as the reasons for the existence of near-wall increased particle fluctuating velocities. We also challenge the current understanding of two- and four-way flow classification by providing examples of different levels of turbulence modulation through variation of density ratio as opposed to particle diameter. The work carried out in the final chapter begins to elucidate the dynamics of particle-particle interaction on the most fundamental level, with both phases modelled with very high accuracy. All of this understanding can be used to make better decisions when designing and improving the cost-effectiveness, efficiency and safety of fluid-particle flows, whether that be in nuclear waste-processing or any other industry which deals with such.

7.2 Recommendations for further work

The nature of the work performed here is such that it has opened up various new avenues for exploration by offering new tools with which to explore the dynamics of particle-laden flows. It also provides new questions surrounding our current understanding of these types of systems.

In the first two results chapters, a key observation was that of inertial particles migrating from the bulk flow to the near-wall regions. This has consequences for deposition rates and velocities which should be investigated to determine the extent of this mechanism's role in collisions with the wall. Furthermore, particles migrating to the near-wall regions which collide on the way produce strong wall-normal momentum transfer. We have already observed an increase in particle wall-normal turbulence intensities as a result of collisions, but this mechanism may have consequences for the resuspension of 'deposited' particles, wherein particles that are trapped in low speed streaks close to the wall could be ejected and reintroduced to the main flow by particles possessing greater energy. Further useful work would be to monitor this process and determine the extent of it for various particle Stokes numbers.

It is assumed in the literature that the fluid response to two- and four-way coupling is governed by both the Stokes number (based on the Kolmogorov scale) and the volume

fraction (or concentration of particles for monodispersed flows). The work presented in this thesis shows that the density ratio also has a key role to play in the effect of particle-turbulence interaction. This is likely because, at low density-ratio, even for high volume fractions the mass loading is still low and so the two-way coupling effects are small. A suggestion for further work would therefore be to study the effects of various diameters and density ratios at a fixed volume fraction to determine how both of these parameters affect the turbulence, instead of fixing one and varying the other to obtain the desired Stokes number. The flow-regime map of Elghobashi (1994) should then be revisited in light of new results to take into account mass-loading as well as volume-fraction and particle diameter.

The deterministic agglomeration model tested in the second results chapter provided a good indication that the type of nuclear simulant (or test material) particles considered are capable of aggregating, particularly in regions of high concentration such as those close to the wall. These types of simulations should be continued to observe the effects over larger timeframes. This is because even low Stokes number particles, which show little interaction with the wall, will form structures over larger timeframes with increased Stokes numbers. This provides the possibility for more interesting behaviour over the lifetime of a waste-processing system which should be investigated.

Furthermore, based on the results of the third chapter, the agglomeration model should be modified such that the agglomeration efficiency is altered depending upon the local turbulence level. At present, the agglomeration occurs if the interaction energy is sufficiently low that the particle cannot escape the potential well created by the van der Waals attraction. However, we have observed that the interaction process is not so simple, with results such as bouncing or missing particles potentially occurring based on the type of turbulence encountered. With more work on fundamental particle-particle interaction, one could correlate the agglomeration requirements with not only the interaction energy, but also the local rms velocity fluctuations.

Another drawback to the deterministic agglomeration model is that it does not take into account the fractal dimension associated with the formed structure. Large quantities of particles may form chain-like objects, and so the assumption that they form larger ‘spheres’ of constituent particles may not be accurate. To determine whether this is the case, immersed boundary simulations should be performed with tens of particles in

differing regions of turbulence in order to identify the type of structures formed. A stochastic model could then be formed by which agglomeration events could lead to modifications of the fractal dimension, or even the particle aspect ratio, for the case of non-spherical particles.

A lot of recent work has begun to investigate the behaviour of non-spherical particles in turbulent flows. The way the immersed boundary method-based solid phase solver has been developed is such that it can accurately predict the motion of any concave mesh, and so is perfect for simulation of non-spherical particles. Axisymmetric ellipsoidal particles such as needles and discs are prevalent in many industries and their interaction and aggregation is much more complex than that of two spheres. A similar LPT investigation should be carried out to deduce the types of interaction orientations, velocities and angular velocities present in non-spherical particle-laden channel flows. These could then be used in a similar manner to before to predict binary particle interactions, to determine how non-spherical particles collide and aggregate.

Finally, we demonstrated that behavioural modification techniques are capable of being developed based upon the effects observed through modification of key flow properties. The role of fluid/particle chemical and physical properties such as ionic strength and Hamaker constant should be investigated further, beyond the ranges of those presented in this thesis and at different Reynolds numbers to create a more complete representation of the conditions which either promote or discourage particle-particle aggregation.

8 REFERENCES

Aly, A., Trupp, A. and Gerrard, A. 1978. Measurements and prediction of fully developed turbulent flow in an equilateral triangular duct. *Journal of Fluid Mechanics.* **85**(1), pp.57-83.

Bäbler, M.U., Moussa, A.S., Soos, M. and Morbidelli, M. 2010. Structure and kinetics of shear aggregation in turbulent flows. I. Early stage of aggregation. *Langmuir.* **26**(16), pp.13142-13152.

Bagchi, P. and Balachandar, S. 2003. Effect of turbulence on the drag and lift of a particle. *Physics of Fluids.* **15**(11), pp.3496-3513.

Balachandar, S. 2009. A scaling analysis for point–particle approaches to turbulent multiphase flows. *International Journal of Multiphase Flow.* **35**(9), pp.801-810.

Balachandar, S. and Eaton, J. 2010. Turbulent Dispersed Multiphase Flow. *Annual Review of Fluid Mechanics.* **42**(1), pp.111-133.

Balachandar, S. and Maxey, M. 1989. Methods for evaluating fluid velocities in spectral simulations of turbulence. *Journal of Computational Physics.* **83**(1), pp.96-125.

BEIS. 2017. *Energy and Climate Change Public Attitude Tracker - Wave 21.* BEIS.

Bergström, L. 1997. Hamaker constants of inorganic materials. *Advances in Colloid and Interface Science.* **70**, pp.125-169.

Beyer, R.P. and LeVeque, R.J. 1992. Analysis of a one-dimensional model for the immersed boundary method. *SIAM Journal on Numerical Analysis.* **29**(2), pp.332-364.

Blackburn, H.M., Mansour, N.N. and Cantwell, B.J. 1996. Topology of fine-scale motions in turbulent channel flow. *Journal of Fluid Mechanics.* **310**, pp.269-292.

Blackwelder, R.F. and Haritonidis, J.H. 1983. Scaling of the bursting frequency in turbulent boundary layers. *Journal of Fluid Mechanics.* **132**, pp.87-103.

Boersma, B.J. 2011. Direct numerical simulation of turbulent pipe flow up to a Reynolds number of 61,000. In: *Journal of Physics: Conference Series*: IOP Publishing, p.042045.

Boivin, M., Simonin, O. and Squires, K.D. 1998. Direct numerical simulation of turbulence modulation by particles in isotropic turbulence. *Journal of Fluid Mechanics.* **375**, pp.235-263.

Boivin, M., Simonin, O. and Squires, K.D. 2000. On the prediction of gas–solid flows with two-way coupling using large eddy simulation. *Physics of Fluids.* **12**(8), pp.2080-2090.

Borée, J. and Caraman, N. 2005. Dilute bidispersed tube flow: Role of interclass collisions at increased loadings. *Physics of Fluids.* **17**(5), p055108.

Bradshaw, P. 1967. 'Inactive' motion and pressure fluctuations in turbulent boundary layers. *Journal of Fluid Mechanics.* **30**(2), pp.241-258.

Bremhorst, K. and Walker, T. 1973. Spectral measurements of turbulent momentum transfer in fully developed pipe flow. *Journal of Fluid Mechanics.* **61**(1), pp.173-186.

Breuer, M., Alletto, M. and Flow, F. 2012. Efficient simulation of particle-laden turbulent flows with high mass loadings using LES. *International Journal of Heat and Fluid Flow.* **35**, pp.2-12.

Breuer, M. and Almohammed, N. 2015. Modeling and simulation of particle agglomeration in turbulent flows using a hard-sphere model with deterministic collision detection and enhanced structure models. *International Journal of Multiphase Flow*. **73**, pp.171-206.

Brown, G.L. and Thomas, A.S. 1977. Large structure in a turbulent boundary layer. *The Physics of Fluids.* **20**(10), pp.S243-S252.

Brundrett, E. and Baines, W.D. 1964. The Production and Diffusion of Vorticity in Duct Flow. *Journal of Fluid Mechanics.* **19**(3), pp.375-394.

Burmester de Bessa Ribas, R., Lourenco, L. and Riethmuller, M. 1980. A kinetic model for a gas-particle flow. Pneumotransport 5. In: *Proceedings of the Fifth International Conference on the Pneumatic Transport of Solids in Pipes, Paper B*, pp.99-112.

Caraman, N., Borée, J. and Simonin, O. 2003. Effect of collisions on the dispersed phase fluctuation in a dilute tube flow: Experimental and theoretical analysis. *Physics of Fluids.* **15**(12), pp.3602-3612.

Choi, J., Park, Y., Kwon, O. and Lee, C. 2016. Interparticle collision mechanism in turbulence. *Physical Review E.* **93**(1), p013112.

Chong, M.S., Perry, A.E. and Cantwell, B.J. 1990. A general classification of three-dimensional flow fields. *Physics of Fluids A: Fluid Dynamics.* **2**(5), pp.765-777.

Claymath. 2018. *Existence and smoothness of the Navier-Stokes equation.* [Online]. [Accessed 16th May]. Available from: http://www.claymath.org/sites/default/files/navierstokes.pdf

Clift, R., Grace, J.R. and Weber, M.E. 2005. *Bubbles, drops, and particles.* Courier Corporation.

Comte-Bellot, G. 1976. Hot-wire anemometry. *Annual Review of Fluid Mechanics.* **8**(1), pp.209-231.

Crowe, C., Gore, R. and Troutt, T. 1985. Particle dispersion by coherent structures in free shear flows. *Particulate Science and Technology.* **3**(3-4), pp.149-158.

Crowe, C., Sommerfeld, M. and Tsuji, Y. 1998. *Multiphase flows with particles and droplets*. CRC Press, New York.

Crowe, C.T. 2000. On models for turbulence modulation in fluid–particle flows. *International Journal of Multiphase Flow.* **26**(5), pp.719-727.

Crowe, C.T. 2005. *Multiphase flow handbook.* CRC press.

Dandy, D.S. and Dwyer, H.A. 1990. A sphere in shear flow at finite Reynolds number: effect of shear on particle lift, drag, and heat transfer. *Journal of Fluid Mechanics.* **216**, pp.381-410.

Deardorff, J.W. 1970. A numerical study of three-dimensional turbulent channel flow at large Reynolds numbers. *Journal of Fluid Mechanics.* **41**(2), pp.453-480.

Demuren, A.O. and Rodi, W. 1984. Calculation of Turbulence-Driven Secondary Motion in Non-Circular Ducts. *Journal of Fluid Mechanics.* **140**(3), pp.189-222.

Den Toonder, J. and Nieuwstadt, F. 1997. Reynolds number effects in a turbulent pipe flow for low to moderate Re. *Physics of Fluids.* **9**(11), pp.3398-3409.

Derjaguin, B. and Landau, L. 1941. Theory of the stability of strongly charged lyophobic sols and of the adhesion of strongly charged particles in solutions of electrolytes. *Acta Physicochim. URSS.* **14**(6), pp.633-662.

Doering, C.R. and Petrov, N.P. 2005. Low-wavenumber forcing and turbulent energy dissipation. *Progress in Turbulence.* Springer, pp.11-18.

Driscoll, R.J., Kennedy, L.A. and Y., P. 1983. A model for the turbulent energy spectrum. *The Physics of Fluids.* **26**(5), pp.1228-1233.

Dritselis, C.D. and Vlachos, N.S. 2008. Numerical study of educed coherent structures in the near-wall region of a particle-laden channel flow. *Physics of Fluids.* **20**(5), p055103.

Dritselis, C.D. and Vlachos, N.S. 2011. Large eddy simulation of gas-particle turbulent channel flow with momentum exchange between the phases. *International Journal of Multiphase Flow.* **37**(7), pp.706-721.

Druzhinin, O. 2001. The influence of particle inertia on the two-way coupling and modification of isotropic turbulence by microparticles. *Physics of Fluids.* **13**(12), pp.3738-3755.

Durst, F., Melling, A. and Whitelaw, J.H. 1976. Principles and practice of laser-Doppler anemometry. *NASA STI/Recon Technical Report A.* **76**.

Eaton, J.K. and Fessler, J. 1994. Preferential concentration of particles by turbulence. *International Journal of Multiphase Flow.* **20**, pp.169-209.

Eaton, J.K. and Segura, J.C. 2006. On Momentum Coupling Methods for Calculation of Turbulence Attenuation in Dilute Particle-Laden Gas Flows. In: *IUTAM Symposium on Computational Approaches to Multiphase Flow, 2006, Dordrecht*. Springer Netherlands, pp.39-42.

Eggels, J., Unger, F., Weiss, M., Westerweel, J., Adrian, R., Friedrich, R. and Nieuwstadt, F. 1994. Fully developed turbulent pipe flow: a comparison between direct numerical simulation and experiment. *Journal of Fluid Mechanics.* **268**(1), pp.175-210.

Eggels, J., Westerweel, J., Nieuwstadt, F. and Adrian, R. 1993. Direct numerical simulation of turbulent pipe flow. *Applied Scientific Research.* **51**(1), pp.319-324.

El Khoury, G.K., Schlatter, P., Noorani, A., Fischer, P.F., Brethouwer, G. and Johansson, A.V. 2013. Direct numerical simulation of turbulent pipe flow at moderately high Reynolds numbers. *Flow, turbulence and combustion.* **91**(3), pp.475-495.

Elghobashi, S. 1991. Particle-laden turbulent flows: direct simulation and closure models. *Applied Scientific Research.* **48**(3-4), pp.301-314.

Elghobashi, S. 1994. On predicting particle-laden turbulent flows. *Applied Scientific Research.* **52**(4), pp.309-329.

Elghobashi, S. 2007. An Updated Classification Map of Particle-Laden Turbulent Flows. In: *IUTAM Symposium on Computational Approaches to Multiphase Flow: Proceedings of an IUTAM Symposium held at Argonne National Laboratory, October 4-7, 2004*: Springer Science & Business Media, p.3.

Fairweather, M. and Hurn, J.-P. 2008. Validation of an anisotropic model of turbulent flows containing dispersed solid particles applied to gas–solid jets. *Computers & Chemical Engineering.* **32**(3), pp.590-599.

Fairweather, M. and Yao, J. 2009. Mechanisms of particle dispersion in a turbulent, square duct flow. *AIChE journal.* **55**(7), pp.1667-1679.

Farmer, R.A. 1969. *Liquid droplet trajectories in two-phase flow*. thesis, Massachusetts Institute of Technology.

Fessler, J.R., Kulick, J.D. and Eaton, J.K. 1994. Preferential concentration of heavy particles in a turbulent channel flow. *Physics of Fluids.* **6**(11), pp.3742-3749.

Fischer, P.F., Lottes, J.W. and Kerkemeier, S.G. 2008. *Nek5000.* [Online]. [Accessed 1st September]. Available from: http://nek5000.mcs.anl.gov

Flannery, B.P., Press, W., Teukolsky, S. and Vetterling, W. 1992. Numerical recipes in FORTRAN: The art of scientific computing. *Cambridge University Press.* pp.704-716.

Forney, L.J. and Spielman, L.A. 1974. Deposition of coarse aerosols from turbulent flow. *Journal of Aerosol Science.* **5**(3), pp.257-271.

Friedlander, S. and Johnstone, H. 1957. Deposition of suspended particles from turbulent gas streams. *Industrial & Engineering Chemistry.* **49**(7), pp.1151-1156.

Gavrilakis, S. 1992. Numerical simulation of low-Reynolds-number turbulent flow through a straight square duct. *Journal of Fluid Mechanics.* **244**, pp.101-129.

Gessner, F.B. and Jones, J.B. 1965. On Some Aspects of Fully-Developed Turbulent Flow in Rectangular Channels. *Journal of Fluid Mechanics.* **23**, pp.689-713.

Gessner, F.B., Po, J. and Emery, A. 1979. Measurements of developing turbulent flow in a square duct. *Turbulent Shear Flows I.* Springer, pp.119-136.

Gore, R.A. and Crowe, C.T. 1989. Effect of particle size on modulating turbulent intensity. *International Journal of Multiphase Flow.* **15**(2), pp.279-285.

Gosman, A.D. and loannides, E. 1983. Aspects of Computer Simulation of Liquid-Fueled Combustors. *Journal of Energy.* **7**(6), pp.482-490.

Grant, I. 1997. Particle image velocimetry: a review. *Proceedings of the Institution of Mechanical Engineers, Part C: Journal of Mechanical Engineering Science.* **211**(1), pp.55-76.

Große, S. and Schröder, W. 2008. Dynamic wall-shear stress measurements in turbulent pipe flow using the micro-pillar sensor MPS 3. *International Journal of Heat and Fluid Flow.* **29**(3), pp.830-840.

Guha, D., Ramachandran, P.A. and Dudukovic, M.P. 2007. Flow field of suspended solids in a stirred tank reactor by Lagrangian tracking. *Chemical Engineering Science.* **62**(22), pp.6143-6154.

Hill, R.J. 1978. Models of the scalar spectrum for turbulent advection. *Journal of Fluid Mechanics.* **88**(3), pp.541-562.

Hinsch, K.D. 2002. Holographic particle image velocimetry. *Measurement Science and Technology.* **13**(7), pR61.

Hoagland, L.C. 1962. *Fully developed turbulent flow in straight rectangular ducts: secondary flow, its cause and effect on the primary flow*. thesis, Massachusetts Institute of Technology.

Holmén, V. 2012. *Methods for vortex identification*. (Doctoral thesis).

Hu, H.H. 1996. Direct simulation of flows of solid-liquid mixtures. *International Journal of Multiphase Flow.* **22**(2), pp.335-352.

Ilori, T.A. 1971. *Turbulent deposition of aerosol particles inside pipes*. (Doctoral thesis)

Inthavong, K., Tian, Z.F., Li, H.F., Tu, J.Y., Yang, W., Xue, C.L. and Li, C.G. 2006. A Numerical Study of Spray Particle Deposition in a Human Nasal Cavity. *Aerosol Science and Technology.* **40**(11), pp.1034-1045.

Kajishima, T. and Miyake, Y. 1992. A discussion on eddy viscosity models on the basis of the large eddy simulation of turbulent flow in a square duct. *Computers & Fluids.* **21**(2), pp.151-161.

Kiger, K. and Pan, C. 2002. Suspension and turbulence modification effects of solid particulates on a horizontal turbulent channel flow. *Journal of Turbulence.* **3**(19), pp.1-17.

Kim, J., Moin, P. and Moser, R. 1987. Turbulence statistics in fully developed channel flow at low Reynolds number. *Journal of Fluid Mechanics.* **177**(1), pp.133-166.

Kolmogorov, A. 1941. AN Kolmogorov, Dokl. Akad. Nauk SSSR 30, 301 (1941). In: *Dokl. Akad. Nauk SSSR*, p.301.

Kovasznay, L.S., Kibens, V. and Blackwelder, R.F. 1970. Large-scale motion in the intermittent region of a turbulent boundary layer. *Journal of Fluid Mechanics.* **41**(2), pp.283-325.

Kreplin, H.P. and Eckelmann, H. 1979. Behavior of the three fluctuating velocity components in the wall region of a turbulent channel flow. *The Physics of Fluids.* **22**(7), pp.1233-1239.

Kuerten, J.G. and Vreman, A. 2015. Effect of droplet interaction on droplet-laden turbulent channel flow. *Physics of Fluids.* **27**(5), p053304.

Kulick, J.D., Fessler, J.R. and Eaton, J.K. 1994. Particle response and turbulence modification in fully developed channel flow. *Journal of Fluid Mechanics.* **277**(1), pp.109-134.

Kussin, J. and Sommerfeld, M. 2002. Experimental studies on particle behaviour and turbulence modification in horizontal channel flow with different wall roughness. *Experiments in Fluids.* **33**(1), pp.143-159.

Laín, S., Sommerfeld, M. and Kussin, J. 2002. Experimental studies and modelling of four-way coupling in particle-laden horizontal channel flow. *International Journal of Heat and Fluid Flow.* **23**(5), pp.647-656.

Laufer, J. 1951. *Investigation of turbulent flow in a two-dimensional channel*. (Doctoral thesis).

Laufer, J. 1954. The structure of turbulence in fully developed pipe flow. *National Advisor Committee for Aeronautics.* p1174.

Launder, B.E. and Ying, W.M. 1972. Secondary Flows in Ducts of Square Cross-Section. *Journal of Fluid Mechanics.* **54**(7), pp.289-295.

Lawn, C. 1971. The determination of the rate of dissipation in turbulent pipe flow. *Journal of Fluid Mechanics.* **48**(3), pp.477-505.

Lee, J. and Lee, C. 2015. Modification of particle-laden near-wall turbulence: Effect of Stokes number. *Physics of Fluids.* **27**(2), p023303.

Lee, S. and Durst, F. 1982. On the motion of particles in turbulent duct flows. *International Journal of Multiphase Flow.* **8**(2), pp.125-146.

Li, A. and Ahmadi, G. 1992. Dispersion and deposition of spherical particles from point sources in a turbulent channel flow. *Aerosol Science and Technology.* **16**(4), pp.209-226.

Li, A., Ahmadi, G., Bayer, R.G. and Gaynes, M.A. 1994. Aerosol particle deposition in an obstructed turbulent duct flow. *Journal of Aerosol Science.* **25**(1), pp.91-112.

Li, J., Wang, H., Liu, Z., Chen, S. and Zheng, C. 2012. An experimental study on turbulence modification in the near-wall boundary layer of a dilute gas-particle channel flow. *Experiments in Fluids.* **53**(5), pp.1385-1403.

Li, Q., Song, J., Li, C., Wei, Y. and Chen, J. 2013. Numerical and experimental study of particle deposition on inner wall of 180° bend. *Powder Technology.* **237**, pp.241-254.

Li, Y., McLaughlin, J.B., Kontomaris, K. and Portela, L. 2001. Numerical simulation of particle-laden turbulent channel flow. *Physics of Fluids.* **13**(10), pp.2957-2967.

Lin, J.T. 1972. Velocity spectrum of locally isotropic turbulence in the inertial and dissipation ranges. *The Physics of Fluids.* **15**(1), pp.205-207.

Liu, B.Y., Berglund, R.N. and Agarwal, J.K. 1974. Experimental studies of optical particle counters. *Atmospheric Environment.* **8**(7), pp.717-732.

Longmire, E.K., Khalitov, D.A. and Pothos, S. 2001. Experiments on Turbulent Particle-Laden Flows. *Energy and Environment.* Springer, pp.221-238.

Loth, E. 2000. Numerical approaches for motion of dispersed particles, droplets and bubbles. *Progress in Energy and Combustion Science.* **26**(3), pp.161-223.

Lund, E.G. 1977. *Mean flow and turbulence characteristics in the near corner region of a square duct*. thesis, University of Washington.

Lundgren, T. 2003. Linearly Forced Isotropic Turbulence. *Annual Research Briefs.* Minnesota University Minneapolis.

M. Kuerten, J.G. 2016. Point-Particle DNS and LES of Particle-Laden Turbulent flow - a state-of-the-art review. *Flow, Turbulence and Combustion.* **97**(3), pp.689-713.

Madabhushi, R.K. and Vanka, S. 1991. Large eddy simulation of turbulence-driven secondary flow in a square duct. *Physics of Fluids A: Fluid Dynamics.* **3**(11), pp.2734-2745.

Maday, Y. and Patera, A.T. 1989. Spectral element methods for the incompressible Navier-Stokes equations. In: *State-of-the-art Surveys on Computational Mechanics*, pp.71-143.

Marchioli, C., Giusti, A., Salvetti, M.V. and Soldati, A. 2003. Direct numerical simulation of particle wall transfer and deposition in upward turbulent pipe flow. *International Journal of Multiphase flow.* **29**(6), pp.1017-1038.

Marchioli, C. and Soldati, A. 2002. Mechanisms for particle transfer and segregation in a turbulent boundary layer. *Journal of Fluid Mechanics.* **468**(10), pp.283-315.

Marchioli, C., Soldati, A., Kuerten, J., Arcen, B., Taniere, A., Goldensoph, G., Squires, K., Cargnelutti, M. and Portela, L. 2008. Statistics of particle dispersion in direct numerical simulations of wall-bounded turbulence: Results of an international collaborative benchmark test. *International Journal of Multiphase Flow.* **34**(9), pp.879-893.

Mark, A. and van Wachem, B.G. 2008. Derivation and validation of a novel implicit second-order accurate immersed boundary method. *Journal of Computational Physics.* **227**(13), pp.6660-6680.

Matsumoto, S. and Saito, S. 1970. On the mechanism of suspension of particles in horizontal pneumatic conveying: Monte Carlo simulation based on the irregular bouncing model. *Journal of Chemical Engineering of Japan.* **3**(1), pp.83-92.

Maxey, M. 1987. The motion of small spherical particles in a cellular flow field. *The Physics of Fluids.* **30**(7), pp.1915-1928.

Maxey, M.R. and Riley, J.J. 1983. Equation of motion for a small rigid sphere in a nonuniform flow. *The Physics of Fluids.* **26**(4), pp.883-889.

McCoy, D. and Hanratty, T. 1977. Rate of deposition of droplets in annular two-phase flow. *International Journal of Multiphase Flow.* **3**(4), pp.319-331.

McKeon, B. and Smits, A. 2002. Static pressure correction in high Reynolds number fully developed turbulent pipe flow. *Measurement Science and Technology.* **13**(10), p1608.

Mckeon, B.J., Li, J.-d., Jiang, W., Morrison, J.F. and Smits, A.J. 2004. Further observations on the mean velocity distribution in fully developed pipe flow. *Journal of Fluid Mechanics.* **501**(2), pp.135-147.

McLaughlin, J.B. 1989. Aerosol particle deposition in numerically simulated channel flow. *Physics of Fluids A: Fluid Dynamics.* **1**(7), pp.1211-1224.

Mei, R. 1992. An approximate expression for the shear lift force on a spherical particle at finite Reynolds number. *International Journal of Multiphase Flow.* **18**(1), pp.145-147.

Melling, A. and Whitelaw, J.H. 1976. Turbulent-Flow in a Rectangular Duct. *Journal of Fluid Mechanics.* **78**(23), pp.289-315.

Moin, P. and Kim, J. 1985. The structure of the vorticity field in turbulent channel flow. Part 1. Analysis of instantaneous fields and statistical correlations. *Journal of Fluid Mechanics.* **155**(4), pp.441-464.

Mortensen, P., Andersson, H., Gillissen, J. and Boersma, B. 2008. Dynamics of prolate ellipsoidal particles in a turbulent channel flow. *Physics of Fluids.* **20**(9), p093302.

Moser, R. and Moin, P. 1984. Direct numerical simulation of curved turbulent channel flow. *NASA Technical Memorandum.* **10**.

Moser, R.D. and Moin, P. 1987. The effects of curvature in wall-bounded turbulent flows. *Journal of Fluid Mechanics.* **175**(4), pp.479-510.

NAO. 2015. *Progress on the Sellafield site: and update.* Comptroller and Auditor General.

NDA. 2017. *NDA Annual Report and Accounts 2016 to 2017.* Nuclear Decomissioning Authority.

NEA. 2016. *Five Years after the Fukushima Daiichi Accident.*

Nikuradse, J. 1926. *Untersuchung über die Geschwindigkeitsverteilung in turbulenten Strömungen.* Vdi-verlag.

Njobuenwu, D. and Fairweather, M. 2015a. Dynamics of single, non-spherical ellipsoidal particles in a turbulent channel flow. *Chemical Engineering Science.* **123**, pp.265-282.

Njobuenwu, D.O. and Fairweather, M. 2015b. Deterministic modelling of particle agglomeration in turbulent flow. In: *ICHMT DIGITAL LIBRARY ONLINE*: Begel House Inc.

Pan, Y. and Banerjee, S. 1996. Numerical simulation of particle interactions with wall turbulence. *Physics of Fluids.* **8**(10), pp.2733-2755.

Pao, Y.H. 1965. Structure of Turbulent Velocity and Scalar Fields at Large Wavenumbers. *The Physics of Fluids.* **8**(6), pp.1063-1075.

Paris, A. 2001. *Turbulence attenuation in a particle-laden channel flow.* thesis, Stanford University.

Patel, V. and Head, R. 1968. Reversion of turbulent to laminar flow. *Journal of Fluid Mechanics.* **34**(2), pp.371-392.

Patera, A.T. 1984. A spectral element method for fluid dynamics: laminar flow in a channel expansion. *Journal of Computational Physics.* **54**(3), pp.468-488.

Perry, A.E. 1982. *Hot-wire anemometry*. Clarendon Press.

Peskin, C.S. 2002. The immersed boundary method. *Acta numerica.* **11**, pp.479-517.

Picano, F., Breugem, W.-P. and Brandt, L. 2015. Turbulent channel flow of dense suspensions of neutrally buoyant spheres. *Journal of Fluid Mechanics.* **764**, pp.463-487.

Picano, F., Sardina, G. and Casciola, C. 2009. Spatial development of particle-laden turbulent pipe flow. *Physics of Fluids.* **21**(9), p093305.

Picciotto, M., Marchioli, C. and Soldati, A. 2005. Characterization of near-wall accumulation regions for inertial particles in turbulent boundary layers. *Physics of Fluids.* **17**(9), p098101.

Piomelli, U., Moin, P. and Ferziger, J.H. 1988. Model consistency in large eddy simulation of turbulent channel flows. *The Physics of Fluids.* **31**(7), pp.1884-1891.

Po, J.K.-o. 1975. *Developing turbulent flow in the entrance region of a square duct*. thesis, University of Washington.

Pope, S.B. 2001. *Turbulent flows*. IOP Publishing.

Portela, L.s.M., Cota, P. and Oliemans, R.V. 2002. Numerical study of the near-wall behaviour of particles in turbulent pipe flows. *Powder Technology.* **125**(2), pp.149-157.

Prandtl, L. 1927. Uber den Reibungswiderstand stromender Luft. *Munchen-Berlin.* **1**(5).

Reynolds, O. 1895. On the dynamical theory of incompressible viscous fluids and the determination of the criterion. *Philosophical Transactions of the Royal Society of London. A.* **186**, pp.123-164.

Richardson, L.F. 1922. *Weather prediction by numerical process.* Cambridge: University Press.

Riley, J.J. and Patterson Jr, G. 1974. Diffusion experiments with numerically integrated isotropic turbulence. *The Physics of Fluids.* **17**(2), pp.292-297.

Rosales, C. and Meneveau, C. 2005. Linear forcing in numerical simulations of isotropic turbulence: Physical space implementations and convergence properties. *Physics of Fluids.* **17**(9), p095106.

Rouson, D.W. and Eaton, J.K. 2001. On the preferential concentration of solid particles in turbulent channel flow. *Journal of Fluid Mechanics.* **428**(2), pp.149-169.

Rudman, M. and Blackburn, H.M. 1999. Large eddy simulation of turbulent pipe flow. In: *Second International Conference on CFD in the Minerals and Process Industries, Melbourne, Australia, Dec*, pp.6-8.

Sabot, J. and Comte-Bellot, G. 1976. Intermittency of coherent structures in the core region of fully developed turbulent pipe flow. *Journal of Fluid Mechanics.* **74**(4), pp.767-796.

Sadowski, Z. 1994. A study on hydrophobic aggregation of calcite aqueous suspensions. *Powder Technology.* **80**(2), pp.93-98.

Saffman, P. 1965. The lift on a small sphere in a slow shear flow. *Journal of Fluid Mechanics.* **22**(2), pp.385-400.

Sardina, G., Picano, F., Schlatter, P., Brandt, L. and Casciola, C.M. 2014. Statistics of particle accumulation in spatially developing turbulent boundary layers. *Flow, Turbulence and Combustion.* **92**(1-2), pp.27-40.

Sardina, G., Schlatter, P., Brandt, L., Picano, F. and Casciola, C.M. 2012. Wall accumulation and spatial localization in particle-laden wall flows. *Journal of Fluid Mechanics.* **699**(4), pp.50-78.

Schenkel, J. and Kitchener, J. 1960. A test of the Derjaguin-Verwey-Overbeek theory with a colloidal suspension. *Transactions of the Faraday Society.* **56**, pp.161-173.

Schiller, L. 1934. Neue quantitative Versuche zur Turbulenzentstehung. *ZAMM-Journal of Applied Mathematics and Mechanics/Zeitschrift für Angewandte Mathematik und Mechanik.* **14**(1), pp.36-42.

Schmidt, S., Mclver, D., Blackburn, H.M., Rudman, M. and Nathan, G. 2001. Spectral element based simulation of turbulent pipe flow. In: *14th Australasian Fluid Mechanics Conference, Adelaide, Australia, Dec*, pp.10-14.

Secker, J., Young, M. and Bradfute, J. 2004. Evaluation and mitigation of crud induced power shift. In: *19th KAIF/KNS Annual Conference*.

Sehmel, G.A. 1980. Particle and gas dry deposition: a review. *Atmospheric Environment (1967).* **14**(9), pp.983-1011.

Shahidzadeh, N., Bonn, D., Ragil, K., Broseta, D. and Meunier, J. 1998. Sequence of Two Wetting Transitions Induced by Tuning the Hamaker Constant. *Physical Review Letters.* **80**(18), pp.3992-3995.

Sharma, G. and Phares, D.J. 2006. Turbulent transport of particles in a straight square duct. *International Journal of Multiphase Flow.* **32**(7), pp.823-837.

Short, M.P., Hussey, D., Kendrick, B.K., Besmann, T.M., Stanek, C.R. and Yip, S. 2013. Multiphysics modeling of porous CRUD deposits in nuclear reactors. *Journal of Nuclear Materials.* **443**(1-3), pp.579-587.

Sippola, M.R. and Nazaroff, W.W. 2004. Experiments measuring particle deposition from fully developed turbulent flow in ventilation ducts. *Aerosol Science and Technology.* **38**(9), pp.914-925.

Smagorinsky, J. 1963. General circulation experiments with the primitive equations: I. The basic experiment. *Monthly Weather Review.* **91**(3), pp.99-164.

Soldati, A. and Marchioli, C. 2009. Physics and modelling of turbulent particle deposition and entrainment: Review of a systematic study. *International Journal of Multiphase Flow.* **35**(9), pp.827-839.

Squires, K.D. and Eaton, J.K. 1990. Particle response and turbulence modification in isotropic turbulence. *Physics of Fluids A: Fluid Dynamics.* **2**(7), pp.1191-1203.

Squires, K.D. and Eaton, J.K. 1991. Preferential concentration of particles by turbulence. *Physics of Fluids A: Fluid Dynamics.* **3**(5), pp.1169-1178.

Stenhammar, J., Linse, P., Wennerström, H. and Karlström, G. 2010. An Exact Calculation of the van der Waals Interaction between Two Spheres of Classical Dipolar Fluid. *The Journal of Physical Chemistry B.* **114**(42), pp.13372-13380.

Stokes, G.G. 1851. *On the effect of the internal friction of fluids on the motion of pendulums.* Pitt Press Cambridge.

Su, M. and Friedrich, R. 1994. Investigation of fully developed turbulent flow in a straight duct with large eddy simulation. *Journal of Fluids Engineering.* **116**(4), pp.677-684.

Sundaram, S. and Collins, L.R. 1999. A numerical study of the modulation of isotropic turbulence by suspended particles. *Journal of Fluid Mechanics.* **379**(1), pp.105-143.

Tao, B., Katz, J. and Meneveau, C. 1999. Application of HPIV data of turbulent duct flow for turbulence modeling. In: *3rd ASME/JSME Joint Fluids Engineering Conference*, pp.18-22.

Townsend, A. 1961. Equilibrium layers and wall turbulence. *Journal of Fluid Mechanics.* **11**(1), pp.97-120.

Tracy, H.J. 1963. *Turbulent flow in a three-dimensional channel*. thesis, Georgia Institute of Technology.

Tseng, Y.-H. and Ferziger, J.H. 2003. A ghost-cell immersed boundary method for flow in complex geometry. *Journal of Computational Physics.* **192**(2), pp.593-623.

Tsuji, Y. and Morikawa, Y. 1982. LDV measurements of an air–solid two-phase flow in a horizontal pipe. *Journal of Fluid Mechanics.* **120**(4), pp.385-409.

Tsuji, Y., Morikawa, Y. and Shiomi, H. 1984. LDV measurements of an air-solid two-phase flow in a vertical pipe. *Journal of Fluid Mechanics.* **139**(4), pp.417-434.

Uhlmann, M. 2005. An immersed boundary method with direct forcing for the simulation of particulate flows. *Journal of Computational Physics.* **209**(2), pp.448-476.

Uijttewaal, W. and Oliemans, R. 1996. Particle dispersion and deposition in direct numerical and large eddy simulations of vertical pipe flows. *Physics of Fluids.* **8**(10), pp.2590-2604.

van Wachem, B., Zastawny, M., Zhao, F. and Mallouppas, G. 2015. Modelling of gas–solid turbulent channel flow with non-spherical particles with large Stokes numbers. *International Journal of Multiphase Flow.* **68**, pp.80-92.

Varaksin, A.Y. and Polyakov, A. 1998. Measurements of the velocities of large particles using laser doppler anemometers. *Measurement Techniques.* **41**(8), pp.716-723.

Verwey, E.J.W. and Overbeek, J.T.G. 1955. Theory of the stability of lyophobic colloids. *Journal of Colloid Science.* **10**(2), pp.224-225.

Von Kármán, T. 1931. Mechanical similitude and turbulence.

Vreman, A. 2015. Turbulence attenuation in particle-laden flow in smooth and rough channels. *Journal of Fluid Mechanics.* **773**(6), pp.103-136.

Vreman, A. 2016. Particle-resolved direct numerical simulation of homogeneous isotropic turbulence modified by small fixed spheres. *Journal of Fluid Mechanics.* **796**(4), pp.40-85.

Vreman, A.W. and Kuerten, J.G.M. 2014. Comparison of direct numerical simulation databases of turbulent channel flow at Re-tau=180. *Physics of Fluids.* **26**(1).

Vreman, B., Geurts, B.J., Deen, N., Kuipers, J. and Kuerten, J.G. 2009. Two-and four-way coupled Euler–Lagrangian large-eddy simulation of turbulent particle-laden channel flow. *Flow, Turbulence and Combustion.* **82**(1), pp.47-71.

Wallace, J.M. 1985. The vortical structure of bounded turbulent shear flow. In: *Berlin, Heidelberg*. Springer Berlin Heidelberg, pp.253-268.

Walters, D.K. and Luke, W.H. 2010. Computational Fluid Dynamics Simulations of Particle Deposition in Large-Scale, Multigenerational Lung Models. *Journal of Biomechanical Engineering.* **133**(1), pp.011003-011003-011008.

Wang, J., Shen, Y. and Guo, Y. 2010. Seasonal circulation and influence factors of the Bohai Sea: a numerical study based on Lagrangian particle tracking method. *Ocean Dynamics.* **60**(6), pp.1581-1596.

Wang, Q. and Squires, K. 1996a. Large eddy simulation of particle deposition in a vertical turbulent channel flow. *International Journal of Multiphase Flow.* **22**(4), pp.667-683.

Wang, Q. and Squires, K.D. 1996b. Large eddy simulation of particle-laden turbulent channel flow. *Physics of Fluids.* **8**(5), pp.1207-1223.

Wattendorf, F.L. 1935. A study of the effect of curvature on fully developed turbulent flow. In: *Proceedings of the Royal Society of London A: Mathematical, Physical and Engineering Sciences*: The Royal Society, pp.565-598.

Westerweel, J., Draad, A., Van der Hoeven, J.T. and Van Oord, J. 1996. Measurement of fully-developed turbulent pipe flow with digital particle image velocimetry. *Experiments in Fluids.* **20**(3), pp.165-177.

Wilcken, H. 1967. *Effect of curved surfaces on turbulent boundary layers.*

Willmarth, W. 1975. Structure of turbulence in boundary layers. *Advances in Applied Mechanics.* Elsevier, pp.159-254.

Willmarth, W. and Lu, S. 1972. Structure of the Reynolds stress near the wall. *Journal of Fluid Mechanics.* **55**(1), pp.65-92.

Willmarth, W. and Tu, B.J. 1967. Structure of turbulence in the boundary layer near the wall. *The Physics of Fluids.* **10**(9), pp.S134-S137.

Winkler, C., Rani, S.L. and Vanka, S. 2004. Preferential concentration of particles in a fully developed turbulent square duct flow. *International Journal of Multiphase Flow.* **30**(1), pp.27-50.

Winkler, C., Rani, S.L. and Vanka, S. 2006. A numerical study of particle wall-deposition in a turbulent square duct flow. *Powder Technology.* **170**(1), pp.12-25.

WMSYM. 2016. *Sellafield Additional Sludge Retrievals, A Significant Step in Decommissioning Part of the U.K.'s Nuclear Legacy.* WMSYM.

World Nuclear Association. 2018. *Radioactive Waste Management.* [Online]. [Accessed 10th May]. Available from: http://www.world-nuclear.org/information-library/nuclear-fuel-cycle/nuclear-wastes/radioactive-waste-management.aspx

Wu, X. and Moin, P. 2008. A direct numerical simulation study on the mean velocity characteristics in turbulent pipe flow. *Journal of Fluid Mechanics.* **608**, pp.81-112.

Yao, J. and Fairweather, M. 2010. Inertial particle resuspension in a turbulent, square duct flow. *Physics of Fluids.* **22**(3), p033303.

Yeh, Y. and Cummins, H. 1964. Localized fluid flow measurements with an He–Ne laser spectrometer. *Applied Physics Letters.* **4**(10), pp.176-178.

Yeung, P. and Pope, S. 1989. Lagrangian statistics from direct numerical simulations of isotropic turbulence. *Journal of Fluid Mechanics.* **207**, pp.531-586.

Zagarola, M.V. and Smits, A.J. 1998. Mean-flow scaling of turbulent pipe flow. *Journal of Fluid Mechanics.* **373**, pp.33-79.

Zamansky, R., Vinkovic, I. and Gorokhovski, M. 2011. DNS and LES with stochastic modelling of subgrid acceleration applied to solid particles in a high Reynolds number channel flow. In: *TSFP DIGITAL LIBRARY ONLINE*: Begel House Inc.

Zhang, J., Tao, B. and Katz, J. 1997. Turbulent flow measurement in a square duct with hybrid holographic PIV. *Experiments in Fluids.* **23**(5), pp.373-381.

Zhao, F., George, W. and Van Wachem, B. 2015. Four-way coupled simulations of small particles in turbulent channel flow: The effects of particle shape and Stokes number. *Physics of Fluids.* **27**(8), p083301.

Zhao, L., Andersson, H.I. and Gillissen, J. 2010. Turbulence modulation and drag reduction by spherical particles. *Physics of Fluids.* **22**(8), p081702.